SERDP

FINAL REPORT

Application of Carbon and Nitrogen Stable Isotope Analysis to Evaluate Biotic and Abiotic Degradation of DNAN and NTO

Neil C. Sturchio
Chunlei Wang
Linnea Heraty
University of Delaware

Paul Hatzinger
Mark Fuller
APTIM Federal Services LLC.

September 2022

SERDP Project ER-2726

REPORT DOCUMENTATION PAGE					*Form Approved* *OMB No. 0704-0188*
The public reporting burden for this collection of information is estimated to average 1 hour per response, including the time for reviewing instructions, searching existing data sources, gathering and maintaining the data needed, and completing and reviewing the collection of information. Send comments regarding this burden estimate or any other aspect of this collection of information, including suggestions for reducing the burden, to the Department of Defense, Executive Services and Communications Directorate (0704-0188). Respondents should be aware that notwithstanding any other provision of law, no person shall be subject to any penalty for failing to comply with a collection of information if it does not display a currently valid OMB control number. **PLEASE DO NOT RETURN YOUR FORM TO THE ABOVE ORGANIZATION.**					
1. REPORT DATE *(DD-MM-YYYY)* 22-09-2022		**2. REPORT TYPE** SERDP Final Report		**3. DATES COVERED** *(From - To)* 28/09/2017 - 28/09/2022	
4. TITLE AND SUBTITLE Application of Carbon and Nitrogen Stable Isotope Analysis to Evaluate Biotic and Abiotic Degradation of DNAN and NTO				**5a. CONTRACT NUMBER** W912HQ-17-C-0025	
				5b. GRANT NUMBER NA	
				5c. PROGRAM ELEMENT NUMBER NA	
6. AUTHOR(S) Sturchio Neil C.; Wang, Chunlei; Heraty, Linnea J. (University Delaware) Fuller, Mark E.; Hatzinger, Paul J. (Aptim Federal Services, LLC)				**5d. PROJECT NUMBER** ER-2726	
				5e. TASK NUMBER NA	
				5f. WORK UNIT NUMBER NA	
7. PERFORMING ORGANIZATION NAME(S) AND ADDRESS(ES) University of Delaware 222 S. Chapel St. Newark, DE 19716				**8. PERFORMING ORGANIZATION REPORT NUMBER** ER-2726	
9. SPONSORING/MONITORING AGENCY NAME(S) AND ADDRESS(ES) Strategic Environmental Research and Development Program 4800 Mark Center Drive, Suite 16F16 Alexandria, VA 22350-3605				**10. SPONSOR/MONITOR'S ACRONYM(S)** SERDP	
				11. SPONSOR/MONITOR'S REPORT NUMBER(S) ER-2726	
12. DISTRIBUTION/AVAILABILITY STATEMENT Distribution Statement A: Approved for Public Release, Distribution is Unlimited					
13. SUPPLEMENTARY NOTES None					
14. ABSTRACT The key objectives of this project were (1) to develop and validate compound-specific stable isotope analysis (CSIA) methods for carbon and nitrogen in the insensitive munitions constituents 2,4-dinitroanisole (DNAN) and 3-nitro-1,2,4-triazol-5-one (NTO) and (2) to quantify kinetic isotope effects in carbon and nitrogen during the biotic and abiotic degradation of these compounds. These objectives were accomplished. The resulting isotopic enrichment parameters provide insights into natural and engineered degradation pathways and new diagnostic measurement tools that will allow the extent of in situ degradation to be quantified in soils and natural waters on ranges and other contaminated sites. This research was responsive to ERSON-17-03 as it provides new methods to "develop an improved understanding of the fate and effects of the components DNAN and NTO that are used in the insensitive munitions formulations. This project also provides a valuable means by which to assess the necessity and effectiveness of in situ enhancement of biotic and/or abiotic degradation strategies for these insensitive munitions compounds.					
15. SUBJECT TERMS DNAN, NTO, insensitive munitions, stable isotopes, carbon, nitrogen, CSIA, isotope effect, abiotic, biotic, degradation, photolysis					

16. SECURITY CLASSIFICATION OF:			**17. LIMITATION OF ABSTRACT**	**18. NUMBER OF PAGES**	**19a. NAME OF RESPONSIBLE PERSON** Neil C. Sturchio
a. REPORT	**b. ABSTRACT**	**c. THIS PAGE**	UU	140	
U	U	U			**19b. TELEPHONE NUMBER** *(Include area code)* 302-831-8706

TABLE OF CONTENTS

List of Tables

List of Figures

instantaneous product) and DNP (accumulated products) associated with a normal secondary kinetic isotope effect during S_N2Ar nucleophilic substitution in a closed reaction container.

List of Acronyms and Abbreviations

2-ANAN	3-nitro-4-methoxyaniline
4-ANAN	4-amino-2-nitroanisole
ATCC	American Type Culture Collection
ATO	3-amino-1,2,4-triazol-5-one
BSM	basal salts medium
^{12}C	carbon-12
^{13}C	carbon-13
Cl^-	chloride
CO_2	carbon dioxide
cm	centimeter
CSIA	compound-specific isotope analysis
CT	Connecticut
δ	delta; stable isotope ratio notation
DAAN	2,4-diaminoanisole
DFT	density-functional theory
DNAN	2,4-dinitroanisole
DNP	2,4-dinitrophenol
DoD	Department of Defense
ε	epsilon; stable isotope enrichment factor
EA-IRMS	elemental analyzer-isotope ratio mass spectrometer
EISL	Environmental Isotope Science Laboratory
EPA	Environmental Protection Agency
Fe	iron
FID	flame ionization detector
FTIR	Fourier-Transform infrared
GC	gas chromatogaph
GC-qMS	gas chromatograph-quadrupole mass spectrometer
GC-IRMS	gas chromatograph-isotope ratio mass spectrometer
h	hour
HTO	3-hydroxyamino-1,2,4-triazol-5-one
HPLC	high-performance liquid chromatography
IM	insensitive munitions
IRMS	isotope-ratio mass spectrometer
KIE	kinetic isotope effect
L	liter
MA	Massachusetts
MCT	mercury cadmium telluride
MD	Maryland
MeOH	methanol
2-M-5-NP	2-methoxy-5-nitrophenol
4-M-2-NP	4-methoxy-2-nitrophenol
MENA	2-methoxy-5-nitroaniline
MMO	methane monooxygenase
MMOB	regulatory protein component of MMO

MMOH	hydroxylase component of MMO
MMOR	reductase component of MMO
MNTO	4-methyl-3-nitro-1,2,4-triazol-5-one
MOPS	3-(N-morpholino)propanesulfonic acid buffer
μg	microgram
2-NA	2-nitroanisole
4-NA	4-nitroanisole
NADH	nicotinamide adenine dinucleotide (NAD) + hydrogen
NAD(P)H	nitrite reductase
ng	nanogram
^{14}N	nitrogen-14
^{15}N	nitrogen-15
NMR	nuclear magnetic resonance
NTO	3-nitro-1,2,4-triazol-5-one
NO_3^-	nitrate
NO_2^-	nitrite
^{16}O	oxygen-16
^{18}O	oxygen-18
OD	optical density
PA	Pennsylvania
PAH	polyaromatic hydrocarbons
‰	per mil
PI	Principal Investigator
pMMO	particulate methane monooxygenase
RAMM	revised anaerobic minimal medium
RDX	hexahydro-1,3,5-trinitro-1,3,5-triazine
RNS	reactive nitrogen species
ROS	reactive oxygen species
rpm	revolutions per minute
SERDP	Strategic Environmental Research and Development Program
sMMO	soluble methane monooxygenase
SPE	solid phase extraction
S.U.	standard unit
TCD	thermal conductivity detector
TC/EA-IRMS	thermal conversion/elemental analyzer-isotope rato mass spectrometer
TNT	trinitrotoluene
UALLE	ultrasonic-assisted liquid-liquid extraction
UD	University of Delaware
USGS	United States Geological Survey
VA	Virginia
VPDB	Vienna Pee Dee Belemnite
VSMOW	Vienna Standard Mean Ocean Water

Keywords

Acknowledgements

Executive Summary

Introduction

The U.S. Department of Defense (DOD) is developing and testing explosive compounds, formulations, and munitions that are safer to transport, handle, and store than current formulations. DNAN (2,4-dinitroanisole) is being tested as a replacement for TNT (2,4,6-trinitrotoluene), while NTO (3-nitro-1,2,4-trazol-5-one) is being evaluated as a replacement for RDX (hexahydro-1,3,5-trinitro-1,3,5-triazine). DNAN was used in some munitions during World War II due to a shortage of TNT (Boddu et al., 2009), and is widely used as a precursor for dye manufacture (Fishbein, 1979). Only in the last 15 years have measurements of the fundamental chemical properties of DNAN (solubility, K_{ow}, Henry's Law constant; Boddu et al., 2008) been reported. By comparison, there is significantly more information available regarding the chemical properties and biodegradation of NTO, some of which was published more than two decades ago (Smith et al., 1999; Le Campion et al., 1998, 1999). Of particular interest from these early reports is the high aqueous solubility of NTO (>10,000 mg/L) compared to RDX (~40 mg/L), which is likely to dramatically influence its transport, degradation, uptake, and toxicity. While several recent SERDP-funded projects have provided new insights into the fate and transport of insensitive munition formulations (IM) and their constituent compounds, there remain substantial data gaps. This project addressed crucial data gaps in the knowledge of kinetic isotope effects during biotic and abiotic transformations of DNAN and NTO. Such data will provide a tool for improved understanding and prediction of the environmental behavior of DNAN and NTO.

Objectives

The key objectives of this project were (1) to develop and validate compound-specific stable isotope analysis (CSIA) methods for carbon and nitrogen in DNAN and NTO; and (2) to use these new CSIA methods and other analytical and modeling tools to quantify kinetic isotope effects in C and N during the biotic and abiotic transformations of these insensitive munition compounds. Laboratory experiments were performed to examine a variety of commonly occurring biotic and abiotic transformations, and the measured isotope effects provided new diagnostic measurement tools that may allow these transformations to be more clearly assessed and quantified in natural environments.

Technical Approach

The overall approach of this project was to first develop and validate CSIA methods for DNAN and NTO and then to perform a series of laboratory experiments to evaluate the kinetic isotope effects in DNAN and NTO during abiotic and biotic degradation. The CSIA method for DNAN was developed by modification of the GC-IRMS (gas chromatography/isotope-ratio mass spectrometry) method that our team had developed earlier for RDX as part of ESTCP Project ER-201208 (Fuller et al., 2016). For NTO, a new approach was necessary as the strong polarity of the NTO molecule precluded its direct isotopic analysis by GC-IRMS. This challenge was overcome by developing a derivatization method to convert NTO to methyl-NTO which is a molecule that is amenable to isotopic analysis by GC-IRMS (Wang et al., 2021c). Once the CSIA methods for DNAN and NTO were available, we proceeded to perform experiments to examine isotope effects during biotic transformations of DNAN and NTO in relatively simple laboratory systems under aerobic and anoxic conditions using pure bacterial cultures and

bacterial microcosms prepared from environmental samples. We also performed experiments to examine isotope effects during abiotic transformations involving alkaline hydrolysis, chemical reduction, and UV irradiation (Wang et al., 2021a). In addition, we performed an ^{18}O tracer experiment to resolve the mechanism of alkaline hydrolysis of DNAN (Wang et al., 2020) and performed ancillary measurements by ^{13}C NMR and density-functional theory calculations to better understand the position-specific carbon and nitrogen isotope effects within the DNAN molecule during alkaline hydrolysis (Wang et al., 2021b).

Results and Discussion

Task 1 of this project involved the development and validation of compound-specific isotope analysis methods for DNAN and NTO. For DNAN, a combined gas chromatography (TRACE™ 1310 GC)/quadrupole mass spectrometer (Thermo Scientific ISQ II LT)/isotope ratio mass spectrometer (Thermo Scientific Delta V Plus) (i.e. GC-qMS/IRMS) method was developed and validated for analysis of chemical concentrations (external standard calibration) together with compound-specific C and N isotope ratios in DNAN and its reaction products DNP (2,4-dinitrophenol), 2-ANAN (2-amino-4-nitroanisole), and 4-nitroguaiacol (4-NG) (Wang et al., 2021a). This method yielded $\delta^{13}C$ and $\delta^{15}N$ values having typical 1σ reproducibility of ± 0.2 ‰, with at least 0.15 micrograms of carbon and 2 micrograms of nitrogen required for isotope ratio analysis. Separation GC-IRMS runs were required for carbon and nitrogen isotope analyses. For NTO, which has high polarity and is not readily separable by gas chromatography, a derivatization procedure was required to convert NTO to methyl-NTO, which is a semivolatile compound that could be separated by gas chromatography to enable its isotopic analysis by GC-IRMS. The method developed for isotopic analysis of NTO thus required a correction for the added carbon atom of the methyl group; the method requires at least 0.79 micrograms of NTO and yields a 1σ reproducibility of ± 0.3 ‰ for measured values of both $\delta^{13}C$ and $\delta^{15}N$ (Wang et al., 2021c). The $\delta^{13}C$ measurements for methyl-NTO by this method are subject to potential interference from co-eluting organic compounds if the NTO extract is not sufficiently pure during the derivatization reaction, and in such cases it may be necessary to further purify NTO prior to derivatization by using additional SPE (solid-phase extraction) and/or liquid-liquid extraction (LLE) steps.

Methods for extraction of DNAN from aqueous solutions were also investigated, including SPE and ultrasonic assisted liquid-liquid extraction (UALLE). Solid-phase extraction using Supelclean ENVI-Chrom P SPE columns was found to be effective in preconcentrating DNAN and NTO from aqueous solutions, followed by elution with acetonitrile, evaporation of acetonitrile, and uptake of DNAN or NTO into ethyl acetate for GC-IRMS analyses. The SPE preconcentration step had a high yield (~85%) and did not cause significant isotopic fractionation of carbon or nitrogen in DNAN or NTO. Ultrasonic liquid-liquid extraction (water/ethyl acetate) was found to have nearly quantitative yield (>99%) for DNAN and ~82% for NTO; when used for NTO extraction from microbial culture media it was effective at removing phosphate and sugars that interfere with the derivatization reaction.

Task 2 of this project involved characterization of the carbon and nitrogen kinetic isotope effects accompanying biotransformation of DNAN and NTO by selected pure cultures and consortia under aerobic and anoxic conditions. The ability of methanotrophs to transform DNAN and NTO under aerobic conditions was confirmed and interpreted to be caused by an oxygen-insensitive nitro-reductase enzyme system (Fuller et al., 2020). Kinetic isotope effects accompanying biotransformation of DNAN and NTO by three aerobic pure cultures and three

microbial consortia were examined in this study. The pure cultures were *Pseudomonas fluorescens* I-C (Blehert et al., 1999; Fuller et al., 2009), *Rhodococcus Ruber* ENV-425 (Steffan et al., 1997; Fournier et al., 2009; Tupa and Matsuda, 2018), and *Rhodococcus aetherivorans* ENV-493 (isolated from groundwater at a Naval Air Station as part of ESTCP Project 201733). The two anaerobic enrichment cultures we examined were MBR (isolated from a membrane bioreactor system) and Dahlgren Runoff (a culture derived from surface runoff from the Dahlgren (Virginia) facility of the U. S. Navy); we also examined an aerobic enrichment culture Dahlgren Methanotrophs (derived from groundwater at the Dahlgren facility).

The general approach for evaluating isotope effects associated with biotransformation of DNAN and NTO is described here. All cultures used were first prepared for testing by washing via centrifugation. The washing process was as follows: cultures were centrifuged and resuspended in their respective media unless otherwise noted, and then centrifuged again under the same conditions before final resuspension into a fresh one-liter batch of their respective media in a two-liter glass bottle, then amended with DNAN or NTO at a nominal concentration of 30 mg/L. Carbon sources were added, and the solution was incubated at room temperature on a magnetic stir plate with air sparging for aerobic conditions. Tests performed under anoxic conditions were not sparged with any gases during the experiment. The carbon source concentration was periodically measured, and more was added as needed until degradation was complete. The temperature during these experiments averaged 22°C. At set intervals, samples were collected to monitor DNAN or NTO concentrations. When designated target residual concentrations were reached, larger sample aliquots were taken for isotope measurements. These samples for GC-IRMS measurements of carbon and nitrogen isotope ratios were centrifuged, and the supernatant was removed and acidified to pH <2 with 1:1 HCl. Aliquots from DNAN experiments were stored at 4 °C until they were processed via SPE. DNAN was eluted from the SPE cartridges with acetonitrile, and then shipped to the University of Delaware for isotopic analysis. Aliquots from NTO experiments were stored at -80 °C and not processed by SPE. Instead, they were kept frozen and transported to the University of Delaware where they were thawed and processed by ultrasonic liquid-liquid extraction immediately before isotopic analysis.

DNAN biotransformation by aerobic pure cultures ENV425 and ENV493 required several days to reach completion. DNAN transformation by *Pseudomonas fluorescens* I-C required approximately 11 days. The DNAN breakdown products 2-ANAN and 4-ANAN were observed in all replicates and were generally dominated by 2-ANAN. Anoxic DNAN transformation by the MBR enrichment culture was completed in about 24 hours. Breakdown product 2-ANAN dominated 4-ANAN roughly 2:1. In contrast, the Runoff enrichment transformed all the DNAN in less than three hours, and final 2-ANAN concentrations were only slightly higher than 4-ANAN. Isotope enrichment factors accompanying biotransformation of DNAN for carbon (ϵ_C values) ranged from -0.74 to -2.24 ‰ in the pure aerobic cultures and the aerobic enrichment consortium, while those for nitrogen (ϵ_N values) ranged from -10.8 to -15.7 ‰. The eC values for the anoxic enrichment consortia were -1.93 for the Dahlgren Runoff culture and -4.34 for the MBR culture, whereas the ϵ_N values indistinguishable from each other (-23.2 ‰ and -22.7 ‰, respectively). The relatively high ϵ_N values and low ϵ_C values in all DNAN biotransformation experiments, as well as the principal DNAN breakdown product being 2-ANAN, are consistent with nitro-reduction as the first stage of the DNAN biotransformation pathway.

NTO biotransformation by the aerobic pure culture *Pseudomonas fluorescens* I-C took 48 days to reach completion. The Dahlgren Methanotrophs consortium took 57 days to transform all the NTO under aerobic conditions. In contrast, the MBR consortium took only about 3.5 days to transform NTO under anoxic conditions. In all NTO biotransformation experiments, ATO was the sole breakdown product detected. Unfortunately, the presence of a high abundance of chromatographic interferences with methyl-NTO precluded reliable measurement of εC values for these experiments by GC-IRMS. The εN values were -20.9 ‰ for the aerobic pure culture *Pseudomonas fluorescens* I-C, -10.3 ‰ for the aerobic consortium Dahlgren Methanotrophs, and -9.6 ‰ for the anoxic consortium MBR. The εN values measured for NTO biotransformation were all within the range of those measured for DNAN biotransformation, and the sole breakdown product observed in the NTO experiments was ATO. These results indicate that nitro-reduction was the first stage of the biotransformation pathway for NTO under both aerobic and anaerobic conditions.

Task 3 involved measurements of the kinetic isotope effects in DNAN and NTO during abiotic transformations including alkaline hydrolysis, UV-induced photolysis upon irradiation at ~254 nm and ~350 nm wavelengths, nitro-reduction by electron transfer from quinone, and nitroreduction by electron transfer from Fe^{2+} adsorbed on hematite.

Position-specific isotope effects during alkaline hydrolysis were examined with several experiments conducted at 55 ºC in dilute NaOH solutions (initial pH values of 11.0, 11.7, and 12.0) having initial DNAN concentration of 0.126 mM. The reaction was quenched at varying extent by reducing the pH to < 3 with HCl. DNAN was extracted into ethyl acetate from the acidifed solution by ultrasonic-assisted liquid-liquid extraction prior to isotopic analysis of carbon and nitrogen by GC-IRMS (Wang et al., 2021b). The bulk isotope enrichment factor measured for carbon, ε_C, was -40.8 ‰ and that for nitrogen, εN, was -3.2 ‰. Using a combination of density-functional theory calculations and quantitative ^{13}C NMR, position-specific isotope enrichment factors for both ^{13}C and ^{15}N were determined (Wang et al., 2021b).

The pathway of the net alkaline hydrolysis reaction DNAN + H2O ==> DNP + CH3OH at 55 ºC and pH 12 was resolved using ^{18}O-labeled water. The verified reaction pathway is a SN2Ar nucleophilic aromatic substitution with –OH replacing the methoxy leaving group (–OCH3) at the DNAN C1 site. Free energies of alkaline hydrolysis of DNAN by two putative reaction pathways were calculated by density-functional theory, including explicit solvation of DNAN with 10 H2O molecules and one OH^- ion, gave a prediction in agreement with the experimental result (Wang et al., 2020).

Phototransformation of aqueous DNAN and NTO by UV irradiation was examined experimentally at nominal wavelengths of ~350 nm (UV-A) and ~254 nm (UV-C) in 0.2 mM aqueous solutions. Experiments were performed using a photolysis reactor where aqueous solution was continuously recycled through a UV-irradiated volume from a non-irradiated external reservoir. Phototransformation with 1st-order kinetics was complete in ~600 h with UV-A irradiation and ~60 h with UV-C irradiation; reaction products under both UV wavelengths included DNP, 2-ANAN, NO_2^-, and NO_3^-. By tracking C and N isotopic fractionation in DNAN and its reaction products during the reaction, we observed normal ^{13}C fractionation ($\varepsilon C = -3.34‰$) and inverse ^{15}N fractionation ($\varepsilon N = +12.30‰$) under UV-A irradiation, in contrast to inverse ^{13}C fractionation ($\varepsilon C = +1.45‰$) and normal ^{15}N fractionation ($\varepsilon N = -3.79‰$) under UV-C irradiation.

A similar set of experiments was performed with 0.8 mM NTO solutions. One experiment was performed with equal concentrations of NTO and NaCl under UV-C irradiation

to examine the effect of NaCl on the phototransformation of NTO. The observed kinetics of NTO photolysis were best approximated by one-stage 0.5^{th}-order (UV-C irradiation) and two-stage 0.5^{th}-order (UV-A irradiation) rate laws, respectively; the rate was ~50% lower in NaCl-bearing solution than in NaCl-free solution under UV-C irradiation. Reactions went to completion in ~350 h (UV-A) and ~80 h (UV-C in pure NTO solution) or ~170 h (UV-C in NTO+NaCl solution); reaction products included ATO (UV-C only), NO_2^-, NO_3^-, and NH_4^+. In residual NTO extracted from NaCl-free solutions, nitrogen isotope fractionation was observed with similar bulk enrichment factor values of ε_N = -6.64 ± 0.51 ‰ under UV-C irradiation and ε_N = -7.58 ± 0.39 ‰ under UV-A irradiation. In contrast, carbon isotope fractionations in NaCl-free solutions had opposite signs of enrichment factor values: ε_C = +4.75 ± 0.01 ‰ under UV-C irradiation and ε_C = -2.85 ± 0.01 ‰ under UV-A irradiation. In NaCl-bearing solution under UV-C irradiation, the nitrogen isotope enrichment factor, ε_N, had a value of -7.87 ± 0.40 ‰, indistinguishable from that in NaCl-free solution. However, the enrichment factor value for carbon in NaCl-bearing solution under UV-C irradiation was ε_C = -4.27 ± 0.03, similar in magnitude but opposite in sign to that observed in NaCl-free solution.

Isotope effects for carbon and nitrogen were examined during reductive transformation of DNAN by 9,10-anthraquinone-2-disulfonate, a surrogate for humic substances. The experimental solution contained initial AQS and DNAN concentrations of 26 mM and 0.65 mM, respectively. Reduction of DNAN occurred rapidly with a first-order rate constant of 0.0096 s^{-1}. The observed isotope enrichment factors for this abiotic transformation were εC = -0.57 ‰ and εN = -19.72 ‰, respectively.

One experiment was performed to examine the isotope effect associated with DNAN reduction by the hematite/aqueous Fe^{2+} redox couple. The value of ε_N obtained from this set of data was $-15.69 ± 1.46$ ‰. This value agrees well with those obtained for abiotic reduction of DNAN in systems containing the Fe^{3+}-bearing minerals goethite and magnetite in contacted with dissolved Fe^{2+} (Berens et al., 2020).

The ratio of isotope enrichment factors, $\varepsilon N/\varepsilon C$, is commonly denoted as $\Lambda^{N/C}$. This ratio is defined by the slope of a data array in a $\Delta\delta^{15}N$ $vs.$ $\Delta\delta^{13}C$ plot, and specific $\Lambda^{N/C}$ values (or ranges of values) are characteristic of different transformation pathways. For example, various $\Lambda^{N/C}$ values are evident in a $\Delta\delta^{15}N$ $vs.$ $\Delta\delta^{13}C$ diagram showing data generated by our team during this project (Fig. ES-1). Values of $\Lambda^{N/C}$ have relatively large positive values of 37.5 for the AQS reduction abiotic transformation and 10.7 for the aerobic Runoff consortium nitro-reduction biotransformation, a relatively small value of 0.55 for the alkaline hydrolysis reaction, and negative values of -3.75 and -2.55 for abiotic phototransformation under UV-A and UV-C irradiation, respectively. These characteristic $\Lambda^{N/C}$ may be diagnostic tools for evaluating DNAN attenuation pathways in natural waters.

Implications for Future Research and Benefits

This project achieved its objectives of the development and application of methods for compound-specific stable isotope analysis of carbon and nitrogen in DNAN and NTO. The new analytical methods developed here were used to measure isotopic enrichment factors and enrichment factor ratios of carbon and nitrogen for different biotic and abiotic transformation pathways of DNAN and NTO. These data provide new diagnostic measurement tools that enable transformation mechanisms to be more clearly evaluated in groundwater and other environments, along with quantitative assessments of the extents of transformation of DNAN and NTO on ranges and other contaminated field sites.
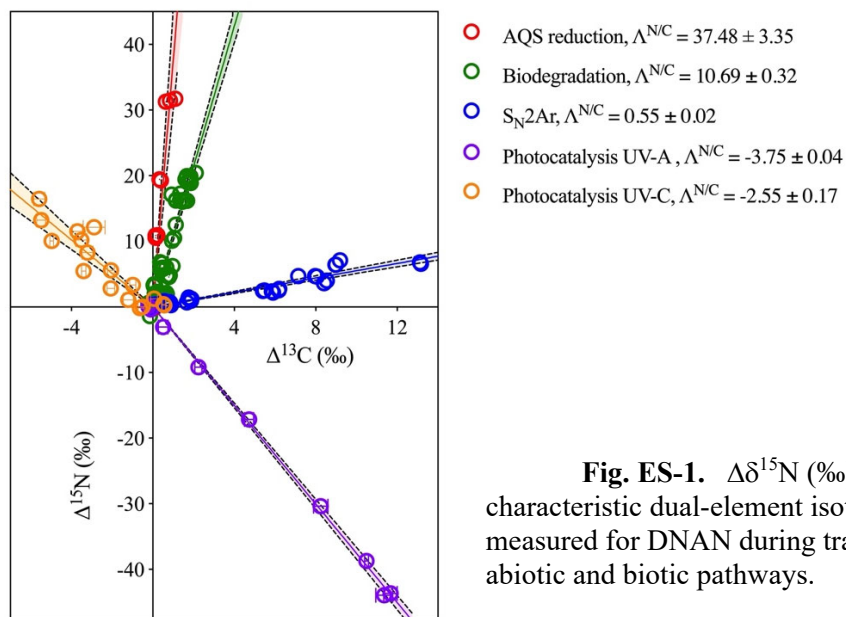
Fig. ES-1. $\Delta\delta^{15}N$ (‰) vs. $\Delta\delta^{13}C$ (‰) diagram showing characteristic dual-element isotope enrichment correlation trends measured for DNAN during transformation by a variety of abiotic and biotic pathways.

The results of this project highlighted several areas in which additional research is recommended: (1) further investigations of biotransformation-induced isotope effects under a range of physical conditions and variable substrate concentrations and solution compositions, to elucidate the variability of enzymatic isotope effects for given enzyme systems; (2) further investigation of direct and indirect photolytic isotope effects for a wide range of contaminant concentrations and bulk solution composition, including isotope measurements of photo-transformation products to elucidate interactions of transient intermediates such as those involved in re-nitration and chlorination pathways. These are especially needed for UV wavelengths present in the solar radiation spectrum at Earth's surface; (3) development and application of compound-specific oxygen isotope analysis methods, to explore the extent to which oxygen isotope effects may give further insights into both abiotic and biotic transformation pathways; (4) development of methods for the application of orbitrap-based hybrid mass spectrometers to whole-molecule stable isotope analysis, to facilitate further progress in the realm of compound-specific stable isotope analysis; and (5) further development of quantum mechanical/molecular mechanics modeling to predict reaction pathways and isotope effects. Even at the current state of knowledge of multi-element compound-specific isotope effects that accompany abiotic and biotic transformations under typical environmental conditions, such data are clearly useful and provide cost-effective value for remedial investigations and cleanup of contaminated sites. Further research to expand this knowledge base will contribute to increasing the value of multi-element compound-specific isotope analysis for environmental restoration programs.

1.0   Introduction

1.1. Objectives

The objectives of this project were to develop and validate CSIA methods for the insensitive munitions (IM) constituents DNAN and NTO, and to apply these methods to measure kinetic isotope effects associated with biotic and abiotic degradation of these compounds.   This provides a new measurement tool and valuable diagnostic criteria that can be used by DoD to quantify the extents, rates, and pathways of abiotic and biotic degradation of DNAN and NTO at field sites. This approach yields critical data to support monitored natural attenuation as a remedy for treating these energetic compounds in soil, surface water and groundwater at DoD sites, and to confirm the effectiveness of other *in situ* remediation strategies.

1.2. Background

New insensitive munitions formulas have been developed to replace the conventional explosives TNT (2,4,6-trinitrotoluene) and RDX (hexahydro-1,3,5-trinitro-1,3,5-triazine). Principal consituents of these new formulas include DNAN (2,4-dinitroanisole) and NTO (3-nitro-1,2,4-triazol-5-one). The physical and chemical properties of DNAN and NTO have been investigated extensively, not only for their applications in munitions, but also with the aim of understanding their environmental behavior and ecological risk. Previous environmentally-oriented investigations of DNAN and NTO have focused mainly on biological transformations (Le Campion et al., 1999; Platten et al., 2010; Perreault et al., 2012; Olivares et al., 2013; Richard and Weidhaas, 2014; Hawari et al., 2015; Krzmarzick et al., 2015; Madeira et al., 2017; Jog et al., 2020), abiotic transformations (Le Campion et al., 1999; Rao et al., 2013; Salter-Blanc et al., 2013; Shen et al., 2013; Sviatenko et al., 2014; Taylor et al., 2017; Becher et al., 2019; Cardenas-Hernandez et al., 2020; Murillo-Gelvez et al., 2021), and ecotoxicity (Haley et al., 2009; Dodard et al., 2013; Liang et al., 2013; Quinn et al., 2014; Crouse et al., 2015; Stanley et al., 2015; Madeira et al., 2018; Lent et al., 2020).

One potential alternative for remediation of energetic nitro-organic contaminants on military ranges and other facilities is monitored natural attenuation (MNA), in which contaminant losses by naturally-occurring physical, chemical, and biological processes are evaluated. When intrinsic loss rates are sufficient, these processes alone can be utilized to meet groundwater protection standards for a contaminant without human intervention. MNA is now commonly implemented as a remedy for chlorinated solvents, and this approach has been evaluated for various other contaminants, including the explosive 2,4,6-trinitrotoluene (TNT). The USEPA has issued a guidance document for using compound-specific isotope analysis (CSIA) for biodegradation rate determinations, wherein they confirm the unique value of this method for MNA (Hunkeler et al., 2009).

Compound-specific isotope analysis is increasingly being applied as an analytical tool to quantify and distinguish the biological and abiotic degradation of a variety of industrial and military pollutants, including chlorinated solvents (Liang et al., 2007; Elsner et al., 2008; Cretnik et al., 2013), nitroaromatic compounds (Hartenbach et al., 2006; Tobler et al., 2007; Wijker et al., 2013), fuel components and additives (Kuder et al., 2005; Vogt et al., 2008; Kuder et al., 2012) and anions, such as perchlorate and nitrate (Sturchio et al., 2003, 2007; Hatzinger et al., 2009). Our research team has recently developed and applied a CSIA method for RDX to quantify stable isotope fractionation of C and N during RDX biodegradation by bacterial strains (Hatzinger et al., 2014; Fuller et al., 2016) and *in situ* in field settings (Fuller et al., 2020). This

approach relies on the fact that heavier isotopologues (e.g., an RDX molecule that contains a ^{15}N atom substituting for a ^{14}N atom) will typically react more slowly than lighter ones due to the greater bond stabilities and slower reaction rates of the heavy isotope-substituted sites in the molecules. This leads to a characteristic enrichment of heavy isotopes within the residual parent molecules and a depletion in heavy isotopes in the products. Subsequently, if isotope fractionation is sufficiently large, analysis of stable isotope ratios of a contaminant along the flow path of a plume and/or in contaminated groundwater can be used to document natural attenuation or engineered remediation *in situ*. In addition, CSIA can provide critical information on specific reaction mechanisms, because the breaking of a specific bond is typically associated with a characteristic kinetic isotope effect (KIE). Different degradation pathways (e.g., abiotic vs. biotic, or aerobic vs. anaerobic) may result in different isotopic enrichment factors for C, N, and H (Hartenbach et al., 2006, 2008; Liang et al., 2007; Elsner et al., 2005; Elsner, 2010; Hatzinger et al., 2013; Hofstetter et al., 2014; Broholm et al., 2014; Elsner and Imfeld, 2016; Ulrich et al., 2018; Berens et al., 2019). Thus, CSIA is clearly a powerful tool to quantify and potentially distinguish biotic and abiotic degradation of organic contaminants in natural environments. In this project, we have developed new CSIA methods for carbon and nitrogen isotope ratio measurements of DNAN and NTO, and applied these methods to measure characteristic kinetic isotope effects for these compounds during a variety of biotic and abiotic transformations that are relevant to conditions in soil, surface water, and groundwater at ranges and other contaminated sites.

2.0 Project Task 1: Development and validation of compound-specific isotope analysis (CSIA) methods for DNAN and NTO

This section of the report describes the methods we developed for compound-specific isotope analysis (CSIA) of C and N in DNAN and NTO. Our method of choice for these analyses was gas chromatography/isotope-ratio mass spectrometry (GC-IRMS). GC-IRMS methods have the advantage of being able to separate multiple compounds present in a mixture so that isotope ratios of C and N in each compound can be measured, provided that the mixture contains compounds that are separable on a GC. For DNAN measurements, we used a modified version of the GC-IRMS analytical method that we had developed earlier as part of ESTCP Project ER-201208: *Validation of Stable Isotope Ratio Analysis to Document the Biodegradation and Natural Attenuation of RDX* (Fuller et al., 2016). For NTO, because its polarity precludes direct CSIA by GC-IRMS, it was first necessary to develop a derivatization method to transform NTO into a GC-separable compound. This was accomplished by using a low-temperature methylation reaction to produce methyl-NTO (MNTO), which is amenable to GC separation for isotopic analysis by GC-IRMS. The GC-IRMS method used for CSIA of MNTO was identical to that used for DNAN. All GC-IRMS measurements for this project were performed on a newer (installed in 2015) GC-qMS-IRMS system that allowed simultaneous quadrupole mass scans and isotope-ratio analysis of GC peaks. The in-line quadrupole mass spectrometer (qMS) facilitated the positive identification and quantitation of compounds present in GC peaks from their primary *m/z* values and diagnostic electron-impact induced fragmentation patterns, with reference to the NIST Chemistry Webbook (https://webbook.nist.gov). This capability was useful for verification of DNAN and MNTO at their expected GC retention times, as well as for the identification of transformation products of DNAN and NTO.

2.1. Method for CSIA of carbon and nitrogen in DNAN
2.1.1. Chemicals
2,4-Dinitroanisole (DNAN, CAS #119-27-7; ≥98%) was obtained from Alfa Aesar (Ward Hill, MA USA). Ethyl acetate (CAS #141-78-6; ≥99.9%, Optima LC/MS grade), acetonitrile (CAS #75-05-8; ≥99.9%, Optima LC/MS grade), and methanol (CAS #67-56-1; ≥99.9%, Optima LC/MS grade) were obtained from Fisher Scientific (Fair Lawn, NJ).

2.1.2. Quantitation of DNAN
A gas chromatograph-quadrupole mass spectrometer (GC-qMS) method was developed for identification and quantitation of DNAN using a Thermo Scientific TRACE 1310 GC coupled with a Thermo Scientific ISQ LT mass spectrometer. An RTX-5MS GC column (15-m length by 0.53-mm inner diameter with a 0.5-μm film thickness; Restek, Inc.) was used with a 20-mL/min flow of He carrier gas. The following GC program was used for separating the chemicals in experimental samples: 50°C for 2 min, ramped at 20°C/min to 220°C, and then ramped at 8°C/min to 245°C, which was maintained for 2 min. The flow rate of gas in the GC column was 1.4 mL/min. A standard calibration curve was established by injecting 1μL of DNAN standards at various concentrations (ranging from 0.01 μg/μL to 0.5 μg/μL) before and after running the sequences of experimental samples (Figure 2.1). The method detection limit (MDL) was 0.05 μg/μL for DNAN.
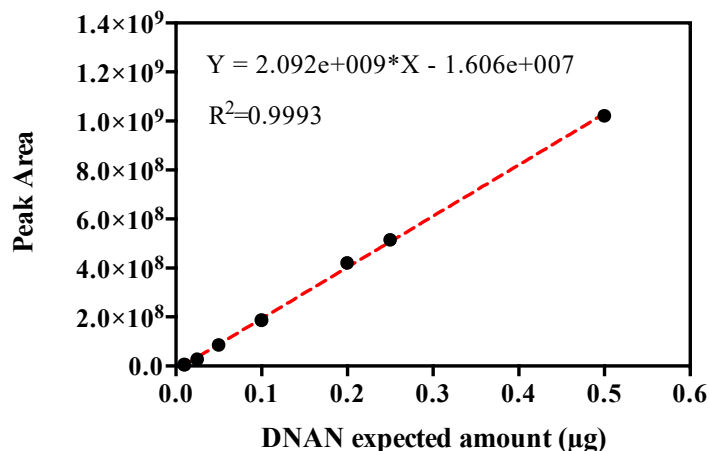
Figure 2.1.1. Example of a standard calibration curve obtained by linear regression of the expected amounts of DNAN standards versus the measured peak area in GC-qMS chromatography. $R^2 =$ 0.9993. $p < 0.0001$.

2.1.3. C and N isotope ratio analysis of DNAN by GC-IRMS

A GC-isotope ratio mass spectrometry (IRMS) (Thermo Scientific DELTA V PLUS system) method was developed for C and N isotope ratio analysis of DNAN. Our method detection limits (MDLs) to obtain $\delta^{13}C$ and $\delta^{15}N$ values for DNAN are, respectively, 0.15 µg and 2.0 µg per injection with ±0.15 to ±0.3‰ precision. However, injecting larger amounts (within an acceptable range from 0.2 µg to 0.35 µg for $\delta^{13}C$, and from 2.5 µg to 4 µg for $\delta^{15}N$) of DNAN yielded improved GC-IRMS resolution for both C and N isotopic analysis and provided a better chromatographic separation and improved analytical precision.

For analysis of the C isotope ratio in DNAN, carbon was converted to CO_2 gas after GC separation. An RTX-5MS GC column (15-m length by 0.53-mm inner diameter with a 0.5-µm film thickness; Restek, Inc.) was used with a 20-mL/min flow of He carrier gas. The following GC program was used for CO_2 separation: 50°C for 2 min, ramped at 20°C/min to 220°C, and then ramped at 8°C/min to 245°C, which was maintained for 2 min. The flow rate of gas in the GC column was 1.4 mL/min. From the GC column, the sample passed through a Ni/Cu/Pt combustion furnace (Thermo Scientific GC ISOLink II) which was not pre-oxidized at 940°C, and the combustion products were then reduced in a separate furnace of Cu at 600°C. The resulting CO_2 was introduced to the isotope ratio mass spectrometer (IRMS) by an open-split interface (Thermo Scientific CONFLO IV) for quantification of C isotope amounts.

The C isotope ratio in DNAN is reported as $\delta^{13}C$:

$$\delta^{13}C_{sample} = (^{13}C \, / \, ^{12}C_{sample}) \, / \, (^{13}C \, / \, ^{12}C_{VPDB}) - 1 \qquad (2.1)$$

where VPDB is Vienna Pee Dee Belemnite. The $\delta^{13}C$ values are reported in parts per thousand (‰) and were calibrated against a DNAN in-house reference solution from ChemService (West Chester, PA) for which a $\delta^{13}C$ value of -38.36 ± 0.2‰ was determined independently via EA-IRMS by comparison with international L-glutamic acid isotopic reference materials USGS-40 and USGS-41(Qi et al., 2003) . The MDL for GC-IRMS isotopic analysis of C in DNAN in ethyl acetate solvent was 0.15 µg and the average reproducibility of normalized $\delta^{13}C$ values was ±0.2‰.
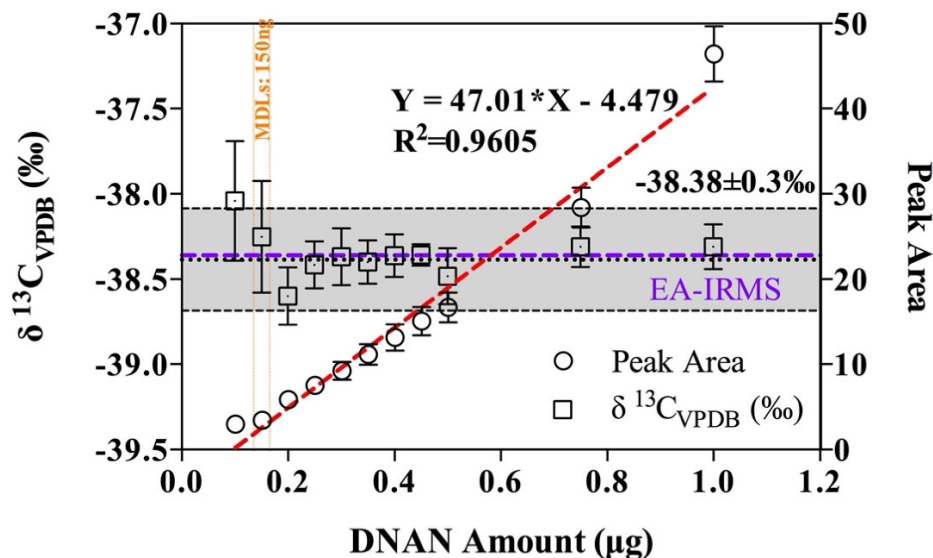
Figure 2.1.2. Evaluation of method detection limit (MDL) and precision for GC-IRMS measurements of $\delta^{13}C_{VPDB}$ in DNAN dissolved in ethyl acetate. The squares represent the $\delta^{13}C_{VPDB}$ values in ‰ and the circles show the GC peak areas. The linear best-fit (red dashed line) and the correlation coefficient for plotting peak areas vs. concentrations are shown. Triplicate measurements were made for each point; error bars indicate the standard deviation. The horizontal dashed line represents the iteratively calculated mean value, with ±0.3‰ standard deviation shown as a gray bar.

The N in DNAN was converted to N_2 gas prior to IRMS analysis. The method for N isotope ratio analysis of DNAN was modified from that for CO_2 as follows. (i) From the GC column, the sample passed through a Ni/Cu/Pt combustion furnace, and then passed through a Cu reduction furnace at 600°C. CO_2 was trapped from the continuous-flow He stream by the use of liquid nitrogen before the analyte N_2 was introduced into the mass spectrometer as described for C. (ii) Following each N_2 isotopic measurement, the open-split interface was isolated and the trapped CO_2 was flushed away by removing the liquid nitrogen trap from the He stream prior to the next analysis. Each data point generated was the mean of replicate GC-IRMS injections (two to seven per sample). We tested the method with and without pre-oxidation of the combustion furnace, with DNAN dissolved in acetonitrile, ethyl acetate, and methanol. Results obtained for DNAN in each solvent were comparable (Fig. 2.1.3)

The N isotope ratio in DNAN is reported as $\delta^{15}N$:

$$\delta^{15}N_{sample} = (^{15}N \, / \, ^{14}N_{sample}) \, / \, (^{15}N \, / \, ^{14}N_{AIR}) - 1 \qquad\qquad (2)$$

where AIR is N_2 in air. The $\delta^{15}N$ data are reported in parts per thousand (‰) and were calibrated against an in-house DNAN reference material, for which a $\delta^{15}N$ value of -2.27 ± 0.05‰ was determined independently by EA-IRMS in comparison with L-glutamic acid isotope reference materials USGS-40 and USGS-41(Qi et al., 2003). The average reproducibility of DNAN $\delta^{15}N$ values determined by GC-IRMS was approximately ±0.2‰.
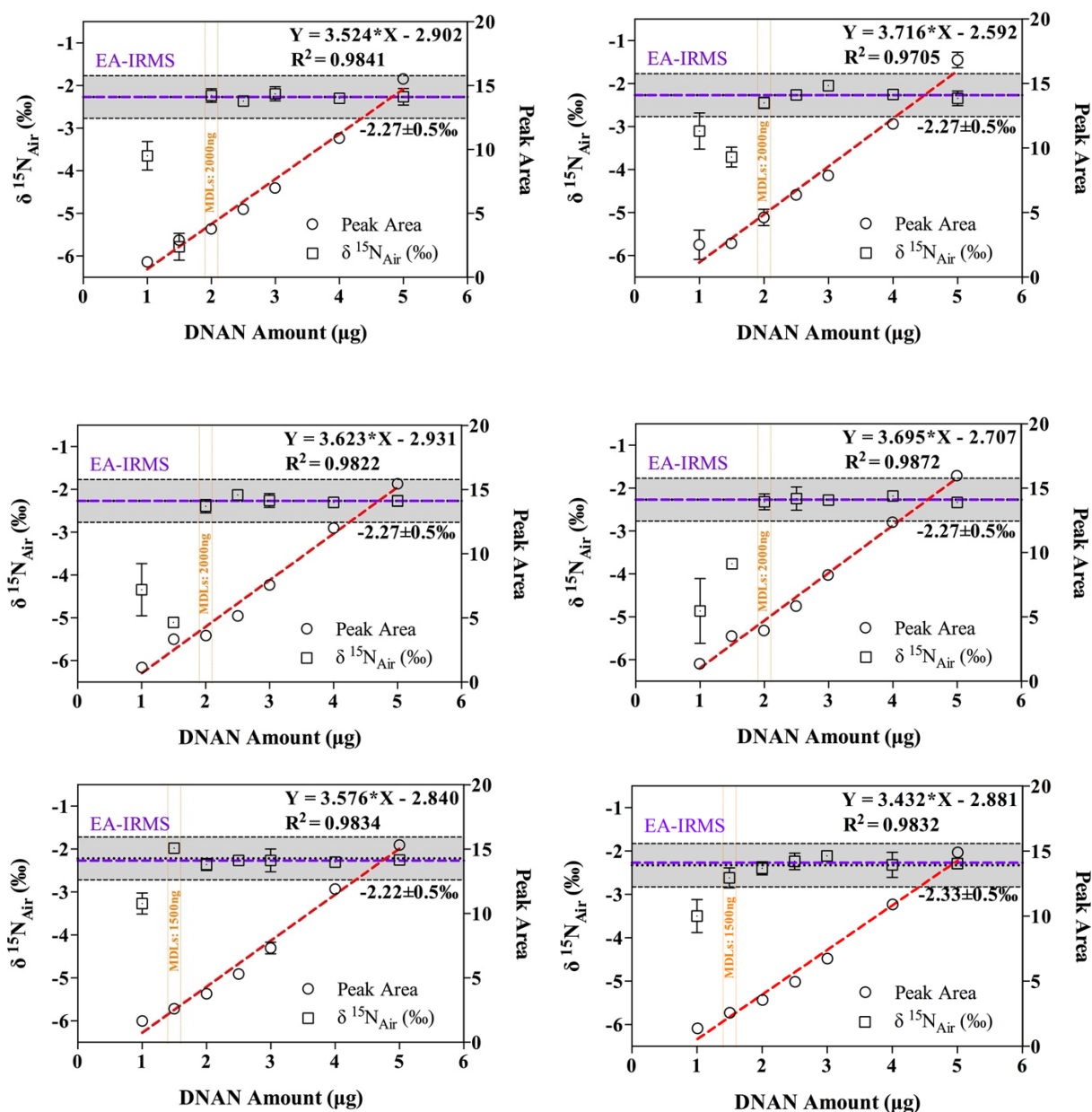
Figure 2.1.3. Evaluation of method detection limits (MDLs) for $\delta^{15}N_{Air}$ in DNAN solutions dissolved in three solvents: (top left) acetonitrile without pre-oxidation of combustion furnace; (top right) acetonitrile with pre-oxidation; (middle left) ethyl acetate without pre-oxidation; (middle right) ethyl acetate with pre-oxidation; (bottom left) methanol without pre-oxidation; and (bottom right) methanol with pre-oxidation. The squares represent the $\delta^{15}N_{Air}$ values in ‰ and the circles show the peak area in gas chromatography. The linear best-fit (red dashed line) and the correlation coefficient for peak areas vs. concentrations are shown in each graph. Triplicate measurements were made for each point; error bars indicate the standard deviation. Values of $\delta^{15}N_{Air}$ determined by GC-IRMS are normalized to that determined by EA-IRMS with reference to standard reference materials. The horizontal gray bars indicate ±0.5‰ standard deviation.

2.2. Method for CSIA of carbon and nitrogen in NTO

NTO (3-nitro-1,2,4-triazole-5-one), a widely used insensitive munition component, has high solubility (16,642 mg/L at 25 °C) and high mobility in water. Experimental studies of the phase partitioning, as well as biotic and abiotic transformations of NTO have been reported (Najafi and Samangani, 2011; Taylor et al., 2013; Richard et al., 2014; Krzmarzick et al., 2015; Linker et al., 2015; Becher et al., 2019; Mark et al., 2016, 2017; Madeira et al., 2017, 2021; Fuller et al., 2020; Cardenas-Hernandez et al., 2021). Monitoring concentration changes of NTO in natural environments makes it difficult to discern losses caused by adsorption, dilution, and/or dispersion from those caused by biotic or abiotic degradation. One potential technique to distinguish degradation from non-degradative losses of NTO is monitoring changes in its isotopic composition via compound-specific isotope analysis (CSIA).

The most widely used CSIA method involves a gas chromatograph coupled through a combustion interface with an isotope-ratio mass spectrometer (GC-IRMS). This method is applicable only for GC-separable compounds that are relatively volatile and non-polar. An on-line derivatization/GC-IRMS method has been used successfully for compound-specific C and N isotope analysis of certain polar compounds that are normally analyzed by liquid chromatography (Reinnicke et al., 2010; Melsbach et al., 2019). However, this online method has not been successful for CSIA of compounds with more complex molecular structures (e.g., pharmaceuticals, amino and fatty acids, explosives) and less-reactive functional groups (e.g., amino-, amide-, and hydroxyl-groups). Liquid chromatography-isotope ratio mass spectrometry (LC-IRMS) methods were developed to address the technical difficulties of CSIA of compounds that are not amenable to GC separation. LC-IRMS methods are currently feasible only for C isotope ratio measurements and have generally higher average method detection limits than those for GC-IRMS (e.g., 160 ng of C on column for LC-IRMS analyses vs. 10 ng of C or 43 ng of N on column for GC-IRMS analyses (Krummen et al., 2004; Elsner et al., 2012). To better assess the environmental behavior of NTO by precise multi-element isotope analysis, we sought a derivatization procedure that would produce a molecule amenable to GC-IRMS analysis. Our goal was to optimize a simple method that would yield low method detection limits and minimal isotope fractionation.

Initially, we test high-temperature (200 – 250 °C) derivatization methods using tetramethylammonium hydroxide (TMAH) and trimethylsulfonium hydroxide (TMSH). These derivatization methods have commonly been used in studies of natural organic matter. However, we did not achieve acceptable results when we attempted to use them to derivatize NTO, and we sought a more appropriate derivatizatioin method. The offline low-temperature derivatization/GC-IRMS method presented here for NTO is based upon a previously published technique for alkylation of the heterocyclic N-H group in nitrozoles (Klapötke et al., 2016). Methyl iodide (MeI) was used as the derivatization agent to alkylate deprotonated NTO with triethylamine (Et$_3$N) as a base catalyst. This work was implemented in two parts (i) development, identification, and optimization of the NTO methylation reaction, and (ii) assessment of the sensitivity, accuracy, and reproducibility of C and N isotope ratio determinations by GC-IRMS. The accuracy of isotope analyses using this new derivatization/GC-IRMS method was verified by comparing GC-IRMS results with elemental analyzer (EA)-IRMS measurements of three different bulk NTO source materials. The stability of the NTO derivative was evaluated by replicate analyses of derivatized samples stored in solvent for a period of up to 12 months.

2.2.1. Chemicals

3-nitro-1,2,4-triazol-5-one (NTO, CAS# 932-64-9) was obtained from Dr. Stephen Fallis at the Naval Air Warfare Center Weapons Division (China Lake, CA, USA). Methyl iodide (MeI, CAS# 74-88-4, LOT# 136780) was purchased from Fisher Scientific (Fair Lawn, NJ USA). Triethylamine (Et$_3$N, CAS# 121-44-8, LOT# MKCJ7915) was purchased from Sigma-Aldrich (St. Louis, MO USA). Solvents, including acetone, acetonitrile and ethyl acetate, were Optima™ LC/MS Grade and purchased from Fisher Scientific (Fair Lawn, NJ USA).

2.2.2. Derivatization Procedure

All glassware was prepared by baking at 550°C for 2 hours prior to use. In derivatization reactors (headspace screw-thread vials, 18 mm, amber, volume 10 mL, Restek, Inc.), 1.0 mg of an aqueous stock solution of NTO was added to 5 mL of acetone to achieve a NTO concentration of 1.54 mM. Next, 2.145 µL of Et$_3$N was added to bring its concentration to 3.1 mM in acetone (twice the NTO concentration). The solution was stirred magnetically for 10 min, then 10 µL of MeI was added to bring its concentration to 32 mM and the solution was further stirred for 24 hr at ambient temperature (~22°C) in the dark. Derivatization was quenched by removing the reactors from the magnetic stirring plate and evaporating the solvent under a gentle flow of N$_2$ gas to produce a yellow solid residue (including MNTO as shown in Scheme 2.1). The solid was dissolved in 625 µL of acetonitrile/ethyl acetate (50:50, v:v) and transferred to a 2-mL glass autosampler vial for GC-IRMS analysis. Experiments were performed in at least two batches with duplicates in each batch. Control samples were prepared without NTO. The Et$_3$N:NTO ratio, MeI:NTO ratio, derivatization reaction time, and NTO concentration were varied systematically to validate the procedure and to optimize the recovery and the accuracy and precision of δ^{13}C and δ^{15}N values of MNTO. All solution preparations and derivatization reactions were done in a fume hood.

Scheme 2.1. Low-temperature methylation reaction of NTO with methyl iodide (MeI) to produce MNTO (methyl-NTO).
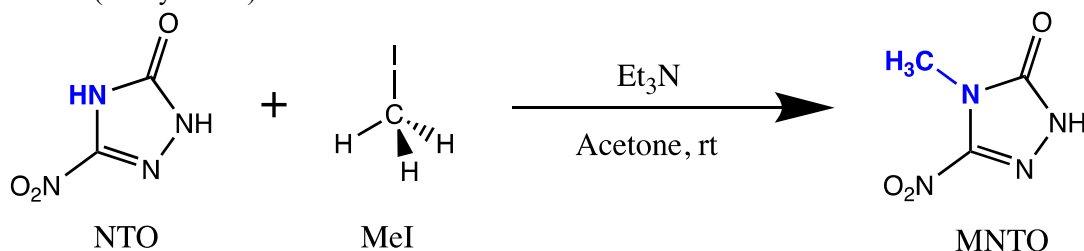
The NTO derivative compound MNTO in acetonitrile/ethyl acetate solvent (50:50, v:v) was identified by both GC-qMS and by direct injection on the Q-Exactive Orbitrap™ high-resolution mass spectrometer (HRMS). Following GC separation, MNTO was detected at *m/z* 144 by qMS under positive EI mode at 200°C. The direct-injection Orbitrap™ analysis involved one injection in positive ion mode and another in negative ion mode. MNTO was identified at *m/z* 143 in negative ion mode.

2.2.3. δ¹³C and δ¹⁵N values in DNAN and NTO reference materials

The δ^{13}C and δ^{15}N values of our in-house secondary isotopic reference materials DNAN_EIGL and DNAN_PEI, and three NTO source materials (NTO_RM1, NTO_RM2 and NTO_RM3) were determined by EA-IRMS (Tables 2.2.1, 2.2.2, and 2.2.3). The EA IsoLink CN-

IRMS system (Thermo Fisher Scientific, Germany) consisting of a MAS Plus Autosampler and a Flash IRMS elemental analyzer was connected in continuous-flow mode to a dual-inlet Delta V Plus IRMS via a Conflo-IV reference interface. The C isotope ratios are reported as $\delta^{13}C$ values (equation 1) and the N isotope ratios are reported as $\delta^{15}N$ values (equation 2). The $\delta^{13}C$ values of -38.36 ‰ for DNAN_EIGL and -29.50 ‰ for DNAN_PEI, respectively, were determined for these two in-house secondary DNAN reference materials that were used to normalize the $\delta^{13}C$ values obtained for MNTO by GC-IRMS. The average reproducibilities of $\delta^{13}C$ values obtained by GC-IRMS for DNAN and MNTO were approximately ±0.2 ‰ and ±0.3 ‰, respectively. The $\delta^{15}N$ values of +2.27 ‰ for DNAN_EIGL and -11.92 ‰ for DNAN_PEI, respectively, were also determined by EA-IRMS and used as internal standards to normalize the $\delta^{15}N$ values obtained for MNTO by GC-IRMS. The average reproducibilities of $\delta^{15}N$ values obtained by GC-IRMS for DNAN and MNTO were ±0.2 ‰.

Table 2.2.1. $\delta^{13}C$ values of three different NTO source materials determined by EA-IRMS ($n \geq 5$). The $\delta^{13}C$ values of MNTO derivatized from these NTO source materials were determined by GC-IRMS. The $\delta^{13}C$ value of methyl reactant from the methyl iodide stock reagent was estimated by averaging $\delta^{13}C$ values derived according to eq 3. Normalized $\delta^{13}C$ values of MNTO were obtained by using the average estimated $\delta^{13}C$ value of the methyl reactant and GC-IRMS results.

^{13}C isotope analytical methods	NTO_RM1		NTO_RM2		NTO_RM3	
	Mean	SD	Mean	SD	Mean	SD
EA-IRMS	-40.89	1.17	-38.21	0.33	-50.93	0.38
GC-IRMS	-73.65	0.29	-72.04	0.25	-80.38	0.38
Estimated $\delta^{13}C$ of methyl	**-139.18**		**-139.70**		**-139.27**	
Average $\delta^{13}C$ of methyl	**-139.38**	**0.28**				
Normalized GC-IRMS	**-73.72**	**0.87**	**-71.93**	**0.31**	**-80.41**	**0.35**

Table 2.2.2. $\delta^{15}N$ values of three different NTO source materials determined by EA-IRMS ($n \geq 6$). The $\delta^{15}N$ values of MNTO derivatized from these NTO source materials were determined by GC-IRMS.

^{15}N isotope analytical methods	NTO_RM1		NTO_RM2		NTO_RM3	
	Mean	SD	Mean	SD	Mean	SD
EA-IRMS	-3.22	0.59	-3.36	0.37	-4.93	0.32
GC-IRMS	-2.92	0.24	-3.38	0.27	-5.41	0.22

Table 2.2.3. $\delta^{13}C$ and $\delta^{15}N$ values of two DNAN in-house reference materials (RMs) determined by EA-IRMS(For DNAN_EIGL, $n \geq 24$; for DNAN_PEI, $n \geq 8$).

	DNAN_EIGL		DNAN_PEI	
	Mean	SD	Mean	SD
$\delta^{13}C$	-38.36	0.16	-29.50	0.11
$\delta^{15}N$	-2.27	0.05	-11.92	0.17

2.2.4. C and N isotope analysis of MNTO by GC-IRMS

For C and N isotope analysis of MNTO, we used the same method as that described above for DNAN (Section 2.1.3). Measured $\delta^{13}C$ and $\delta^{15}N$ values of MNTO were normalized to a scale defined by the values of our two in-house DNAN reference materials (Table 2.3). Validation and optimization of recovery and reproducibility of bulk $\delta^{13}C$ and $\delta^{15}N$ values of MNTO were performed before correcting for the $\delta^{13}C$ value of the added methyl group carbon. It was assumed that the methyl group added to NTO from methyl iodide (MeI) had a fixed $\delta^{13}C$ value. This assumption was tested by comparing $\delta^{13}C$ values for the added methyl group for each of the three different NTO samples calculated as follows:

$$\delta_{calc}{}^{13}C_{MeI} = \delta_{bulk}{}^{13}C_{MNTO} * 3 - \delta_{bulk}{}^{13}C_{NTO} * 2 \tag{3}$$

where $\delta_{calc}{}^{13}C_{MeI}$ is the calculated $\delta^{13}C$ value of the methyl group, $\delta_{bulk}{}^{13}C_{MNTO}$ is the bulk $\delta^{13}C$ value of MNTO obtained by GC-IRMS, and $\delta_{bulk}{}^{13}C_{NTO}$ is the bulk $\delta^{13}C$ value of NTO obtained by EA-IRMS (Table 2.1). The $\delta^{15}N$ values measured by GC-IRMS for MNTO were identical, within error, to those measured for NTO by EA-IRMS, indicating negligible N isotope fractionation during the methylation of NTO to MNTO.

2.2.5. Results and Discussion
2.2.6. NTO Methylation Pathway

The low-temperature derivatization of NTO was performed by methylation in an acetone solution containing methyl iodide and triethylamine (Scheme 1). The derivatized product of this reaction was identified as 4-methyl-3-nitro-1,2,4-triazol-5-one (MNTO), by GC-qMS (Fig. 2.2.1) and Orbitrap HRMS (Fig. 2.2.2). A comparison of the mass fragmentation patterns of NTO (Fig. 2.2.1a) and MNTO (Fig. 2.2.1b) shows that many of the same fragments are present for both compounds, including fragments in the m/z 83-85 range that are triazole rings, fragments in the m/z 42-45 range that are triazole ring fragments, and the fragment at m/z 46 is NO_2 (Ostmark et al., 1993). The MNTO mass fragmentation pattern also shows additional peaks at m/z 58, 96, and 114 that appear to be unique to MNTO. This comparison of the mass fragmentation patterns of NTO and MNTO supports the identification of MNTO as the derivatization product obtained by simple methylation of NTO at the N_4 site.
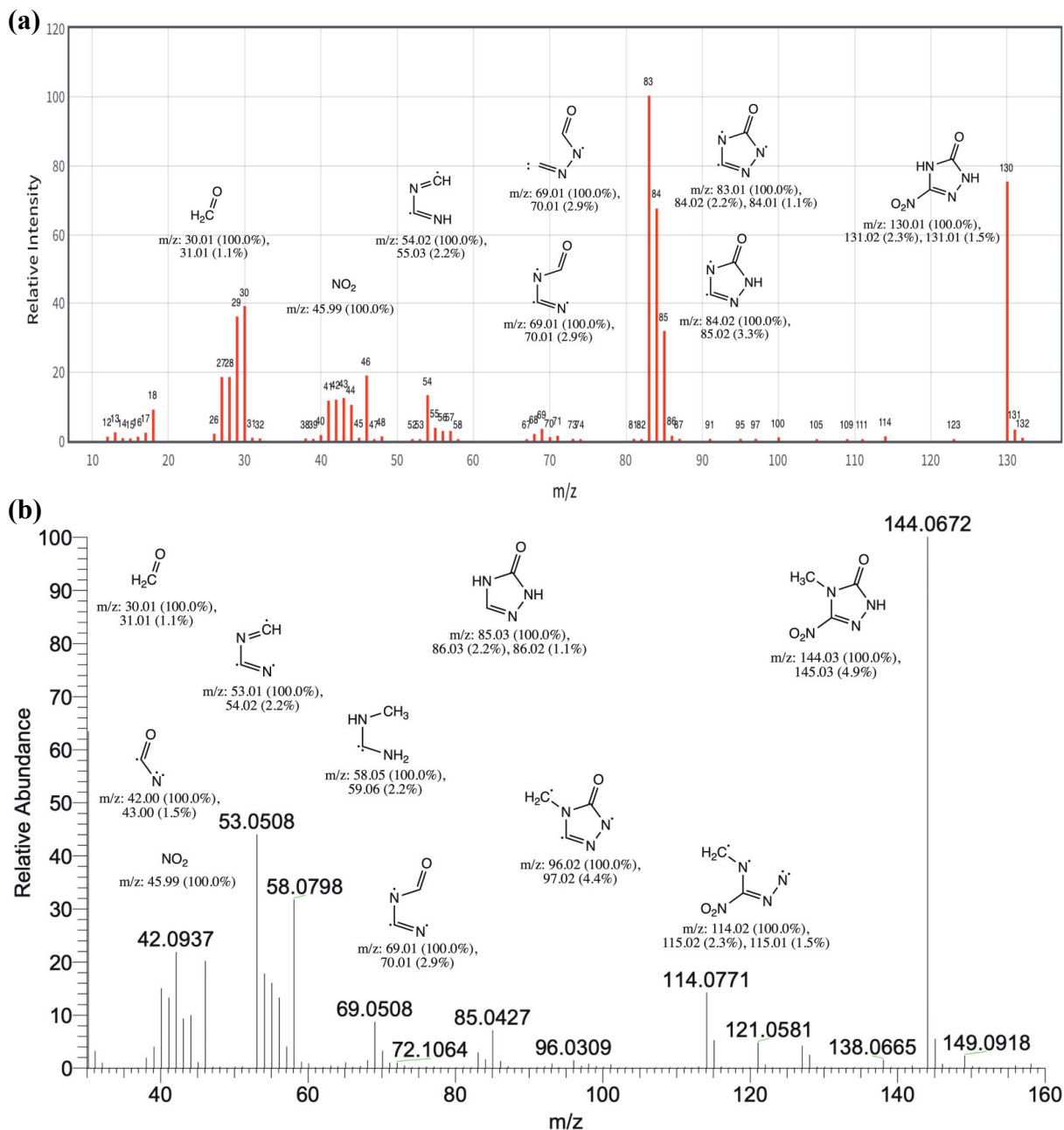
Figure 2.2.1. Mass spectrum (electron ionization) of NTO from NIST Mass Spectrometry Data Center (NIST, 2021) (Panel a). Quadrupole GC-qMS spectrum (electron ionization) showing MNTO fragmentation pattern (Panel b) following derivatization. Tentative fragment identifications (MacLafferty et al., 1993) in both panels were drawn by ChemDraw 20.0.

17

143.01929
C₃H₃O₃N₄
-4.74079 ppm

Chemical Formula: C₃H₄N₄O₃
Molecular Weight: 144.09
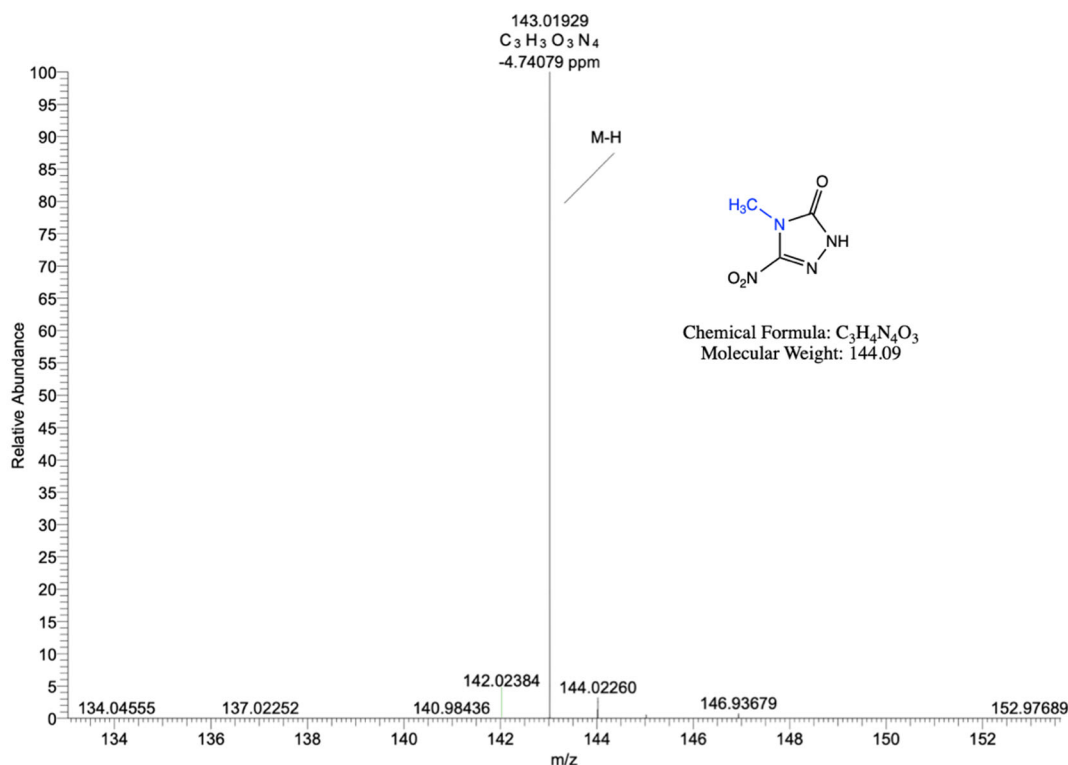
Figure 2.2.2. High-resolution mass spectrum of deprotonated 4-methyl-3-nitro-1,2,4-triazole-5-one (MNTO), obtained by Orbitrap Q-Exactive with electrospray ionization in negative mode. The identified chemical formula is that proposed in Scheme 1 for MNTO.

2.2.7. GC-IRMS analyses of C and N isotope ratios in MNTO

Method development, optimization, and validation of ^{13}C- and ^{15}N-CSIA for MNTO was performed in two stages. First, we developed and optimized the protocols and conditions of the offline low-temperature derivatization reaction for NTO. Second, the accuracy, reproducibility, and method detection limits (MDLs) of ^{13}C- and ^{15}N-CSIA by GC-IRMS were validated for MNTO. To evaluate the chemical yields and C and N isotope fractionations during NTO methylation, as well as the accuracies and reproducibilities of δ^{13}C and δ^{15}N values for MNTO, we systematically tested the procedure by varying molar ratios of MeI:NTO and Et₃N:NTO, NTO concentrations, and derivatization reaction times. Figure 2.2.3a shows the measured chemical yields of MNTO, as well as δ^{13}C and δ^{15}N values of MNTO with increasing MeI:NTO molar ratios, under the conditions of 0.2 mg/mL NTO in acetone and Et₃N:NTO = 2:1. Stable chemical yields and acceptable precisions of δ^{13}C and δ^{15}N values in MNTO were achieved with the MeI:NTO molar ratios greater than 20. In Figure 2.2.3b, stable chemical yields, as well as acceptable precisions of δ^{13}C and δ^{15}N values in MNTO appeared within the range of Et₃N:NTO molar ratios of 2–10. Increasing the concentration of NTO in the derivatization reactors potentially contributed to the increase in chemical yield of MNTO while the observed changes in δ^{13}C and δ^{15}N values of MNTO in this experimental group remained comparable with the EA-IRMS results (Figure 2.2.3c). As shown in Figure 2.2.3d, derivatization reactions lasting less than 12 hrs resulted in lower yields (<30%) of MNTO, as well as substantial C and N isotope fractionations, which made the δ^{13}C and δ^{15}N values of MNTO determined by GC-IRMS

18

unacceptable when compared with EA-IRMS results. However, even with incomplete yields (30% ~ 40%) of MNTO, no side reaction pathways were identified by either GC-qMS or Orbitrap in this study.
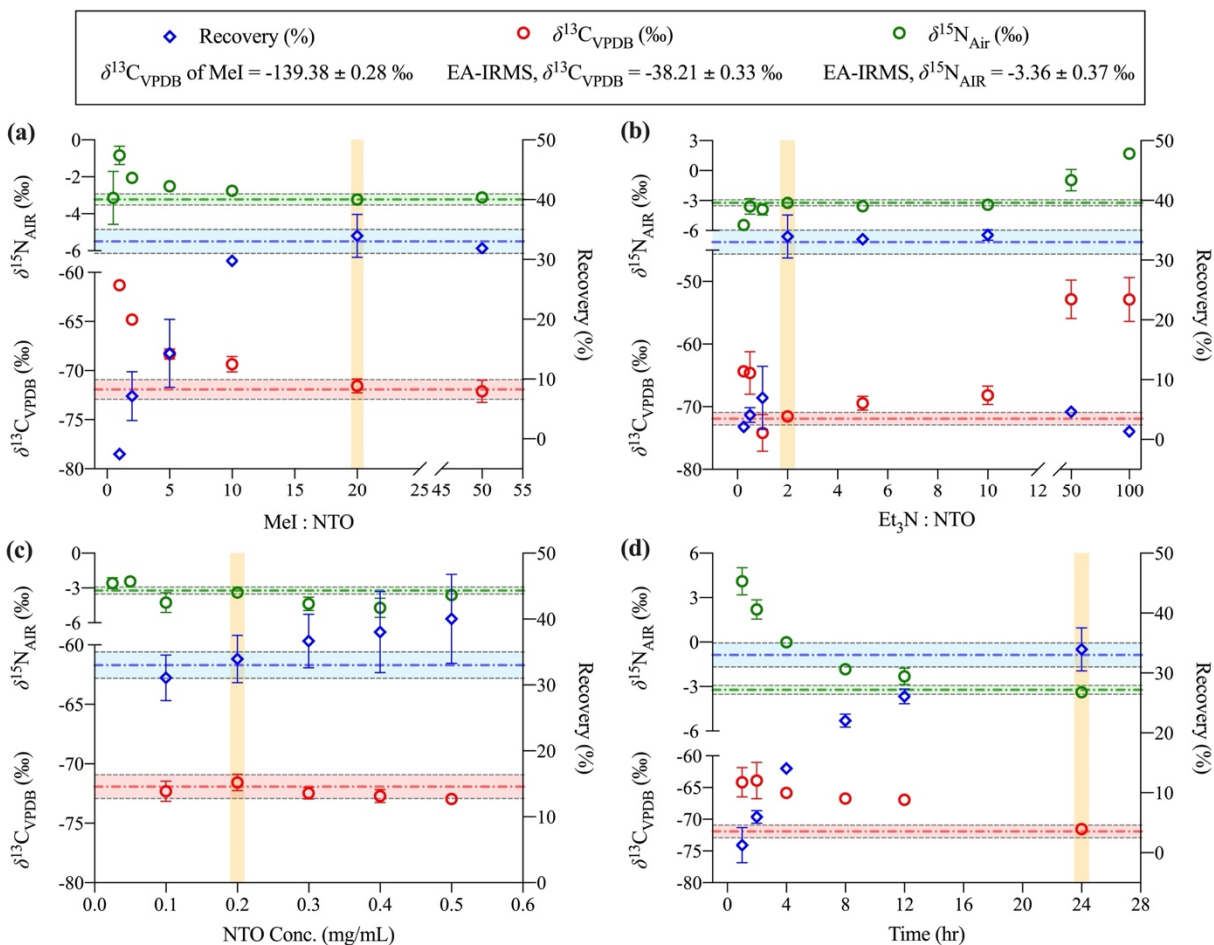
Figure 2.2.3. On-column recoveries of NTO, and $\delta^{13}C_{VPDB}$ (‰) and $\delta^{15}N_{AIR}$ (‰) values of MNTO determined by GC-IRMS, as a function of (a) MeI:NTO molar ratio; (b) Et₃N:NTO molar ratio; (c) NTO concentration (mg/mL) in acetone; and (d) derivatization time. Blue diamonds represent the NTO recoveries (%) in each derivatization experimental group. The horizontal blue dashed lines show the average recoveries under optimized derivatization reaction conditions, with ±2% standard deviation shadowed in light blue. Red circles represent $\delta^{13}C$ values of MNTO in each derivatization experimental group. The horizontal red dash lines show the bulk average $\delta^{13}C$ value in MNTO derived from the EA-IRMS determined $\delta^{13}C$ value in parent compound NTO and the simulated position-specific $\delta^{13}C$ value of the methyl group of MNTO (eq. 3), with an acceptable standard deviation of ±1‰ shadowed in light red. Green circles indicate $\delta^{15}N$ values of MNTO in each derivatization experimental group. The horizontal green dashed lines show the EA-IRMS determined $\delta^{15}N$ value in parent compound NTO, with an acceptable standard deviation of ±0.3‰ shadowed in light green. Optimized NTO derivatization reaction conditions are highlighted as yellow vertical rectangles. No derivatized products were detected in the control groups.

19

MNTO was not found to be available from commercial sources for method calibration. To quantify the amount of MNTO per injection on column, we followed a three-step data processing protocol: (i) we hypothesized that after GC separation, MNTO and DNAN were quantitatively transformed to CO_2 (in ^{13}C-CSIA mode) and N_2 (in^{15}N-CSIA mode); (ii) Linear relationships of nmol C versus the amplitude of the m/z 44 signal and nmol N versus the amplitude of the m/z 28 signal were based on a calibration with known amounts of DNAN internal standards (Figure 2.2.4a and 2.2.4b, black diamonds); (iii) molar amounts of on-column MNTO were quantified (Figure 2.2.4a, purple diamonds; Figure 2.2.4b, green diamonds), and then the recoveries of parent NTO were calculated (Figure 2.2.3).

Isotope ratio scales for C and N measurements of MNTO were normalized against two isotopically distinct DNAN secondary reference materials. The normalized $\delta^{13}C$ and $\delta^{15}N$ values in MNTO were plotted respectively as a function of the amplitudes of the signals measured for the CO_2^+ ion at m/z 44 (Figure 4a, red circles) and the N_2^+ ion at m/z 28 (Figure 4b, green circles).
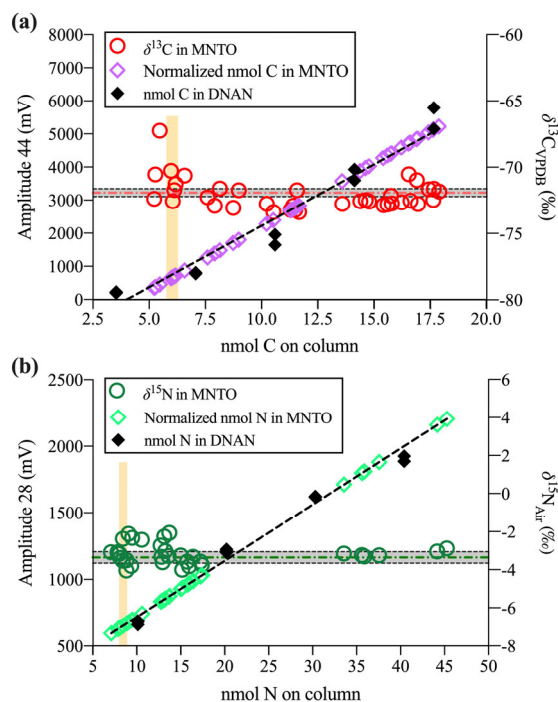
Figure 2.2.4. Quantification of the on-column C (Panel a) and N (Panel b) molar amounts in MNTO by GC-IRMS, as well as correlation of amount-dependency tests for the $\delta^{13}C$ (Panel a) and $\delta^{15}N$ (Panel b) values. Black diamonds represent the intensities for each amount of DNAN in-house reference material on-column. Linear regressions were established to predict the molar amount of MNTO on-column. Purple and green diamonds represent the normalized molar amounts of C and N in MNTO on-column. Red and green circles represent the corresponding δ values for each injection of replicate measurements. The method detect limits (MDLs) of ^{13}C- and ^{15}N-CSIA for MNTO were determined according to the protocol proposed by Jochmann et al.[45] and highlighted as the yellow rectangles. The horizontal red dashed line (Panel a) represents the bulk average $\delta^{13}C$ value of MNTO derived from the EA-IRMS determined $\delta^{13}C$ value in parent compound NTO and the simulated position-specific $\delta^{13}C$ value of the methyl group of MNTO (eq 3). The horizontal green dashed line (Panel a) indicates the $\delta^{15}N$ value of NTO determined by EA-IRMS. The gray dashed lines show the standard deviation of ±0.3‰ for both $\delta^{13}C$ and $\delta^{15}N$ values.

The MDLs of ^{13}C- and ^{15}N-CSIA were determined to be 8 nmol of N and 6 nmol of C for MNTO, which corresponds to 788 ng of NTO parent compound, to achieve optimal reproducibilities for δ^{13}C and δ^{15}N values. The stability of MNTO dissolved in acetonitrile/ethyl acetate (v:v, 1:1) was examined by reanalyzing a set of samples over time. Isotopic values were stable for up to two months. The derivatization method was also tested with a sample in which NTO was mixed with its two principal nitroreduction products, 3-hydroxyamino-1,2,4-triazol-5-one (HTO) and 3-amino-1,2,4-triazol-5-one (ATO). No evidence of substantial methylation of HTO or ATO was observed.

2.2.8. Application to NTO in environmental samples

The derivatization method presented here has been applied successfully to characterize kinetic isotope effects of C and N during photodegradation of NTO during UV irradiation in pure water (Wang et al., 2021c). The method is currently being applied in this project to characterize isotope effects during microbial degradation by pure cultures and consortia. Soluble organic substrates (e.g., lactate) and inorganic solutes (e.g., phosphate buffer) in the microbial culture growth media were found to interfere with the derivatization of NTO, so we investigated methods to separate NTO from the interfering solutes using solid-phase extraction (SPE) and ultrasonic-assisted liquid-liquid extraction (UALLE) (Section 2.4). The simple UALLE method was found to separate lactate and phosphates quantitatively from NTO (Table 2.4.2). Routine application of such extraction/purification methods may be needed prior to derivatization and GC-IRMS analyses of NTO in environmental samples, depending on the relative concentrations of NTO and other interfering ions. The prevalent pathway that has been observed in the laboratory for both biotic and abiotic degradation of NTO is nitroreduction (Krzmarzick et al., 2015; Fuller et al., 2020; Madeira et al., 2017, 2021; Cardenas-Hernandez et al., 2020; Khatiwada et al., 2018). By analogy with kinetic isotope effects measured during nitroreduction of a variety of nitroaromatic compounds, relatively large N isotope fractionation and small C isotope fractionation can be expected during nitroreduction of NTO (Hofstetter et al., 2014).

2.2.9. Conclusions

An offline, low-temperature derivatization/GC-IRMS method for accurate and precise isotopic analysis of NTO was developed. This optimized NTO methylation reaction technique enables precise and accurate ^{13}C- and ^{15}N-CSIA measurements by GC-IRMS with the following parameters: MeI:NTO = 20:1, Et$_3$N:NTO = 2:1, NTO concentration (mg/mL in acetone) = 0.2 mg/mL, and reaction time = 24 hrs. Given the reported high aqueous solubility and mobility of NTO, as well as the potential environmental hazard from accumulation of IMX-104 residues after detonation (Walsh et al., 2014; Kennedy et al., 2017; Johnson et al., 2017), this new analytical method in combination with solid and/or liquid phase extraction and purification of NTO from environmental samples enables better evaluation of its environmental fate and transport in aqueous environments. Considering NTO as a surrogate for other heterocyclic compounds, the simple derivatization method presented here may help to expand the list of environmental contaminants for which multi-element compound-specific isotope analysis can be achieved by GC-IRMS.

2.3 Extraction and purification of DNAN and NTO from aqueous solutions

GC-IRMS analyses of DNAN and NTO from aqueous solutions require extraction by using either a solid-phase extractant (SPE) or ultrasonic-assisted liquid-liquid extraction (UALLE), especially when other solutes are present that may co-elute with DNAN or may interfere with NTO derivatization. We evaluated both extraction methods to determine their recoveries and potential effects on isotopic compositions of DNAN and NTO.

2.3.1 Ultrasound-assisted liquid-liquid extraction of DNAN from aqueous solutions

An ultrasound-assisted liquid-liquid extraction (UALLE) method was developed and validated for extraction of DNAN from aqueous solution. Based on the method detection limits (MDLs) and the base line tests of GC-IRMS chromatograms with acetonitrile, ethyl acetate and methanol, ethyl acetate was chosen as the extracting solvent in the present work. Amber glass sample bottles and vials were sealed with PTFE/silicone septa caps and placed in an ultrasonic water bath (Sper Scientific, model 100004; Scottsdale, AZ) for 8 mins. After extraction, all bottles/vials were set aside to allow the density separation of the water and the solvent for at least 20 mins. The solvent layer with nitroaromatic compounds (NACs) was transferred by pipet to a clean amber vial and left in a fume hood overnight in the dark for solvent evaporation. The samples were then transferred by rinsing the amber vials into a 2-mL wide-mouth screw-cap vial with a PTFE/silicone septum (Restek Corporation; Bellefonte, PA USA) for GC-qMS-IRMS analyses. Recovery of DNAN was determined under a range of extraction times and water to solvent ratios. The recovery of DNAN from pure water samples with UALLE is $98.4 \pm 2.6\%$ based on 18 replicate analyses; this recovery was not affected by extraction time or water to solvent ratio (Figs. 2.3.1).
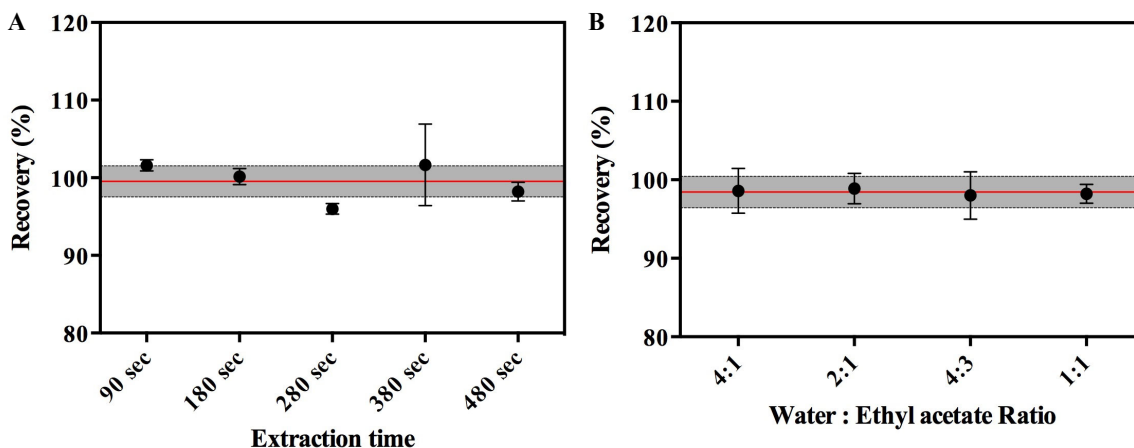
Fig. 2.3.1. Recoveries of DNAN from water samples extracted with ethyl acetate by UALLE: A. with different extraction times; B. with different water to ethyl acetate ratios. The red lines represent the average recoveries of these two experimental groups, 99.52% and 98.43%, respectively. The gray area represents the uncertainty of recovery at ~2%. Error bars represent the standard deviations from at least 5 replicates for each setting.

2.3.2 Solid-phase extraction (SPE) of DNAN from microbiological culture media

For some solutions, the UALLE extraction method for DNAN may not produce a sufficiently pure product, or perhaps a relatively large volume of solution is needed for extraction. An SPE extraction method may be preferable in such cases; we have used SPE routinely for extracting RDX and DNAN from microbiological culture media (e.g., Fuller et al., 2016). Samples (40 to 250 ml) of culture media for isotopic analysis are removed sequentially during a microbiological culture experiment in a 1-liter bottle designed to provide sequential samples representing progressive fractions of DNAN degradation in the range of approximately 0.05 to 0.95. Each sample was filtered through a glass microfiber filter (25-mm diameter by 0.45-µm pore size) to remove cells. The filtered sample was then passed over a preconditioned Supelclean ENVI-Chrom P solid phase extraction (SPE) column (250 mg packing; Sigma-Aldrich, St. Louis, MO, USA) to concentrate residual DNAN and organic degradation products. The analytes on the SPE column were eluted with acetonitrile, and then the extract was evaporated to a volume of 1 ml for subsequent C and N isotopic analysis of DNAN. This SPE concentration procedure did not result in significant isotopic fractionation of C or N in DNAN in either distilled water or groundwater. This is consistent with both the high molecular weight of DNAN (198.13 g/mol) and the high yield of the extraction procedure (~85% recovery).

2.3.3 Solid-phase extraction of NTO from microbiological culture media

A method of solid phase extraction (SPE) was developed and validated for the purpose of removing the potentially interfering dissolved organic matter from NTO in aqueous samples from microbiological culture experiments. This method uses a different SPE material than that described above for DNAN, because NTO is a more polar molecule. The SPE columns were purchased from Phenomenex (Strata™-X-A 33 µm Polymeric Strong Anion, 500 mg / 6 mL, P/N: 8B-S123-HCH). For conditioning, 2 x 5 mL of LC/MS grade methanol followed by 2 x 5 mL of NanoPure water were passed through the columns. Subsequently, NTO aqueous matrix samples were loaded to the columns at an approximate flow rate of 10 mL/min, and then the columns were dried with nitrogen for a minimum of 10 mins. To elute the sample, 2 x 10 mL of 2% (v:v) hydrochloric acid (HCl) in LC/MS grade methanol were slowly flushed through each SPE column, with the eluates collected in clean glass vials. Finally, the eluates were evaporated to ~1 mL under warm nitrogen gas, and then transferred to clean HPLC vials for analysis. Results for NTO capture and recovery efficiencies from different culture media are shown in Table 2.3.1.

2.3.4 Ultrasound-assisted liquid-liquid extraction of NTO from aqueous solutions

Although the SPE method described above is effective at removing most organic interferences from NTO in the culture media, it was not effective at removing phosphate that is present as a pH buffer in some of the media. Phosphate interferes with the derivatization procedure that we developed for GC-IRMS analysis of C and N isotope ratios in derivatized NTO. Therefore, we tested the UALLE method to evaluate its effectiveness for removing phosphate and lactate (a common nutrient in the culture media) from NTO.

Briefly, NTO stock solution (5 g/L) was prepared by mixing into 10XBSM buffer stock to achieve a 100 mg/L of NTO + 0.1XBSM solution and a 100 mg/L of NTO + 1XBSM solution. The 100 mg/L of NTO solution was made as a positive control of this experiment. 1 mL of experimental samples and the positive controls were acidified to pH < 1 by adding 37% HCl (Fisher Scientific, Fair Lawn, NJ USA), and then mixed with 1 mL of ethyl acetate in an

ultrasonic water bath (Sper Scientific, model 100004; Scottsdale, AZ) for 8 mins. After mixing, samples and controls were sitting in the fume hood for at least 30 mins until the upper layer (ethyl acetate phase) and bottom layer (water phase) were separated. Ethyl acetate phase was transferred to a clean container, and the aqueous solution was re-extracted two more times. Subsequently, ethyl acetate extracts were evaporated under dry N_2 gas, and then dissolved in DI water for ion chromatographic analyses of NTO, phosphates, and lactate, using a Dionex ICS-2100 Ion Chromatography System (Thermo Fisher Scientific, Waltham, MA) equipped with Dionex IonPac^{TM} AS20 4-mm column (Analytical 4 x 250mm, Product No. 063148), following EPA 300.0 method (Table 2.3.2).

Table 2.3.1. Capture and recovery of NTO by the solid phase extraction (SPE) method described above.

NTO matrix samples	pH	SPE Capture (%)	SPE Recovery (%)
NanoPure Water	3.6	100	79
Acidified & Neutralized PO4 Buffer	7.1	78	62
Acidified & Neutralized NaOH	7.1	98	78
Artificial Groundwater (AGW)	4.6	100	80
1/10 Basal Salts Medium (BSM)	7	100	90
Methanotroph Medium (MM)	5.7	99	79

Table 2.3.2. Recoveries of NTO, phosphates and lactate in 0.1XBSM, 1XBSM and NTO control samples, respectively, following UALLE extraction method.

	NTO			Phosphates			Lactate		
	Mean	SD	N	Mean	SD	N	Mean	SD	N
0.1XBSM	83.25%	12.57%	5	0.01%	0%	5	0%	N/A	5
1XBSM	82.55%	7.36%	5	0.49%	1.08%	5	0%	N/A	5
NTO control in H_2O	82.27%	7.70%	5	N/A	N/A	5	N/A	N/A	5

2.4   Method for bulk oxygen isotope analysis of DNAN

During this project, we began to explore applications of O isotope analysis in understanding degradation pathways of DNAN. As there is currently no method for compound-specific isotope analysis of oxygen in DNAN, we used a method known as thermal conversion (TC)/EA-IRMS. A Thermal Conversion/Elemental Analysis (TC/EA) reduction unit (ThermoFinnigan) equipped with a Costech Zero-Blank 50-position autosampler was used, following the method of Qi et al. (2011). The helium carrier gas (purity 99.999 %, Keen Gas, Wilmington, DE) flow rate was 100 mL/min. The samples were dropped into the reactor packed with glassy carbon chips with the temperature controller set at 1380 ºC. A 1.5 m ¼-inch GC

packed with 60-80 mesh 5-Å mol sieve was installed to replace original 0.6- m ¼-inch GC packed with 80-100 mesh 5-Å mol sieve. The GC temperature was set to 90 °C. The effluent from the gas chromatograph was coupled to a Delta Plus XP IRMS via a ConFlo IV interface (both ThermoFinnigan). To divert N_2 peaks produced from N-bearing materials, an automated diverter valve was installed.

Oxygen isotope ratios were measured in CO gas as ratios of *m/z* 30/28 and normalized to those of CO produced from a set of standard reference waters VSMOW, UC03, and UC04 (http://www.isotopes.usgs.gov) with accepted $\delta^{18}O$ values of 0.00 ‰, +29.79 ‰, and +38.95 ‰ , respectively [28-30]. Corrections for the contribution of $^{13}C^{17}O$ to the *m/z* 30 signal are insignificant as the isotopic composition of carbon in CO produced from samples and standards is controlled by that of the glassy carbon in the reactor. Oxygen isotope data are reported in the conventional delta (δ) notation whereby $\delta^{18}O = [(^{18}O)/^{16}O)_{sample}/(^{18}O/^{16}O)_{VSMOW} - 1]$, and $\delta^{18}O$ values are reported in units of per mil (‰). The typical analytical uncertainty of this method as applied to reagent DNAN samples is ±0.1-0.2 ‰.

For O isotope analysis of pure DNAN, solid DNAN was loaded into a silver capsule for high-temperature reaction with glassy carbon to produce CO for isotopic analysis of oxygen. Silver capsules (pressed 8 x 5 mm, light weight, SKU D2308) and cell wells (96 positions, flat bottom with lid, SKU E2079) were purchased from EA Consumables, Inc. (Pennsauken, NJ USA). For this method, we extracted DNAN from aqueous solution using 24 mL of ethyl acetate added to 48 mL of aqueous sample (pH=7) for 2:1 (v/v) water to ethyl acetate UALLE. After UALLE, the top layer solution (ethyl acetate containing DNAN) was transferred to a 25-mL amber bottle for solvent evaporation, then re-dissolution and concentration adjustment. An aliquot of sample solution yielding 0.302 ~ 0.329 mg DNAN was loaded into a silver capsule and the solvent was evaporated before compacting the capsule for O isotope analysis. O isotope fractionation during solvent evaporation was determined to be negligible by comparing $\delta^{18}O$ values of neat DNAN powder with those of DNAN recovered by evaporation of ethyl acetate stock solution (Fig. 2.4.1).
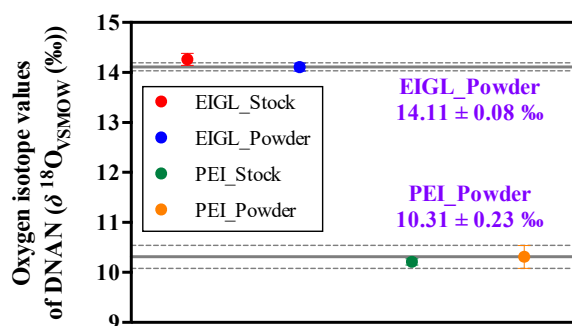
Fig. 2.4.1. $\delta^{18}O$ values of two DNAN working standards (EIGL and PEI) in powder and stock solutions. Solid lines represent average $\delta^{18}O$ values; dashed lines represent standard deviations (n=8).

3.0 Project Task 2: Isotope effects during biotransformation of DNAN and NTO under aerobic and anaerobic conditions

This section of the report describes experimental results from our investigation of the potential of methanotrophs to degrade DNAN and NTO under aerobic conditions, as well as C and N isotope effects accompanying biodegradation of DNAN and NTO by several pure cultures and enrichment consortia under aerobic and anaerobic conditions.

3.1 Biotransformation of DNAN and NTO by aerobic methane-oxidizing consortia and pure cultures

3.1.1. Introduction

The biotransformation of NTO typically involves an initial 2-step reduction, first to 3-hydroxyamino-1,2,4-triazol-5-one (HTO) and then to 3-amino-1,2,4-triazol-5-one (ATO), which has been observed to persist under anoxic conditions, but to biodegrade aerobically (Madeira et al., 2017; Krzmarzick et al., 2015). In order to promote NTO biodegradation, high concentrations of soluble organic substrates such as sucrose, glucose, or pyruvate, are typically added as electron donors. While NTO degradation under bulk aerobic conditions has been reported (Le Campion et al., 1999; Richard and Weidhaas, 2014), it remains unclear whether high concentrations of the substrates actually caused anoxia, thus promoting anaerobic degradation of NTO, rather than aerobic degradation as suggested by Madeira et al., (2017).

Biodegradation of DNAN has been recently observed under both aerobic (Richard and Weidhaas, 2014) and anoxic conditions (Hawari et al., 2015), and a pure culture has been isolated that utilizes DNAN as a sole source of C and N under aerobic conditions, degrading it initially to 2,4-dinitrophenol, and then releasing nitrite prior to entering the typical TCA pathway (Fida et al., 2014; Karthikeyan and Spain, 2016). However, aerobic degradation of DNAN in environmental samples is frequently either not observed or observed at much lower rates than anaerobic degradation (Olivares et al., 2016; Indest et al., 2017). Anaerobically, DNAN has been reported to degrade initially to 2- methoxy-5-nitroaniline (2-ANAN or MENA) and then to 2,4-diaminoanisole (DAAN), which then forms dimers or undergoes a series of secondary substitution reactions leading to a variety of products (Olivares et al., 2016; Olivares et al., 2013).

Based on what is known about the biological degradation of NTO and DNAN, nitroreductase enzymes are likely responsible, and a recent report using whole transcriptome analysis observed up-regulation of a putative nitroreductase during degradation of both compounds in a sequencing batch bioreactor (Weidhaas et al., 2017). While most nitroreductases operate under anoxic or anaerobic conditions, some oxygen-insensitive nitroreductases have been isolated and characterized (Kutty and Bennett, 2005; Kitts et al., 2000). Most nitroreductases operate by accepting electrons from reduced NAD(P)H (generated by the cell during metabolism of labile carbon) and transferring the electrons to the nitro group ($-NO_2$) of the target compound (Valiauga et al., 2018). The resulting product may stop after formation of a nitroso ($-NO$) group, as is the case with the nitramine explosive hexahydro 1,3,5 trinitro- 1,3,5-triazine (RDX) (Kitts et al., 2000), or undergo additional reactions with the eventual formation of an amino ($-NH_2$) moeity, as in the case with nitroaromatic explosives like 2,4,6-trinitrotoluene (TNT) (Kutty and Bennett, 2005; Jain et al., 2004; Oh et al., 2001).

Methanotrophs are a group of widely distributed aerobic microorganisms whose primary carbon and energy source is methane. The methane monooxygenase (MMO) enzymes possessed

by methanotrophs (soluble methane monooxygenase [sMMO] and/or particulate methane monooxygenase [pMMO]), which convert methane to methanol, have been shown to transform a range of environmental pollutants via cometabolism, including chlorinated solvents (e.g., trichloroethylene) (Oldenhuis et al., 1989; Shukla et al., 2009) and various aromatic compounds (e.g., chlorobenzene, PAH) (Rockne et al., 1998; Adriaens and Grbic-Galic, 1994; Jechorek et al., 2003) among many others. However, the ability of these organisms to transform NTO and DNAN, either by their MMO or other enzymes (e.g., nitroreductases), has not been reported.

The present study was undertaken to examine the capacity for biotransformation of NTO and DNAN under aerobic conditions by methane-oxidizing consortia derived from groundwater at two military installations, as well as by two different pure cultures of methanotrophs (*Methylocella palustris* and *Methylosinus trichosporium* OB3b). The extent to which NTO and DNAN serve as substrates for purified sMMO from OB3b was also examined. To our knowledge, this study represents the first report of the degradation of NTO and DNAN by methanotrophs, as well as compelling evidence of the aerobic biotransformation of NTO.

3.1.2. Materials and methods
3.1.2.1. Chemicals

DNAN, DAAN (neat and as sulfate salt), the DNAN breakdown products 2-methoxy-5-nitrophenol (2-M-5-MP) and 4-methoxy-2-nitrophenol (4-M-2-NP), and nitroreductase inhibitors dicoumarol (Yang et al., 2007; Nyanhongo et al., 2006) and 2-iodosobenzoic acid (2-IBA) (LinWu et al., 2009) were purchased from Sigma-Aldrich (St. Louis, MO, USA). The potential DNAN breakdown products, 3-nitro-4-methoxyaniline (2-ANAN), 4-amino-2-nitroanisole (4-ANAN), 2-nitroanisole (2-NA) and 4-nitroanisole (4-NA) were purchased from Santa Cruz Biotechnology (Dallas, TX, USA). NTO was obtained from Dr. Stephen Fallis at the Naval Air Warfare Center Weapons Division (China Lake, CA, USA). The NTO breakdown products 3-hydroxyamino-1,2,4-triazol-5-one (HTO) and 3-amino-1,2,4-triazol-5-one (ATO) were synthesized according to the method of Krzmarzick et al., (2015). All other chemicals were reagent grade or purer. Chemical structures of NTO, DNAN, and their respective breakdown products are shown in Appendix A, Supplemental Information, Table S1.

3.1.2.2. Methanotroph consortia and strains

Methanotrophic consortia were enriched from aquifer samples collected from two Department of Defense sites: Dahlgren Naval Surface Warfare Center (VA), and Indian Head Division Naval Surface Warfare Center (MD). The two consortia are referred to as Dahlgren and IH57 henceforth. Details on the enrichment process are presented elsewhere (Hatzinger and Chu, 2017).   The methanotrophic pure cultures *Methylosinus trichosporium* OB3b (ATCC 35070, OB3b henceforth) and *Methylocella palustris* (ATCC 700799, *Methylocella* henceforth) were obtained from the American Type Culture Collection (ATCC). OB3b was grown in the OB3b Medium of Cornish et al., (1984) with no added copper (Cu) to induce production of sMMO. The consortia were grown in ATCC Medium 2157 (ATCC, 1994) also without added Cu, while *Methylocella* was grown in the same medium (at pH 5 S.U.) (*Methylocella* only possesses sMMO). The pH of the medium was reduced to approximately 4.5 S.U. using phosphoric acid for the two consortia because they were isolated from moderately acidic groundwater. Unless otherwise noted, the consortia and pure cultures were grown in their respective media in sterilized glass Erlenmeyer flasks sealed with silicone stoppers equipped with polystyrene Luer stopcocks. Methane was added to a final concentration of 3–5% (v:v), and flasks were shaken at

150 rpm at room temperature. Methane concentrations were monitored, and additional methane was added as the substrate was depleted. Biomass was collected by centrifugation (20 min @ 10,000×g), washed once with sterile medium, and concentrated again to produce an inoculum for biotransformation experiments.

3.1.2.3. Biotransformation experiments

Experiments were performed in sterilized glass serum bottles under an air headspace. NTO and DNAN were added as sterile aqueous solutions to achieve initial nominal concentrations of 20 mg/L. Methane was added to achieve 3–5% (v:v). Biomass was added at an initial optical density measured at 600 nm (OD600) of approximately 0.4 unless otherwise noted. Controls consisted of: methane only (no cells); cells with methane plus acetylene (5–10%, v:v) as an inhibitor of methane monooxygenase (Prior and Dalton, 1985); cells with acetylene only. A minimum of two replicates per treatment were included during each experiment. Bottles were incubated at room temperature with shaking (150 rpm) in the dark. Methane and acetylene were monitored in the headspace and more methane was added when depleted. A representative methane consumption plot (observed during NTO degradation) is presented in Fig. S1. Periodic liquid samples were removed and analyzed for NTO, DNAN, and their respective breakdown products as described below. Parallel experiments were performed with the consortia using nitrogen-free ATCC Medium 2157 to allow for detection of nitrite, nitrate, and nitrous oxide (N_2O) from the explosive compounds, and also to more closely monitor headspace oxygen concentrations during the biotransformation of NTO and DNAN. The initial cell density was OD600 = 1.0 for these parallel experiments to increase the biotransformation rates. Controls without the explosives present were included to account for any mineralization and release of biomass nitrogen during the incubation.

Experiments were performed to distinguish whether sMMO was directly involved with NTO and/or DNAN transformation. For these studies, the two consortia were either grown on methane (3–5% v:v headspace), methanol (1000 mg/L or 30 mM), or formate (900 mg/L or 20 mM). After biomass was washed and concentrated, the biotransformation of NTO and DNAN in the presence of added methane, methanol, or formate, was assessed as described above. To more definitively rule out the direct role of sMMO, the two consortia were first grown on methanol with or without acetylene, followed by an assessment of their ability to degrade NTO and DNAN when supplied methanol with or without acetylene. These experiments were done with a higher initial cell density (OD600 = ~1.0) to avoid any confounding factors associated with cell growth and long incubation times.

Follow-on experiments were performed to assess the role of nitroreductases in NTO and DNAN biotransformation. OB3b was grown on methane, and washed biomass was then incubated with methane in the presence or absence of dicoumarol (10 mM) or 2-IBA (50 μM), with subsequent sampling over time (Yang et al., 2007; Nyanhongo et al., 2006).

3.1.2.4. Enzyme assays

The degradation of NTO and DNAN by purified sMMO (cell free from OB3b) was evaluated. The hydroxylase component (MMOH), regulatory component (MMOB), and reductase component (MMOR) were expressed and purified following established protocols (Banerjee et al., 2013). The ability of purified sMMO to transform NTO and DNAN was examined by steady-state kinetics (dissolved oxygen consumption) and single turnover transient kinetic measurements by following the decay of sMMO intermediate **Q**. Dissolved oxygen

consumption testing was performed with a Hansatech Instruments Oxytherm + system equipped with an S1 Clark-type oxygen electrode. The total volume of the reactions was 1 mL. The reaction contents include: 0.2 μM hydroxylase (MMOH), 0.4 μM regulatory protein (MMOB), 1.2 μM reductase (MMOR), 250 μM O2, 400 μM NADH, 100 mM MOPS pH 7.5, and varying concentrations of NTO & DNAN. NADH was used to initiate the reaction. The O_2 view software package was used to calculate the initial rate of O_2 consumption. Transient kinetic single-turnover experiments were performed on an Applied Photophysics stopped-flow instrument (model SX 0.18MV with the SX Pro-Data upgrade). Briefly, the experiment involved a rapid mixing (1:1) of diferrous MMOH (120 μM active sites) with oxygen-saturated buffer (pH 7.0) containing MMOB (120 μM) and substrate (DNAN or NTO) on the stopped flow instrument at 4 °C. The sMMO reaction is followed at 430 nm because the substrate-reactive catalytic intermediate **Q** absorbs light at this wavelength. The single-wavelength transient kinetic data were analyzed with the Pro-Data Viewer program from Applied Photophysics and fit to a summed exponential expression (Brazeau and Lipscomb, 2000).

3.1.2.5. Microbial community analysis

The composition of the IH57 and Dahlgren consortia was determined by next generation sequencing performed by Microbial Insights (Knoxville, TN), as per their in-house DNA extraction, sequencing, and data analysis procedures. Briefly, DNA extractions were performed, and 16S metagenomic sequencing was conducted using bacterial primers designed for the high throughput Illumina MiSeq platform. Taxonomic classification of 16S rRNA amplicon reads was performed with the Illumina 16S Metagenomics application which utilizes a curated version of the Green Genes taxonomic database and a high-performance implementation of the Ribosomal Database Project (RDP) Classifier algorithm (Wang et al., 2007). Phylogenetic operational taxonomic unit (OTU) assignment was analyzed according to the *Quantitative Insights Into Microbial Ecology* (QIIME2) bioinformatics pipeline (Caporaso et al., 2010).

3.1.2.6. Chemical analysis methods

Methane and acetylene were analyzed via EPA Method 3810, RSK- 175, using a Varian 3900 GC (Palo Alto, CA) equipped with a flame ionization detector (FID) and an Rt-Alumina Bond/Na2SO4 column (Restek, Bellefonte, PA). The method detection limit was approximately 5 μg/L. Headspace oxygen concentrations were measured during selected experiments using a Varian CP-3800 GC (Palo Alto, CA) equipped with thermal conductivity detector (TCD), with a detection limit of 5000 ppmv (0.5%) for oxygen. Qualitative detection of headspace nitrous oxide (N2O) was performed using an Agilent Cary 660 Fourier-Transform infrared (FTIR) spectrophotometer equipped with a 10 cm single-pass glass gas cell with KBr windows (Buck Scientific, East Norwalk, CT) and a liquid nitrogen cooled linearized mercury cadmium telluride (MCT) detector (Agilent Technologies, Wilmington, DE, USA). Data was collected using Agilent Resolutions software (v. 5.2 and 5.3) over wavenumber range from 4000 to 650 cm^{-1}. The N2O detection limit via this FTIR method was on the order of 20 ppmv. Anions (e.g., nitrite, nitrate) were analyzed via EPA Method 300.0 using an ICS-2000 ion chromatograph (Thermo Fisher Scientific, Waltham, MA).

Concentrations of DNAN and NTO were monitored via high performance liquid chromatography (HPLC) using a Dionex 3000 Ultimate HPLC (Themo-Fisher, Waltham, MA) with a Agilent Zorbax Bonus-RP column (4.6 × 75 mm, 3.5 μm particle diameter) (Santa Clara, CA), variable wavelength detector (254 nm for DNAN and 210 nm for NTO), and a photodiode

array detector collecting peak spectral data. The mobile phase was 50:50 methanol:0.2% (v:v) trifluoroacetic acid in water at a flow rate of 1 mL/min. The column temperature was 33 °C. The injection volume ranged from 15 t 75 µL. The practical quantitation limit of DNAN and NTO with this injection volume was approximately 50 µg/L.

To assess the production of NTO breakdown products, samples were also analyzed using an Agilent 1100 HPLC with a Thermo Scientific Hypercarb column (100 × 4.6 mm, 5 µm particle diameter), variable wavelength detector (340 nm NTO, 360 nm for HTO, and 217 nm for ATO), and a photodiode array detector collecting peak spectral data. The HPLC mobile phase consisted of 0.1% trifluoroacetic acid and 100% acetonitrile for the following time intervals and in ratios: 0–3 min 100:0; 11 min 85:15; 17 min 50:50; 20 min 100:0 at a flow rate of 1 mL/min. The column temperature was 34 °C. The injection volume was 75 µL. The practical quantitation limits of NTO, HTO, and ATO with this injection volume were 50, 500, and 500 µg/L, respectively.

Potential breakdown products of DNAN were analyzed using an Agilent 1100 HPLC with an Acclaim Explosives E1 column (250 mm × _4.6 mm × 5 µm; Thermo Scientific), a Dionex UltiMate 3000 variable wavelength detector (300 nm DNAN, 2-ANAN, 4-ANAN2-NA, 4-NA and 210 nm for DAAN), and a photodiode array detector collecting peak spectral data. The mobile phase was 60:40 H2O:MeOH at a flow rate of 1.0 mL/min. The column temperature was 34 °C. The injection volume was 75 µL. The practical quantitation limits with this injection volume were (µg/L): DNAN, 50; 2-ANAN, 50; 4-ANAN, 50; 2-NA, 50; 4-NA, 50; and DAAN, 100.

3.1.3. Results and discussion
3.1.3.1. Microbial community analysis

Next generation sequencing of the two methane-oxidizing consortia indicated they were dominated by the strictly aerobic methanotrophic genus *Methylosinus* (66% and 81% of the IH57 and Dahlgren consortia, respectively) (Fig. S1). The consortia also shared the aerobic methylotrophic genus *Hyphomicrobium* (4% in each). Other non-methanotrophs (*Chitinophaga*, *Rhodanobacter*, *Cupriavidus*, *Variovorax*, and *Sphingomonas*) were detected in one or both of the consortia at low percentages. Thus, the microbial analyses indicate that the consortia possess a range of organisms, but each is dominated by a single methanotrophic genus – _*Methylosinus*. *Methylosinus* spp. are known to have strains that degrade a range of environmental pollutants, including a wide variety of chlorinated aliphatics (Oldenhuis et al., 1989; Lee et al., 2006), ortho-substituted biphenyls (Lindner et al., 2003), and simple aromatics (Hesselsoe et al., 2005) via sMMO and/or pMMO. Identifying the dominant methanotrophic genera in the consortia allowed us to perform follow-on biotransformation experiments with a pure culture of *Methylosinus trichosporium* OB3b, as well as with purified sMMO enzyme.

3.1.3.2. NTO biotransformation

Biodegradation of NTO by the Dahlgren and IH57 consortia in the presence of methane is presented in Fig. 3.1.1. Rapid production and subsequent disappearance of the reduced NTO breakdown products HTO and ATO was observed, although on a molar basis, these products accounted for only ~16% and 40% of the original NTO, respectively, for the two consortia. NTO degradation occurred under aerobic conditions, with the oxygen concentration in the headspace remaining around 10–15% (equivalent to 4–5 mg/L dissolved oxygen at equilibrium at 24 ◦C)
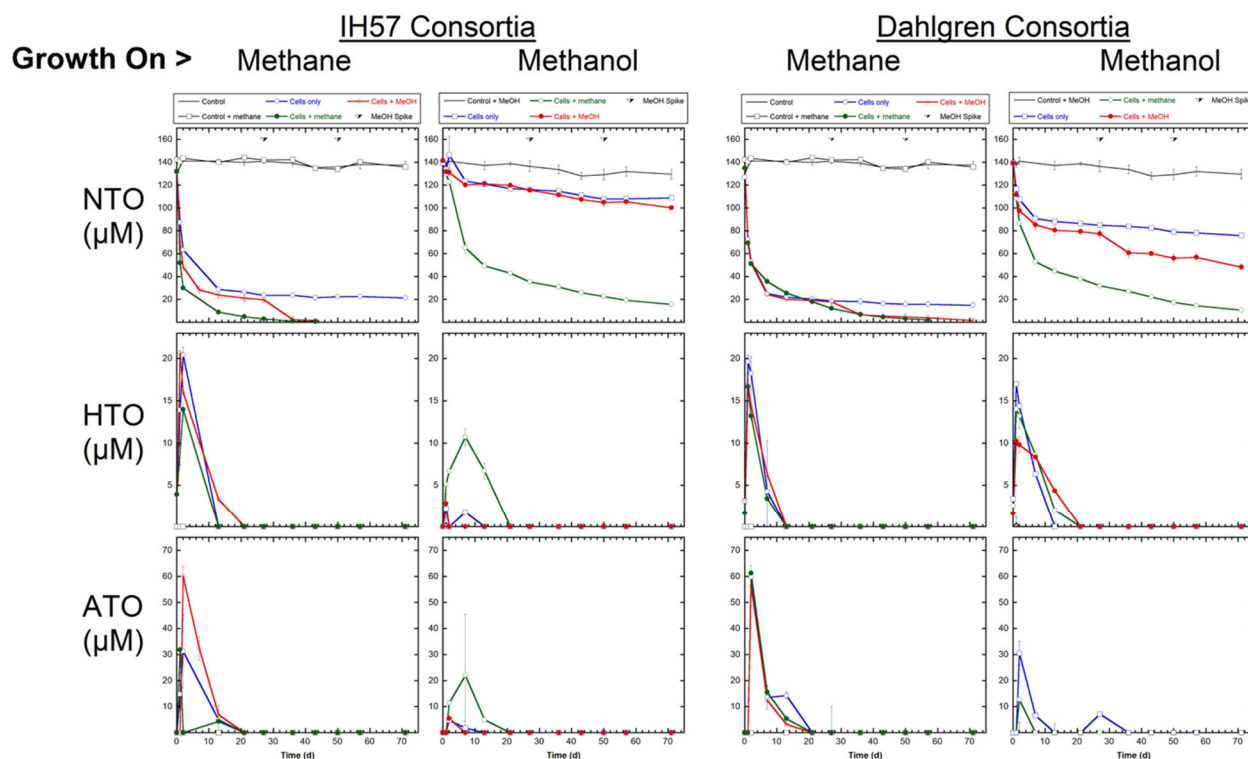
Fig. 3.1.1. Degradation of NTO by two methanotrophic consortia. Data represent average ± one standard deviation of duplicate bottles. Methane spikes were 10% (v:v) during this experiment. Methanol spikes (100 mg/L) were only made to bottles which had received methanol (initial addition of 10 mg/L) at the start of the biotransformation experiment. Initial culture OD was 0.4.

during the studies. Further verification that NTO was degraded under aerobic conditions was obtained during experiments with a higher initial biomass. As shown in Fig. S3, NTO transformation to HTO (as well as HTO transformation to ATO) was completed while the calculated equilibrium dissolved oxygen concentrations were greater than 4 mg/L.

Cells grown on methane and then incubated with NTO in the absence of methane exhibited incomplete NTO removal (Fig. 3.1.1). It is likely that, in the absence of methane, these cells were depleted in reducing equivalents (e.g., NADH, NADPH) during the course of the study, preventing the continued degradation of NTO. This indicates that methane-oxidizers were responsible for NTO degradation in the consortia, but that they required some source of energy (e.g., methane, methanol, etc.) in order to support the process.

Acetylene, which is a suicide substrate for monooxygenase enzymes, inhibited the consumption of methane in both consortia, as expected (data not shown). The presence of acetylene, alone or in the presence of methane, also inhibited NTO and DNAN biotransformation in the IH57 consortium (Fig. S4). This inhibition could indicate the involvement of a monooxygenase in NTO and DNAN degradation, or may just reflect the inhibition of cell metabolism, and resulting lack of necessary reducing equivalents for enzymatic reactions. However, cells grown on methanol, which is generally assumed to not induce sMMO gene expression, and in the presence of acetylene, which would result in the irreversible inactivation of sMMO, were able to transform NTO as well as cells given methanol without acetylene present (Fig. 3.1.2A), largely ruling out a direct role of sMMO in NTO transformation. These results also verified that NTO transformation was occurring under aerobic conditions, as headspace oxygen

measurements indicated equilibrium dissolved oxygen concentrations remained higher than 4 mg/L. Interestingly, acetylene also inhibited the degradation of DNAN in the Dahlgren consortium in the presence or absence of methane, but not NTO degradation under either condition (Fig. S4). The reason for this is not clear, but perhaps suggests involvement of different enzymes in NTO and DNAN degradation in this consortium.
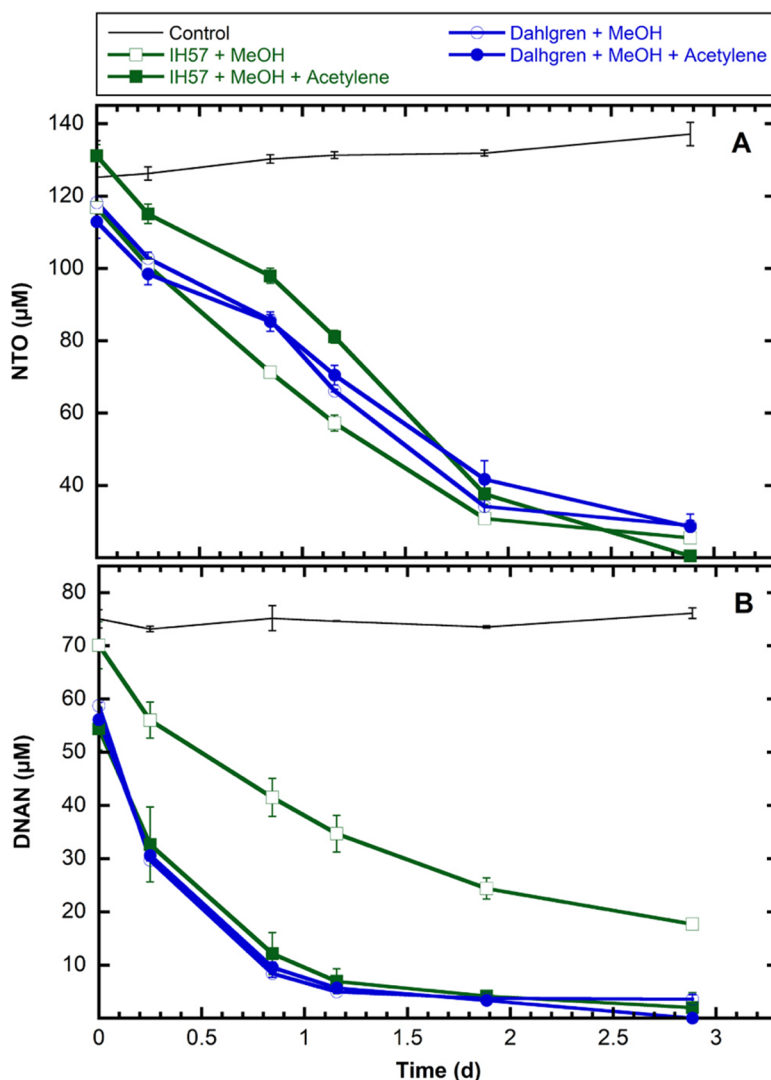
Fig. 3.1.2. Degradation of (A) NTO or (B) DNAN by two methanotrophic consortia supplied methanol (initial concentration 1000 mg/L) in the presence of acetylene. Data represent average ± one standard deviation of duplicate bottles. Initial culture OD was 1.0.

Methane grown cells in the consortia that were supplied with methanol instead of methane as a electron donor and carbon source exhibited similar degradation of NTO to cultures receiving methane, and additional methanol inputs appeared to stimulate activity (Fig. 3.1.1). Methanol grown cells supplied with methane degraded NTO slightly slower than methane grown cells receiving methane, but degradation was apparent. Interestingly, methanol grown cells supplied with methanol exhibited only partial NTO degradation, and complete degradation was not

observed even with repeated methanol additions. This is also in contrast with the experiments performed at higher initial cell densities in which NTO was rapidly and completely degraded (Fig. 3.1.2A). Furthermore, cells grown on methanol then incubated with NTO without methanol evidenced very limited NTO degradation compared to cells grown on methane and incubated with NTO without methane. These results suggest that growth and consumption of methanol leads to less internal energy storage compared to methane (and hence, less ability to generate reducing equivalents when no carbon and energy source is supplied). It is also possible that the microbial community grown on methanol differed somewhat from that grown on methane, thus leading to the observed differences in NTO biodegradation.

In contrast to methanol, formate did not support significant NTO degradation by cells grown on either methane or formate (Fig. S5). Given that formate, like methanol, is a known downstream metabolite of methane oxidation, it is surprising that it did not support appreciable NTO degradation in the consortia. This may also represent a shift in the dominant organisms in the consortia (i.e., to those that do not degrade NTO) rather than a direct physiological effect (e.g., methanol and formate not supporting the methanotrophs' ability to reduce NTO).

The degradation of NTO by the consortia was also tested in N free medium to determine if inorganic N species could be detected as terminal products. No significant increases in nitrite, nitrate, or nitrous oxide were detected during degradation of NTO compared to the controls with no NTO added. These results indicate that either the HTO and ATO produced from NTO broke down to unknown compounds that were not mineralized, or that NTO breakdown products were mineralized, and the resulting inorganic nitrogen was assimilated into biomass rather than accumulating to detectable levels (>0.2 mg/L) the medium.

NTO was biodegraded by the pure culture *M. trichosporium* OB3b, albeit at a relatively slow rate (Fig. 3.1.3). ATO was not observed, in contrast to the consortia, but HTO was detected as an initial degradation product (<10% molar basis), and only degraded after an extended incubation, either biologically or via abiotic processes. Additionally, in the absence of methane, and the presence of acetylene with or without methane, OB3b did not degrade NTO (Fig. 3.1.3). Unlike OB3b, a pure culture of *Methylocella* was not observed to degrade NTO. NTO degradation by OB3b in the presence and absence of the nitroreductase inhibitors dicoumarol and IBA is shown in Fig. S7. IBA inhibited NTO degradation, while dicoumarol did not. Neither compound inhibited methane consumption, indicating that sMMO was still active. The lack of inhibition by dicoumarol may have been due to the inability of a sufficient amount to enter the cells to elicit a response, as reports of dicoumarol-sensitive nitroreductase activity in bacteria have used cell-free or purified enzyme systems (Kutty and Bennett, 2005; Tatsumi et al., 1981; Somerville et al., 1995). The alternative is that a dicoumarol-insensitive nitroreductase is responsible for NTO transformation. These results support involvement of some type of (nitro) reductase in the transformation of NTO, as opposed to sMMO. This is clearly an area for further investigation.

Fig. 3.1.3. Degradation of NTO by *Methylosinus trichosporium* OB3b. Data represent average ± one standard deviation of duplicate bottles. Methane spikes were 3–5% (v:v) during this experiment. Initial culture OD was 0.4.

Steady-state kinetics, single-turnover transient kinetics, and HPLC detection of substrate turnover experiments were performed to assess if sMMO derived from OB3b catalyzes NTO degradation. Purified *M. trichosporium* (Mt) sMMO did not oxidize or otherwise interact with NTO based on the steady-state and single-turnover transient kinetics data (Table S2, Fig. S8). If NTO was an sMMO substrate, the rate of oxygen consumption and the decay rate constant of **Q** would increase in the presence of NTO. Instead, adding various amounts of NTO did not increase the rate of oxygen consumption (Fig. S8) or affect the decay rate constant of intermediate **Q** (Table S2). Additionally, analysis of the post-steady state reaction mixture using HPLC detected no loss of NTO or formation of any NTO breakdown products. The absence of NTO breakdown products, no elevated O2 consumption, and no change in the decay rate constant of **Q** clearly indicated that NTO is not a sMMO substrate.

This is the first known report of NTO biotransformation by methanotrophic bacteria. Additionally, NTO degradation was observed to occur under aerobic conditions by the two consortia, and by strictly aerobic strain OB3b under oxic conditions when methane was supplied. The general consensus thus far has been that NTO is only reduced to ATO under anoxic conditions, and that ATO is only degraded further under aerobic conditions (Madeira et al., 2017; Krzmarzick et al., 2015). While Le Champion (1999) reported that NTO was transformed to ATO by a *Bacillus* strain, maintenance of aerobic conditions in the presence of 5 g/ L of glucose was not definitively confirmed. Similarly, during a study of the biodegradation of IMX-101 (which includes both NTO and DNAN), Richard and Weidhaas (2014) reported aerobic NTO biodegradation, but only in the presence of soluble carbon substrates which may also have led to anoxia in the media (Madeira et al., 2017; Krzmarzick et al., 2015).

Culture and purified enzyme data indicate that sMMO is not directly involved with the transformation of NTO, which is consistent with the initial reaction being reductive rather than oxidative. It is likely that a reductase enzyme is responsible for the initial reduction of NTO to HTO, with the metabolism of methane (or methanol) providing reducing equivalents to drive the reduction. The full genome of *M. trichosporium* Ob3b was recently sequenced, and two nitroreductases, as well as multiple other unknown reductases, were detected. It is very likely that one of these enzymes, which are likely oxygen- and dicoumarol-insensitive, was responsible for the observed aerobic degradation of NTO. Methanotrophs have also been shown to have the ability to reduce inorganic compounds such as chromium (VI) under aerobic conditions (Hamad, 2009; Lai et al., 2016), so the aerobic reduction of NTO is not without precedent. Further studies are required both to confirm the enzyme(s) responsible for reducing NTO and to determine the downgradient fate of the compound.

3.1.3.3. DNAN biotransformation

Biodegradation of DNAN by the Dahlgren and IH57 consortia in the presence of methane is presented in Fig. 3.1.4. Dissolved oxygen concentrations remained around 4–5 mg/L based on headspace measurements during DNAN transformation (Fig. S3). Production of the reduced DNAN breakdown products 2-ANAN and 4-ANAN (combined ~44% and ~52% observed. 2-ANAN persisted for the duration of the incubation, while the concentrations of 4-ANAN appeared to level off and then decrease slightly at latter timepoints in both consortia. The other potential products (DAAN, 2-AN, 4-AN, 2-M-5-NP, 4-M-2-NP) were not detected. Similar to NTO, DNAN degradation was completely inhibited in the IH57 consortium by acetylene, regardless of the presence of methane. For the Dahlgren consortium, in contrast to what was

observed with NTO, the presence of acetylene, alone or in the presence of methane, inhibited DNAN degradation (Fig. S4).

Methanol supplied to methane grown cells supported slow DNAN degradation compared to when methane was supplied (Fig. 3.1.4). Methanol grown cells supplied with methane degraded DNAN much slower than methane grown cells supplied with methane, and methanol grown cells supplied with methanol exhibited a reduced capacity for DNAN degradation. Methanol grown cells incubated with DNAN without additional methanol did not exhibit substantial DNAN degradation, likely due to limited reducing power. As observed with NTO, cells grown on methanol in the presence of acetylene evidenced transformation of DNAN similar
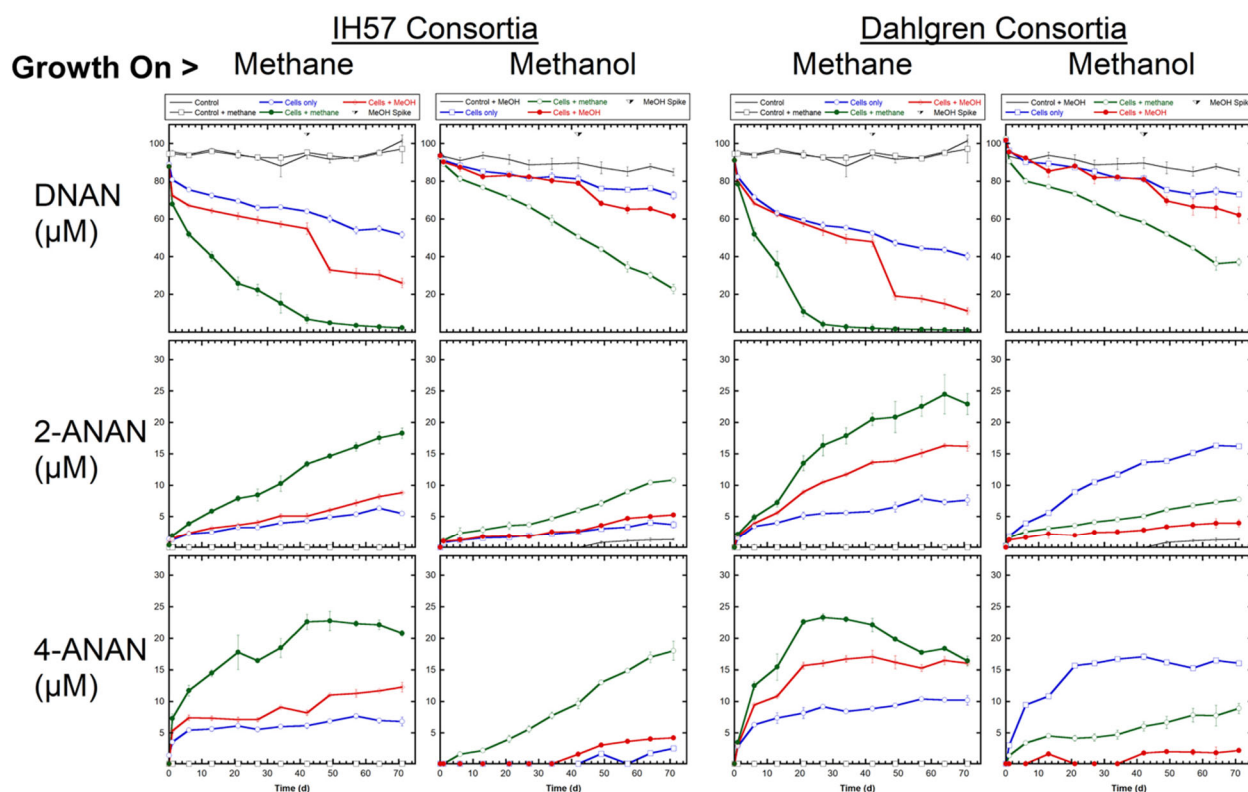
Fig. 3.1.4. Degradation of DNAN by two methanotrophic consortia. Data represent average ± one standard deviation of duplicate bottles. Methane spikes were 3–5% (v:v) during this experiment. Methanol spikes (100 mg/L) were only made to bottles which had received methanol (initial addition of 10 mg/L) at the start of the biotransformation experiment. Initial culture OD was 0.4.

to that of cells not exposed to acetylene (Fig. 3.1.2B), ruling out a direct role of sMMO in DNAN transformation as well.

Formate did not support significant DNAN degradation by cells grown on methane or formate (Fig. S6), but cells grown on formate and supplied with methane degraded DNAN, albeit at a slower rate than methane grown cells supplied with methane. Cells grown with formate then incubated with DNAN without formate evidenced very limited DNAN degradation (Fig. 3.1.4). These data were like those for NTO and were assumed to be due to lack of generation of sufficient reducing equivalents to drive the transformation of DNAN.

No significant increase in nitrite, nitrate, or nitrous oxide were detected in nitrogen free medium during the degradation of DNAN by the consortia compared to the no DNAN controls. Similar to NTO, this indicates that the detectable breakdown products of DNAN (2-ANAN and 4-ANAN) were either mineralized with assimilation of the inorganic nitrogen, or the products were not detectable using the analytical methods available during this research. Strain OB3b degraded DNAN with the production of 2-ANAN and 4- ANAN (maximum combined 45% of initial DNAN on a molar basis), which did not further degrade. No other identifiable organic products were observed. In contrast to what was observed with NTO, slow DNAN degradation was observed in the absence of methane, and in the presence of acetylene with or without methane, with some accumulation of 2-ANAN and 4-ANAN (Fig. 3.1.5). Acetylene effectively inhibited methane consumption by OB3b, so energy to support the transformation was assumed
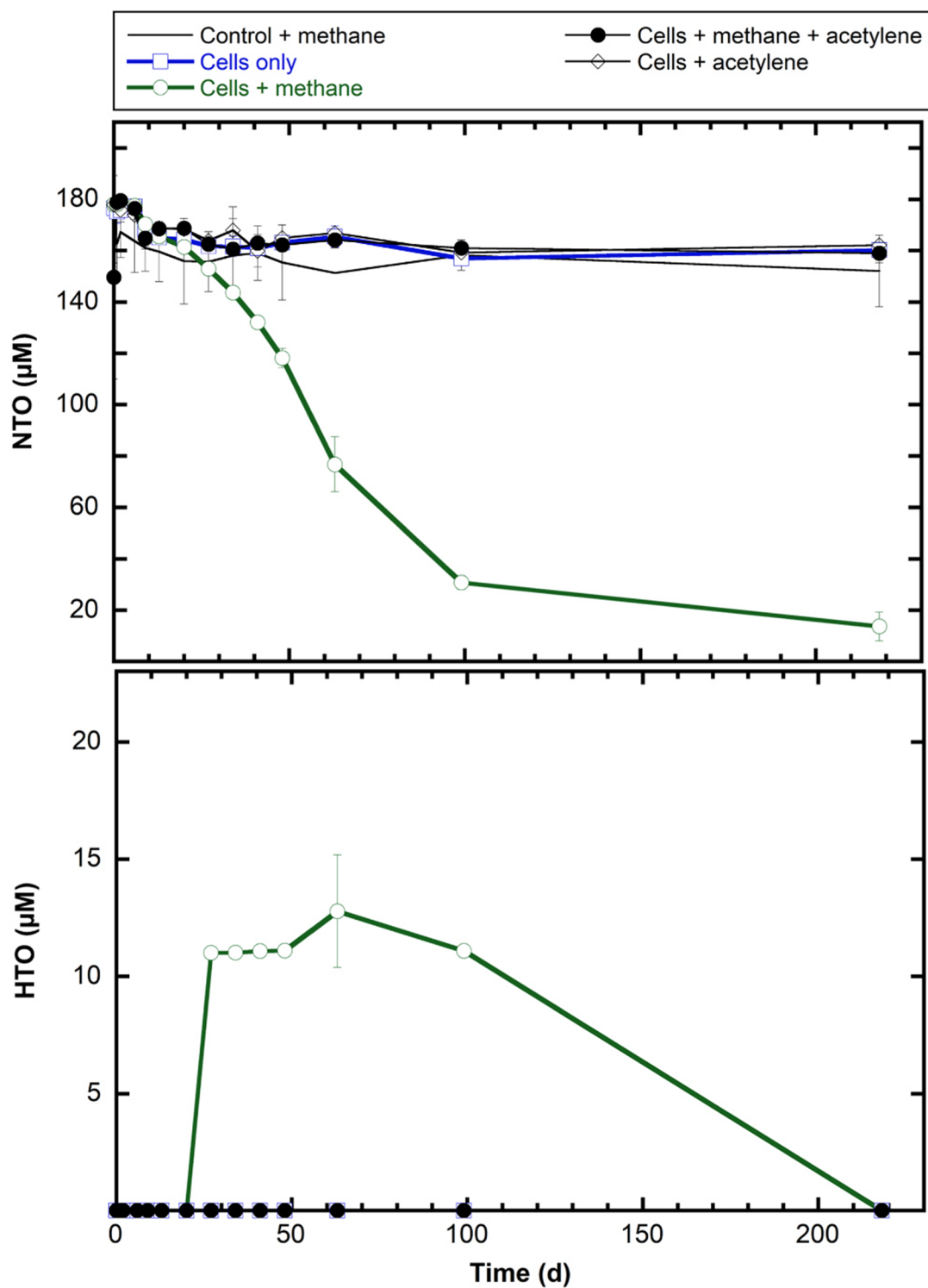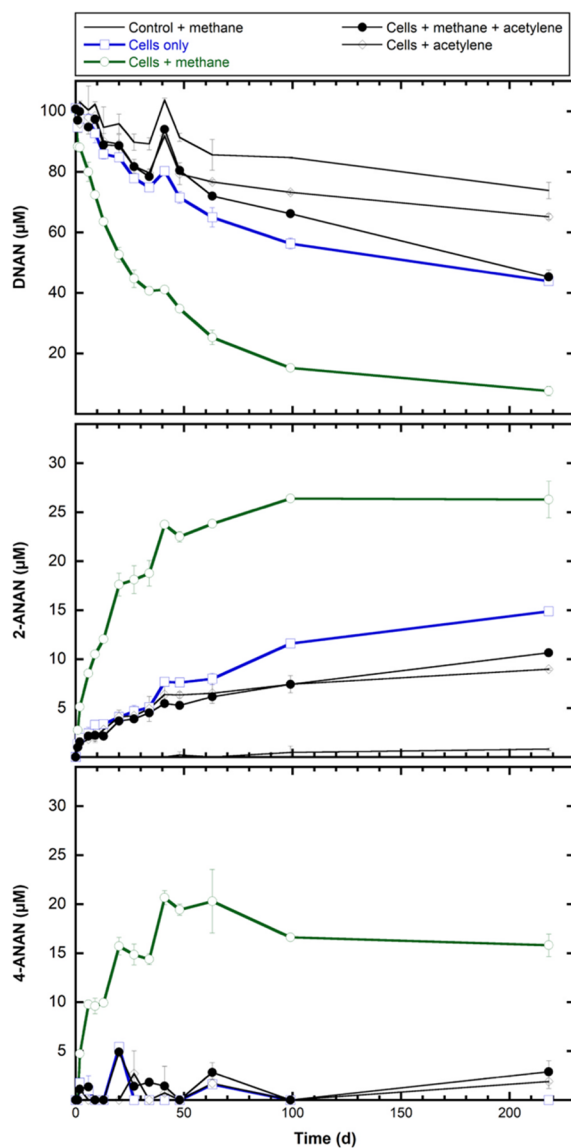

Fig. 3.1.5. Degradation of DNAN by *Methylosinus trichosporium* OB3b. Data represent average ± one standard deviation of duplicate bottles. Methane spikes were 3–5% (v:v) during this experiment. Initial culture OD was 0.4.

to be coming from other cellular energy stores. Similar to NTO, DNAN was not significantly degraded by a pure culture of *Methylocella*.

As with NTO, the nitroreductase inhibitor dicoumarol had no impact on DNAN degradation, whereas DNAN degradation was inhibited by IBA (Fig. S7), again supporting the potential role of a dicoumarol-insensitive (nitro)reductase in DNAN transformation, rather than sMMO.

Unlike the steady-state kinetics of the reconstituted sMMO system in the presence of NTO, the addition of DNAN caused the rate of dissolved O_2 consumption to increase (Fig. S8). The elevated consumption rate would normally indicate that DNAN is an sMMO substrate, but HPLC analysis of the post steady-state reaction showed no loss of DNAN or formation of any DNAN breakdown products. It was expected that DNAN breakdown products would be present, since increasing the concentration of DNAN increased the rate of dissolved oxygen consumption, but the lack of apparent DNAN breakdown indicated that oxygen was being removed from solution by an alternative reaction. Upon further investigation of this phenomenon, the steady-state kinetics showed that the increased O_2 consumption was due to a side reaction involving four components of the assay (NADH, MMOR, DNAN, and O_2) (Table S2). A similar phenomenon was reported when spin-traps were used to detect sMMO substrate radical intermediates (Liu et al., 2005). The authors concluded that the autooxidation of reduced MMOR creates reactive oxygen species which then were sequestered by the spin-traps. We reasoned that DNAN, by an unknown mechanism, enhances the autooxidation of reduced MMOR, which resulted in an apparent increase in dissolved oxygen consumption as O_2 was converted to activated oxygen species such as superoxide and/or hydroxyl radicals.

A direct assessment of DNAN reactivity by single turnover stopped flow transient kinetics indicated that DNAN is not an sMMO substrate, since the formation and decay rates of intermediate **Q** were not elevated in the presence of DNAN above that observed in the no substrate control (Table S3). Coupled with steady-state kinetics data, HPLC analysis of post steady-state reactions, and transient kinetics, we conclude that DNAN is not an sMMO substrate, and that sMMO was not directly involved in the transformation of DNAN by our consortia and OB3b.

The apparent reduction of DNAN to the amino-intermediates 2-ANAN and 4-ANAN under aerobic conditions is assumed to be carried out by the same or similar oxygen- and dicoumarol-insensitive (nitro) reductases involved with NTO reduction. However, unlike NTO, the reduced intermediates of DNAN were not observed to be completely degraded by the consortia or OB3b, likely due to a lack of enzymes necessary for downstream metabolism of these intermediates. Other methanotrophs have been shown to have the ability to degrade aromatic compounds such as PAHs (Rockne et al., 1998) and biphenyls (Adriaens and Grbic-Galic, 1994), so the reason for the accumulation of 2-ANAN and 4-ANAN, albeit at relatively low concentrations, is not evident at this time.

3.1.4. Conclusions

In this section, we showed for the first time that methane-oxidizing bacteria (two groundwater consortia and the pure culture *M. trichosporium* (OB3b) are capable of biodegrading both NTO and DNAN under oxic conditions. Based upon the degradation products, as well as studies with purified sMMO enzyme and various inhibitors, we hypothesize that degradation is mediated by one or more (nitro)reductase enzymes rather than sMMO, which is

known to catalyze the degradation of a wide variety of different pollutants. However, sMMO appears to serve the supporting role of providing reducing equivalents to drive the activity of the presumptive oxygen- and dicoumarol-insensitive (nitro)reductases. Neither NTO nor DNAN were used as the sole source of carbon and/or energy by these cultures. However, NTO may be used as nitrogen source for these cultures based on the results from experiments in nitrogen-free medium, although additional studies would be required to definitively demonstrate this.

While it is likely that *Methylosinus* spp. accounted for the degradation of these compounds in the two consortia, based on the high relative density of this genus, as well as the findings with the pure culture OB3b, the contribution of other members of the consortia cannot be completely ruled out. Confirmation of the members of the consortia directly involved with biotransforming NTO and DNAN (and their respective breakdown products) via stable isotope probing or other techniques was beyond the scope of the current study, as was further examination of the enzyme(s) responsible for the observed degradation.

Importantly, the results reported herein provide a new potential mechanism for the degradation of NTO and DNAN in the environment and suggest the potential for loss under aerobic, methane-oxidizing conditions. Methanotrophic bacteria are widespread in nature, and would be expected in surface soils, vadose soils, aquifers, and marshes that characterize many range environments where NTO or DNAN may enter the environment. Thus, natural attenuation of these compounds by methanotrophic communities is possible. Similarly, these findings lay the groundwork for possible enhanced groundwater remediation through methane addition. These results may also lead to effective munition manufacturing wastewater treatment approaches using these or similar methanotrophic consortia.

The initial findings also raise further questions, including: which enzyme(s) are responsible for the observed degradation of NTO and DNAN, what species or groups of methanotrophs carry out this activity, why does it vary among different genera (e.g., *Methylocella* vs. *Methylosinus*), and what environmental factors significantly affect this process. Measurements of the isotope effects associated with DNAN and NTO during transformation by these methanotrophic consortia are reported below in section 3.2 (DNAN isotope effects) and section 3.3 (NTO isotope effects).

3.2. Isotope effects during biotransformation of DNAN and NTO

Kinetic isotope effects associated with biotransformations of DNAN and NTO by pure cultures and consortia under aerobic and anaerobic conditions were measured in this project. Experiments were performed with three aerobic pure cultures: *Pseudomonas fluorescens* I-C (Blehert et al., 1999; Fuller et al., 2009), *Rhodococcus Ruber* ENV-425 (Steffan et al., 1997; Fournier et al., 2009; Tupa and Matsuda, 2018), and *Rhodococcus aetherivorans* ENV-493 (isolated from groundwater at a Naval Air Station as part of ESTCP Project 201733), two anaerobic enrichment cultures (MBR, isolated from a membrane bioreactor system, and Runoff , a consortium derived from surface runoff from the Dahlgren, Virginia facility of the U. S. Navy), and one aerobic enrichment culture (Dahlgren Methanotrophs, derived from groundwater at the Dahlgren facility, and consisting ~81 % of the strictly aerobic genus *Methylosinus*).

3.2.1. Materials and methods
DNAN. Experiments performed with DNAN were done with three aerobic pure cultures: (1) *Pseudomonas fluorescens* I-C (Blehert et al., 1999; Fuller et al., 2009), (2) *Rhodococcus Ruber* ENV-425 (Steffan et al., 1997; Fournier et al., 2009; Tupa and Matsuda, 2018), and (3) *Rhodococcus aetherivorans* ENV-493 (isolated from groundwater at a Naval Air Station as part

of ESTCP Project 201733); two anaerobic enrichment cultures (1) MBR, isolated from an anaerobic membrane bioreactor system, and (2) Runoff , a consortium derived from surface runoff from the Dahlgren, Virginia facility of the U. S. Navy; and an aerobic enrichment culture Dahlgren Methanotrophs, derived from groundwater at the Dahlgren facility, and consisting ~81 % of the strictly aerobic genus *Methylosinus*.

At set intervals, samples were collected to monitor DNAN concentrations. Samples were centrifuged (14,000 rpm, 4 min), and 0.5 mL of the supernatant was added to 0.5 mL methanol, shaken vigorously, and analyzed by HPLC (details of analytical method given in section 4.3.2.3 of this report). When designated target residual concentrations were reached, larger sample aliquots were taken for isotope measurements.   Sample volume varied depending on the volume of solution needed to obtain 100 µg of DNAN for isotopic analysis. These samples for GC-IRMS measurements of carbon and nitrogen isotope ratios were centrifuged (1,390 x g, 20 °C, 20 min), and the supernatant was removed and acidified with 1:1 HCl to pH <2. Aliquots from DNAN experiments were stored at 4 °C until they were processed via SPE (details of SPE extraction given in section 2.3.2 of this report). DNAN was eluted from the SPE cartridges with acetonitrile, and then shipped to the University of Delaware for isotopic analysis. Aliquots from NTO experiments were stored at -80 °C and not processed by SPE. Instead, they were kept frozen and transported to the University of Delaware where they were thawed and processed by ultrasonic liquid-liquid extraction immediately before isotopic analysis (Wang et al., 2021d).

Additional information specific to the experiments performed with each culture are given below:

Rhodococcus ruber ENV-425 inoculum was prepared by picking a single colony from an R2A plate growing in BSM with 1000 mg/L lactate. The first replicate started with an initial OD_{600} of 1.83 and concluded with a final OD_{600} of 6.02. The second replicate was started with a heavier inoculum, with an initial OD_{600} of 3.12 and a final OD_{600} of 6.88.

Rhodococcus aetherivorans ENV-493 inoculum was prepared by picking a single colony from an R2A plate growing in BSM with 1000 mg/L lactate. The first replicate started with an initial OD_{600} of 2.91 and concluded with a final OD_{600} of 3.35. The second replicate started with an initial OD_{600} of 2.5 and a final OD_{600} of 1.26.

MBR enrichment culture inoculum was prepared by removing 500 mL from a 7-L batch anaerobic reactor degrading a mix of explosives (HMX, RDX, TNT, NTO, DNAN) plus perchlorate and nitrate. Cells were pelleted (details of floor centrifuge), washed once with anaerobic phosphate (4 mM) buffer, and then stored at 4°C in phosphate buffer under an argon headspace until the start of the experiment. The experiment was done under anoxic conditions in revised anaerobic minimal medium (RAMM) (Shelton and Tiedje, 1984). The bottles and media were initially purged with nitrogen to remove oxygen, then overlain with argon to maintain anoxic conditions. Fructose was added at a concentration of 1000 mg/L. The first replicate started with an initial 1.66 and a final OD_{600} of 1.27.

Runoff enrichment inoculum was cultured under anoxic conditions in BSM with a mixture of glucose, fructose, lactate, and acetate (all at 1000 mg/L). The experiment was done under anoxic conditions in a two-liter Erlenmeyer flask with BSM using the same carbon source mixture. The bottles and media were initially purged with nitrogen to remove oxygen. The first replicate started with an initial OD_{600} of 0.53 and concluded with a final OD_{600} of 0.84. The second replicate was started with an initial OD_{600} of 0.55 and a final OD_{600} of 0.86.

A separate set of experiments evaluated DNAN degradation by *Pseudomonas fluorescens* I-C under air-purged, 100% nitrogen-purged, and 100% oxygen-purged conditions. These

experiments were performed in 500 mL glass bottles with 200 mL of BSM amended with initial DNAN concentration of 25 mg/L sealed with unlined polypropylene caps. The caps were equipped with three ports made from 16.5-gauge needles. Two of the ports were attached to FEP tubing inside the cap that allowed the solution inside to be purged with various gases and for samples of the solution to be removed using a sterile syringe. The third port served as a vent and was plugged with a sterile polypropylene syringe filter. Compressed air, nitrogen, or oxygen gas (flow rate = 50 mL/min) was sterilized by passage through a sterile PTFE syringe filter prior to entering the bottle. Bottles were placed on a multi-position stir plate and mixed using a teflon-coated stir bar at 500 rpm. The temperature during these experiments averaged 26°C. Sampling, processing, and analysis were done as described above.

NTO. Isotope fractionation experiments with NTO were performed using pure culture *Ps. fluorescens* I-C and an aerobic consortium Dahlgren Methanotrophs, as well as an anaerobic consortium collected from an anaerobic membrane bioreactor (MBR) degrading explosives that was derived from the anaerobic bioreactor mentioned above.

Isotope effects during biotransformation of NTO were examined by experiments similar to those performed for DNAN, with the following specific details for each culture:

The *Ps. fluorescens* I-C experiment started with an initial OD_{600} of 0.31 and a final OD_{600} of 1.44. Only one replicate experiment was performed.

The Dahlgren Methanotrophs experiment started with an initial OD_{600} of 4.11 and a final OD_{600} of 0.98 (indicating some cell lysis during the experiment). Only one replicate experiment was performed.

The first replicate of the MBR experiment started with an initial OD_{600} of 2.62 and ended with a final OD_{600} of 1.94. The second replicate started with an initial OD_{600} of 2.59 and ended with a final OD_{600} of 2.30

Aliquots from NTO experiments for isotope analysis were centrifuged and the supernate was filtered through a 0.2 μm cellulose acetate membrane filter prior to storage at -80 °C. NTO samples were kept frozen and transported to the University of Delaware, where they were thawed and processed by ultrasonic liquid-liquid extraction immediately before isotopic analysis (Wang et al., 2021c).

3.2.2. Results and discussion
3.2.2.1. Kinetics and products of DNAN biotransformation experiments

DNAN transformation by aerobic pure cultures ENV425 and ENV493 required several days to reach completion. The DNAN breakdown products 2-ANAN and 4-ANAN were observed in all replicates (Figs. 3.2.1 and 3.2.2). The combined products represented 20% to 70% of the initial DNAN on a molar basis and were generally dominated by 2-ANAN. The variability between replicates of these aerobic pure cultures likely reflects that the experiments were temporally separated, leading to differences in the initial cell densities and/or metabolic condition of the inocula.
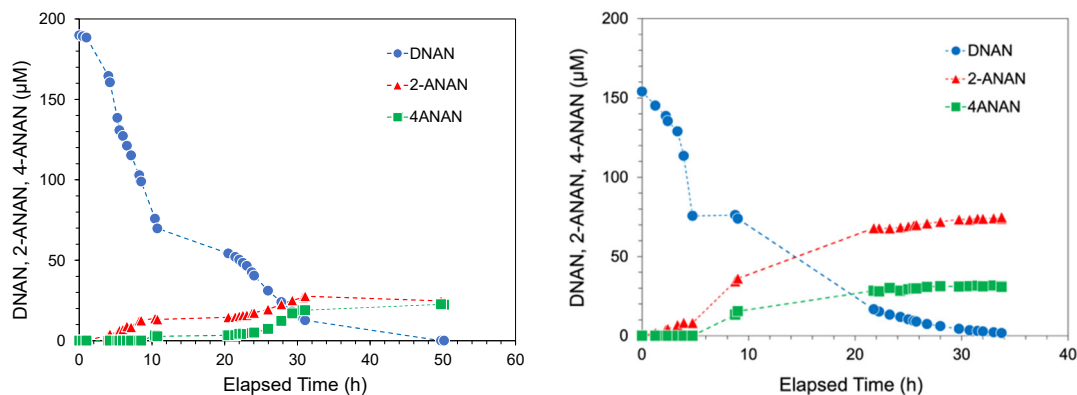
Fig. 3.2.1. Concentrations of DNAN, 2-ANAN, and 4-ANAN (μM) vs. elapsed time (h) during two replicate biodegradation experiments with bacterial strain ENV-425 *Rhodococcus ruber*.
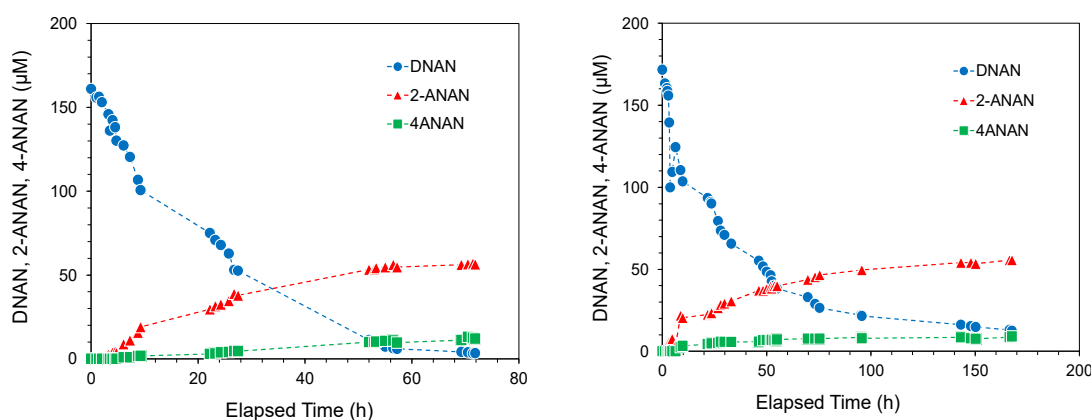
Fig. 3.2.2. Concentrations of DNAN, 2-ANAN, and 4-ANAN (μM) vs. elapsed time (h) during two replicate biodegradation experiments with bacterial strain ENV-493 *Rhodococcus aetherivorans.*

Anoxic DNAN transformation by the MBR enrichment culture was completed in about 24 h. Breakdown products constituted approximately 90% of the initial DNAN, and 2-ANAN dominated 4-ANAN roughly 2:1 (Fig. 3.2.3). In contrast, the Runoff enrichment transformed all the DNAN in less than 3 h. 2-ANAN and 4-ANAN represented approximately 45% of the initial DNAN. Final 2-ANAN concentrations were only slightly higher than 4-ANAN (Fig. 3.2.4)
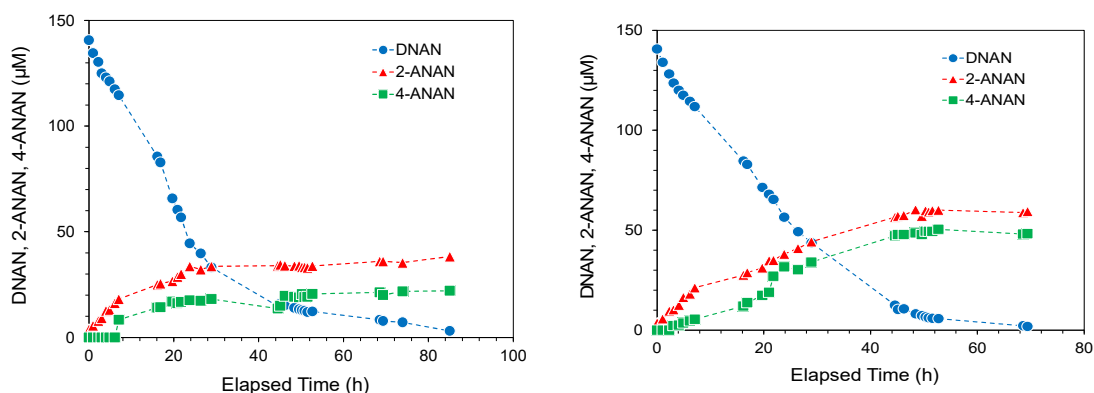
Fig. 3.2.3. Concentrations of DNAN, 2-ANAN, and 4-ANAN (μM) vs. elapsed time (h) during two replicate biodegradation experiments with bacterial enrichment culture MBR.
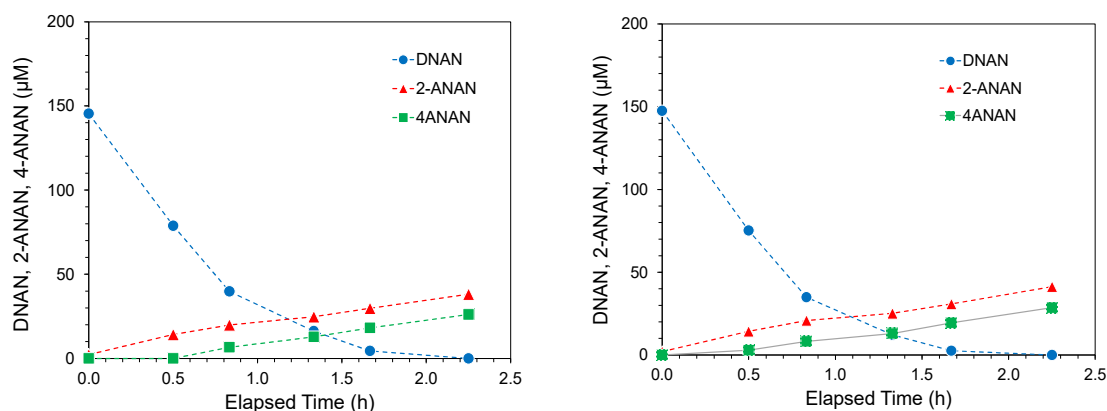
Fig. 3.2.4. Concentrations of DNAN, 2-ANAN, and 4-ANAN (μM) vs. elapsed time (h) during two replicate biodegradation experiments with "Runoff" bacterial enrichment culture.

The DNAN transformation by *Pseudomonas fluorescens* I-C required approximately 11 days. Degradation was fastest under air-purged conditions compared to either nitrogen- or oxygen-purged conditions (Fig. 3.2.5). This likely indicated that the reduction process required aerobic conditions that allowed the cells to generate reducing equivalents from the added carbon source, while also maintaining the oxygen concentration below a level that would inhibit reduction. Nitrogen-purged conditions resulted in a higher percentage of DNAN converted to reduced products compared to air- and oxygen-purged conditions (66%, 41%, and 30%, respectively; molar basis), and under all conditions, the final percentages of DNAN converted to 2-ANAN were higher than to 4-ANAN (Fig. 3.2.6).
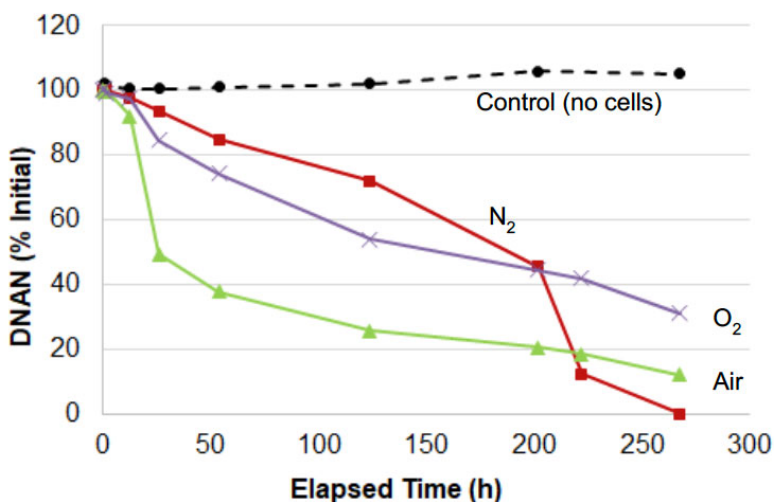
Fig. 3.2.5. DNAN concentration (% initial) vs. elapsed time (hours) for *Pseudomonas fluorescens* I-C biodegradation experiments with sparging by air, 100% N_2, and 100% O_2. Also shown is a control experiment with no cells added.
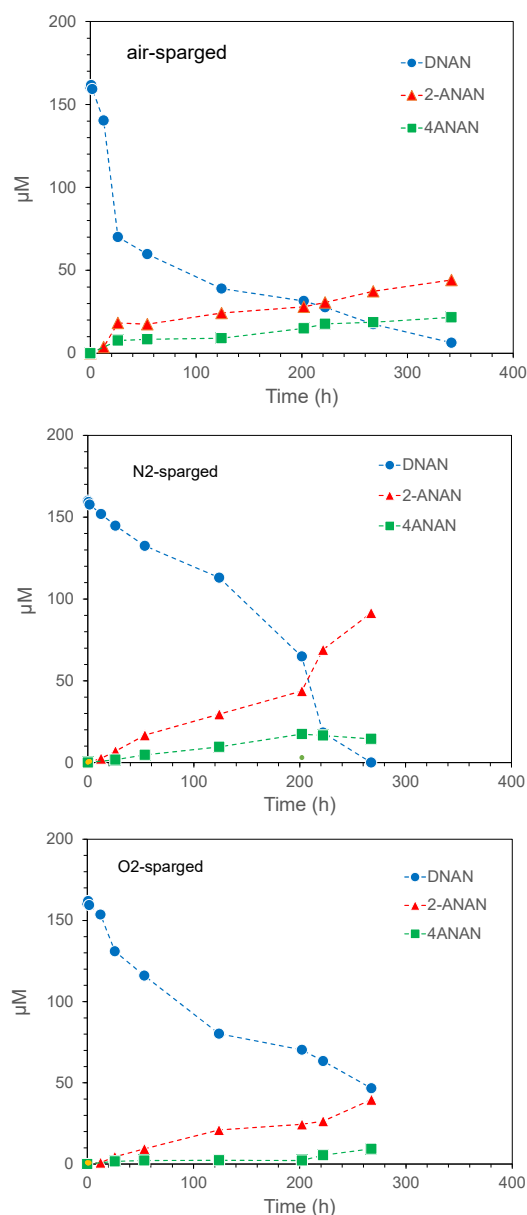
Fig. 3.2.6. Concentrations of DNAN, 2-ANAN, and 4-ANAN vs. time (h) during biodegradation experiments with *Pseudomonas fluorescens* I-C under air-sparged (top), 100% N₂-sparged (middle), and 100% O₂-sparged (bottom) conditions.

3.2.2.2. Isotope effects
3.2.2.2. Kinetics and products of NTO biotransformation experiments

NTO transformation by the aerobic pure culture *Pseudomonas fluorescens* I-C and the aerobic enrichment consortium Dahlgren Methanotrophs was a slow process that required 7 and 8 weeks, respectively, to reach completion under air-sparged conditions. In contrast, the MBR enrichment consortium under anoxic conditions transformed NTO completely in about 3.5 days (Fig. 3.2.7). The only observed breakdown product was ATO, that appeared soon after the reaction began, indicating that nitro-reduction was the first stage in the biotransformation of NTO by these cultures.
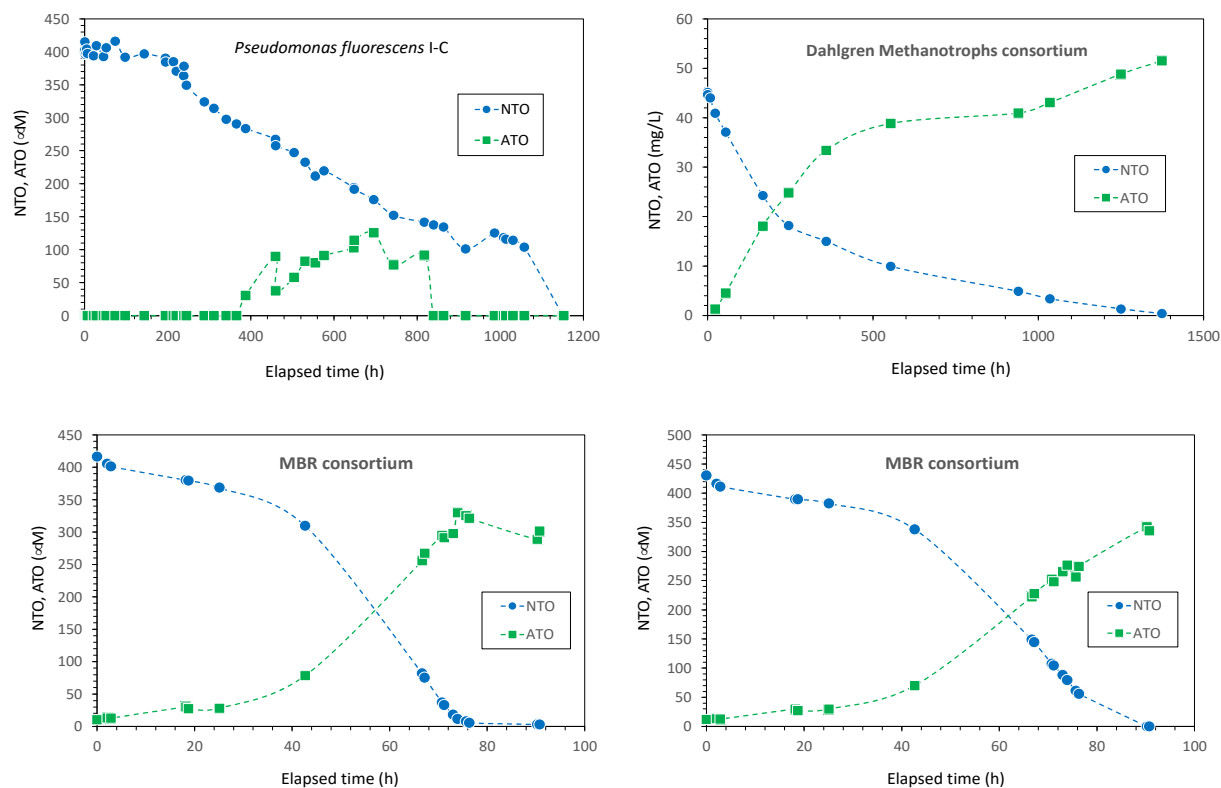
Fig. 3.2.7. Concentrations of NTO and ATO (mg/L) vs. elapsed time (h) during biotransformation experiments with pure aerobic culture *Pseudomonas fluorescens* I-C, aerobic consortium Dahlgren Methanotrophs, and replicate experiments with anoxic consortium MBR.

3.2.2.3 Isotope effects during DNAN biotransformation

The results of GC-IRMS measurements for carbon isotope ratios from six sets of DNAN biodegradation experiments are shown in Fig. 3.2.8. The carbon isotope data show relatively small isotope effects in all experiments, with ε_C values ranging from -0.7 to -4.3 ‰. The smallest carbon isotope effects were observed in the aerobic experiments with the two *Rhodococcus* strains, ENV 495 and ENV 425, for which ε_C values were similar at -0.74 ± 0.10 ‰ and -0.93 ± 0.08 ‰, respectively. The two anaerobic enrichments, MBR and Runoff, had somewhat larger and significantly different ε_C values of -4.34 ± 0.35 ‰ and -1.93 ± 0.19 ‰, respectively. The combined data for *Pseudomonas fluorescens* under three conditions (air-sparged, N_2-sparged, and O_2-sparged) defined an ε_C value of -1.96 ± 0.04 ‰, and the low standard deviation of the ε_C value indicates that the enzymatic degradation mechanism may have been identical under air-sparging, N_2-sparging, and O_2-sparging conditions, despite the observed differences in the rate of DNAN reduction. Thus, it was apparently an oxygen-insensitive enzyme system driving the transformation.

45
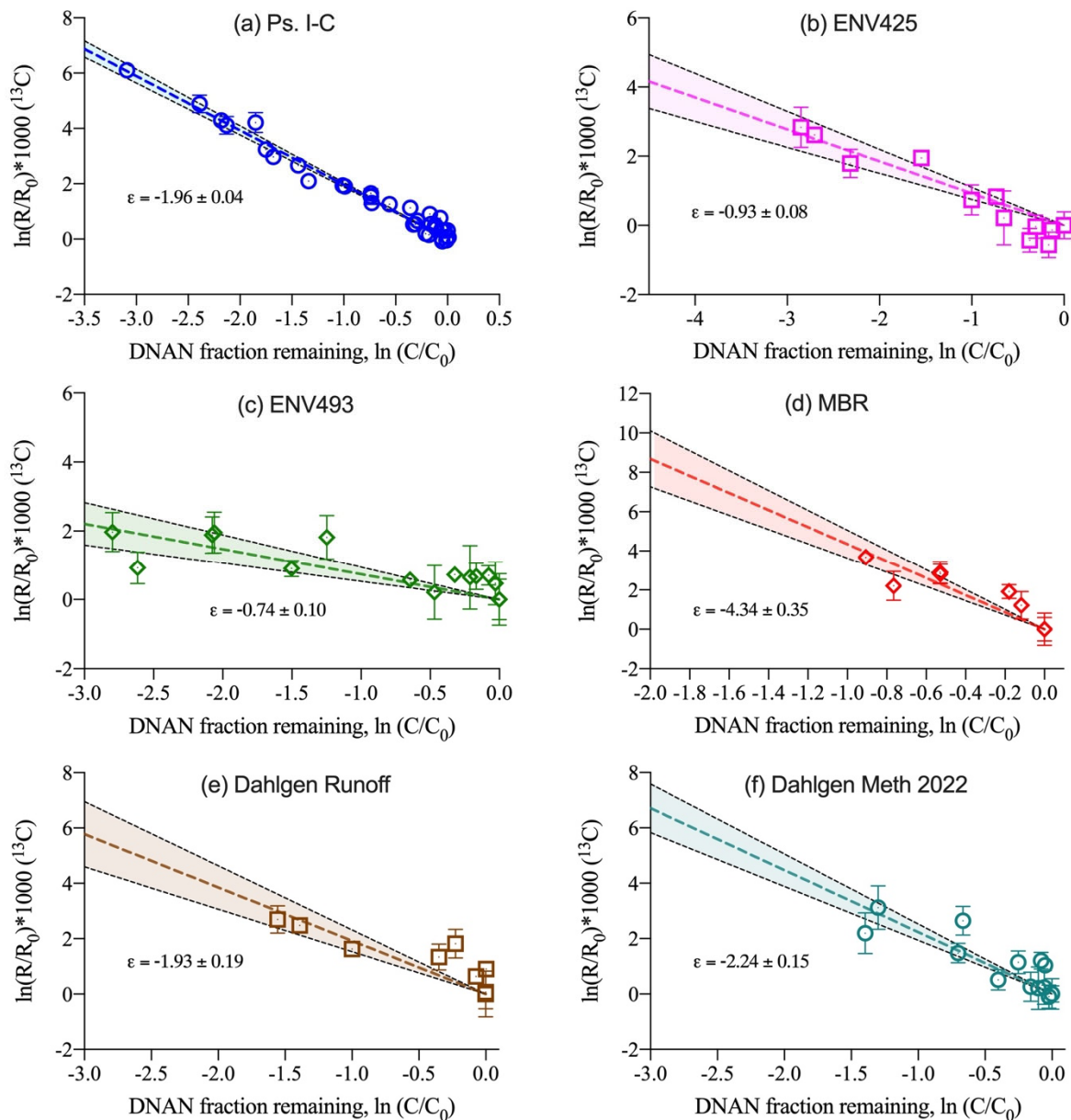
Fig. 3.2.8. Diagram showing ln $(R/R_0) \times 1000$ for carbon isotope ratio ($^{13}C/^{12}C$) in DNAN vs. DNAN fraction remaining (ln C/C_0). Values of ε_C represent best-fit linear regressions and standard errors.

The results of the GC-IRMS measurements for nitrogen isotope ratios in DNAN from six sets of biodegradation experiments are shown in Fig. 3.2.9. These data show that the nitrogen isotope effect is much larger than the carbon isotope effect, which is consistent with the observation that the principal degradation products 2-ANAN and 4-ANAN indicate a nitro-reduction pathway for DNAN degradation. This pathway requires dissociation of a N–O bond, whereas it does not require dissociation of any C–N or C–H bond, thus the nitrogen isotope effect is a primary isotope effect and the carbon isotope effect is a secondary isotope effect. The ε_N values range from -10.75 ± 0.52 ‰ to -23.15 ± 0.27 ‰. The ε_N values for two of the

Fig. 3.2.9. Diagram showing $\ln (R/R_0) \times 1000$ for nitrogen isotope ratio ($^{15}N/^{14}N$) in DNAN vs. DNAN fraction remaining ($\ln C/C_0$). Values of ε_N represent best-fit linear regressions and standard errors.

aerobic pure cultures (ENV 425 and ENV 475) were indistinguishable from each other at -10.79 ± 0.67 ‰ and -10.75 ±0.52 ‰, respectively), as were the ε_N values for the aerobic pure culture *Pseudomonas I-C* and the aerobic consortium Dahlgren Methanotrophs (-15.4 ± 0.81 ‰ and -15.73 ± 0.53 ‰, respectively), as well as the anaerobic enrichment cultures MBR and Dahlgren Runoff (-22.71 ± 0.50 ‰ and - 23.15 ± 0.27 ‰, respectively).

A comparison of the isotope results in terms of nitrogen vs. carbon isotope enrichments ($\Delta^{15}N$ ‰ vs. $\Delta^{13}C$ ‰) for each set of DNAN biodegradation experiments is shown in Fig. 3.2.10.

The range of $\Lambda_{N/C}$ values is from 4.9 to 12.2. These relatively high values are consistent with nitro-reduction as the primary pathway, and indicate that DNAN transformation may be driven by a similar enzymatic pathway for each of the bacterial strains investigated, regardless of redox conditions, indicating the involvement of either an oxygen-insensitive nitro-reductase (Fuller et al., 2021) or possibly the XenB reductase that has recently been shown to reduce TNT in both the presence and absence of oxygen (Pak et al., 2020).
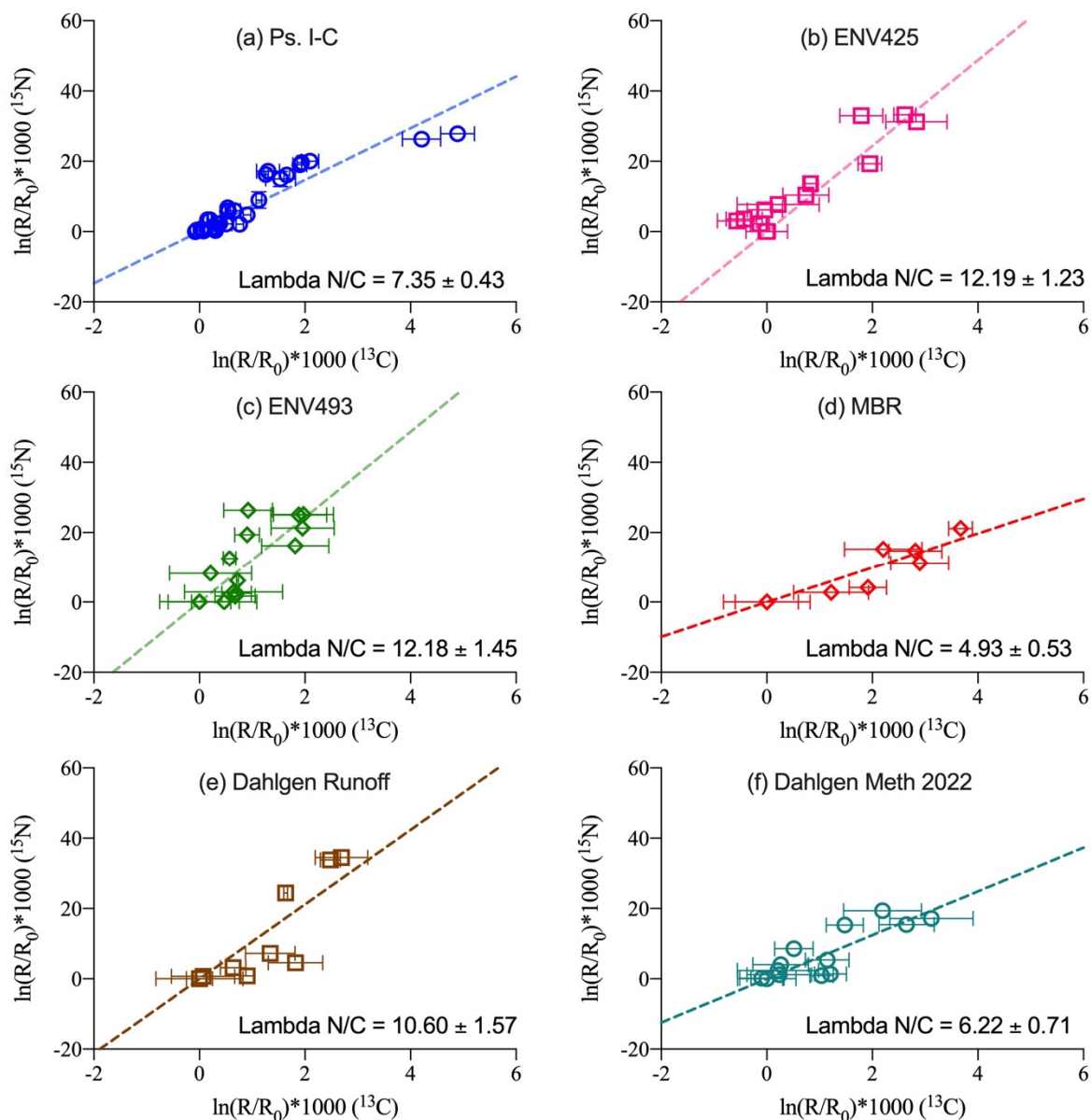
Fig. 3.2.10. Diagram showing nitrogen vs. carbon isotope enrichments ($\Delta^{15}N$ ‰ vs. $\Delta^{13}C$ ‰) for DNAN biodegradation experiments. Values of $\Lambda_{N/C}$ represent the best-fit linear regressions and standard errors.

3.2.2.4. Isotope effects during NTO biotransformation

Three sets of experiments were done to examine the isotope effects associated with biotransformation of NTO under the same growth conditions as those used in the DNAN biotransformation experiments. These NTO experiments were inoculated with some of the same cultures used for the DNAN experiments, including the pure aerobic culture, *Pseudomonas fluorescens I-C*, the aerobic consortium Dahlgren Methanogens, and the anaerobic enrichment culture MBR. Procedures were identical to those described for the DNAN experiments in Section 3.2.1, except that the culture media aliquots saved for isotopic analyses were not extracted with SPE and eluted with acetonitrile as for DNAN, but were instead frozen at -80 °C until thawed and extracted by ultrasonic liquid-liquid extraction prior to derivatization for isotopic analysis of NTO. Unfortunately, the carbon isotope results for these experiments cannot be reported because of chromatographic interference from high concentrations of other carbon-bearing species that interfered with the methylated NTO peak during GC-IRMS measurements. Such high concentrations of interfering compounds were not observed during GC-IRMS measurements of nitrogen isotope ratios in NTO, because the interfering compounds were generally nitrogen-free. Our preliminary interpretation is that the interferences came from metabolic products of the bacteria driving the biotransformation reactions. However, it is likely that the carbon isotope effect in these experiments would be a secondary isotope effect as the observed NTO biotransformation reaction is clearly a nitro-reduction reaction that does not involve a carbon atom at the site of reaction (N-O bond).

The results of GC-IRMS measurements for nitrogen isotope ratios in NTO from the three sets of experiments are shown in Fig. 3.2.11. The ε_N values range from -9.6 to -21.9 ‰. This range in ε_N values is similar to that obtained from the DNAN measurements (-10.9 to -23.3 ‰), and these relatively large values for ε_N are consistent with a nitro-reduction biotransformation pathway as indicated by the observed NTO reaction product, ATO (Fig. 3.2.7).
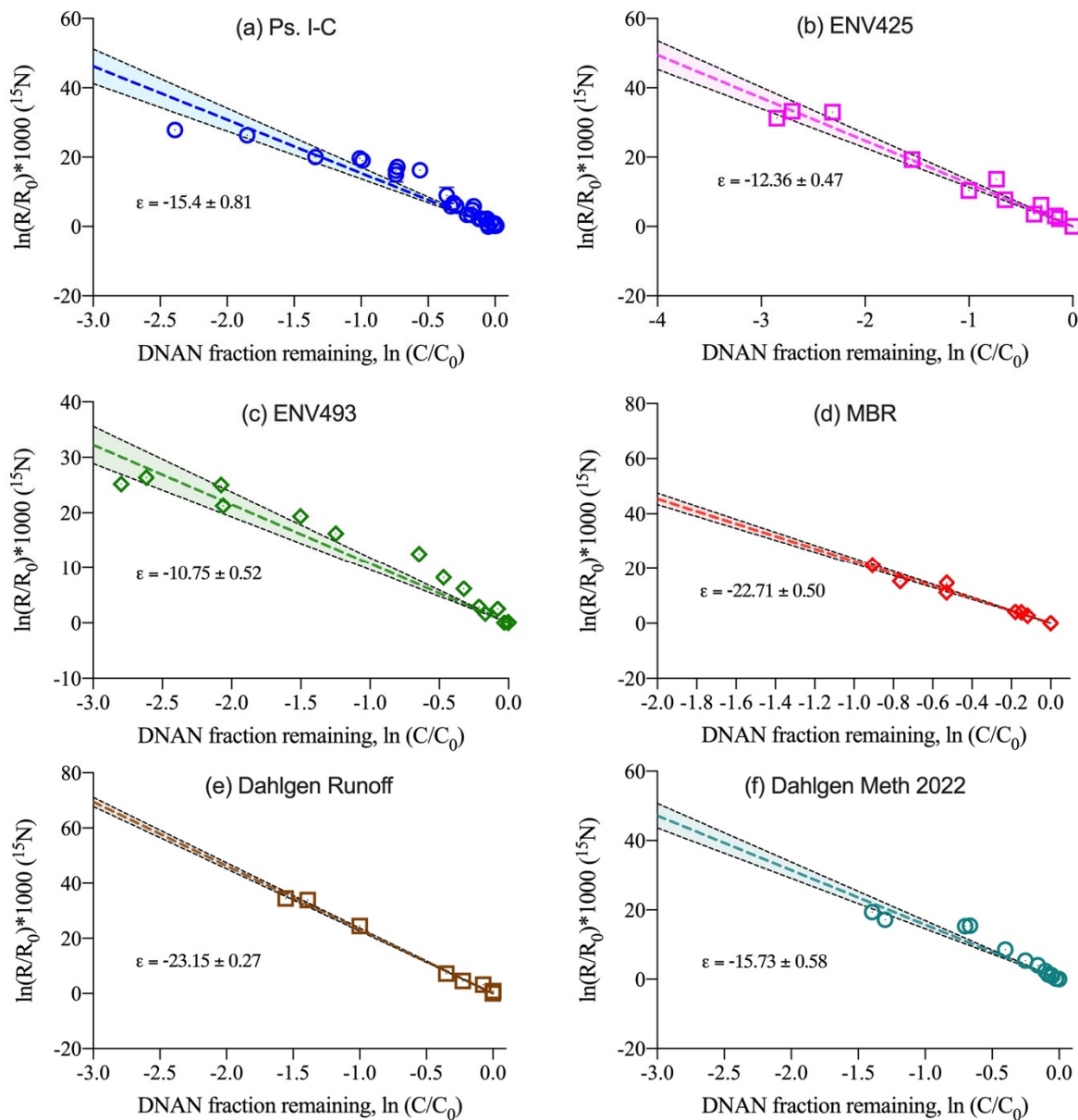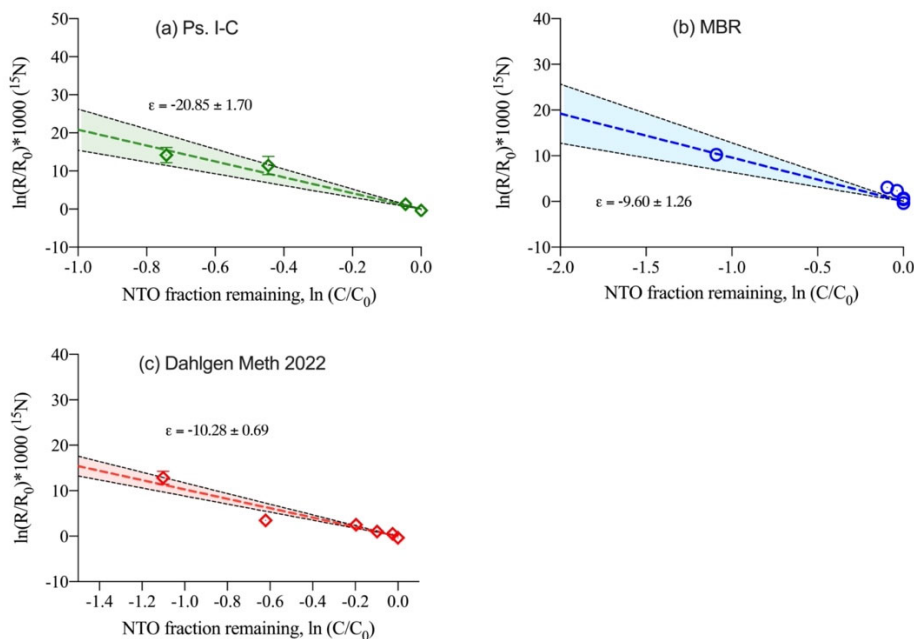

Fig. 3.2.11 Diagram showing $\ln(R/R_0) \times 1000$ for nitrogen isotope ratio ($^{15}N/^{14}N$) in NTO vs. NTO fraction remaining ($\ln C/C_0$). Values of ε_N represent best-fit linear regressions and standard errors.

4.0. Project Task 3: Isotope effects during abiotic transformations of DNAN and NTO

This section describes methods and results from our investigations of abiotic degradation of DNAN and NTO by processes expected to occur in surface waters, soils, and shallow groundwaters, including alkaline hydrolysis, photolysis, and reduction by quinones and Fe^{2+}-hematite. As part of this task, we also calculated position-specific kinetic isotope effects by using density-functional theory (DFT) to compare with GC-IRMS and ^{13}C NMR measurements.

4.1. Position-specific isotope effects of carbon and nitrogen during alkaline hydrolysis of DNAN resolved by compound-specific isotope analysis, ^{13}C NMR, and DFT

4.1.1. Introduction

Compound-specific isotope analysis (CSIA) is a powerful tool that provides compelling evidence of the environmental fate (e.g., biotic and abiotic degradation) of hazardous organic compounds in aqueous systems (Penning et al., 2008; Meyer et al., 2009; Reinnicke et al., 2012; Elsner and Imfeld, 2016), more effectively than methods that measure only the concentrations of these compounds and/or their degradation products. With CSIA, different transformation pathways of organic compounds may be deciphered based on the theory of kinetic isotope effects and a growing database of measurements on isotope effects associated with specific abiotic and enzymatic pathways in controlled laboratory experiments (Hofstetter et al., 2007, 2008; Fuller et al., 2016; Berens et al., 2019; Skarpeli-Liati et al., 2011; Pati et al., 2016; Lihl et al., 2020). Accurate knowledge of the isotope effects associated with specific transformation pathways allows improved understanding of the environmental fate of organic contaminants in the environment.

Small quantities of compounds are required for CSIA analysis (typically micrograms), yielding precise (commonly ±0.2‰ to ±0.5‰) experimentally determined isotope enrichment factors (ε) and apparent kinetic isotope effects (AKIEs) that can be used to document ongoing natural or enhanced degradation processes of contaminants in the environment (Hofstetter et al., 2007; Hofstetter and Berg, 2011; Hatzinger et al., 2009, 2013; Berens et al., 2019). However, bulk isotope ratios determined by CSIA include atoms from non-reacting positions that may dilute or mask the isotope effects of certain reaction pathways; intramolecular isotopic distribution is typically heterogeneous, in contrast to the common assumption of isotopic homogeneity among nonreacting sites (Elsner et al., 2005; Elsener, 2010). A routine method for position-specific isotope analysis (PSIA) would better enable reaction mechanisms associated with specific covalent bonds to be discerned, by providing more definitive characterization of intramolecular isotope distribution than possible by CSIA of the bulk compound. Such knowledge would reduce the overall uncertainty involved in the application of CSIA to studies of organic contaminant transformations in the environment.

Quantitative ^{13}C nuclear magnetic resonance spectrometry (^{13}C NMR, also known as isotope ratio monitoring ^{13}C NMR, irm-^{13}C NMR) has been used as a tool for position-specific isotope analysis (PSIA) for over 15 years (Akoka and Remaud, 2020). The first application of ^{13}C NMR for PSIA of aromatic compounds was a study of vanillin (Tenailleau et al., 2004; Caytan et al., 2007). Recently, ^{13}C NMR has been applied in forensic investigations of counterfeit currency and authentication of a number of organic compounds, based on identification of their source and mode of origin (i.e. synthetic or natural). A few studies have tested the applications of ^{13}C NMR as a tool to understand the transformations of organic

compounds including methyl tert-butyl ether (MTBE), toluene, trichloroethylene, and vanillin (Hohener et al., 2012; Bayle et al., 2015; Julien et al., 2015). To the best of our knowledge, there has been only one published report (Julien et al., 2020) that used a combination of both PSIA and CSIA for evaluating position-specific isotope effects (PSIEs); it examined effects associated with oxidation and acid hydrolysis of MTBE.

A combination of CSIA, quantitative ^{13}C NMR and density-functional theory (DFT) is demonstrated here as an approach to investigate position-specific primary and secondary isotope effects during alkaline hydrolysis of DNAN. As a component of insensitive munitions in place of trinitrotoluene, DNAN is now entering the natural environment as a contaminant along with its potentially toxic degradation products (e.g. 2,4-dinitroanisole (DNP)) (Rao et al., 2013; Ou et al., 2016; Fuller et al., 2020). The kinetics and mechanisms of S_N2Ar nucleophilic substitution of DNAN have been studied by laboratory experiments and by computational methods with DFT (Salter-Blanc et al., 2013; Sviatenko et al., 2014) and measured by ^{13}C- and ^{15}N-CSIA (Ulrich et al., 2018), as well as being further verified with ^{18}O-tracer experiments (Wang et al., 2020a; see Section 4.2 of this report). The present study further elucidates the position-specific isotope effects (PSIEs) associated with a relatively well-known transformation pathway of DNAN.

4.1.2. Materials and methods
4.1.2.1. Chemicals
Three different batches of 2,4-dinitroanisole (DNAN, CAS #119-27-7) having a range of bulk and position-specific isotopic compositions were obtained from commercial sources for this study. This was done to evaluate the effect of initial isotopic composition on the resulting kinetic isotope effects observed during the reactions. (1) DNAN-EIGL ($\geq$98 %, LOT #10173248; Alfa Aesar, Ward Hill, MA USA); (2) DNAN-PEI ($\geq$98 %, LOT #09709CO; Sigma-Aldrich, Milwaukee, WI USA); and (3) DNAN-III ($\geq$98 %, LOT #10148293; Alfa-Aesar, Tewksbury, MA USA). Acetone-d6 and tris (2,4-pentadionato) chromium (III) (Cr(Acac)$_3$, $\geq$99.99%) were obtained from Sigma-Aldrich. All other chemicals, including ethyl acetate, hydrochloric acid, and sodium hydroxide were reagent grade or purer, and obtained from Fisher Scientific (Fair Lawn, NJ, USA).

4.1.2.2. Experimental methods
Triplicate batch experiments were carried out in 20-mL amber screw-thread vials with magnetic screw-thread headspace caps and blue PTFE/silicone septa (Restek Corporation; Bellefonte, PA USA) in an 8-mL aqueous reaction system. A 10 mM solution NaOH solution was prepared, yielding a measured pH of 12.0 standard units (S.U.). The hydrolysis temperature was maintained at 55 $\pm$ 0.5 °C in a thermostat-controlled water bath; NaOH solutions were pre-heated prior to initiation of experiments. A measured aliquot of DNAN stock solution (50.4 mM DNAN in acetonitrile) was added to each vial to bring the initial solution concentration to 0.126 mM DNAN. Each vial was vigorously shaken for one minute to mix contents before being returned to the water bath. At various time intervals, duplicate samples were removed from the water bath and quenched immediately by adding 10 µL of HCl (~37%, 12M) to lower the pH to < 3. Subsequently, ultrasound-assisted liquid-liquid extraction (UALLE) was performed by adding an equal volume of ethyl acetate to each quenched experimental sample, then placing it in an ultrasonic water bath (Sper Scientific, model 100004; Scottsdale, AZ) for 8 min. After extraction, all samples were set aside to allow density separation of water and solvent for at least 20 min. The solvent layer was transferred to a clean amber vial and evaporated in a dark fume

hood overnight. Residues of evaporation were transferred in ethyl acetate to 2-mL wide-mouth screw-top vials with PTFE/silicone septa (Restek Corp.; Bellefonte, PA) for analysis by gas chromatography-mass spectrometry (GC-MS) and gas chromatography-isotope ratio mass spectrometry (GC-IRMS) as described earlier in Section 2.1 of this report.

Experimentally derived ^{13}C and ^{15}N enrichment factors determined from residual DNAN measurements were reported as bulk isotope enrichment factors (ε_{C_bulk} and ε_{N_bulk}) from the natural logarithmic transformations of eq 3 and eq 4 in parts per thousand (‰):

$$(C/C_0)_{DNAN} \wedge (\varepsilon_{C\_bulk}) = (\delta^{13}C_{bulk\_t, DNAN} + 1) / (\delta^{13}C_{bulk\_0, DNAN} + 1) \tag{4.1.1}$$

$$(C/C_0)_{DNAN} \wedge (\varepsilon_{N\_bulk}) = (\delta^{15}N_{bulk\_t, DNAN} + 1) / (\delta^{15}N_{bulk\_0, DNAN} + 1) \tag{4.1.2}$$

where $(C/C_0)_{DNAN}$ represents the fraction of DNAN remaining at time point t. The $\delta^{13}C_{bulk\_0, DNAN}$ and $\delta^{15}N_{bulk\_0, DNAN}$ values represent the bulk values of DNAN starting materials. The $\delta^{13}C_{bulk\_t, DNAN}$ and $\delta^{15}N_{bulk\_t, DNAN}$ represent the bulk values of DNAN at time point t.

The position-specific primary ^{13}C enrichment factor at the reacting position (in this case, aromatic C_1) was derived using eq. 4.1.3 based on the assumptions that (i) intramolecular differences in isotope ratios were small throughout the reaction; (ii) the actual kinetic ^{13}C effect occurs in the reacting bond (in this case, O-C_1 bond formation as DNAN reacts to form MC); and (iii) additional C atoms in residual DNAN dilute this fractionation in the compound average:

$$\varepsilon_{C1} = \varepsilon_{C\_bulk} * 7 \tag{4.1.3}$$

The position-specific ^{15}N enrichment factor is much smaller than that of ^{13}C because ^{15}N at the two nitro groups of DNAN has a secondary kinetic isotope effect that is distributed between the two nitro group positions and is less affected by dilution.

4.1.2.3. Quantitative ^{13}C NMR

Position-specific carbon isotope ratios of DNAN were determined by using quantitative ^{13}C NMR. Aliquots of ~250 mg DNAN were dissolved in ~500 μL acetone-d_6, and ~200 μL 0.1 M Cr(acac)$_3$ in acetone-d_6 was added to reduce T_1 of DNAN. This solution was transferred to a low pressure/vacuum NMR sample tube (Wilmad-LabGlass; Vineland, NJ).

Quantitative ^{13}C NMR measurements were conducted on a Bruker 400 MHz AVANCE III HD NMR spectrometer with a 5mm dual-channel BBFO probe at West Texas A&M University. The temperature of the probe was maintained at 30 °C. Both ^{13}C and ^{1}H channels were carefully tuned and matched. Inverse-gated, adiabatic COS/OIA decoupling sequence was used (Tenailleau et al., 2004, 2007). The delay time was at least 10 times the longest T_1 of DNAN. Each NMR measurement took ~5 hours of acquisition time and had 720 scans with S/N ranging from 250 to 1000. More details of experimental parameters are described in (Chaintreau et al., 2013; Liu et al., 2018).

Perch Software (Perch Solutions Ltd, Kuopio, Finland) was used for the deconvolution, fitting, and integration of NMR peaks. Peak areas were used to calculate the mole fraction of ^{13}C at the position i (f_i):

$$f_i = S_i/S_{tot,} \tag{4.1.4}$$

where i designates isotopically non-equivalent positions within the DNAN molecule. S_i is the peak area of the position i and S_{tot} is the total area of all ^{13}C peaks of DNAN. Small ^{13}C satellite peaks can be observed on both sides of major peaks in ^{13}C NMR spectra due to ^{13}C-^{13}C coupling. The contributions of satellite peaks were calculated by applying the correction factor $(1 + 0.011*n)$, where n is the number of carbons that are attached to the carbon of interest within the DNAN molecule (Tenailleau et al., 2004; Chaintreau et al., 2013). For DNAN, $n = 2$ for all carbon sites except the methoxy group carbon for which $n = 0$. The position-specific isotope ratios relative to the stochastic, random distribution have been defined as Δ_i (Caytan et al., 2007):

$$\Delta_i = (f_i/F_i - 1) \cdot 1000‰ \qquad (4.1.5)$$

where F_i is the statistical mole fraction of a heavy isotope at the site i. For DNAN, $F_i = 1/7$ for all carbon sites. From the bulk isotope ratios (δ_{bulk}) and the position-specific isotope deviations (Δ_i) of DNAN, the C isotope ratio at each position i (δ_i) of DNAN can be calculated from the equation (Liu et al., 2018):

$$(1 + \delta_i) = (1 + \Delta_i) * (1 + \delta_{bulk}) \qquad (4.1.6)$$

4.1.2.4. Computational methods

The Gibbs free energies of isotopically substituted DNAN, its hydrolysis products and intermediate transition states were calculated with the Gaussian 09 software package [41] at the M062X/6-311++G(2d,2p) level of DFT [42, 43]. The optimized geometries and corresponding normal modes of each stationary point encountered along the hydrolysis pathway were obtained using an ultrafine integration grid, the SMD polarizable continuum solvation model [43], and Pauling atomic radii [44] to define the solute cavity, as implemented in Gaussian 09. For the purpose of deriving kinetic isotope effects (i.e. predicted values of ^{13}C-KIE and ^{15}N-KIE), we performed calculations with position-specific substitutions of ^{12}C and ^{14}N by ^{13}C and ^{15}N, respectively. According to the principles of mass-dependent isotope fractionation and transition-state theory, KIEs were derived from the calculated Gibbs free energies (G) [16]:

$$KIE = {}^{l}A / {}^{h}A * \exp\left(- [\Delta_{h-l}(\Delta G_{TS}) - \Delta_{h-l}(\Delta G_Q)] / RT\right) \qquad (4.1.7)$$

where A is the pre-exponential factor of the Arrhenius equation for light isotope (l) and heavy isotope (h); Δ_{h-l} represented the difference between the activation free energies for the light and heavy isotopologues; R is the universal gas constant (8.3145 J K^{-1} mol^{-1}) and T is the absolute temperature in K. Q represents either DNAN or the Meisenheimer complex for the first step or second step of the S_N2Ar reaction, and TS denotes a transition state. We hypothesized ${}^{l}A / {}^{h}A = 1$ in this study because we did not empirically build up the relationship between temperature and rate coefficient respectively for ^{12}C and ^{13}C during both O-C$_1$ bond formation from DNAN to Meisenheimer complex and C$_1$-O bond cleavage from Meisenheimer complex to DNP, and also because we did not quantitatively control the time scales of O-C$_1$ bond formation and C$_1$-O bond cleavage.

According to the energy profiles of S_N2Ar of DNAN that we reported, and the fact that no Meisenheimer complex has been detected in previous experimental studies [28, 30, 31], we hypothesized that the first step of the S_N2Ar nucleophilic substitution of DNAN was the rate-limiting step. The modeled ^{13}C enrichment factor in the reacting position ($\varepsilon_{C1, model}$) was derived by:

$$\varepsilon_{C1, \text{model}} = [(1/\text{modeled } ^{13}C\text{-KIE}_1) - 1] * 1000 \tag{4.1.8}$$

The secondary ^{15}N enrichment factor in each non-reacting nitro group was obtained by:

$$\varepsilon_{Ni, \text{model}} = [(1/\text{modeled } ^{15}N\text{-KIE}_i) - 1] * 1000 \tag{4.1.9}$$

4.1.3. Results and discussion
4.1.3.1. Bulk and position-specific $\delta^{13}C$ values of DNAN

Bulk and position-specific $\delta^{13}C$ values calculated from NMR data based on eqs. 4.1.5 and 4.1.6 are listed in Table 4.1.1 and portrayed in Fig. 4.1.1. The bulk $\delta^{13}C$ values of DNAN-EIGL (−38.4 ‰), DNAN-PEI (−29.1 ‰) and DNAN-III (−37.2 ‰) were determined by EA-IRMS analyses that were normalized to L-glutamic acid isotopic reference materials USGS40 and USGS41a [33, 34]. The average reproducibility ($n>10$) of normalized $\delta^{13}C$ values was approximately ±0.2 ‰. The bulk $\delta^{13}C$ values of DNP-EIGL (−24.7 ‰), DNP-PEI (−24.9 ‰) and DNP-III (−24.6 ‰) were obtained by averaging the six position-specific $\delta^{13}C$ values of the DNAN aromatic ring.

Table 4.1.1. Position-specific ^{13}C deviations (Δ_i) and normalized position-specific and bulk $\delta^{13}C$ values (δ_i and δ_{bulk}) of DNAN as measured by ^{13}C NMR

Site	DNAN_EIGL ($n=4$)			DNAN_PEI ($n=4$)			DNAN_III ($n=5$)		
	Δ_i /‰	SD /‰	δ_i /‰	Δ_i /‰	SD /‰	δ_i /‰	Δ_i /‰	SD /‰	δ_i /‰
C_1	-8.82	1.38	-46.84	-17.89	1.77	-46.43	-9.77	0.71	-46.62
C_2	22.36	0.83	-16.85	11.04	0.66	-18.34	25.11	1.07	-13.03
C_3	-0.60	1.38	-38.93	-4.59	1.32	-33.51	1.37	1.34	-35.89
C_4	67.89	0.99	26.93	43.98	1.13	13.64	52.42	0.76	13.26
C_5	-5.21	1.87	-43.37	-8.24	1.66	-37.06	-1.36	0.70	-38.52
C_6	9.84	0.87	-28.90	1.63	0.61	-27.47	10.75	1.60	-26.86
C_7	-85.47	0.85	-120.55	-25.94	0.62	-54.24	-78.52	0.97	-112.81
δ_{bulk}_DNAN[a]			-38.36			-29.06			-37.21
δ_{bulk} _DNP[b]			-24.66			-24.86			-24.61

[a] δ_{bulk}_DNAN values were determined by EA-IRMS.
[b] δ_{bulk}_DNP values were estimated by averaging the δ_i values from C_1 to C_6.
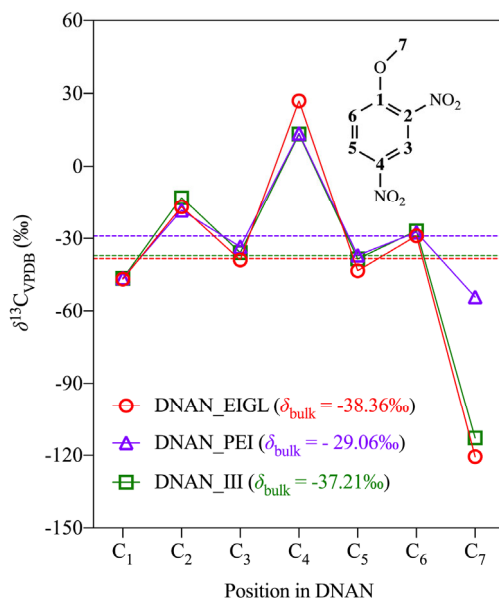
Fig. 4.1.1. Comparison of position-specific $\delta^{13}C$ values of DNAN produced from three different manufacturers, as measured by ^{13}C NMR. Bulk $\delta^{13}C$ values by EA-IRMS are shown for comparison.

Generally, for all three DNAN samples, methoxy group carbons (C_7) were relatively depleted in ^{13}C (Fig. 4.1.1). The aromatic carbons bonding with nitro-groups (C_2 and C_4) were relatively enriched in ^{13}C (Fig. 4.1.1 and Table 4.1.1), indicating that nitro groups tend to bond with ^{13}C during the synthesis of DNAN, which potentially makes the C-N bond stronger (Bariwal and Van der Eycken, 2013).

4.1.3.2. Position-specific ^{13}C-KIE and ^{15}N-KIE

Modeled ^{13}C-KIEs (Table 4.1.2) and modeled ^{15}N-KIEs (Table 4.1.3) were derived for the position-specific isotope-substituted S_N2Ar reaction system by DFT. We considered only singly-substituted DNAN isotopologues having a ^{13}C substitution at one of the seven C positions or a ^{15}N substitution at one of the two N positions; this is justified because the stochastic probabilities of two ^{13}C or ^{15}N substitutions in a single DNAN molecule are negligible (~0.01% for ^{13}C and ~0.0013% for ^{15}N).
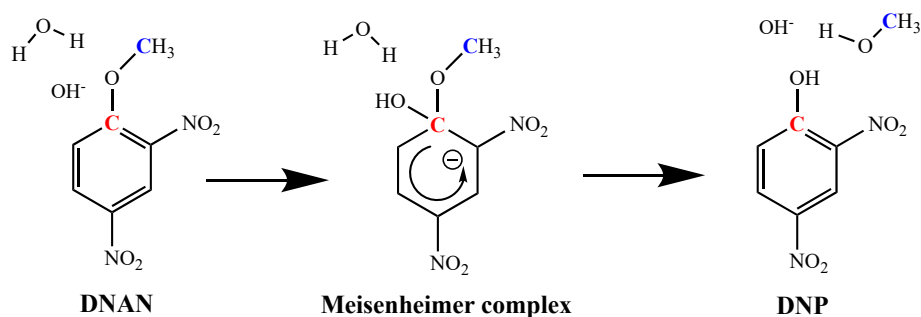
Fig. 4.1.2. Proposed steps for the transformation of 2,4-dinitroanisole (DNAN) by alkaline hydrolysis though nucleophilic aromatic substitution to 2,4-dinitrophenol (DNP). A Meisenheimer complex is likely formed as a transient intermediate during this reaction. Aromatic C_1 is highlighted in red; C_7 at methoxy group is highlighted in blue.

55

For ^{13}C, the maximum KIEs were obtained by substituting ^{13}C at the C_1 position for both steps – from DNAN to transition state 1 (TS1) and from the Meisenheimer complex (MC) to transition state 2 (TS2). The substitution of ^{13}C at other aromatic C positions hardly contributed to the overall ^{13}C-KIE. At C_1 (Table 2, ^{13}C-#1), the value of the computational ^{13}C-KIE of O-C_1 bond formation (DNAN to TS1) was almost equal to that of C_1-O bond cleavage (MC to TS2), not following the Hammond Postulate but instead consistent with the theory that "maximum isotope effects for the transferred element (O or C, respectively) are observed in symmetric transition states that involve equal parts of bond cleavage and formation" (Elsner et al., 2005). At the methoxy C_7 site, the value of the calculated ^{13}C-KIE in ^{13}C-#7 indicated no ^{13}C isotope effect during the rate-limiting step (O-C_1 bond formation) from DNAN to TS1, and a negligible ^{13}C fractionation from Meisenheimer complex (MC) to TS2 (C_1-O bond cleavage).

Table 4.1.2. Calculated ^{13}C-KIE values for singly-substituted DNAN isotopologues (eq 9). The monoisotopic DNAN (^{12}C and ^{14}N only) was set as a base energy state with ^{13}C-KIE = 1.

Isotopic reaction system ID	Isotopic substituting positions	Modeled ^{13}C-KIE	
		DNAN to TS1	MC to TS2
^{13}C-#1		**1.038**	**1.035**
^{13}C-#2		1.003	0.999
^{13}C-#3		1.001	0.997
^{13}C-#4		1.004	0.998
^{13}C-#5		1.001	1.000
^{13}C-#6		1.002	1.000
^{13}C-#7		**1.000**	**1.003**
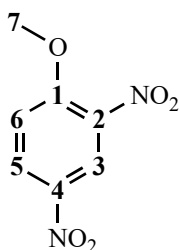
At the reacting position C_1, calculated position-specific ^{13}C enrichment factors ($\varepsilon_{C1, model}$) were -36.6 ‰ and -33.8 ‰, from DNAN to TS1 and from MC to TS2 respectively (eq. 4.1.8). The experimentally determined position-specific ^{13}C enrichment factors (ε_{C1}), obtained by combining the results from CSIA and quantitative NMR (eqs. 4.1.1 and 4.1.3), ranged from -38.9 ‰ to -42.7 ‰. These values are larger (i.e. more negative) than those predicted by the DFT calculations. This is because (i) we derived $\varepsilon_{C1, model}$ from the primary isotopologue in ^{13}C-#1, without considering the abundances and weighted combinations of other isotopologues with ^{13}C at non-reacting aromatic sites, which may contribute non-negligibly to bulk ^{13}C fractionations; and (ii) the DFT model in this study, even if well developed and validated, cannot exactly describe the changes in energy during C_1 evolution. Thus, we observed that the predicted value of $\varepsilon_{C1, model}$ obtained from DFT calculations was several ‰ smaller than the experimentally derived value of ε_{C1}.
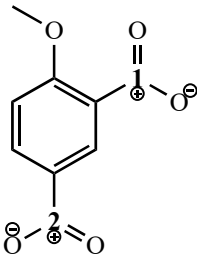
For the rate-limiting step from DNAN to TS1, predicted ^{15}N-KIEs indicated normal ^{15}N fractionation with a derived bulk ^{15}N enrichment factor ($\varepsilon_{bulk, model}$) of -3.0 ‰ in DNAN (eqs. 4.1.9 and 4.1.10). We reported $\varepsilon_{N\_bulk, model}$ instead of $\varepsilon_{N1, model}$ and $\varepsilon_{N1, model}$ because ^{15}N was experiencing secondary kinetic isotope effects during S_N2Ar nucleophilic substitution of DNAN.

The value obtained for $\varepsilon_{N\_bulk, model}$ in DNAN agreed well with the experimentally derived ε_{N_bulk} value of -3.2 ‰ observed for all three DNAN starting materials (eq. 4.1.2):

$$\varepsilon_{N\_bulk, model} = \varepsilon_{N1, model} / 2 = \varepsilon_{N2, model} / 2 \qquad (4.1.10)$$

The good agreement between ε_{N_bulk} and $\varepsilon_{N\_bulk, model}$ verified our hypothesis that at most one heavy isotope of each element tends to substitute for the light isotope in each isotopologue.

Table 4.1.3. Calculated ^{15}N-KIE values of singly-substituted DNAN isotopologues (eq. 4.1.7). The monoisotopic DNAN with ^{14}N was set as a base energy state with ^{15}N-KIE = 1.

Isotopic reaction system ID	^{15}N substituting positions	Modeled ^{15}N-KIE	
		DNAN to TS1	MC to TS2
^{15}N-#1		**1.006**	0.994
^{15}N-#2		**1.006**	0.994

Interestingly, the modeled ^{15}N-KIEs of the C_1-O bond-cleavage (MC to TS2, non-rate-limiting) step predicted an inverse ^{15}N fractionation with a derived bulk ^{15}N enrichment factor of +3.0‰ in the Meisenheimer complex. However, the Meisenheimer complex was not measurable, and it transformed completely to DNP during the reaction, so the ^{15}N-KIE of the rate-determining step (DNAN to TS1) is reflected in the $\delta^{15}N$ value of DNP.

4.1.3.3. Evolution of bulk and position-specific $\delta^{13}C$ values during alkaline hydrolysis

The evolutions of bulk and position-specific $\delta^{13}C$ values, respectively, in DNAN, instantaneous product (Meisenheimer complex, MC), and average of accumulated products (DNP+MeOH) as a function of DNAN remaining are shown in Fig. 4.1.3. The observed changes (relative to the initial isotopic compositions) as a function of DNAN remaining are independent of the initial isotopic compositions of the three DNAN starting materials.

We hypothesize that negligible fractionation occurred at the methoxy C_7 because (i) the O-C_7 bond was not directly involved during S_N2Ar nucleophilic substitution of DNAN; (ii) the predicted ^{13}C-KIE of ^{13}C substitution at C_7 was equal to 1; (iii) the calculated $\delta^{13}C_{7, t}$ values (i.e., the $\delta^{13}C_t$ values of MeOH) had standard deviations of ±1.10 ‰, ±1.05 ‰ and ±0.72 ‰, respectively for DNAN-EIGL, DNAN-PEI and DNAN-III during the bulk ^{13}C evolution (eq 13); and (iv) the differences between the average values of $\delta^{13}C_{7, t}$ and δ_7 of DNAN (Table 4.1.1) were $-0.05‰$, $+0.33‰$ and $-0.24‰$, respectively for DNAN_EIGL, DNAN_PEI and DNAN_III. Thus, we derived the $\delta^{13}C$ values of the average of accumulated products (DNP+MeOH) at time point t by summing the GC-IRMS measured $\delta^{13}C_{bulk\_t, DNP}$ values and ^{13}C NMR measured $\delta^{13}C_{7\_t}$ values (i.e. $\delta^{13}C_{t, MeOH}$).

$$\delta^{13}C_{7\_t} = \delta^{13}C_{t,\,MeOH} =$$
$$[\delta^{13}C_{bulk\_0,\,DNAN} * 7 - (C/C_0)_{DNAN} * \delta^{13}C_{bulk\_t,\,DNAN} * 7] \,/\, [1 - (C/C_0)_{DNAN}] - \delta^{13}C_{bulk\_t,\,DNP} * 6$$

$$(4.1.13)$$

The modeled $\delta^{13}C$ values of the average of accumulated products (DNP+MeOH) at time point t were derived by eq. 4.1.14.

$$\delta^{13}C_{bulk\_t,\,DNP+MeOH\_Model} = \frac{(1000 + \delta^{13}C_{bulk\_0,\,DNAN}) * [1 - (C/C_0)_{DNAN}{}^{\wedge}(1 + \varepsilon_{C\_bulk,DNAN})]}{1 - (C/C_0)_{DNAN}} - 1000 \qquad (4.1.14)$$

Given that the Meisenheimer complex was proposed as the intermediate during S_N2Ar of DNAN but was not detectable, we modeled the isotopic fractionation in the instantaneous product as that in Meisenheimer complex ($\delta^{13}C_{bulk\_t,\,MC}$) according to the theory of kinetic isotope effects (eq. 4.1.15).

$$\sigma^{13}C_{bulk\_t,\,MC\_model} = \delta^{13}C_{bulk\_t,\,DNAN} - \varepsilon_{C\_bulk,DNAN} \qquad (4.1.15)$$
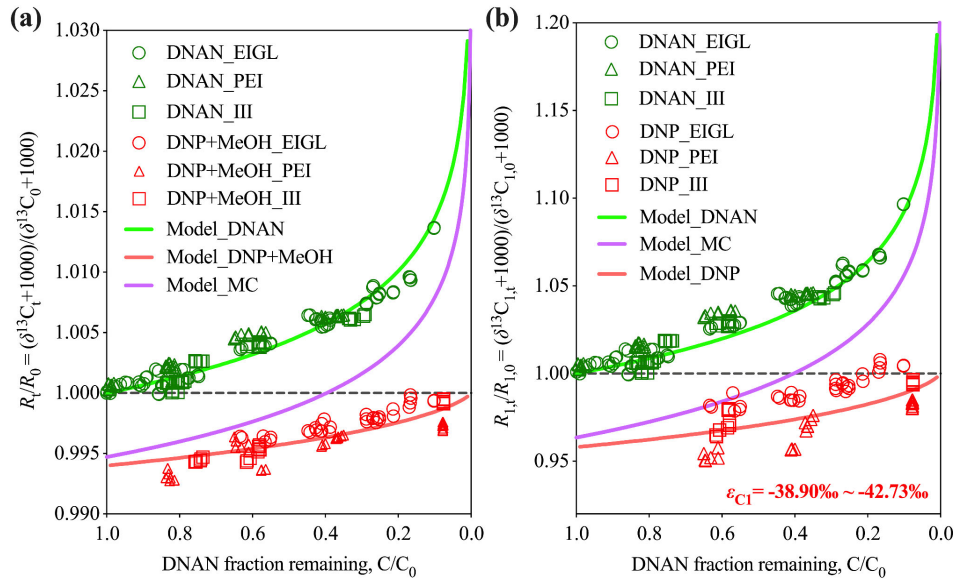
Fig. 4.1.3. Evolution of bulk $\delta^{13}C$ values of DNAN and DNP+MeOH (average of accumulated products) (Panel a) and $\delta^{13}C$ values at reacting positions (C_1) in DNAN and DNP (accumulated product) (Panel b) associated with a normal primary kinetic isotope effect during S_N2Ar nucleophilic substitution in a closed reaction container. The green symbols in Panel (a) show $\delta^{13}C_{bulk\_t,\,DNAN}$ values measured from laboratory experiments. The red symbols in Panel (a) represent the sum of laboratory analyzed $\delta^{13}C_{bulk\_t,\,DNP}$ values and calculated $\delta^{13}C_{t,\,MeOH}$ values obtained by cross-checking of ^{13}C NMR and CSIA (eq. 4.1.13). The green symbols in Panel (b) show $\delta^{13}C_{1\_t,\,DNAN}$ values calculated based on eq. 4.1.16. The red symbols in Panel (b) represent $\delta^{13}C_{1\_t,\,DNP}$ values calculated based on eq. 4.1.17. In both Panel (a) and (b), solid green lines describe Rayleigh fractionation of DNAN as the parent reactant in S_N2Ar; solid purple and red lines represent the modeled evolution of the instantaneous product (i.e. MC) (eqs. 4.1.15 and 4.1.18) and accumulated product(s) (i.e. DNP+MeOH or DNP) (eqs. 4.1.14 and 4.1.19).

To further understand the evolution of C isotope ratios for S_N2Ar nucleophilic substitution of DNAN, we calculated $\delta^{13}C_{1\_t}$ values of DNAN ($\delta^{13}C_{1\_t, DNAN}$) and DNP ($\delta^{13}C_{1\_t, DNP}$) by combining the results from CSIA and quantitative ^{13}C NMR (eqs. 4.1.16 and eq 4.1.17).

$$\delta^{13}C_{1\_t, DNAN} = \delta^{13}C_{bulk\_t, DNAN} * 7 - (\delta_2 + \delta_3 + \delta_4 + \delta_5 + \delta_6 + \delta_7) \tag{4.1.16}$$

$$\delta^{13}C_{1\_t, DNP} = \delta^{13}C_{bulk\_t, DNP} * 6 - (\delta_2 + \delta_3 + \delta_4 + \delta_5 + \delta_6) \tag{4.1.17}$$

The $\delta^{13}C_1$ values in the Meisenheimer complex (MC) at time point t were derived using eq. 4.1.18.

$$\delta^{13}C_{1\_t, MC\_model} = \delta^{13}C_{1\_t, DNAN} - \varepsilon_{C\_bulk, DNAN} * 7 \tag{4.1.18}$$

A model evolution of $\delta^{13}C_{1\_t, DNP}$ ($\delta^{13}C_{1\_t, DNP\_model}$) was calculated according to the theory "maximum isotope effects for the transferred element (i.e. C and O respectively) are observed in symmetric transition states that involve equal parts of bond cleavage and formation" (eq. 4.1.19). The position-specific primary ^{13}C evolution obtained from experimental measurements and a Rayleigh fractionation model was shown in Fig. 4.1.3b.

$$\delta^{13}C_{1\_t, DNP\_model} = \frac{(1000 + \delta^{13}C_{1\_0, DNAN}) * [1 - (C/C_0)_{DNAN} {}^\wedge (1 + \varepsilon_{C\_bulk, DNAN} * 7)]}{1 - (C/C_0)_{DNAN}} - 1000 \tag{4.1.19}$$

In Fig. 4.13b, the position-specific primary evolution of $\delta^{13}C$ values in experimentally measured DNP and modeled DNP followed the same trend and agreed well. Thus, C_1 at the reacting position experienced symmetric kinetic isotope effects during S_N2Ar of DNAN, with O-C_1 bond formation from DNAN to MC as the rate-limiting step. In a parallel investigation, we verified by using ^{18}O-enriched water that the phenolic O atom attached to the C_1 site in DNP produced by alkaline hydrolysis of DNAN is from the aqueous phase (Wang et al., 2020a).

Knowledge of the position-specific $\delta^{13}C$ values of DNAN during the transformation to DNP + MeOH allows a more accurate assessment of the KIE at the C_1 reacting position than would be the case if only bulk $\delta^{13}C$ measurements were available (Ulrich et al., 2018). In general, position specific isotope data enable better resolution of contaminant transformation mechanisms in both laboratory and field settings, especially when such data are available for multiple elements in a compound and its reaction products (Elsner, 2010).

4.1.3.4. Evolution of $\delta^{15}N$ values

The evolution of $\delta^{15}N$ values was derived from experimentally measured bulk $\delta^{15}N$ values in DNAN ($\delta^{15}N_{bulk\_t, DNAN}$) and DNP ($\delta^{15}N_{bulk\_t, DNP}$) (Fig. 4.1.4). The instantaneous product of S_N2Ar of DNAN was proposed to have $\delta^{15}N_t$ ($\delta^{15}N_{bulk\_t, MC\_model}$) as described in eq. 4.1.20.

$$\delta^{15}N_{bulk\_t, MC\_model} = \delta^{15}N_{bulk\_t, DNAN} - \varepsilon_{N\_bulk, DNAN} \tag{4.1.20}$$

The modeled $\delta^{15}N$ values of accumulated products DNP+MeOH at time point t were derived by eq. 4.1.21.

$$\delta^{15}N_{bulk\_t, DNP\_Model} = \frac{(1000 + \delta^{15}N_{bulk\_0, DNAN}) * [1 - (C/C_0)_{DNAN} {}^\wedge (1 + \varepsilon_{N\_bulk, DNAN})]}{1 - (C/C_0)_{DNAN}} - 1000 \tag{4.1.21}$$

The changes in $\delta^{15}N$ values as a function of DNAN remaining were smaller than those of $\delta^{13}C$ as the two N atoms in DNAN are positioned at the C_2 and C_4 sites which do not participate in the reaction. Thus, the ^{15}N-KIE value reflects a secondary isotope effect.
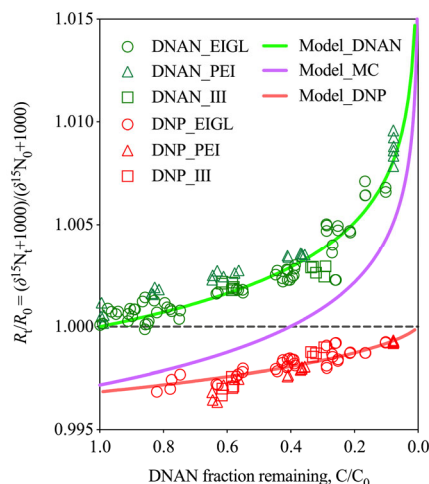
Fig. 4.1.4. Evolution of bulk $\delta^{15}N$ values of DNAN, Meisenheimer Complex (MC, instantaneous product) and DNP (accumulated products) associated with a normal secondary kinetic isotope effect during S_N2Ar nucleophilic substitution in a closed reaction container. The green and red symbols show $\delta^{15}N_{bulk\_t,\,DNAN}$ and $\delta^{15}N_{bulk\_t,\,DNP}$ values measured by GC-IRMS. Solid green line describes Rayleigh fractionation of DNAN as the parent reactant in S_N2Ar. Solid purple and red lines represent the modeled evolutions of instantaneous product (MC) (eq, 4.1.20) and accumulated product (DNP) (eq. 4.1.21).

4.1.4. Conclusions

With a combination of EA-IRMS, GC-IRMS, and quantitative ^{13}C NMR measurements, in conjunction with DFT models, this work examined the position-specific kinetic isotope effects of a reactive element (carbon) and a nonreacting element (nitrogen) during a S_N2Ar nucleophilic substitution. Using DNAN as a model nitroaromatic hydrocarbon, kinetic isotope effects associated with the S_N2Ar nucleophilic substitution mechanism could be fully determined. The combined approach of PSIA and CSIA may enable a better understanding of the reaction mechanisms involved in biotic and abiotic degradation of organic contaminants in cases where a single measurement approach is inconclusive. The larger sample size requirement for quantitative NMR measurements (~ 200 mg), however, may restrict their practical use to laboratory experiments rather than field studies.

Extending these methods to other reactive elements (e.g. oxygen, chlorine, bromine, sulfur) at the reacting bond(s) of rate-limiting step(s) is an area deserving further study. irm-^{13}C and irm-^{15}N NMR with lower MDLs (a few mg or lower) would be a tremendous improvement. Further progress in alternative methods for PSIA (e.g., Orbitrap MS; Eiler et al., 2017) may ultimately prove more useful than NMR methods. In addition, more accurate and precise simulations using hybrid quantum mechanics/molecular mechanics (QM/MM) approaches should benefit not only in the verification of experimental observations, but also in predicting the fates of organic contaminants in the environment.

4.2 Alkaline hydrolysis pathway of DNAN verified by ^{18}O tracer experiment

DNAN may be transformed through alkaline or enzymatic hydrolysis and abiotic or enzymatic reduction in groundwater [Khatiwada et al., 2018; Nudelman & Palleros, 1983; Ou et al., 2016; Niedzwiecka et al., 2017; Ding et al., 2018; Ulrich et al., 2018). The consistent detection of the reaction product 2,4-dinitrophenol (DNP), and the absence of observable intermediate(s), leaves the specific pathway for alkaline hydrolysis an open question, even with large kinetic isotope effects reported for carbon in both DNAN and DNP (Fig. 4.2.1) (Salter-Blanc et al., 2013; Sviatenko et al., 2014; Ulrich et al. 2018). We hypothesized that the mechanism of DNAN alkaline hydrolysis could be resolved conclusively by performing experiments using water with contrasting isotopic abundances of ^{18}O.
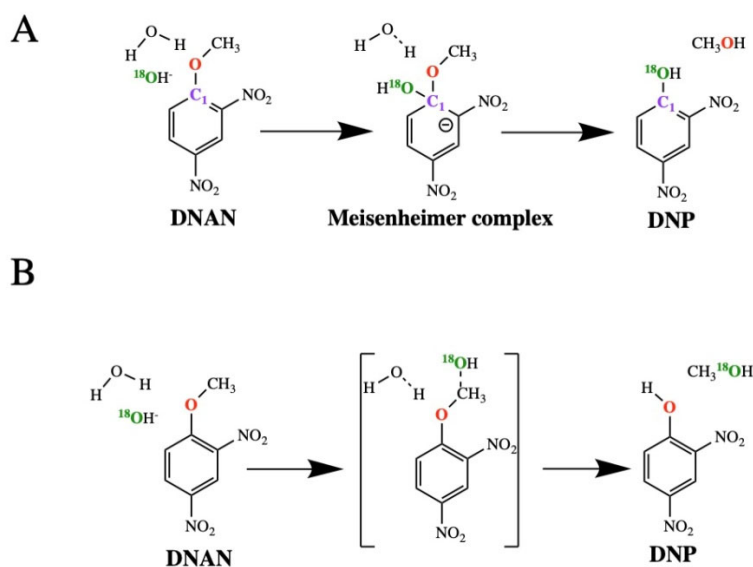
Fig. 4.2.1. Two proposed pathways during alkaline hydrolysis of DNAN (A – nucleophilic substitution at the C1 aromatic site; B – *O*-demethylation by nucleophilic substitution at the aliphatic carbon of the –OCH$_3$ group) both result in products DNP plus CH$_3$OH. Only one of the resonance structures of postulated Meisenheimer complex intermediates is shown in Pathway A. The oxygen atom of the –OCH$_3$ group in DNAN (shown in red) is part of the –OCH$_3$ leaving group produced in Pathway A and is replaced at the C1 site by an oxygen atom from H$_2$O, but in Pathway B, the oxygen atom of the –OCH$_3$ group remains bonded to the C1 carbon and –CH$_3$ is the leaving group. Thus, in the presence of ^{18}O-labeled H$_2$O, substantial ^{18}O enrichment would be observed in DNP produced by Pathway A, but not by Pathway B.

Carbon and nitrogen isotope fractionations accompany both alkaline and enzymatic hydrolysis of DNAN (Ulrich et al., 2018). Even though the magnitudes of reported apparent kinetic isotope effects for carbon were different by roughly a factor of two during these two hydrolysis reactions, implying the possibility of two distinct hydrolysis pathways, there was no other direct evidence to identify the pathway of DNAN alkaline hydrolysis, as the Meisenheimer complex was not observed experimentally and oxygen isotope ratios were not measured in previous work.

Calculations by density-functional theory (DFT) have been useful for identifying the reaction pathways and rate-limiting step(s) within multi-step transformations of nitroaromatic

compounds (Skarpeli-Liati et al., 2011; Pati et al., 2016: Schutt and Shukla, 2019; Murillo-Gelvez et al., 2019). DFT calculations were performed previously by others to evaluate the kinetics and mechanisms of DNAN alkaline hydrolysis (Sviatenko et al., 2014; Zhou et al., 2018). Hydrolysis at the C1 site by nucleophilic aromatic substitution of $-OH^-$ for $-OCH_3$ via Meisenheimer complex formation was predicted to be kinetically and thermodynamically favorable, even though reaction free energies and activation free energies differed between experimental and computational results (Sviatenko et al., 2014).

In the nucleophilic aromatic substitution at the C1 site, the oxygen atom of the methoxy group ($-OCH_3$) becomes part of the $-OCH_3$ leaving group and is replaced by an incoming oxygen from the nucleophile ($-OH$) that becomes the phenol(ate) group of the product DNP, whereas in the O-demethylation case the oxygen atom of the methoxy group remains attached to the aromatic ring and becomes singly protonated (Fig. 4.2.1). In this study, we measured the oxygen isotopic compositions of the initial reactant DNAN and its hydrolysis product DNP in basic solutions prepared from both deionized water (DIW) and ^{18}O-labeled water (LW), using TC/EA-IRMS (method described in Section 2.4 of this report). From the observed ^{18}O isotopic mass balances we determined that there had been 1:1 replacement of the oxygen atom at the C1 site by an oxygen atom from H_2O. We also performed a set of DFT calculations with explicit solvation of DNAN by 10 water molecules and one OH^- ion that supported earlier theoretical work (Sviatenko et al., 2014; Zhou et al., 2018) showing the nucleophilic substitution Pathway A (via Meisenheimer complex formation at the C1 site) was energetically favorable compared with Pathway B (via O–demethylation at the aliphatic C site).

4.2.1   Test for oxygen isotope exchange between DNAN and water

The initial $\delta^{18}O$ value of the DNAN reagent (2,4-dinitroanisole (CAS 119-27-7; ≥98%), purchased from Alfa Aesar (Ward Hill, MA USA), LOT#10173248) used for this experiment (DNAN-EIGL) was measured at $+14.11 \pm 0.08$ ‰, and that for another DNAN reagent (2,4-dinitroanisole (CAS 119-27-7; ≥98 %), purchased from Sigma-Aldrich (Milwaukee, WI USA), LOT#09709CO) in our laboratory (DNAN-PEI) was $+10.31 \pm 0.23$ ‰. To test for oxygen isotope fractionation during UALLE, and to evaluate DNAN solid-water oxygen isotope exchange, oversaturated DNAN solutions were prepared by adding excess DNAN (10 mg, 6 mg and 4 mg) to 5 mL of deionized water or ^{18}O-labeled water for a 15-day batch experiment in a 55 $\pm 0.5°C$ water bath. At various time intervals, duplicate tubes were sampled by centrifuging at 2000 rpm for 10 mins, and then 4 mL of supernate solution was transferred to a 20-mL amber vial, diluted by adding 4 mL of deionized water or ^{18}O-labeled water and then extracted in a 1:1 (v/v) water to ethyl acetate mixture. For the remaining 1 mL of each aqueous solution, including residual undissolved DNAN particles, water was evaporated at room temperature in the dark, and then the dried DNAN was re-dissolved for O isotope analysis.
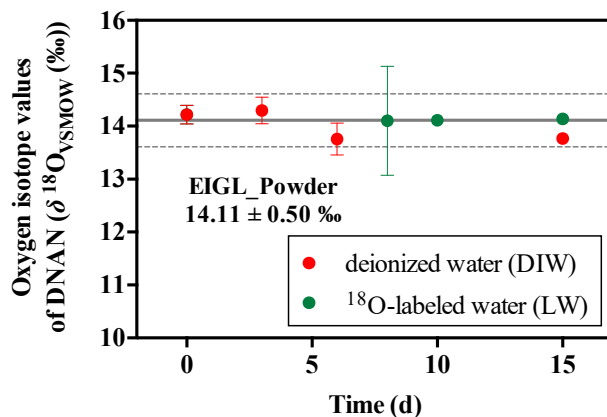
Fig 4.2.2. $\delta^{18}O$ values of the working standard DNAN-EIGL extracted from deionized water (DIW) and ^{18}O-labeled water (LW) during a 15-day experiment at $55 \pm 0.5°C$. Solid line represents the average $\delta^{18}O$ value of DNAN (EIGL powder) by TC/EA-IRMS (n=8). Dashed lines represent the standard deviation.
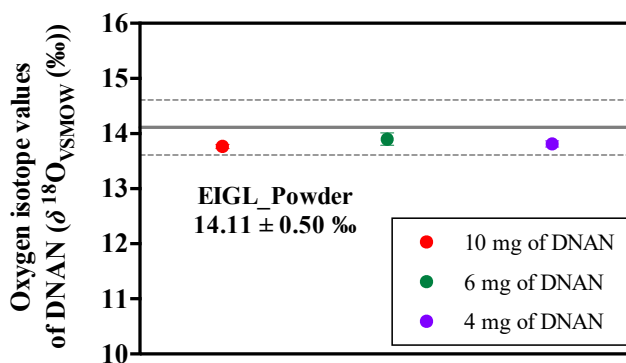
Fig. 4.2.3. Final $\delta^{18}O$ values of residual solid DNAN-EIGL samples after a 15-day test for DNAN-water oxygen isotope exchange at $55 \pm 0.5°C$. Solid line represents the average $\delta^{18}O$ value of DNAN-EIGL powder by TC/EA-IRMS (n=8) and dashed lines represent the standard deviation.

During the 15-day DNAN solid-water partitioning experiment and after UALLE, O isotope exchange between DNAN and water was negligible in both aqueous phase (Fig. 4.2.2) and solid phase (Fig. 4.2.3). This indicates that the DNAN nitro group oxygens were stable with respect to oxygen exchange with water at $55 \pm 0.5°C$ for at least 15 days, which is much longer than the typical duration of our alkaline hydrolysis experiments (~6 hours).

4.2.2. Computational methods

Density-functional theory (DFT) calculations were performed on DNAN and its hydrolysis products in the solution phase with the Gaussian 09 software package (Frisch et al., 2016). The optimized geometries and corresponding normal modes of each minimum energy and transition state structure encountered along the putative reaction pathways were evaluated with the M06-2X hybrid functional (Zhou & Truhlar, 2007) in conjunction with the standard 6-311++G(2d,2p) basis set and an ultrafine integration grid as implemented in Gaussian. The SMD

polarizable continuum solvation model (Marenich et al., 2009) was used with Pauling atomic radii (Besler et al., 1990) in all computations. DNAN was also explicitly solvated with 10 water molecules and one hydroxyl ion. The reaction pathways were constructed by first using brute force potential energy scans to identify intermediate and product states. Once the optimized structures of these local minima were obtained, the synchronous transit quasi-Newton method (Peng et al., 1996) was used to refine the transition state structures between them. The free energies of each local minimum and transition state structure were obtained by normal mode vibrational analysis.

4.2.3. Results and discussion
4.2.3.1 Hydrolysis kinetics

Kinetics of DNAN alkaline hydrolysis were measured using samples collected over six hours of reaction (Fig. 4.2.4). The kinetics were fit well by a pseudo-first order relation based on eq 4.2.1.

$$\ln\left(\frac{C}{C_0}\right) = -k_{obs} \cdot t \tag{4.2.1}$$

Where, C and C_0 represent the concentration of DNAN at time point t and the initial concentration of DNAN, respectively. The pseudo-first order rate constant k_{obs} obtained under our experimental conditions was 0.345 ± 0.010 hr^{-1}, in general agreement with the range of values determined previously (Salter-Blanc et al., 2018). Although the alkaline hydrolysis of DNAN was nearly complete after six hours, the experiments were extended to 24 hours to ensure that the reaction proceeded to completion and all DNAN was transformed to DNP (where $f_{DNAN} = C_{DNAN}/C_{0,DNAN} = 0$). This allowed a direct evaluation of the net oxygen isotope mass balance of the alkaline hydrolysis reaction.
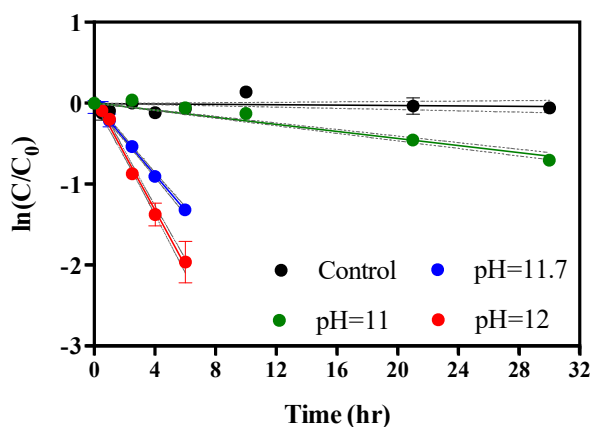
Fig. 4.2.4. Kinetics of alkaline hydrolysis of DNAN in terms of ln (C/C$_0$) vs time (hr). Best-fit solid lines show the pseudo-first order kinetic description of concentration dynamics according to eq 4.2.1. Dashed lines represent 95% confidence intervals around the best-fit solid lines. At pH 12, the slope indicates a pseudo-first order rate constant of $k_{obs} = 0.345 \pm 0.010$ hr^{-1}.

4.2.3.2 Oxygen isotope balance and verification of DNAN alkaline hydrolysis pathway

We measured $\delta^{18}O$ values of combined DNAN + DNP as a function of the remaining DNAN fraction (C/C_0) during alkaline hydrolysis in batch solution experiments prepared with either natural-abundance deionized water or ^{18}O-labeled deionized water (Table 4.2.1). This experimental strategy allowed us to consider the alkaline hydrolysis reaction as an isotope exchange reaction, and thus to determine conclusively which of the following pathways occurred, where the ^{18}O atom is indicated by an asterisk:

Pathway A: DNAN + H_2O* $\Rightarrow$ MC* $\Rightarrow$ DNP* + CH_3OH (4.2.2)

Pathway B: DNAN + H_2O* $\Rightarrow$ DNP + CH_3OH*   (4.2.3)
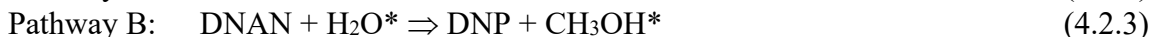
The experimental data show that the mixtures of DNAN + DNP are well fit with linear regressions that can be simply explained as two-component mixtures of the initial DNAN ($\delta^{18}O$ = +14.1 ‰) with final DNP ($\delta^{18}O$ = +4.7 ‰ in deionized water experiment; $\delta^{18}O$ = +15.6 ‰ in ^{18}O-labeled water experiment) (Fig. 4.2.5). The relatively higher $\delta^{18}O$ value of DNP produced in the experiment with ^{18}O-labeled water, in comparison with that produced in the experiment with unlabeled water, is strong evidence for oxygen exchange by Pathway A. Although we did not measure individual compound-specific $\delta^{18}O$ values for the reactant DNAN or products DNP and CH_3OH during the progress of the reaction in our experiments, we assume that any oxygen kinetic isotope effects would have been equal in the two sets of experiments because they were conducted under identical conditions with the only difference being the $\delta^{18}O$ value of H_2O. It follows that the $\delta^{18}O$ value of the final CH_3OH product should be equal in the unlabeled and labeled experiments. We assumed negligible oxygen isotopic fractionation between H_2O and the –OH nucleophile during formation of the Meisenheimer complex, and also that the –OCH_3 leaving group retained its initial $\delta^{18}O$ value during dissociation of the Meisenheimer complex. With these assumptions, we estimated the $\delta^{18}O$ value of CH_3OH as follows:

$$\delta^{18}O_{CH3OH,f} = 5\ \delta^{18}O_{DNAN,0} + \delta^{18}O_{H2O,0} - 5\ \delta^{18}O_{DNP,f}$$ (4.2.4)

where $\delta^{18}O_{DNAN,0}$ and $\delta^{18}O_{H2O,0}$ are the initial $\delta^{18}O$ values of DNAN and H_2O, and $\delta^{18}O_{CH3OH,f}$ and $\delta^{18}O_{DNP,f}$ are the final $\delta^{18}O$ values of the DNP and CH_3OH products. Based on equation (4.2.4) and the data in Table 4.2.1, the resulting values obtained for $\delta^{18}O_{CH3OH}$ were +40.1 ± 2.1 ‰ and +42.9 ± 1.2 ‰, respectively, for the unlabeled and ^{18}O-labeled experiments. These values are equal within propagated analytical error, and are thus consistent with alkaline hydrolysis by Pathway A. The relatively high value of the $\delta^{18}O_{CH3OH}$ product indicates a strong intramolecular isotopic fractionation of oxygen between the –OCH_3 group and the –NO_2 groups in the DNAN used for these experiments. The average $\delta^{18}O$ value estimated for the –NO_2 groups is about +7.5 ‰.

Table 4.2.1 Oxygen isotope analyses of DNAN + DNP.

C/C_0 DNAN	$\delta^{18}O$, ‰ DNAN+DNP	$\pm 1\sigma$	# analyses n
Deionized water (initial $\delta^{18}O = -6.9 \pm 0.4$ ‰)			
1.00	14.1	0.1	8
0.72	12.5	0.5	7
0.52	11.3	0.6	8
0.37	10.5	1.3	8
0.27	8.0	0.3	4
0.23	7.9	0.5	4
0.19	7.1	0.1	4
0.16	7.5	1.2	4
0.14	6.0	0.4	4
0.00	4.7	0.5	12
^{18}O-labeled water (initial $\delta^{18}O = +50.3 \pm 0.4$ ‰)			
1.00	14.1	0.1	8
0.52	14.8	1.1	2
0.27	15.2	0.1	2
0.19	14.9	0.1	2
0.14	15.2	0.2	2
0.00	15.6	0.2	2
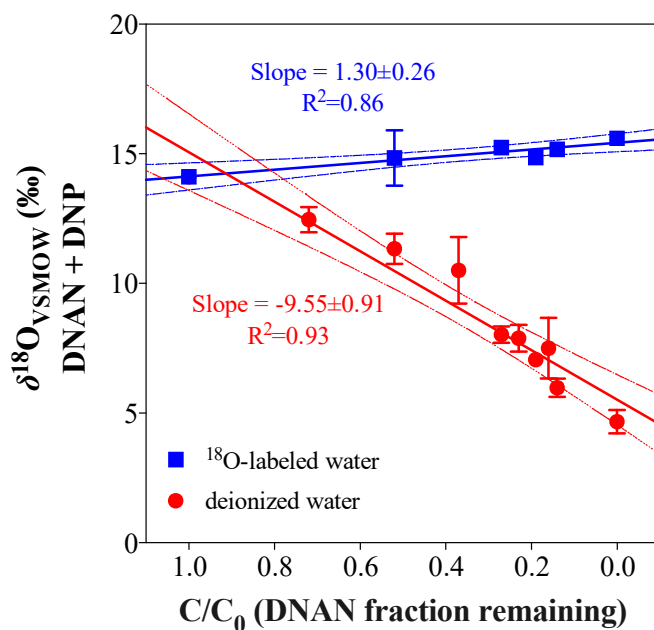
Fig. 4.2.5. The $\delta^{18}O$ values of combined DNAN + DNP vs. fraction of DNAN remaining (C/C_0) from alkaline hydrolysis experiments with unlabeled deionized water (circles) and ^{18}O-labeled water (squares). Error bars are standard deviations of replicate measurements. Dashed lines represent best-fit linear regressions with respective R^2 values shown.

4.2.3.3 Calculations of reaction pathway energetics

Gibbs free energy changes through two putative alkaline hydrolysis pathways (Figs. 4.2.1A & B) were calculated by DFT methods (Fig. 4.2.6). These calculations represent an advance over earlier work (Salter-Blanc et al., 2013; Sviatenko et al., 2014) in that we included explicit solvation by 10 H_2O molecules and one hydroxyl ion.
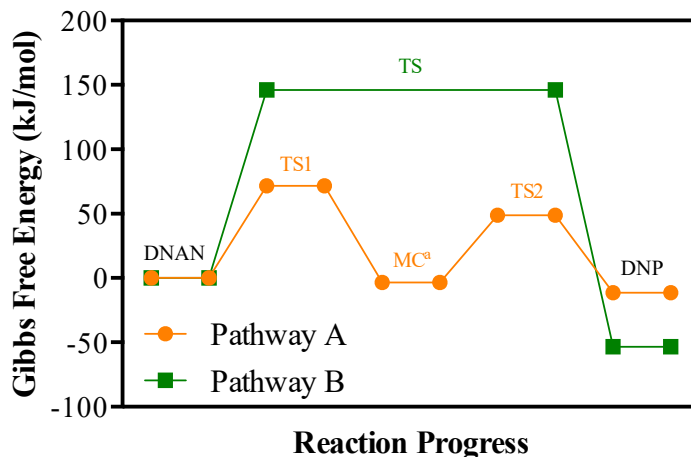
Fig. 4.2.6. Gibbs free energies of stationary points and transition states during DNAN hydrolysis reaction. Pathway A represents the reaction pathway shown in Fig. 4.2.1, panel A; while Pathway B represents the reaction mechanism shown in Fig. 4.2.1, panel B. [a]MC represents the Meisenheimer complex intermediate.

In Pathway A, the calculated energy barrier from reactant DNAN to the first transition state (TS1) is +71.5 kJ/mol, and that from the Meisenheimer complex intermediate to the second transition state (TS2) is +49.0 kJ/mol. In Pathway B, the energy barrier from DNAN to TS1, +146.1 kJ/mol, is much larger than that for Pathway A. This relatively large activation energy for Pathway B may explain why Pathway A is favored, as demonstrated clearly by our experimental results.

The above results can be compared with earlier efforts using DFT calculations to predict DNAN transformations during alkaline hydrolysis. One group also used the same general approach with the Gaussian 09 suite of programs optimized at the SMD(Pauling)/M06-2X/6-311++G(2d,2p) level, but with hydroxide modeled as a species hydrated by three water molecules (Sviatenko et al., 2014). They found that direct substitution at nitro sites was the most energetically favorable transformation, but also found that Meisenheimer complex formation at C1 and methyl abstraction were also allowed. Their activation free energies for all of these transformations were generally lower than those obtained by our calculations, and their ΔG_{rxn} values were less negative. Another group employed a different DFT computational approach with the NWChem suite of programs, optimized at the COSMO/B3LYP and MP2/6-311++G(2d,2p) levels, and concluded that the Meisenheimer complex formation at C1 is the most likely initial reaction step, although their calculated ΔG_{rxn} values were positive (Salter-Blanc et al., 2013). They obtained negative ΔG_{rxn} values for direct nitro substitutions at C2 and C4 and suggested that these were less likely because of their relatively high activation free energies of activation. Variations in the DFT results obtained by different groups are likely attributable to differences in the treatment of solvation in the electronic structure calculations. The study by Salter-Blanc et al. (2013) includes only implicit solvation effects, through the use

of a self-consistent reaction field method (COSMO); this study also differs from the present study and Sviatenko et al. (2014) in that it utilizes the B3LYP density functional and MP2 level perturbation theory to model hydrolysis. Further, while this study employs the same DFT and implicit solvation method as Sviatenko et al. (2014), more solvent molecules are considered explicitly here.

These DFT calculations performed by three different groups, with slightly different approaches and results, nonetheless point to a qualitatively similar conclusion in that DNAN alkaline hydrolysis likely begins with Meisenheimer complex formation at the C1 site. This is consistent with the occurrence of DNP as the principal reaction product observed experimentally by all three groups, as well as the new oxygen isotope evidence obtained in the present study.

4.2.3.4. Conclusion

This study demonstrated the use of a classical isotope-tracer approach to verify the alkaline hydrolysis pathway of DNAN. Such an approach could be generally helpful to refine mechanistic interpretations in other cases where reaction pathways may be ambiguous in terms of kinetic isotope effects determined from CSIA (Elsner and Imfeld, 2016). The measurement of oxygen isotope ratios, in addition to the more commonly measured carbon and nitrogen isotope ratios by CSIA of organic pollutants, adds an important constraint for deciphering environmental transformations of compounds that contain oxygen in participating functional groups. In addition, photochemical reaction products may incorporate environmental oxygen from reactive oxygen-bearing species. Oxygen isotope analysis provides an unexplored tool by which to further interrogate these complex pollutant degradation processes in the laboratory and in the environment.

4.3. Photocatalytic mechanisms of DNAN degradation in water deciphered by carbon and nitrogen isotope fractionation

4.3.1. Introduction

At military testing and training grounds, DNAN is predicted to enter the environment through dissolution of material from unexploded or partially detonated explosives. Understanding the transport and transformation mechanisms of DNAN in surface waters, soils and groundwater is important for environmental remediation of DNAN-contaminated sites. For industrial treatment of wastewater, photocatalysis and direct photolysis under UV-C irradiation (λ = 100–280 nm) have been examined as mechanisms for degrading DNAN (Su et al., 2019) and other nitroaromatic compounds (e.g., nitrobenzene) (Bhatkhande, 2004) in munitions manufacturing wastewaters. The main products of direct and indirect DNAN photolysis have been identified as 2,4-dinitrophenol (DNP) and other related acids or aldehydes, as well as inorganic nitrogen species (e.g., nitrite and nitrate) (Rao et al., 2013; Taylor et al., 2017). Additionally, denitration of DNAN and re-nitration of its products were reported to occur simultaneously in the presence of $^{15}NO_2$-labeled explosive CL-20 during photolysis in a solar simulating photoreactor (Halasz et al., 2018). It is therefore likely that DNAN released into surface water and exposed to sunlight may undergo photolysis via transformation pathways like those observed in laboratory experiments. Compound-specific isotope analysis (CSIA) has proven to be a powerful tool to decipher the transformation mechanisms of pollutants based on kinetic isotope effects (KIEs) associated with bond breaking between certain elements (e.g., C, N, H, Cl, S and O) and also to evaluate the effectiveness of different remediation strategies (Schmidt et al., 2004; Hofstetter et al., 2007; Tobler et al., 2007; Bernstein et al., 2008; Meyer et al., 2009; Fuller et al., 2016; Wang et al., 2020; Hatzinger et al., 2013; Elsner and Imfeld, 2016; Vogt et al., 2016). The successful applications of CSIA to investigate various biotic and abiotic contaminant degradation pathways have led to its use to examine photolysis reactions. For example, inverse ^{13}C and ^{15}N fractionation of atrazine during direct photolysis (unlike typical dechlorination) vs. normal ^{13}C and ^{15}N fractionation during photooxidation (like typical biotic/abiotic oxidation) have been observed, indicating the importance of photophysical processes involving the excited states of atrazine and magnetic isotope effects (Hartenbach et al., 2008). According to a comprehensive understanding of inverse ^{15}N fractionation in aniline from the partial aromatic imine formation after one-electron oxidation (deprotonation) (Skarpeli-Liati et al., 2011), substituted anilines have been chosen as a group of model compounds to further investigate (i) How heterolytic aromatic dechlorination of excited singlet and triplet states affect apparent kinetic isotope effects (AKIEs) under direct photolysis (Ratti et al., 2015); (ii) How spin selective isotope effects are reflected in highly variable ^{13}C-AKIEs and ^{15}N-AKIEs associated with photolytic dechlorination of chloroaniline isomers (Ratti et al., 2015); and (iii) How electron donating properties of the para-substitutes shift ^{13}C-AKIEs and ^{15}N-AKIEs during indirect photolysis (photooxidation) (Ratti et al., 2015). However, stable isotope fractionation trends associated with specific photolysis pathways of micropollutants generally remain difficult to assign and categorize. The influence of excited singlet/triplet states of the target contaminants and the spin sensitivity of certain functional groups (e.g., $-NH_2$ and $-NO_2$) on stable isotope effects require further research.

In the present study, we investigated photolysis pathway(s) of DNAN by interpreting the dual C and N isotope effects associated with UV light-induced reactions. We hypothesized that the excited triplet state of DNAN ($^3DNAN^*$) is a photosensitizer (e.g., $^3CDOM^*$). Also, we considered the important roles that nitrite/nitrate generated during denitration could play in both

nitration-denitration and photooxidation reactions (Mack and Bolton, 1999; Vione et al., 2007; Shankar et al., 2008; Xu et al., 2019; Vione et al., 2005; Pang et al., 2019; Dhar et al., 1934). To this end, we performed two continuous-flow batch experiments under the irradiation of UV-A light (with bulbs of nominal 350 nm wavelength) and UV-C light (with bulbs of nominal 254 nm wavelength), respectively. From these experiments we derived typical kinetics and ^{13}C- and ^{15}N-enrichment factors associated with photolysis of DNAN.

4.3.2 Materials and methods
4.3.2.1. Chemicals
2,4-Dinitroanisole (DNAN) was purchased from Alfa-Aesar (Tewksbury, MA). 2,4-dinitrophenol (DNP) was purchased from Sigma-Aldrich (Saint Louis, MO). The potential DNAN breakdown products, 3-nitro-4- methoxyaniline (2-ANAN), 4-amino-2-nitroanisole (4-ANAN), 2-nitroanisole (2-NA) and 4-nitroanisole (4-NA) were purchased from Santa Cruz Biotechnology (Dallas, TX, USA). All chemicals were reagent grade or higher purity. A stock solution of DNAN (~180 mg/L) dissolved in laboratory grade purified water (specific conductivity >18 MΩ) was further diluted with purified water to prepare test solutions.

4.3.2.2. Photolysis experiments
Photolysis experiments were performed using a Rayonet RPR-200 photoreactor (Southern New England Ultraviolet Company, Branford, CT). A photograph and diagram of the experimental setup is shown in Fig. 4.3.1. Photolysis at different wavelengths was examined using 16 UV lamps with nominal wavelengths of either 254 nm or 350 nm depending on the experiment. The reaction zone consisted of 2.5 cm external diameter quartz tubes (2.2 cm ID × 45.7 cm length; 1 mm wall thickness; G. Finkenbeiner, Inc., Waltham, MA) positioned in the center of the reactor. Each tube had 0.64 cm OD × 7.6 cm inlet and outlet regions which allowed connection to the rest of the tubing. A peristaltic pump recycled the test solution from the reservoir (900 mL amber glass bottle) at a flow rate of approximately 100 mL/min, resulting in a residence time of about 2 min in the quartz tube. All other tubing was Teflon or Teflon-lined, except for a short length of Norprene tubing in the pump heads. All fittings were white acetal. Fittings and tubing directly exposed to UV illumination were wrapped with aluminum foil tape to prevent photodegradation. The estimated ultraviolet power delivered to the sample was 16,000–21,000 µW/cm^2 at ~ 254 nm and 267–351 µW/cm^2 at ~ 350 nm. The temperature of the solution in the reservoir and the air temperature inside the reactor were monitored and recorded. The solution in the reservoir was sampled over time for residual DNAN, breakdown products of DNAN, nitrite, and nitrate (see below). The cumulative UV exposure was calculated based on the time the UV lamps were turned on. All experiments were performed in duplicate unless otherwise noted.

4.3.2.3. Chemical analysis
Concentrations of DNAN were monitored via high performance liquid chromatography (HPLC) using a Dionex 3000 Ultimate HPLC (Thermo-Fisher, Waltham, MA) with an Agilent Zorbax Bonus-RP column (4.6 × 75 mm, 3.5 µm particle diameter) (Santa Clara, CA), variable wavelength detector (254 nm for DNAN), and a photodiode array detector collecting peak spectral data. The mobile phase was 50:50 methanol:0.2 % (v:v) trifluoroacetic acid in water at a flow rate of 1 mL/ min. The column temperature was 33 °C. The injection volume ranged from
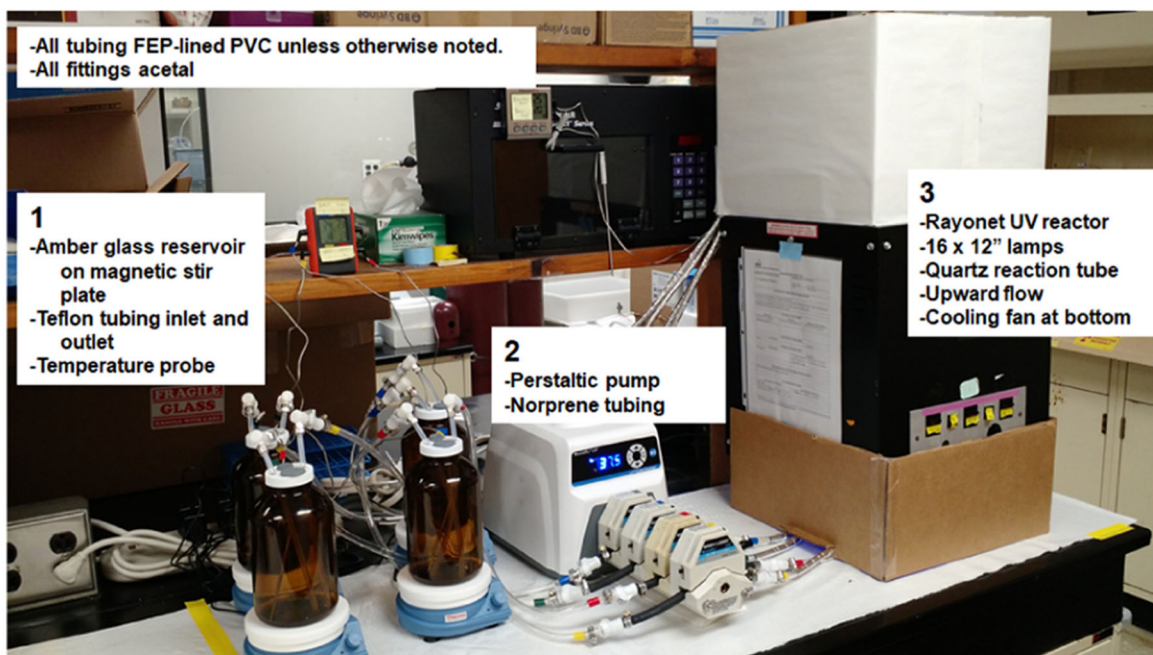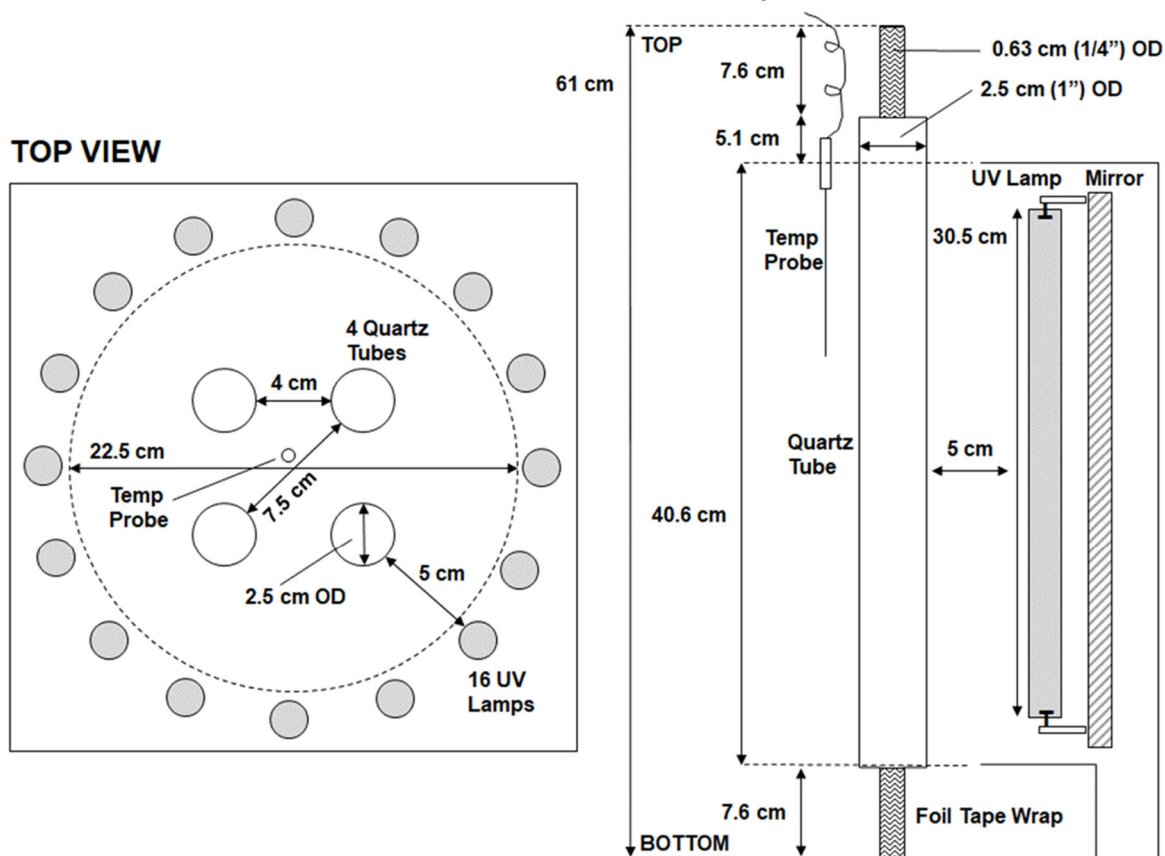
Fig. 4.3.1. Photograph and diagram of the photolysis experimental setup.

15 to 75 µL. The practical quantitation limit of DNAN with this injection volume was approximately 50 µg/L. More detailed analyses of DNAN and its potential breakdown products 2-amino-4-nitroanisole (2-ANAN), 4-amino-2-nitroanisole (4-ANAN), 2-nitroanisole (2-NA), 4-nitroanisole (4-NA), and 2,4-diaminoanisole (DAAN), were performed using an Agilent 1100 HPLC with an Acclaim Explosives E1 column (250 mm × 4.6 mm × 5 µm; Thermo Scientific), a Dionex UltiMate 3000 variable wavelength detector (300 nm for DNAN, 2-ANAN, 4-ANAN, 2-NA, 4-NA and 210 nm for DAAN), and a photodiode array detector collecting peak spectral data. The mobile phase was 60:40 H_2O:MeOH at a flow rate of 1.0 mL/min. The column temperature was 34 °C. The injection volume was 75 µL. The practical quantitation limits with this injection volume were (µg/L): DNAN, 50; 2-ANAN, 50; 4-ANAN, 50; 2-NA, 50; 4-NA, 50; and DAAN, 100. Anions (nitrite, nitrate) were analyzed via EPA Method 300.0 using an ICS-2000 ion chromatograph (Thermo Fisher Scientific, Waltham, MA). pH was measured using a pH probe (Oakton pH Testr 10, Cole- Parmer, Vernon Hills, IL, USA). To further identify and verify the by-products, aqueous experimental samples were pretreated by solid phase extraction (SPE) as described in our previous work (Fuller et al., 2016), and then measured by using a combined gas chromatography-quadrupole mass spectrometer (GC-qMS) (Thermo Scientific ISQ II LT)/-isotope ratio mass spectrometer (IRMS) (Thermo Scientific Delta V Plus system). The qMS detector and IRMS detector were connected to the same GC system through a split-flow fitting (SGE™ _SilFlow™ GC 3 Port Splitter), identifying compounds from their ion fragmentation patterns by qMS while simultaneously analyzing their C and N isotope ratios in parallel by IRMS. An Rtx®-5MS GC column (30-m length by 0.25-mm inner diameter with a 0.25-µm film thickness; Restek, Inc.) was used with 1.5 mL/min flow of helium carrier gas. The following GC program was used for CO_2 separation: 50 °C for 2 min, ramped at 20 °C/min to 220 °C, and then ramped at 8 °C/min to 245 ◦C, which was maintained for 2 min. DNP was identified and quantified by GC-qMS with external standard calibration, while 4-nitroguaiacol (4-NG) was identified but not quantified. Chemicals were identified with the NIST spectral library of the Thermo Xcalibur 4.1 data acquisition and processing software.

4.3.2.4. Isotopic analyses

The GC-IRMS method used for analysis of C and N stable isotope ratios in DNAN and its products DNP, 2-ANAN and 4-NG was identical to that described in Section 2.1 of this report.

4.3.2.5. Data evaluation

In transformation processes of DNAN, the ^{13}C- and ^{15}N-substituted isotopologues typically react more slowly than the lighter ones due to the greater bond stabilities and slower reaction rates of the heavier molecules. This normally leads to a characteristic enrichment of heavier isotopes within the residual parent molecules and a depletion in heavier isotopes of the reaction products as the reaction proceeds. Stable isotope ratio R of an organic compound is defined as follows,

$$R = {^h}E/{^l}E = \delta^h E + 1 \tag{4.3.1}$$

where ^{h}E is the total amount of heavier isotope (in the present case, ^{13}C or ^{15}N) in the bulk organic compound molecules (in the present case, DNAN), ^{l}E is the total amount of lighter isotope (in the present case, ^{12}C or ^{14}N) in the bulk organic compound molecules, and δ^hE is the

reported isotope value calibrated normalized to a scale defined by the isotope ratios of international reference materials.

Based on the Rayleigh equation,

$$R/R_0 = f^{\alpha-1} = f^{\varepsilon} \tag{4.3.2}$$

where R and R_0, in the present case, are the C or N isotope ratios of the residual DNAN and the initial (unreacted) DNAN, respectively; f is the fraction of DNAN remaining at the sample time point; α is the isotope fractionation factor; and ε is the isotope enrichment factor. In terms of the $\delta^h E$ values, Eq. (4.3.1) can be rewritten as:

$$(\delta^h E_t + 1)/(\delta^h E_0 + 1) = f^{\varepsilon} \tag{4.3.3}$$

The value of ε can be obtained from the natural logarithmic transformation of Eq. (4.3.3),

$$\varepsilon = \ln((\delta^h E_t + 1)/(\delta^h E_0 + 1))/ \ln f \tag{4.3.4}$$

In this study, values of ε are given in parts per thousand (‰). If lighter isotopologues react faster and isotope fractionation is therefore considered "normal", α values are smaller than one and ε values are negative, which results in enrichment of light isotopes in products and heavy isotopes in residual reactants. "Inverse" isotopic fractionation occurs when α values are greater than one and ε values are positive. For replicate experiments, a single ε value was derived from the slope (Eq. 4.3.4) of a linear regression of data from multiple time points with 95% confidence intervals, as described in Fuller et al. (2016). The C and N isotope enrichment factors of product(s) (in this case, DNP, 2-ANAN and 4-NG), $\varepsilon_{product}$, were obtained by the following equation

$$\varepsilon_{product} = \ln[(\delta^h E_{product,t} + 1)/(\delta^h E_{reactant,0} + 1)]/ \ln f_{reactant} \tag{4.3.5}$$

Furthermore, we derived the slope of a N and C dual-isotope plot (lambda, $\Lambda^{N/C}$) to specify the photocatalysis mechanisms of DNAN under UV-A ($\lambda \sim 350$ nm) and UV-C ($\lambda \sim 254$ nm) irradiation (Eq. 4.3.6). The differences of $\Lambda^{N/C}$ values were within ±0.3, whether derived from ordinary linear regression (OLR), reduced major axis (RMA), the York method, or from the ratio of separately determined isotope enrichment factors. We reported the $\Lambda^{N/C}$ values derived by OLR with the standard errors (SE) (Ojeda et al., 2019).

$$\Lambda^{N/C} = \Delta\delta^{15}N/\Delta\delta^{13}C \approx \_\varepsilon N/\varepsilon C \tag{4.3.6}$$

4.3.3. Results and discussion
4.3.3.1. Photolysis of DNAN under UV-A ($\lambda \sim 350$ nm) irradiation
After 25 days of cumulative UV exposure, > 98.3% of DNAN was degraded under UV-A ($\lambda \sim 350$ nm) irradiation. A pseudo-first order rate constant was derived to describe the kinetics of UV-A-induced photolysis of DNAN with a half-life of 6.21 days (Fig. 4.3.1a). 2-ANAN was detected quantitatively as a product by HPLC/UV–vis (Fig. 4.3.2b). DNP was determined as another primary product using GC-qMS, which agreed with the previous observation of DNP

formation during DNAN photolysis under sunlight irradiation ($\lambda = 300$–400 nm) (Rao et al., 2013). Nucleophilic substitution of –OH for –OCH$_3$, producing DNP, was apparently one of the primary reaction pathways of DNAN photolysis under UV-A ($\lambda \sim 350$ nm) irradiation. The production of 2-ANAN indicated that nitro-reduction also occurred.
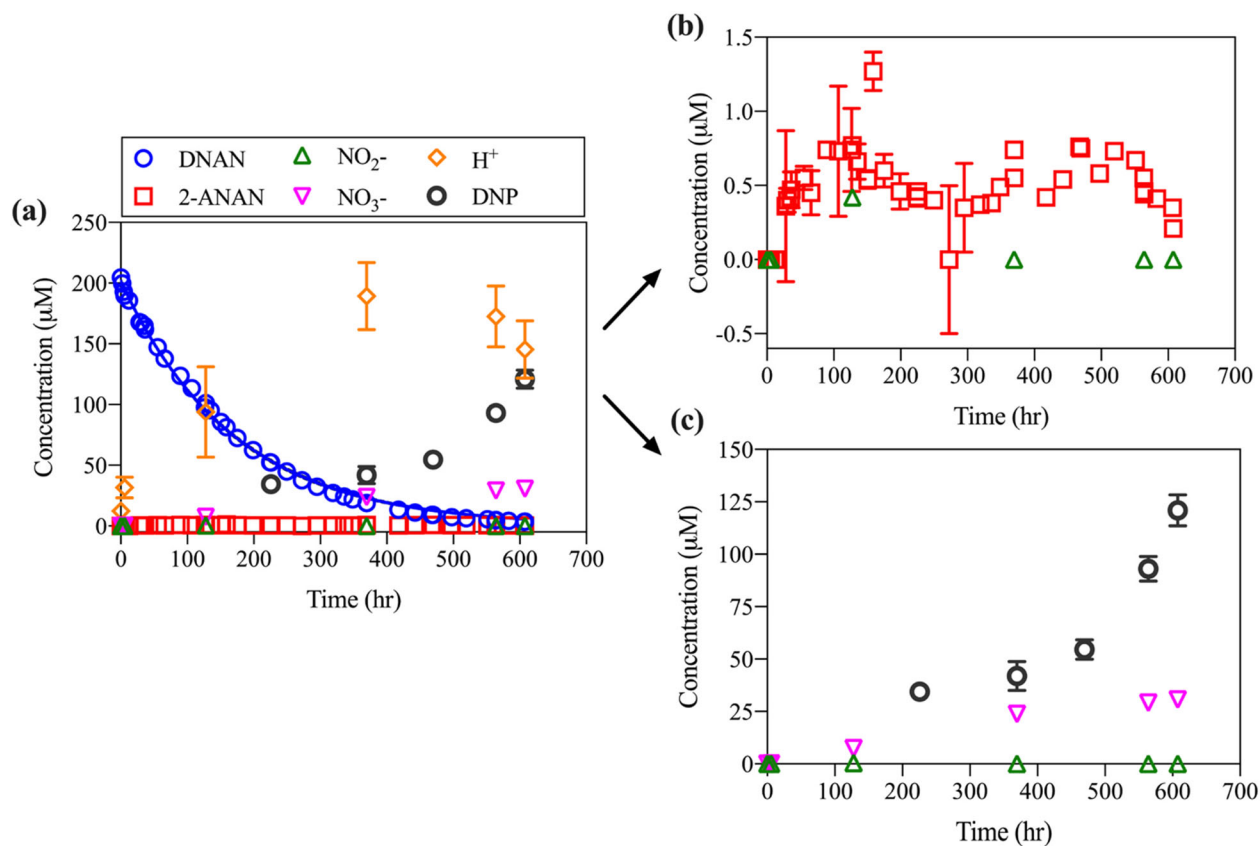
Fig. 4.3.2. (a) Concentrations (μM) of DNAN (blue circles), DNP (bold black circles), 2-ANAN (red squares), nitrite (green triangles), nitrate (purple inverted triangles), and H$^+$ (yellow diamonds) vs. time during photodegradation of DNAN under UV-A ($\lambda \sim 350$ nm) irradiation. Best-fit solid line (blue) shows a pseudo-first order kinetic description of DNAN concentration dynamics. (b) 2-ANAN and nitrite concentrations. (c) DNP, nitrite, and nitrate concentrations. Error bars represent $\pm$ one standard deviation from duplicate batch experiments; not shown where error is smaller than symbol size.

Nitrate, as one of the detected products, reached a maximum concentration of ~ 30 μM during DNAN photolysis under UV-A ($\lambda \sim 350$ nm) irradiation (Fig. 4.3.2c). In contrast, nitrite, which theoretically should be considered as another major product of DNAN photolysis (Rao et al., 2013; Vione et al., 2007, 2005; Albinet et al., 2010), was either not detected or was detected at a much lower concentration than nitrate (i. e., <0.087 μM) (Figs. 4.3.2b and c). The cleavage of nitro groups from the benzene ring structure of DNP may have been the dominant source of nitrite radicals.

UV–vis absorption spectra for the experimental solutions are shown in Fig. 4.3.3. The molar absorption coefficient of DNP reaches ~ 4000 M^{-1} cm^{-1} at $\lambda = 350$ nm (Wang et al., 2018; Albinet et al., 2010) while that of DNAN is ~ 3000 M^{-1} cm^{-1} (Moores et al., 2020), which

indicates that under λ ~ 350 nm irradiation and at pH < 7, DNP absorbs more photon energy than DNAN. Thus, we hypothesized that even though the initial stage of photosensitization (i.e., when
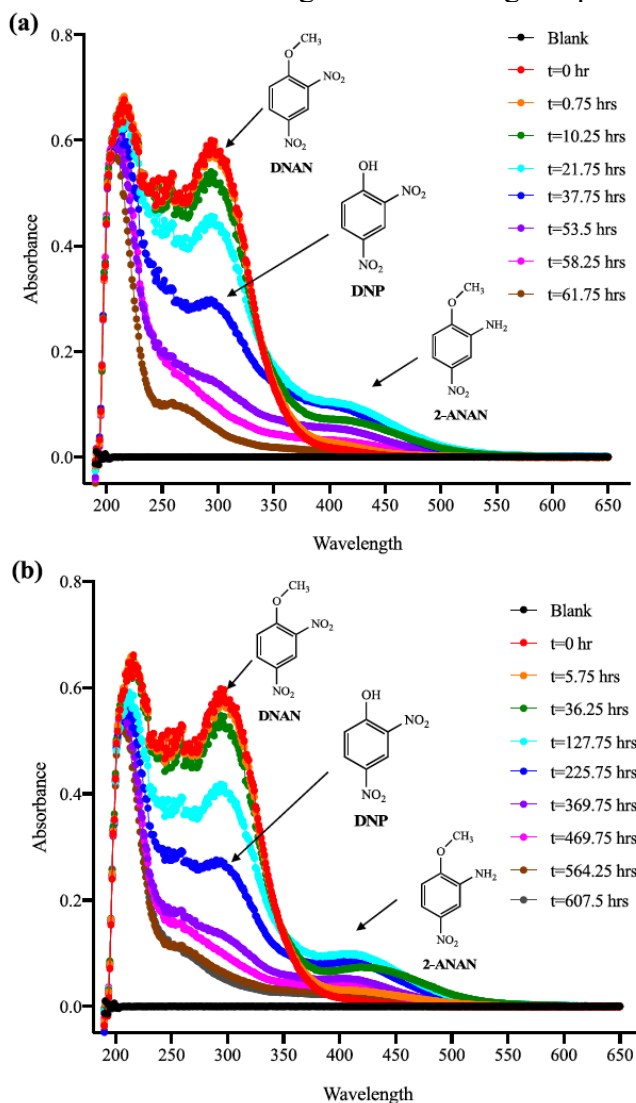
Fig. 4.3.3. Evolution of the overall absorbance of DNAN solutions (200 μM). UV–visible spectra were obtained after photocatalysis under UV-C (Panel a) and UV-A (Panel b) irradiation, respectively.

the fraction of DNAN consumed was < 1%) was triggered by triplet excited DNAN (^{3}DNAN*), further photosensitization may have been activated and promoted by the accumulated triplet excited DNP (^{3}DNP*), nitrite (NO_2^- *) and nitrate (NO_3^- *) (Scheme 4.3.1). Unlike the previous report that NO_2^- and NO_3^- accounted for roughly 100% of the N removed from DNAN during continuous UV-A/sunlight irradiation (Rao et al., 2013), only around 40 μM of NO_2^- and NO_3^- were recovered from the total 200 μM of DNAN consumed in our experimental system. DNP was one of the N-containing compounds produced as DNAN was consumed, demonstrating that in addition to being a primary photolysis product, DNP could have been reassembled from phenol radicals and nitrite radicals by nitration or de-photohydration (Qu et al., 2013; Cwiertny

et al., 2014; Yuan et al., 2016; Wang et al., 2020; Barsotti et al., 2017; Zhou et al., 2018; Ward et al., 2015; Baltrusaitis et al., 2016). The decrease of pH observed during DNAN photolysis may be attributed to (1) the dissociation of DNP to hydrogen cations and phenoxy anions in solution; (2) proton release from the UV light-induced reaction between nitrite radicals and H_2O (Eq. 4.3.7) along with the cleavage of nitro groups from the aromatic ring structures (Mack and Bolton, 1999; Xu et al., 2019; Dhar et al., 1934).

$$2NO_2^{\bullet} + H_2O \rightarrow NO_2^- + NO_3^- + 2H^+ \tag{4.3.7}$$

$$DNAN + 6e^- + 6H^+ \rightarrow 2\text{-}ANAN \tag{4.3.8}$$

Protons (present as H_3O^+ ions) in the aqueous solution reached a concentration of around 200 μM when 90% of DNAN was consumed. According to Eq. 4.3.7 and the mechanisms of nucleophilic substitution of DNAN, the release of H^+ should stoichiometrically balance the removal of DNAN/DNP as 2:1. However, due to nitro-reduction and production of •OH and OH$^-$ (Table 4.3.1, A series) that occurred simultaneously with proton release (Gligorovski et al., 2015), around 50% of the produced H^+ from Eq. 4.3.7 was likely to either be involved in the nitro-reduction of DNAN (Eq. 4.3.8) or bonded with OH$^-$ to produce H_2O in the aqueous solutions. After 90% of DNAN was consumed, we infer that H_3O^+ accumulation slowed and reversed because of the limited availability of nitrite radicals and by continued consumption of H^+ in nitro-reduction of DNAN to 2-ANAN.

Normal ^{13}C and inverse ^{15}N fractionation in both DNAN and DNP were observed during UV-A-induced photodegradation (Fig. 4.3.4). DNAN with isotopically light nitro group(s) ($-^{14}NO_2$) was apparently easier to excite and likely generated triplet excited state molecules ($^3DNAN^*$). $^3DNAN^*$ with $-^{14}NO2$ may have then acted as a photosensitizer to trigger the initial stage of hydroxyl radical (•OH) production (Scheme 4.3.1, Table 4.3.1). In contrast, DNAN with isotopically heavier nitro group(s) ($-^{15}NO2$) likely remained longer at ground singlet states, going through nucleophilic substitution and transformation to DNP, both under the exposure to UV-A ($\lambda \sim 350$ nm) and in the non-irradiated reservoir. The preference for nucleophilic substitution of ^{15}N-enriched DNAN isotopologues may have caused the observed inverse ^{15}N fractionation of +12.30 ‰ (Fig. 4.3.4), even though negligible N isotope fractionation in this compound was reported during both alkaline (SN_2Ar) and enzymatic (SN_1) hydrolysis (Ulrich et al., 2018).

The ^{13}C enrichment factor in DNAN was −3.34 ‰ under UV-A ($\lambda \sim 350$ nm) irradiation. This value agreed well with the reported εC (‰) value of DNAN during enzymatic hydrolysis (Ulrich et al., 2018), indicating that the nucleophilic substitution of DNAN may follow a SN_1 mechanism in our experimental system. However, an SN_2Ar mechanism might also occur due to the accumulation of •OH and/or OH$^-$.

4.3.3.2. Photolysis of DNAN under UV-C ($\lambda \sim 254$ nm) irradiation

In contrast to the pseudo-first order kinetics observed for DNAN photodegradation during UV-A ($\lambda \sim 350$ nm) irradiation, UV-C-induced photolysis of DNAN at a nominal wavelength of 254 nm appeared to exhibit zero-order kinetics (Fig. 4.3.5a). The limited availability of photosensitizer ($^3DNAN^*$, NO_2^-, NO_3^-) or photocatalyst (e.g., •OH) in the aqueous solution could have been the main reason for this concentration-independent kinetic behavior.
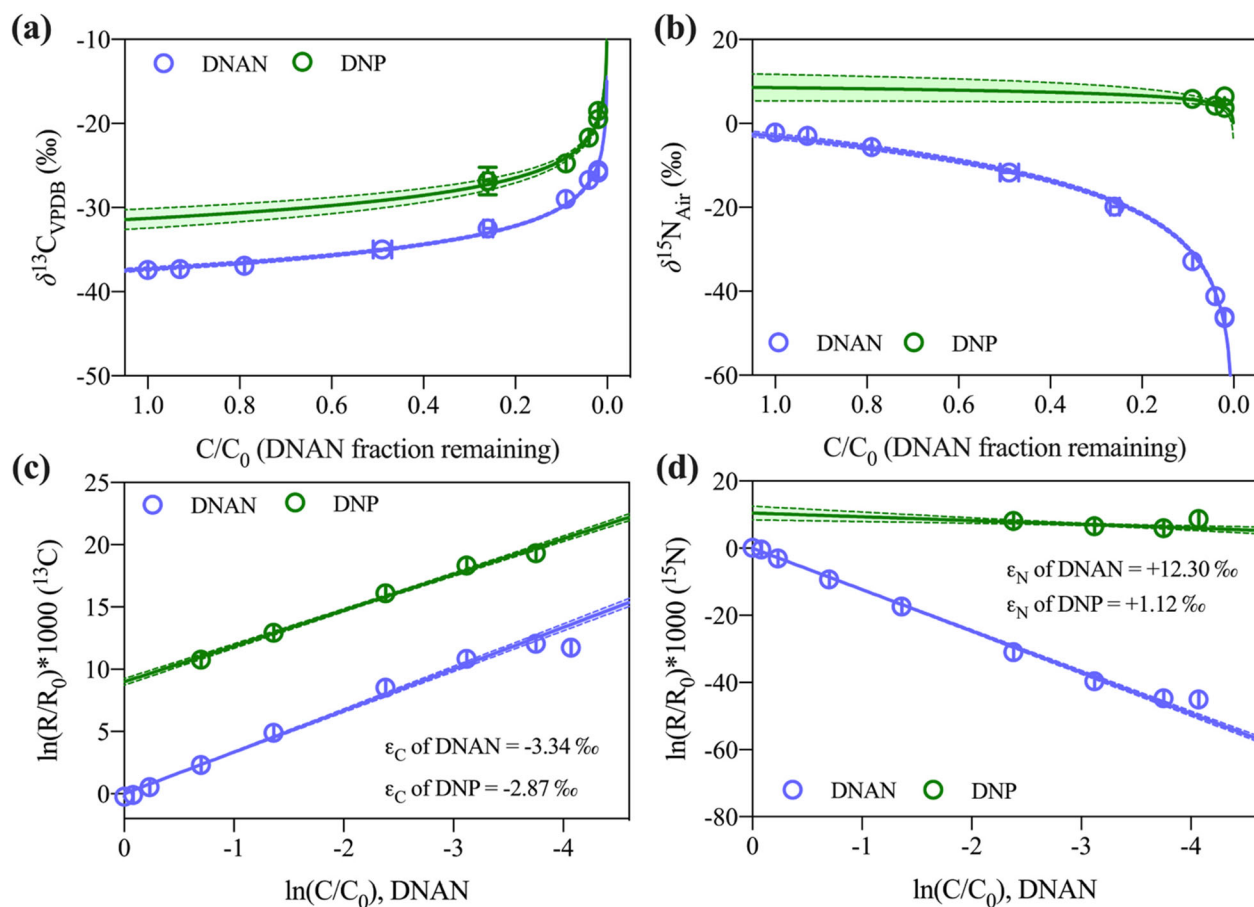
Fig. 4.3.4. Carbon and nitrogen isotope fractionation in DNAN and DNP during photodegradation of DNAN under UV-A ($\lambda \sim 350$ nm) irradiation. Panels a and b show the evolution of $\delta^{13}C_{VPDB}$ (‰) and $\delta^{15}N_{Air}$ (‰) values as a function of DNAN fraction remaining, C/C_0. Panels c and d show carbon and nitrogen isotope enrichment versus the natural log of remaining DNAN. The best-fit lines are based on a non-linear regression as described in Eq. (4.3.3) (Panels a and b) and a simple linear regression as described in Eq. (4.3.4) (Panels c and d). Solid lines represent the best-fit lines with the normal ^{13}C and inverse ^{15}N enrichment factors. Dashed lines represent 95% confidence intervals around the best-fit solid lines. Uncertainties in isotopic measurements represent ± one standard deviation from the combination of duplicate batch experiments and triplicate measurements for each sample. Some error bars are smaller than the symbols.

2-ANAN was identified as one of the principal photodegradation products by HPLC-UV–vis analysis. Additionally, DNP and 4-NG were identified by the GC-qMS method. Instead of nucleophilic substitution, denitration and nitro-reduction were postulated as the primary reaction pathways of DNAN photolysis under UV-C ($\lambda \sim 254$ nm) irradiation in this experimental system. 2-ANAN had a concentration of ~ 20 µM when 50% of the DNAN was transformed (Fig. 4.3.5b). After the concentration of DNAN was lower than 100 µM, the transformation of 2-ANAN outpaced its production, causing the decrease of 2-ANAN concentration after about 25 h of reaction. Compared with the negligible production of nitrite that was observed under UV-A ($\lambda \sim 350$ nm) irradiation, nitrite and 2-ANAN shared the same trend of production and consumption under UV-C ($\lambda \sim 254$ nm) irradiation (Fig. 4.3.5b),

indicating that denitration may have been the dominant reaction. Nitrite and nitrate may have both contributed to photosensitization during the early stage of DNAN photolysis (~ 50% of DNAN conversion). However, we hypothesize that nitrite produced by denitration was subsequently consumed by nitration of nitroaromatic compounds and by oxidation to nitrate at the later stages of DNAN photolysis. As the concentration of nitrite decreased, the concentration of nitrate increased and reached ~ 40 μM after 98% of DNAN was consumed. Nitrite, nitrate, and DNP present at the end of the experiment accounted for only ~ 60% of the total N from the initial DNAN, indicating the presence of other undetected N-containing products (Rao et al., 2013).
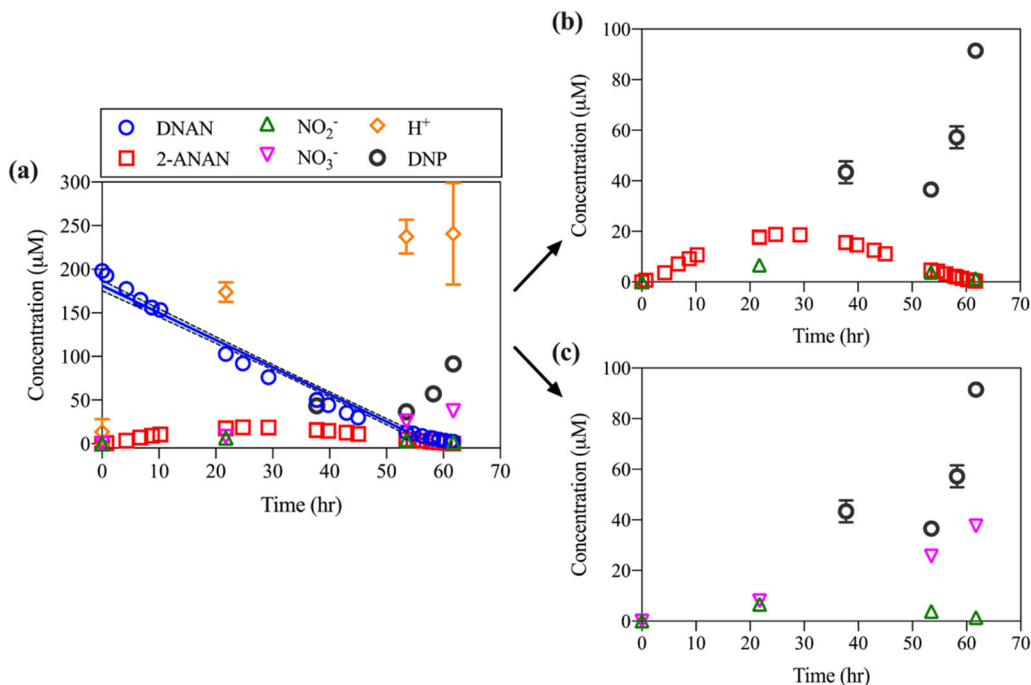
Fig. 4.3.5. (a) Concentrations (μM) of DNAN (blue circles), DNP (bold black circles), 2-ANAN (red squares), nitrite (green triangles), nitrate (purple inverted triangles), and H$^+$ (yellow diamonds) verses time during photo-degradation of DNAN under UV-C ($\lambda \sim 254$ nm) irradiation. Best-fit solid line (blue) shows a zero-order kinetic description of DNAN consumption. Dashed lines (black) represent 95% confidence intervals around the best-fit solid lines. (b) DNP, 2-ANAN and nitrite concentrations. (c) DNP, nitrite, and nitrate concentrations. Uncertainties represent ± _one standard deviation from the combination of duplicate batch experiments. Some error bars are smaller than the symbols.

The increase in H+ may have been caused by dissociation of DNP (pKa ~ 4.0) and photosensitization of NO$_2^•$ in water (Eq. (9)). The final concentration of H$^+$ (as H$_3$O$^+$) in solution was 250 μM (pH ~ 3.6), which equaled 1.25 times the initial concentration of the reactant DNAN (200 μM) and is higher than the pK$_a$ of DNP, indicating an additional source of protons. Nitro-reduction of DNAN to 2-ANAN stopped after 50% of DNAN was transformed, which likely resulted in an increase of the H$_3$O$^+$ concentration during the late stage of DNAN photolysis.

In contrast to the normal ^{13}C and inverse ^{15}N isotopic fractionations observed in DNAN during photolysis reactions under UV-A ($\lambda \sim 350$ nm) irradiation, inverse ^{13}C fractionation and normal ^{15}N fractionation were observed under UV-C ($\lambda \sim 254$ nm) irradiation (Fig. 4.3.6). ^{15}N

may have been enriched in DNAN by denitration and nitro-reduction pathways under UV-C ($\lambda \sim$ 254 nm) irradiation. When exposed to UV-C ($\lambda \sim$ 254 nm) light, it appears that DNAN having isotopically light nitro group(s) ($-^{14}NO_2$) may have been preferentially excited and accumulated in its triplet excited state ($^3DNAN^*$). Instead of playing a role of photosensitizer, $^3DNAN^*$ was likely further de-nitrated and potentially contributed to nitrite and anisole radical formation.

To rationalize the observed isotopic fractionations under UV-C ($\lambda \sim$ 254 nm) irradiation, we speculate that nitrite/nitrite radicals with isotopically light N ($^{14}NO_2^-$ /$^{14}NO_2^\bullet$) preferentially serve as primary photosensitizers to accelerate the generation of hydroxyl radicals for further photooxidation reactions; this would result in normal N isotopic fractionation. However, to explain the inverse C isotopic fractionation, we speculate that nitrite/nitrite radicals with isotopically heavy N ($^{15}NO_2^-$ /$^{15}NO_2^\bullet$) preferentially attack anisole radicals having isotopically light C (^{12}C) through a nitration pathway, which leads to enrichments of ^{12}C and ^{15}N in the ground state DNAN remaining in solution (Zewail, 2000, 1988; Buchachenko, 2001). Moreover, we hypothesize that ground state DNAN should undergo nitro-reduction to 2-ANAN, which also would contribute to the normal N isotope fractionation in the residual DNAN (Hofstetter et al., 2008).
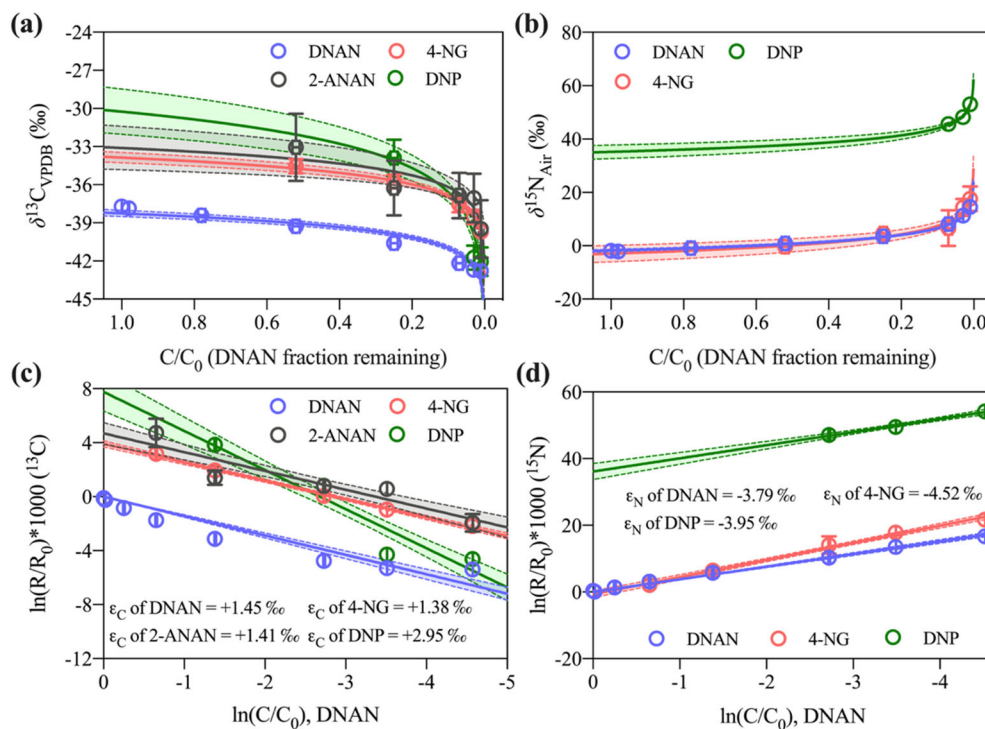
Fig. 4.3.6. Carbon and nitrogen isotope fractionations in DNAN and by-products during photodegradation of DNAN under UV-C ($\lambda \sim$ 254 nm) irradiation. Panels a and b show the evolution of $\delta^{13}C_{VPDB}$ (‰) and $\delta^{15}N_{Air}$ (‰) values as a function of DNAN fraction remaining, C/C$_0$. Panels c and d show carbon and nitrogen isotope enrichments versus the natural log of remaining DNAN in experimental systems. The best-fit lines are based on non-linear regression as described in Eq. (5) (Panels a and b) and a simple linear regression as described in Eq. (6) (Panels c and d). Solid lines represent the best-fit lines with the bulk ^{13}C and ^{15}N enrichment factors. Dashed lines represent 95% confidence intervals around the best-fit solid lines. Uncertainties in isotopic measurements represent ± one standard deviation from the combination of duplicate batch experiments and triplicate measurements for each sample. Some error bars are smaller than the symbols.
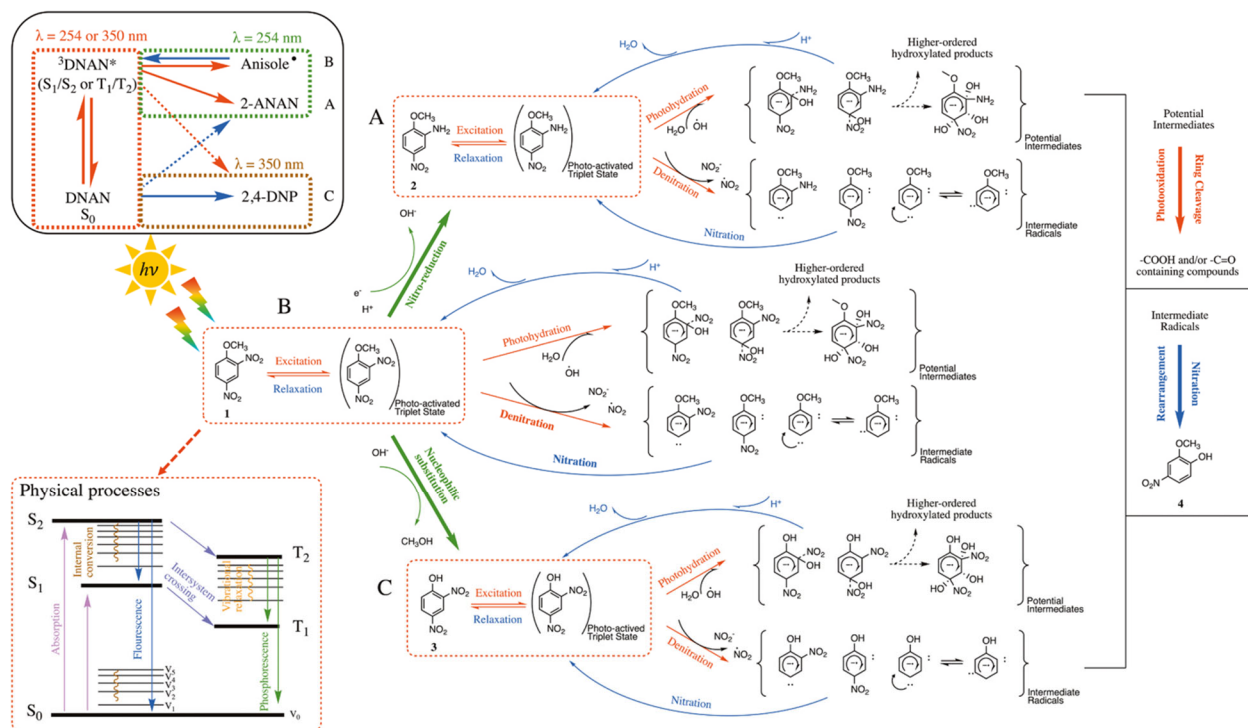
Scheme 4.3.1. Proposed pathways of photolysis of DNAN under UV-A ($\lambda \sim 350$ nm) and UV-C ($\lambda \sim 254$ nm) irradiation. The overall photolysis mechanisms are summarized in the black box. Physical processes under UV-A ($\lambda \sim 350$ nm) and UV-C ($\lambda \sim 254$ nm) irradiation are shown in dashed red boxes. Red arrows represent both physical processes and chemical reactions under UV irradiation. Blue arrows represent either physical processes or chemical reactions in the non-irradiated reservoir. Green arrows represent the chemical reactions that may have occurred both under UV irradiation and in the non-irradiated reservoir. 1: DNAN and 2: 2-ANAN were identified by HPLC; 1: DNAN, 2: 2-ANAN, 3: DNP, and 4: 4-NG were identified by GC-qMS/-IRMS. Panels A, B and C represent the proposed pathways of 2-ANAN, DNAN and DNP, respectively. All the proposed intermediates and radicals, whether detected or not, are consistent with previous reports (Qu et al., 2013; Foote, 1968; Liu et al., 2020). Note: For photo-dehydration and nitro-reduction, DNP dissociation and photocatalysis of nitrite are proposed to be sources of protons, supporting the production of H_2O or OH^-, respectively. Electrons generated from photocatalysis of nitrite (Table 4.3.1, A4) may contribute to the reduction of nitro groups to amino groups (Eq. 4.3.8).

4.3.3.3. Photolysis pathways

Based on our observations of reaction kinetics for DNAN, together with the C and N isotopic fractionations observed in DNAN and its reaction products, we propose there are at least three primary reaction pathways associated with DNAN photodegradation under UV-A ($\lambda \sim 350$ nm) and UV-C ($\lambda \sim 254$ nm) irradiation. These are summarized in Scheme 4.3.1. For photodegradation of DNAN under UV-A ($\lambda \sim 350$ nm) irradiation, DNAN appeared to have experienced mainly indirect photolysis pathways, being transformed to DNP through a SN_1 mechanism. For the photodegradation of DNAN under UV-C ($\lambda \sim 254$ nm) irradiation, DNAN apparently experienced both direct and indirect photolysis pathways, being transformed through denitration and nitro-reduction primarily during irradiation, as well as being transformed to DNP via nucleophilic substitution (possibly during residence in the fluid reservoir outside the UV

Table 4.3.1. Proposed primary reactions involved in the circulation between nitrite, nitrate, and reactive oxygen species in solutions under UV-irradiated and dark conditions.

No.	Reactions	k or Φ	Refs
A1	$NO_2^- + h\nu \rightarrow NO_2^{-*}$		(Mack and Bolton, 1999)
A2	$NO_2^{-*} \rightarrow NO^{\bullet} + O^{\bullet-}$	$\Phi_{OH,300} = 6.7$ $(\pm 0.9)\%$	(Pang et al., 2019)
A3	$O^{\bullet-} + H_2O \rightarrow {}^{\bullet}OH + OH^-$	1.7×10^6 M^{-1} s^{-1}	(Mack and Bolton, 1999; Xu et al., 2019)
A4	$NO_2^{-*} \rightarrow NO_2^{\bullet} + e_{aq}^-$	$\Phi < 10^{-3}$	(Pang et al., 2019)
A5	$HNO_2 + h\nu \rightarrow NO^{\bullet} + {}^{\bullet}OH$		(Xu et al., 2019)
B1	$NO_3^- + h\nu \rightarrow NO_3^{-*}$		(Mack and Bolton, 1999)
B2	$NO_3^{-*} \rightarrow NO_2^- + O (3p)$		(Mack and Bolton, 1999; Dhar et al., 1934)
B3	$NO_3^{-*} \rightarrow NO_2^{\bullet} + O^{\bullet-}$		(Mack and Bolton, 1999; Dhar et al., 1934)
C1	$NO^{\bullet} + {}^{\bullet}OH \rightarrow HNO_2$	1.0×10^{10} M^{-1} s^{-1}	(Xu et al., 2019)
C2	$NO_2^- + {}^{\bullet}OH \rightarrow NO_2^{\bullet} + OH^-$	1.0×10^{10} M^{-1} s^{-1}	(Xu et al., 2019)
C3	$NO_2^{\bullet} + {}^{\bullet}OH \rightarrow HO_2NO$	1.3×10^9 M^{-1} s^{-1}	(Xu et al., 2019; Dhar et al., 1934)
C4	$HO_2NO \rightarrow NO_3^- + H^+$	1.4 s^{-1}	(Xu et al., 2019; Dhar et al., 1934)

Table 4.3.2. Carbon and nitrogen isotope enrichment factors in DNAN and products as derived from eqns. 4.3.4 and 4.3.5, respectively.

	DNAN		4-NG		DNP		2-ANAN	
	ε_C (‰)	ε_N (‰)	ε_C (‰)	ε_N (‰)	ε_C (‰)	ε_N (‰)	ε_C (‰)	ε_N (‰)
254 nm	$+1.45 \pm 0.05$	-3.79 ± 0.08	$+1.38 \pm 0.04$	-4.52 ± 0.17	$+2.95 \pm 0.21$	-3.95 ± 0.31	$+1.41 \pm 0.13$	–
350 nm	-3.34 ± 0.03	$+12.30 \pm 0.09$	–	–	-2.87 ± 0.05	$+1.12 \pm 0.30$	–	–
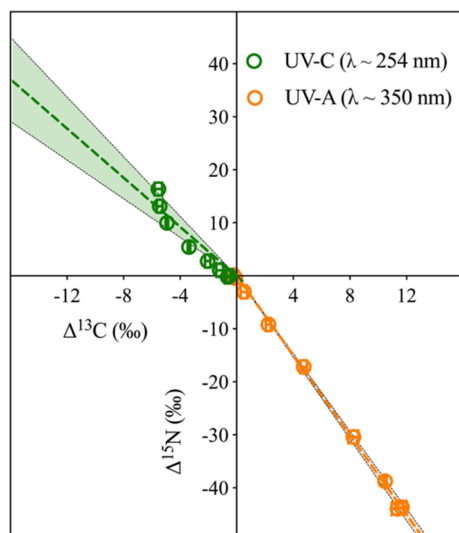
Fig. 4.3.7. $\Delta^{13}C$ (‰) and $\Delta^{15}N$ (‰) in DNAN during photolysis by UV light with nominal wavelengths of 350 nm and 254 nm, respectively (Eq. 4.3.6). Initial DNAN isotopic composition: $\delta^{13}C_{VPDB} = -37.21$ ‰ and $\delta^{15}N_{Air} = -2.45$ ‰. $\Lambda^{N/C}$ of DNAN under UV-C ($\lambda \sim 254$ nm) irradiation was -2.87 ± 0.29; $\Lambda^{N/C}$ of DNAN under UV-A ($\lambda \sim 350$ nm) irradiation was -3.63 ± 0.03. Dashed gray lines represent 95% confidence intervals of the linear regression. Some error bars are smaller than the symbols.

reactor) (Scheme 4.3.1). Nitrite and nitrate can be considered as photosensitizers that produce both hydroxyl radicals and •OH sinks in aqueous solutions. Nitrite, nitrate, reactive oxygen species (ROS) and reactive nitrogen species (RNS) all likely play important roles in DNAN photocatalysis in the recirculation reactor. As listed in Table 4.3.1, the A series of reactions indicates that nitrite plays a role of photosensitizer, generating ROS (e.g., •O⁻, •OH) and releasing electrons. The role of nitrate as photosensitizer is shown in the B series of reactions, producing the triplet state of oxygen. Both nitrite and nitrate can be a sink of ROS and RNS according to the C series of reactions. Nitrate would not be effective in hydroxyl radical production under UV-A ($\lambda \sim 350$ nm) irradiation because of a diffusion control in the aqueous solution (Table 4.3.1, C3 and C4) (Xu et al., 2019; Dhar et al., 1934). Hydroxyl radical produced in this photolysis system were probably consumed by production of nitrous acid or nitrite radicals (Table 4.3.1, C1 and C2). Thus, nitrite may be the primary photosensitizer for DNAN photocatalysis under UV-A ($\lambda \sim 350$ nm) irradiation, with limited production of NO˙ and ˙OH (Table 4.3.1, C1). This could account for the observed negligible increase in nitrite concentration and the delayed increase in nitrate concentration in our experimental system. Under UV irradiation with wavelengths < 300 nm, nitrite and nitrate may work together as photosensitizers. Nitrite may be produced through reaction of NO$_2$˙ and ˙OH generated from the triplet excited state of nitrate (Xu et al., 2019; Dhar et al., 1934). As the evolution of DNAN photocatalysis proceeded, the consumption of ROS and RNS apparently proceeded faster for nitroaromatic degradation than for nitrite production. To this end, we observed an increase in the concentration of nitrite at the early stage of DNAN photocatalysis under UV-C ($\lambda \sim 254$ nm) irradiation, followed by the consumption of nitrite and a delayed increase in nitrate concentration.

4.3.3.4. Environmental implications

The present study yields useful insights into UV-induced photolysis and photocatalysis mechanisms of DNAN through measurement of C and N isotope fractionations (Fig. 4.3.7). These results provide evidence of the fate of DNAN under UV irradiation in both natural environments (e.g., during UV-A-irradiated aerobic surface waters) and industrial treatment plants (e.g., during UV-C irradiation of wastewater). The C and N isotopic enrichment factors in DNAN and its photolysis products reported here expand the isotopic database and may be diagnostic of natural attenuation of DNAN in field studies (Table 4.3.2).

By conducting DNAN photolysis experiments in a recirculation system with both light (in the UV cell) and dark (in the reservoir) phases, we discovered that DNAN, and potentially its photolysis products DNP and 2-ANAN, can perform not only as photosensitizers like other dissolved organic matter, but apparently may also experience product-to-parent reversion. These observations are significant for understanding the fate of DNAN in natural environments as well as to optimize remediation strategies. Future work may target more substituted nitroanisoles or dinitroanisoles to better understand the spin sensitivity of kinetic isotope effects. In addition, the effects of other environmental factors, such as the presence of transition metal ions, halogens, and natural organic matter, should be examined during DNAN photolysis/ photocatalysis.

4.4. Carbon and nitrogen isotope fractionation during UV-A and UV-C photo-transformation of NTO

4.4.1. Introduction

3-nitro-1,2,4-triazol-5-one (NTO), as a high-energy material, is being used in military and industrial applications, including (i) as a substitute for ammonium perchlorate or ammonium nitrate in solid rocket propellants; (ii) as a burning rate modifier for composite propellants [1]; (iii) as a replacement for RDX and HMX in composite solid propellants in IMX-101, IMX-104 and PAX-48 [2, 3]; and (iv) for improving the performance of gun propellant [4]. In contrast with the other high-energy nitro-materials being used in propellants, i.e., 2,4-dinitroanisole (DNAN), nitroguanidine (NQ), 1,3,5-trinitro-1,3,5-triazine (RDX), and 2,4,6-trinitrotoluene (TNT), NTO exhibits the properties of acidity (pK_{a1} ~ 3.7), polarity, and a higher aqueous solubility (~16.6 g/L at 25 °C). These physical and chemical properties allow NTO to occur at relatively high concentrations in natural waters, potentially threatening ecosystems and human health.

In aqueous environments, photolysis and photocatalysis may contribute substantially to the natural attenuation of NTO. Additionally, a cost-effective and environmentally benign method for photocatalytic destruction of NTO would be useful for wastewater treatment. Previous studies of NTO photodegradation revealed an initial step of photo-denitration (Halasz et al., 2018; Becher et al., 2019). However, the conventional approach of tracking the concentrations of NTO and its products during photolytic transformation is not fully diagnostic of the complex reactions that may occur under such conditions. Compound-specific isotope analysis of residual NTO during photodegradation could help to further decipher its photolytic degradation mechanism. Therefore, in this study we employed a new derivatization/GC-IRMS method for the compound-specific isotope analysis of NTO (Wang et al., 2021c; see Section 2.1 of this report) to examine the kinetics and the carbon and nitrogen isotope effects during photodegradation of NTO under UV-C (~254 nm) and UV-A (~350 nm) irradiation, in pure aqueous solution and in NaCl solution.

4.4.2. Materials and Methods

4.4.2.1. Chemicals

Chemicals used in this study are described in Section 2.2 of this report.

4.4.2.2. Photolysis experiments

Photolysis experiments with NTO were done with a Rayonet RPR-200 photoreactor (Southern New England Ultraviolet Company, Branford, CT). Details of the photoreactor experimental setup are given in Wang et al. (2021a) and in Section 4.3 of this report.

4.4.2.3. Chemical analysis

Analytical methods for monitoring the concentrations of NTO and its common transformation products (e.g., 3-hydroxyamino-1,2,4-triazol-5-one (HTO), and 3-amino-1,2,4-triazol-5-one (ATO), nitrite, nitrate, ammonium) are described in Fuller et al., 2020.

4.4.2.4. Analysis of C and N isotope ratios in NTO

The methods used for isotopic analyses of C and N in NTO are described in Section 2.2 of this report.

4.4.2.5. Isotope data evaluation

Isotopic data were evaluated by the same methods described in Section 4.3.2.5 of this report.

4.4.3. Results and discussion
4.4.3.1. Kinetics of NTO photolysis

UV-C (~254 nm) irradiated photolysis of NTO in a pure aqueous solution with $[NTO]_0 = 800$ μM yielded a one-stage 0.5^{th}-order kinetic reaction (Figure 4.4.1a). The determined rate constant was 0.56 $μM^{0.5}$/hr; the calculated half-life of NTO during UV-C irradiated photolysis was 28.4 hr. 3-amino-1,2,4-triazol-5-one (ATO), as a reduction product of NTO, was also measured during the reaction. ATO accumulated in the photolysis samples before the NTO half-life was reached, and its concentration subsequently decreased. The quantity of ATO detected was only a small fraction (21.2 %) of the corresponding loss of NTO, indicating that the product ATO was also degrading and/or that other initial undetected products were formed in addition to ATO. Nitrite, nitrate, and ammonium products increased throughout the irradiation. Ammonium (NH_4^+) was likely released as a product of terminated $^{\bullet}NH_2$ from photo-deamination of ATO. Photo-nitration of NH_4^+/NH_3 (aq) may explain the relatively low production rates of nitrite and nitrate. Urazole was not reported in this study due to lack of a urazole standard in the HPLC calibration, but its production was noted in a previous report (Becher et al., 2019). No nitroguanidine (NQ) or nitrosoguanidine was detected in this work.

A two-stage 0.5^{th}-order kinetic reaction was derived for the photolysis of NTO under UV-A (~350 nm) irradiation (Figure 4.4.1b). A rate constant of 0.25 $μM^{0.5}$/hr was modeled for the first stage of the 0.5^{th}-order kinetic reaction under UV-A, with a half-life of 64.72 hr. For the second stage of the 0.5^{th}-order kinetic reaction, we observed a rate constant of 0.10 $μM^{0.5}$/hr with a half-life of 111.92 hr. Unlike the observations under UV-C (~254 nm) irradiation, ATO was not detected during the UV-A experiment. Ammonium was a more abundant product in the UV-A experiment, which may indicate that $ATO^{\bullet}/ ATO^{\bullet-}$ decomposed to $^{\bullet}NH_2$ and urazole, and/or $^{\bullet}NH_2$ was a more competitive scavenger than urazole for deactivating the ROS.

We consider the sum of nitrite and nitrate produced in the NTO photolysis reactors as NO_x ions. The maximum concentrations of NO_x ions in the UV-C (~254 nm) and UV-A (~350 nm) reactions were 58.18 μM and 63.69 μM, respectively. With over 90% of NTO conversion, the production of NO_x ions reached a plateau of ~60 μM, which equaled ~2% of N from the initial NTO. In contrast, the maximum accumulated ammonium comprised ~32% and ~48% of N from initial NTO in the UV-C (~254 nm) and UV-A (~350 nm) reactions, respectively. The undetected N-bearing species were most likely urazole and/or smaller C-N containing molecules (e.g., hydrocyanic acid).

In NaCl-bearing solution, with equimolar initial concentrations (both 800 μM) of NTO and NaCl, the disappearance of NTO under UV-C irradiation followed a half-order kinetic rate law (Figure 4.4.2a). The rate constant was 0.30 $μM^{0.5}$ hr^{-1} and the calculated half-life of NTO was 53.6 hr. The overall reaction rate of NTO in the NaCl-bearing solution was approximately half that in pure water under UV-C irradiation. Nitrite, nitrate, and ammonium products accumulated throughout the irradiation (Figure 4.4.2b). There was no ATO product detected upon NTO photo-transformation in the NaCl solution under UV-C irradiation, in contrast to the observation of ATO being produced in the pure aqueous NTO solution (i.e., NaCl-free solution). Urazole, nitroguanidine, and nitrosoguanidine products also were not detected in the NaCl-bearing solution.
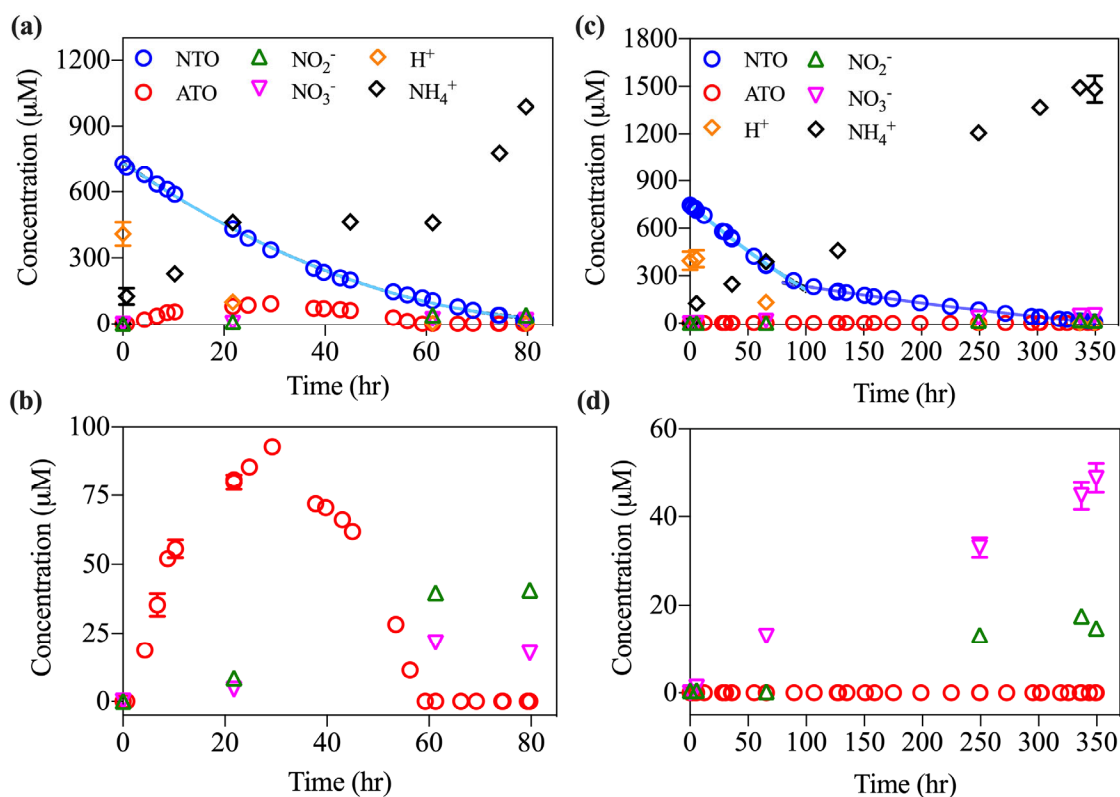
Figure 4.4.1. Concentrations of NTO (blue circles), H^+ (orange diamonds), and NTO photolysis products ATO (red circles), ammonium (black diamonds), nitrite (green triangles) and nitrate (purple triangles) as a function of time under UV-C ($\lambda \sim 254$ nm) (panel (a) and (b)) and UV-A ($\lambda \sim 350$ nm) (panel (c) and (d)) irradiations. The modeled half-order kinetics of NTO are shown as blue solid lines. Error bars represent $\pm$ one standard deviation from duplicate batch experiments. Some error bars are smaller than the symbols.

The maximum concentrations of ΣNO_x^- ions (i.e., $NO_2^- + NO_3^-$) were 58.2 μM, 79.1 μM and 63.7 μM, respectively, in NaCl-free and NaCl-bearing solutions under UV-C irradiation, and in NaCl-free solution under UV-A irradiation. The most abundant NO_x^- ion produced from UV-C photolysis of NTO in NaCl-free and NaCl-bearing solutions was NO_2^-, while that produced from photolysis of NTO under UV-A irradiation was NO_3^-. With over 90% of NTO conversion, the production of ΣNO_x^- ions reached maximum concentrations of ~60 μM to ~80 μM, which was equivalent to only ~2% to ~2.5% of the initial 800 mM NTO concentration. In contrast, ammonium product reached a maximum of ~32% to ~48% of the initial NTO concentration in all three experiments under both UV-C and UV-A irradiations. This N mass balance indicates that substantial fractions of N-bearing species were either lost to the gas phase (e.g., N_2, N_2O, or NH_3) or were aqueous N species that were not detected in this study.

4.4.3.2. Carbon and nitrogen isotope effects in NTO during phototransformation

Nitrogen isotope fractionation in NTO occurred with similar bulk ^{15}N enrichment factors (ε_N) of -6.64 $\pm$ 0.51 ‰ and -7.87 $\pm$ 0.40 ‰, respectively, in NaCl-free and NaCl-bearing NTO

solutions under UV-C irradiation, and with ε_N = -6.58 ± 0.39 ‰ in NaCl-free NTO solution under UV-A irradiation. These values of the N isotope enrichment assume a homogeneous initial
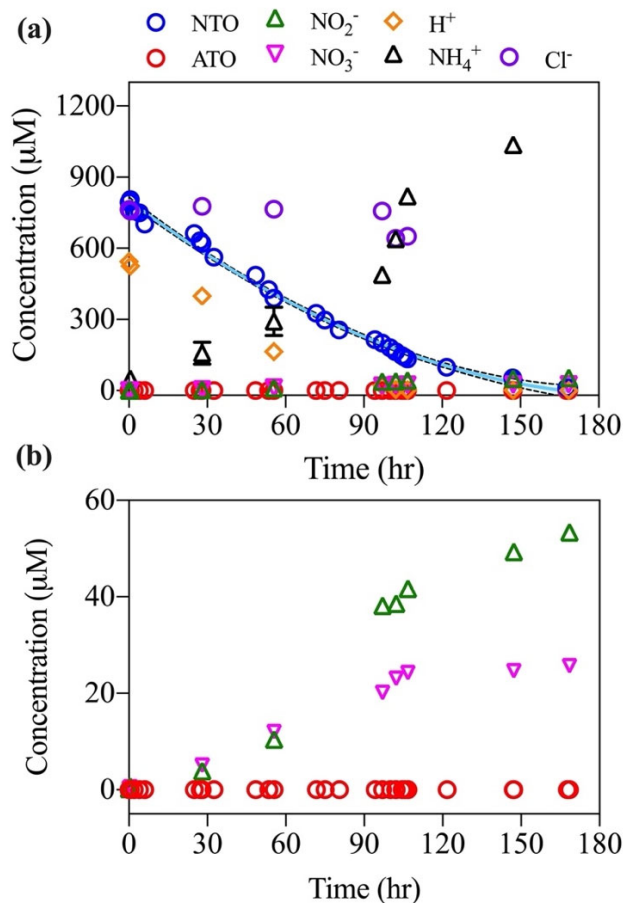
Figure 4.4.2. Concentrations of [NTO] (blue circle), [H⁺] (i.e., hydronium) (orange diamond), [Cl⁻] (purple circle), and product species ATO (red circle), NH₄⁺ (black diamond), NO₂⁻ (green triangle) and NO₃⁻ (purple triangle) vs. time under UV-C (λ ~ 254 nm) irradiation in a NaCl-bearing solution ([NTO]₀ = [NaCl]₀ = 800 μM). The modeled half-order kinetics of NTO are shown as blue solid lines, with 95% confidence limits shown as black dashed lines. Uncertainties represent ± one standard deviation of duplicate batch experiments. Some error bars are smaller than the symbols.

intramolecular nitrogen isotope composition because there is no information available on position-specific nitrogen isotope ratios for the NTO used in this study. Based on the magnitude and sign of the measured ε_N values, we infer that the initial rate-determining step for NTO photo-transformation must have involved reaction at a nitrogen site, either a N-C bond (i.e., denitration), a N-O bond (i.e., nitro-reduction), or a N-H bond (deprotonation). A previous study [36] demonstrated that deprotonation of aromatic amines occurs more rapidly for the ^{14}N-enriched isotopologues, therefore a rate-limiting step involving NTO deprotonation is consistent with the observed normal N isotope effect. The presence of ATO in NaCl-free NTO solution under UV-C irradiation also indicates possible contribution of nitro-reduction to the bulk ^{15}N enrichment factors (ε_N). However, ATO was not detected in NaCl-free NTO solution under UV-A irradiation, nor in NaCl-bearing NTO solution under UV-C irradiation.
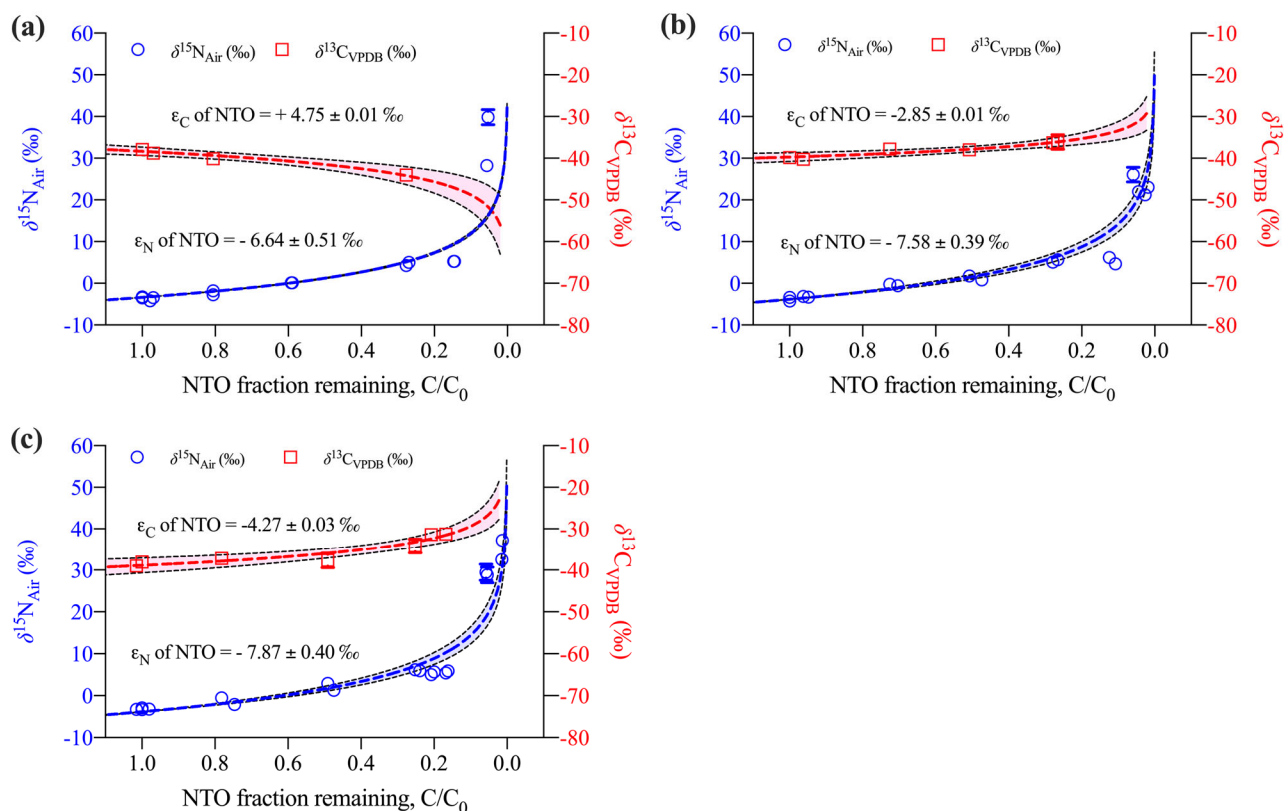
Figure 4.4.3. Carbon (red square, right Y axis) and nitrogen (blue circle, left Y axis) isotope fractionation in NTO during UV-C (panel a) and UV-A (panel b) irradiation in NaCl-free solution, as well as during UV-C irradiation in NaCl-bearing solution (panel c). The enrichment factors were calculated assuming Rayleigh-type fractionation (eq 2). The best-fit models are shown as red dashed lines (for δ^{13}C) and blue dashed lines (for δ^{15}N) within 95% confidence intervals shadowed using corresponding colors. Uncertainties in isotopic measurements represent $\pm$ one standard deviation from the combination of duplicate batch experiments and triplicate measurements for each sample. Some error bars are smaller than the symbols.

In contrast to the normal nitrogen isotope fractionation ($\varepsilon_N < 1$) that we observed under both UV-A and UV-C irradiation, the sign of carbon isotope fractionation changed from $\varepsilon_C = +4.75 \pm 0.01$ ‰ in NaCl-free NTO solution to $\varepsilon_C = -4.27 \pm 0.03$ ‰ in NaCl-bearing NTO solution under UV-C irradiation (Fig. 4.4.4). In NaCl-free NTO solution under UV-A irradiation, we measured a smaller value of $\varepsilon_C = -2.85 \pm 0.01$ ‰. A previous study of NTO degradation in Fe(II)-bearing mineral reduction systems showed that NTO experienced a secondary C isotope fractionation with an ε_C value of -3.2 ± 0.3 ‰, whereas a larger ε_C value of -6.0 ± 1.5 ‰ in NTO was observed in Fenton-like experiments in which both reductive and oxidative (reaction with hydroxyl radical) processes occurred (Arnold et al., 2021). Our observations in the present study imply that, under UV-A irradiation, NTO experienced a primary nitrogen isotope fractionation ($\varepsilon_N = -6.58 \pm 0.39$ ‰) but possibly a secondary carbon isotope fractionation ($\varepsilon_C = -2.85 \pm 0.01$ ‰). These values are consistent with deprotonation as the initial rate-determining step of

NTO photo-transformation in NaCl-free NTO solution under UV-A irradiation. In contrast, NTO apparently experienced both primary nitrogen and carbon isotope fractionations that involved N-C bond cleavage/formation, via denitration-renitration, in both NaCl-free and NaCl-bearing NTO solutions under UV-C irradiation. The sign of carbon isotope fractionation under UV-C irradiation changed from inverse ($\varepsilon_C > 1$) in NaCl-free solution to normal ($\varepsilon_C < 1$) in NaCl-bearing solution, indicating an important role of reactive chlorine species (RCS) in the NTO denitration-renitration pathway, as discussed below.
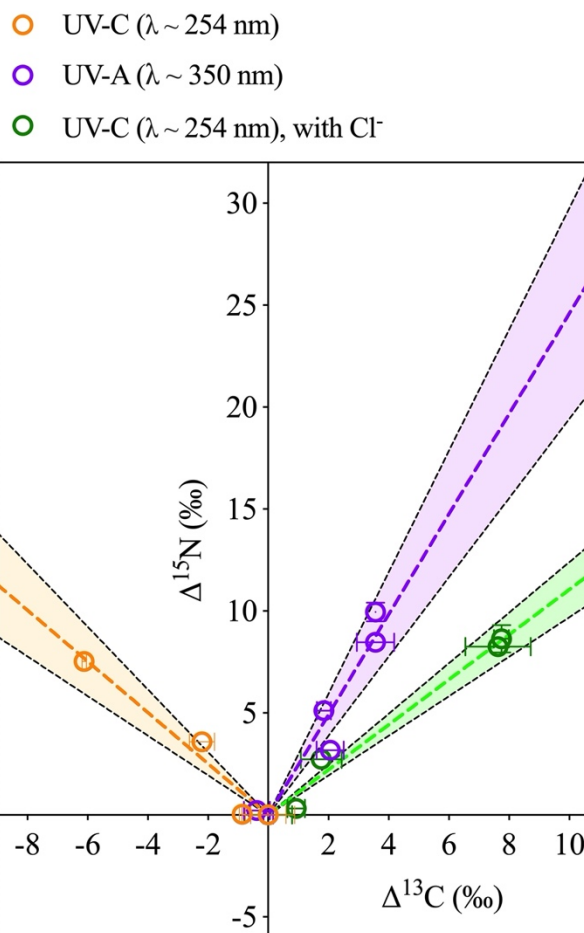
Figure 4.4.4. Diagram showing $\Delta^{13}C$ (‰) vs. $\Delta^{15}N$ (‰) values of NTO during photolysis under UV-A and UV-C irradiation in an NaCl-free ([NTO]$_0$ = 800 µM) solution, and under UV-C irradiation in a NaCl-bearing ([NTO]$_0$ = [NaCl]$_0$ = 800 µM) solution, respectively (eq 5). Initial NTO isotopic composition: $\delta^{13}C_{VPDB} = -38.83 \pm 0.16$ ‰ and $\delta^{15}N_{Air} = -3.39 \pm 0.14$ ‰. The $\Lambda^{\frac{N}{C}}$ value for NTO in NaCl-free solution under UV-A irradiation was $+2.46 \pm 0.20$; that under UV-C ($\lambda \sim 254$ nm) irradiation was -1.25 ± 0.10; in contrast the $\Lambda^{\frac{N}{C}}$ value of NTO in NaCl-bearing solution under UV-C ($\lambda \sim 254$ nm) irradiation was $+1.11 \pm 0.05$. Dashed gray lines represent 95% confidence intervals of the linear regression. Some error bars are smaller than the symbols.

.

4.4.3.3 Role of reactive chlorine species in the photo-transformation of NTO under UV-C irradiation

The contrasting isotope effects observed between the three sets of photo-transformation experiments in this study are best considered in relation to the UV absorption characteristics of NTO, NaCl, and their photo-transformation products. The proposed primary chain reactions are listed in Table 4.4.1 and schemed in Scheme 4.4.1. The maximum molar absorption coefficient of NTO falls in the same spectral range under UV-A irradiation (~320 nm) as that of nitrite (Moores et al., 2020a; Zuo and Deng, 1998) which indicates that denitration may have been an important photo-transformation pathway of NTO under UV-A irradiation, followed by a propagation stage involving chain reactions of nitrite/nitrite radicals (Table 4.4.1 A and C, Scheme 4.4.1B). In this case, re-nitration of NTO would have been limited due to the photo-oxidation that consumed nitrite/nitrite radicals, leading to the elimination of subsequent photo-transformation pathway(s) like nitro-reduction from NTO to ATO. In the contrast, the minimum UV absorption coefficient of NTO falls in the UV-C spectral range at which the maximum UV absorption coefficient of nitrate coincides with a lower UV absorption coefficient of nitrite. Under UV-C irradiation in NaCl-free solution, NTO may thus go through a denitration-renitration as its primary C-N bond associated photo-transformation pathway, whereby the nitrite radical ($NO_2^•$) acts as a scavenger of 1,2,4-triazol-5-one radical ($TO^•$) to produce NTO (i.e. renitration pathway) while nitrate radical ($NO_3^•$) acts as a photo-oxidant to further produce ROS (Table 4.4.1 A and B, Scheme 4.4.1A). Under UV-C irradiation in NaCl-bearing solution, either the rate-limiting step in the photo-transformation of NTO was affected by the presence of RCS, which were not present in the experiment with NaCl-free solution, or perhaps the renitration pathway may have been blocked by RCS that performed the role of scavenger to deactivate $NO_2^•$ and $TO^•$ to prevent the renitration pathway. These differences in reaction pathway may explain the contrast in carbon isotope fractionation from inverse to normal in NaCl-free and NaCl-bearing solutions, respectively, under UV-C irradiation (Table 4.4.1 A and D, Scheme 4.4.1C). The potential presence of RCS can be inferred from the substantial UV-C absorption coefficient of dissolved NaCl that may have produced Cl radicals (in contrast to the negligible UV-A absorption by dissolved NaCl) and from previous studies on the production of chlorine atom precursors by nitrogen oxides (Oum et al., 1998; Peng et al., 2022: Hoffmann et al., 2019) even though we have not directly detected RCS in the present study.

Table 4.4.1. Proposed primary reactions involved in the circulation between reactive oxygen species (ROS), reactive nitrogen species (RNS) and reactive chlorine species (RCS) in solutions under dark and irradiation conditions. A: initiation stage chain reactions of the photo-transformation of NTO. B: propagation stage chain reactions of the photo-transformation of NTO in NaCl-free solution under UV-C irradiation. C: propagation stage chain reactions of the photo-transformation of NTO in NaCl-free solution under UV-A irradiation. D: propagation stage chain reactions of the photo-transformation of NTO in NaCl-bearing solution (μM: μM = 1:1) under UV-C irradiation.

No.	Reactions	k or Φ	Refs
A1	$NTO^- + h\nu \rightarrow NTO^{\bullet} + e_{aq}^-$		This study
A2	$NTO^{\bullet} \rightarrow TO^{\bullet} + NO_2^{\bullet}$		Becher et al., 2019; Halasz et al., 2018; this study
A3	$2NO_2^{\bullet} + H_2O \rightarrow NO_3^- + NO_3^- + 2H^+$		Mack and Bolton, 1999
B1	$NO_3^- + h\nu \rightarrow NO_3^{-}*$		Mack and Bolton, 1999; Krishnan and Guha, 1934
B2	$NO_3^{-}* \rightarrow NO_2^- + O(3p)$	$\Phi_{254} = 17\ \%$ (pH=11.7) $\Phi_{310} = 0.65 \pm 0.04\ \%$ (pH=5.6)	Mack and Bolton, 1999
B3	$O(3p) + NO_3^- \rightarrow NO_2^- + O_2$		Mack and Bolton, 1999; Dhar et al., 1934
B4	$NO_3^{-}* \rightarrow NO_2^{\bullet} + O^{\bullet-}$		Mack and Bolton, 1999; Dhar et al., 1934; Blough and Zepp, 1995; Mostofa et al., 2013
B5	$O^{\bullet-} + H_2O \rightarrow {}^{\bullet}OH + OH^-$	1.7×10^6 M^{-1}s^{-1}	Mack and Bolton, 1999; Xu et al., 2019
B6	$NO_2^{\bullet} + {}^{\bullet}OH \rightarrow HO_2NO$	1.3×10^9 M^{-1}s^{-1}	Dhar et al., 1934; Xu et al., 2019
B7	$TO^{\bullet} + NO_2^{\bullet} \rightarrow NTO^{\bullet} + e_{aq}^- \rightarrow NTO^-$		This study
C1	$NO_2^- + h\nu \rightarrow NO_2^{-}*$		Mack and Bolton, 1999; Krishnan and Guha, 1934
C2	$NO_2^{-}* \rightarrow NO^{\bullet} + O^{\bullet-}$	$\Phi_{OH,300} = 6.7 \pm 0.9\ \%$	Mack and Bolton, 1999; Dhar et al., 1934; Blough and Zepp, 1995; Mostofa et al., 2013; Pang et al., 2019
C3	$NO_2^{-}* \rightarrow NO_2^{\bullet} + e_{aq}^-$	$\Phi < 10^{-3}\ \%$	Buxton et al., 1988
C4	${}^{\bullet}OH + TO^{\bullet} \rightarrow Urazole^{\bullet}$		Becher et al., 2019; Halasz et al., 2018, this study
D1	$NO_2^{\bullet} + Cl^- + h\nu \rightarrow ClONO^{\bullet} + e_{aq}^-$		Behnke et al., 1997; Leu, 1984; this study
D2	$ClONO^{\bullet} + e_{aq}^- + h\nu \rightarrow Cl^{\bullet} + NO_2^-$		Molina and Molina, 1977

D3	$ClONO^{\bullet} + h\nu \rightarrow ClO^{\bullet} + NO^{\bullet}$		Molina and Molina, 1977
D4	$ClO^{\bullet} + \mathbf{O(3p)} \rightarrow Cl^{\bullet} + O_2$		Wayne et al., 1995; Ellis et al., 1971
D5	$ClO^- + \mathbf{O(3p)} + h\nu \rightarrow Cl^{\bullet} + O_2^{\bullet-}$		Ellis et al., 1971; Bielski et al., 1985
D6	$O_2^{\bullet-} + H^+ \rightarrow HO_2^{\bullet}$	$7.2 \times 10^{10}\ M^{-1}s^{-1}$	Xu et al., 2019; Bielski et al., 1985
D7	$HO_2^{\bullet} + O_2^{\bullet-} + H^+ \rightarrow H_2O_2 + O_2$	$< 2\ M^{-1}s^{-1}$	Xu et al., 2019; Bielski et al., 1985
D8	$HO_2^{\bullet} + HO_2^{\bullet} \rightarrow H_2O_2 + O_2$	$< 2\ M^{-1}s^{-1}$	Xu et al., 2019; Bielski et al., 1985
D9	$\mathbf{O(3p)} + H_2O \rightarrow H_2O_2$		Oum et al., 1998; Bielski et al., 1985
D10	$H_2O_2 + h\nu \rightarrow 2^{\bullet}\mathbf{OH}$		Oum et al., 1998; Pang et al., 2019; Bielski et al., 1985
D11	$^{\bullet}\mathbf{OH} + Cl^- \rightarrow Cl^{\bullet} + OH^-$		Oum et al., 1998; Pang et al., 2019
D12	$^{\bullet}\mathbf{OH} + Cl^- \rightarrow HOCl^- + e_{aq}^-$		Oum et al., 1998; Pang et al., 2019
D13	$Cl^{\bullet} + Cl^- + h\nu \rightarrow Cl_2^{\bullet-}$		Oum et al., 1998; Pang et al., 2019
D14	$ClNO_2 + H_2O \rightarrow 2H^+ + Cl^- + NO_2^-$		Hoffmann et al., 2019; Wayne et al., 1995
D15	$Cl^{\bullet} + TO^{\bullet} \rightarrow CTO$		This study
D16	$TO^{\bullet} + H^+ + e_{aq}^- \rightarrow TO$		This study
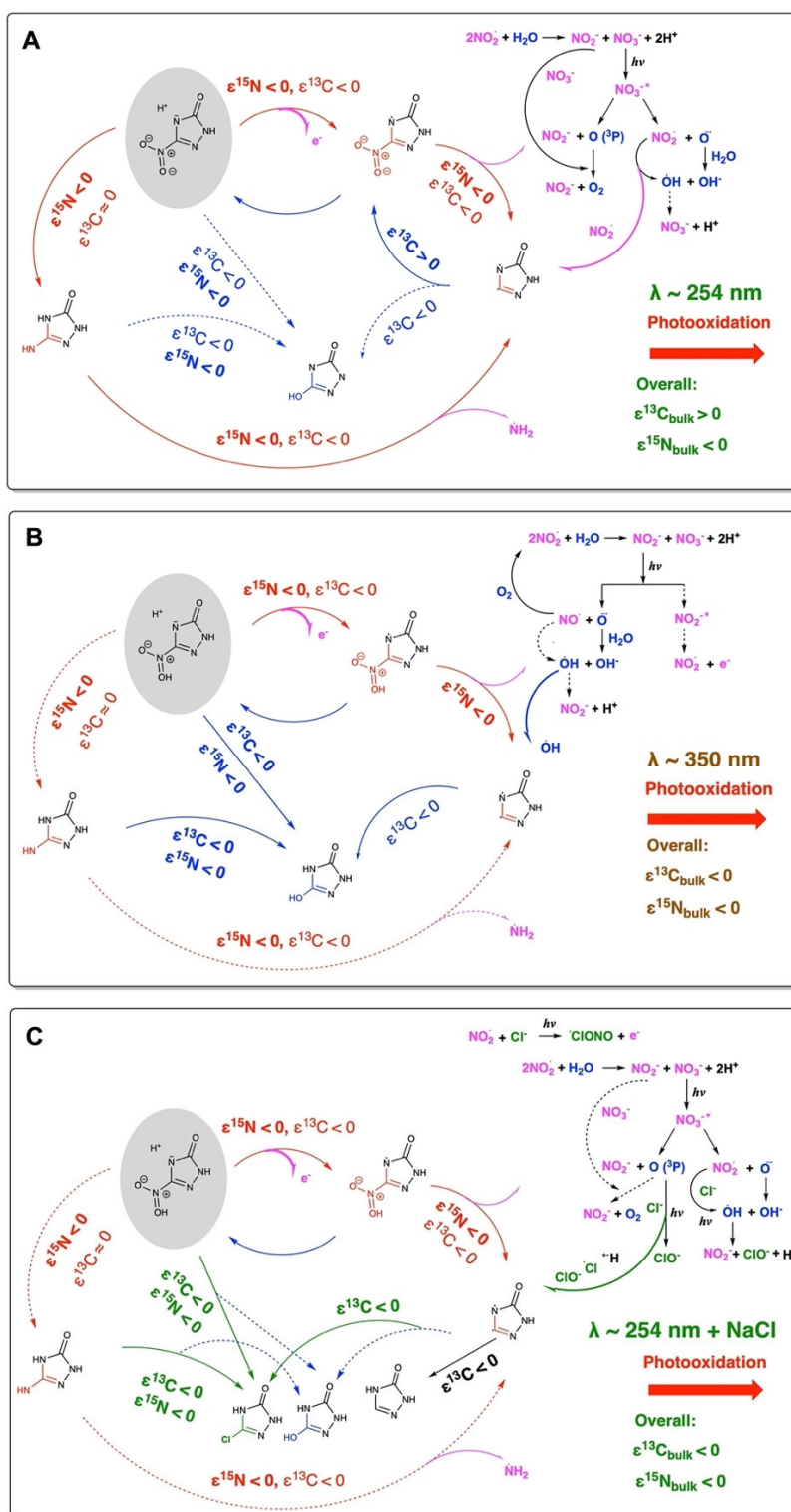
Scheme 4.4.1. Proposed pathways of photolysis of NTO under UV-C (Panel A) and UV-A (Panel B) irradiation in an NaCl-free ([NTO]$_0$ = 800 μM) solution, and under UV-C irradiation in a NaCl-bearing ([NTO]$_0$ = [NaCl]$_0$ = 800 μM) solution (Panel C), respectively.

4.4.4 Environmental Implications

Understanding the photo-transformation mechanisms of NTO in aqueous environments is of importance to both natural attenuation and engineered remediation for sites contaminated with insensitive munitions. There have been several studies of photo-degradation of NTO and IM composites that contain NTO (Halasz et al., 2018; Becher et al., 2019; Moores et al., 2020a, 2020b), and our data complement previous work by demonstrating the crucial roles of deprotonation and photo-nitro-reduction in the reaction propagation stages during NTO photolysis. Ammonia/ammonium radicals were the dominant RNS generated from the deamination of the NTO degradation product ATO. These radicals further experienced photo-oxidation to produce NO_x (i.e., nitrate, nitrate) radicals as a secondary source of ROS (e.g., hydroxyl radicals). NTO, as an acidic and polar nitroaromatic compound, exhibits similar photochemical behavior with other neutral charged nitroaromatic compounds (e.g., DNAN (Rao et al., 2013), dinitrophenol (Vione et al., 2005; 2007), nitroanisole (Evans et al., 1997), nitrophenol (Alif et al., 1991) that also release nitro radicals to the aqueous environment. This work enriches the database of carbon and nitrogen isotope enrichment factors of insensitive munition compounds and NACs for applications to remediation strategies.

4.5   Reductive transformation of DNAN by 9,10-anthraquinone-2-disulfonate
4.5.1   Introduction

Humic substances in the environment are common in soil organic matter and are known to be effective at transforming organic contaminants, by an abiotic process that is largely promoted by the presence of abundant quinone moieties that have substantial capacity for reversible electron transfer and storage (Struyk and Sposito, 2007; Fimmen et al., 2007; Aeschbacher et al., 2010; Murillo-Gelvez et al., 2021). Because DNAN in the environment is likely to be exposed to soil organic matter, we investigated the carbon and nitrogen isotope effects during DNAN reduction by 9,10-antraquinone-2-sulfonic acid (AQS), a surrogate for humic substances that has well-known electrochemical properties. The objective of this experiment was to see if the isotope effects caused by abiotic quinone reduction of DNAN are distinguishable from those of biotic (i.e., enzymatic) reduction of DNAN in the environment.

4.5.2.   Materials and methods
4.5.2.1.   Chemicals

AQS (9,10-anthraquinone-2-sulfonic acid, sodium salt hydrate, 97%) was acquired from Alfa Aesar (Ward Hill, MA). DNAN (≥98 %, LOT #09709CO) was obtained from Sigma-Aldrich, Milwaukee, WI. Sodium dithionite ($Na_2S_2O_4$, >85%) was obtained from Alfa Aesar (Haverhill, MA). Potassium ferricyanide ($K_3Fe(CN)_6$, >99%) was obtained from ACROS Organics (Morris Plains, NJ). Ethyl acetate, hydrochloric acid, and potassium chloride were obtained from Fisher Scientific (Pittsburgh, PA).

4.5.2.2. Experimental procedure

A stock solution of 90% dithionite-reduced AQS in 10 mM KCl was split into seven 100 mL amber bottles to perform sacrificial sampling. The total AQS concentration was 26 mM. Sacrificial sampling was necessary to retrieve enough DNAN mass for isotopic analysis. The pH was initially adjusted to 2.01 and remained relatively constant throughout the reaction (±0.2 change). The experiment was designed to consume maximum ~20% of the electrons initially present in AQS. The reaction was initiated by spiking an aliquot of DNAN from a methanolic

stock solution to achieve an initial concentration of 650 µM. At defined times, 27.2 mL of 500 mM potassium ferricyanide were added to reactors to instantly oxidize all the AQS and terminate the reaction. Prior to the oxidation, 0.5 mL of sample was taken and added to HPLC vials pre-filled with 1.3 mL of 500 mM potassium ferricyanide. DNAN and its reduction products were separated and quantified in these vials by using an Agilent 1200 series HPLC. After the oxidation step, the reactors were adjusted to pH –0.1 by adding concentrated HCl and extracted three consecutive times with 15 mL of ethyl acetate (EA). The acidification step was necessary to protonate 2-amino-4-nitroanisole, thereby preventing its extraction with EA along with DNAN. The extracted DNAN in EA was concentrated by evaporating the contents until a 5 mL sample was obtained. The C and N isotope ratios of DNAN were then measured by GC-IRMS according to the methods described in Section 2.1 of this report.

4.5.3. Results and discussion
4.5.3.1 Reduction kinetics of DNAN by AQS
The DNAN concentration was measured as a function of time during its reaction with AQS as described above. The reduction of DNAN occurred rapidly with a first-order rate constant of 0.0096 s^{-1} (Fig. 4.5.1).
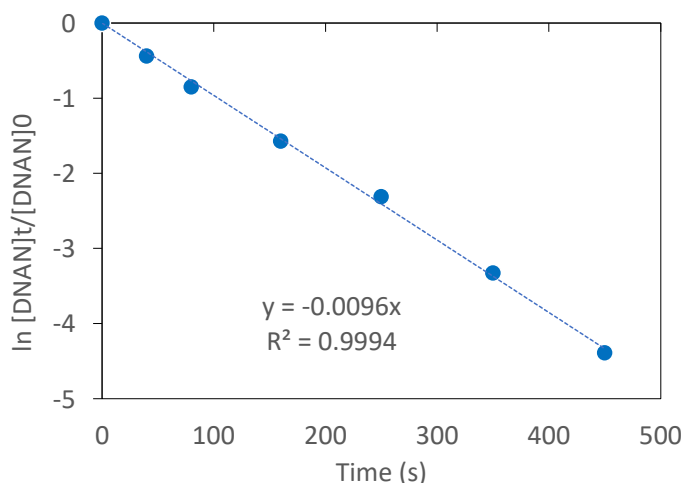
Fig. 4.5.1. Ln [DNAN]$_t$/[DNAN]$_0$ vs. time (seconds) showing rapid reduction of DNAN by AQS with a first-order rate constant of 0.0096 s^{-1}.

4.5.3.2 Carbon and nitrogen isotope effects in DNAN during reduction by AQS
The GC-IRMS measurements of $\delta^{13}C$ and $\delta^{15}N$ of DNAN as a function of time during reduction by AQS are shown in Fig. 4.5.2. A comparison in terms of nitrogen vs. carbon isotope enrichments ($\Delta^{15}N$ ‰ vs. $\Delta^{13}C$ ‰) for this set of DNAN reduction experiments is shown in Fig. 4.5.3. The $\Lambda_{N/C}$ value of 31.63 ± 4.07 associated with DNAN reduction by AQS agrees with the combined value of 50.5 ± 23.2 obtained by Berens et al. (2019) from a set of abiotic reduction experiments conducted with the Fe^{2+}-bearing minerals mackinawite, goethite, and magnetite in the presence and absence of humic acid.
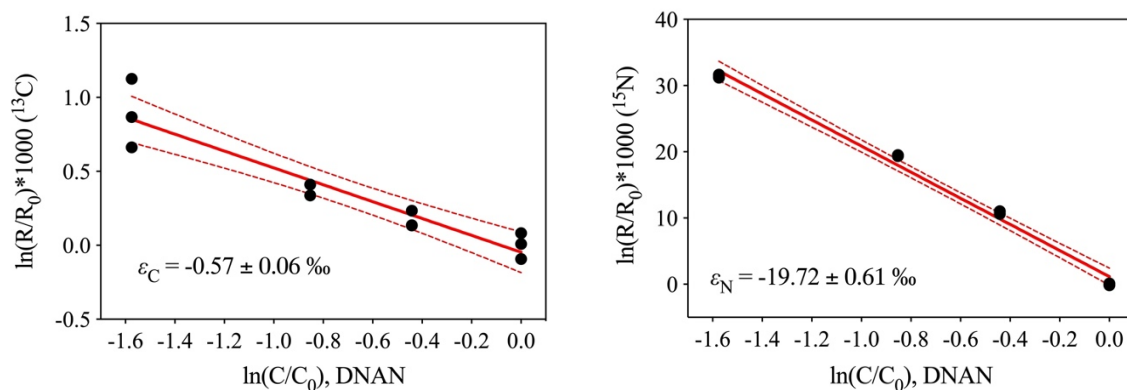
Fig. 4.5.2. Diagrams showing ln (R/R_0) vs. ln (C/C_0) for AQS reduction of DNAN. Left panel shows carbon isotope results, where R is $^{13}C/^{12}C$, and right panel is for nitrogen isotope results, where R is $^{15}N/^{14}N$. Results of triplicate measurements are shown as individual data points. The slopes of the lines indicate the isotope enrichment factors, ε_C and ε_N. The relatively small ε_C value reflects a secondary isotope effect for carbon, whereas the relatively large ε_N value reflects a primary isotope effect related to the N−O bond dissociation.
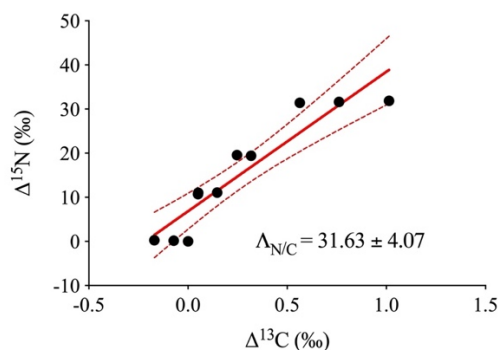
Fig. 4.5.3. Nitrogen vs. carbon isotope enrichments ($\Delta^{15}N$ ‰ vs. $\Delta^{13}C$ ‰) for DNAN reduction by AQS. These data define a $\Lambda_{N/C}$ value of 31.63 ± 4.07.

4.6 Reductive transformation of DNAN by reaction with ferrous iron and hematite

One experiment was performed to examine the isotope effect associated with DNAN reduction by the hematite/aqueous Fe^{2+} redox couple. Nitrogen isotope ratio measurements of DNAN by GC-IRMS as a function of the amount of DNAN remaining are shown in Fig. 4.6.1. The value of ε_N obtained from this set of data was -15.69 ± 1.46 ‰. This value agrees well with those obtained for abiotic reduction of DNAN in systems containing the Fe^{3+}-bearing minerals goethite and magnetite in contacted with dissolved Fe^{2+} (Berens et al., 2019).

95
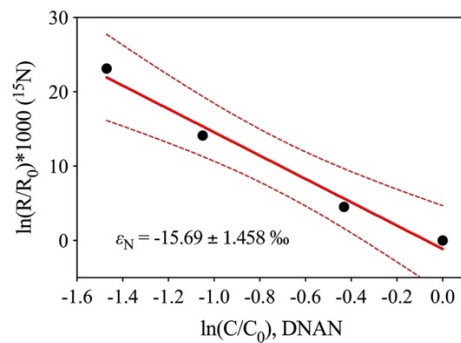
Fig. 4.6.1. Diagrams showing ln (R/R_0) vs. ln (C/C_0) for reduction of DNAN in a hematite-aqueous Fe^{2+} system. The slopes of the lines indicates the value of the nitrogen isotope enrichment factor ε_N.

5.0 Conclusions and Implications for Future Research/Implementation

Methods for compound-specific stable isotope analysis of carbon and nitrogen in DNAN and NTO by GC-IRMS have been developed and applied to the characterization of isotope fractionation accompanying a variety of abiotic and biotic transformations. Substantial differences in the carbon and nitrogen isotope effects were observed. Similar nitrogen and carbon isotope effects accompanied nitro-reduction, whether abiotic or biotic. However, UV-induced photolysis yielded contrasting isotope effects that varied with wavelength and with the presence of chloride. Alkaline hydrolysis of DNAN had isotope effects that were distinct from those of both photolysis and nitro-reduction. Generally, carbon and nitrogen isotope effects show strong potential to distinguish nitro-reduction from photolysis and alkaline hydrolysis of DNAN and NTO in field settings, as well as to estimate the extent to which such transformation processes have operated, and thus provide value in site investigations by indicating the effectiveness of site-specific natural attenuation or engineered remediation measures.

The results of this project indicate several key areas in which future research is recommended: (1) further investigations of biotransformation-induced isotope effects under a range of physical conditions and variable substrate concentrations and solution compositions, to elucidate the variability of enzymatic isotope effects for given enzyme systems; (2) further investigation of direct and indirect photolytic isotope effects for a wide range of contaminant concentrations and bulk solution composition, including isotope measurements of photo-transformation products to elucidate interactions of transient intermediates such as those involved in re-nitration and chlorination pathways. These are especially needed for UV wavelengths present in the solar radiation spectrum at Earth's surface; (3) development and application of compound-specific oxygen isotope analysis methods, to explore the extent to which oxygen isotope effects may give further insights into both abiotic and biotic transformation pathways; and (4) development of methods for the application of orbitrap-based hybrid mass spectrometers to whole-molecule stable isotope analysis, to facilitate further progress in the realm of compound-specific stable isotope analysis. Even at the current state of knowledge of multi-element compound-specific isotope effects that accompany abiotic and biotic transformations under typical environmental conditions, such data are clearly useful and provide cost-effective value for remedial investigations and cleanup of contaminated sites. Further research to expand this knowledge base will contribute to increasing the value of multi-element compound-specific isotope analysis for environmental restoration programs.

6.0 References

ATCC, 1994. Medium: 2157 Methylocella medium.

Gaussian 09, Revision A.02, M. J. Frisch, G. W. Trucks, H. B. Schlegel, G. E. Scuseria, M. A. Robb, J. R. Cheeseman, G. Scalmani, V. Barone, G. A. Petersson, H. Nakatsuji, X. Li, M. Caricato, A. Marenich, J. Bloino, B. G. Janesko, R. Gomperts, B. Mennucci, H. P. Hratchian, J. V. Ortiz, A. F. Izmaylov, J. L. Sonnenberg, D. Williams-Young, F. Ding, F. Lipparini, F. Egidi, J. Goings, B. Peng, A. Petrone, T. Henderson, D. Ranasinghe, V. G. Zakrzewski, J. Gao, N. Rega, G. Zheng, W. Liang, M. Hada, M. Ehara, K. Toyota, R. Fukuda, J. Hasegawa, M. Ishida, T. Nakajima, Y. Honda, O. Kitao, H. Nakai, T. Vreven, K. Throssell, J. A. Montgomery, Jr., J. E. Peralta, F. Ogliaro, M. Bearpark, J. J. Heyd, E. Brothers, K. N. Kudin, V. N. Staroverov, T. Keith, R. Kobayashi, J. Normand, K. Raghavachari, A. Rendell, J. C. Burant, S. S. Iyengar, J. Tomasi, M. Cossi, J. M. Millam, M. Klene, C. Adamo, R. Cammi, J. W. Ochterski, R. L. Martin, K. Morokuma, O. Farkas, J. B. Foresman, and D. J. Fox, Gaussian, Inc., Wallingford CT, 2016.

Adriaens, P. & D. Grbic-Galic (1994) Cometabolic Transformation of Mono- and Dichlorobiphenyls and Chlorohydroxybiphenyls by Methanotrophic Groundwater Isolates. *Environmental Science & Technology,* 28**,** 1325-1330.

Akhavan, J. 2011. *The chemistry of explosives*. Royal Society of Chemistry.

Akoka, S. & G. S. Remaud (2020) NMR-based isotopic and isotopomic analysis. *Progress in Nuclear Magnetic Resonance Spectroscopy,* 120-121**,** 1-24.

Albinet, A., C. Minero & D. Vione (2010a) Phototransformation processes of 2,4-dinitrophenol, relevant to atmospheric water droplets. *Chemosphere,* 80**,** 753-8.

Albinet, A., C. Minero & D. Vione (2010b) UVA irradiation induces direct phototransformation of 2,4-dinitrophenol in surface water samples. *Chemosphere,* 80**,** 759-63.

Alif, A., J. F. Pilichowski & P. Boule (1991) Photochemistry and environment XIII: Phototransformation of 2-nitrophenol in aqueous solution. *Journal of Photochemistry and Photobiology a-Chemistry,* 59**,** 209-219.

Arthur, J. D., N. W. Mark, S. Taylor, J. Simunek, M. L. Brusseau & K. M. Dontsova (2017) Batch soil adsorption and column transport studies of 2,4-dinitroanisole (DNAN) in soils. *J Contam Hydrol,* 199**,** 14-23.

Baltrusaitis, J., E. V. Patterson, M. O'Connor, S. Qu, E. P. Kolodziej & D. M. Cwiertny (2016) Reversible Photohydration of Trenbolone Acetate Metabolites: Mechanistic Understanding of Product-to-Parent Reversion through Complementary Experimental and Theoretical Approaches. *Environ Sci Technol,* 50**,** 6753-61.

Banerjee, R., K. K. Meier, E. Münck & J. D. Lipscomb (2013) Intermediate P* from Soluble Methane Monooxygenase Contains a Diferrous Cluster. *Biochemistry,* 52**,** 4331-4342.

Bariwal, J. & E. Van der Eycken (2013) C-N bond forming cross-coupling reactions: an overview. *Chem Soc Rev,* 42**,** 9283-303.

Barltrop, J. & N. Bunce (1968) Organic photochemistry. Part VIII. The photochemical reduction of nitro-compounds. *Journal of the Chemical Society C: Organic***,** 1467-1474.

Barsotti, F., T. Bartels-Rausch, E. De Laurentiis, M. Ammann, M. Brigante, G. Mailhot, V. Maurino, C. Minero & D. Vione (2017) Photochemical Formation of Nitrite and Nitrous Acid (HONO) upon Irradiation of Nitrophenols in Aqueous Solution and in Viscous Secondary Organic Aerosol Proxy. *Environ Sci Technol,* 51**,** 7486-7495.

Bayle, K., M. Grand, A. Chaintreau, R. J. Robins, W. Fieber, H. Sommer, S. Akoka & G. S. Remaud (2015) Internal Referencing for (1)(3)C Position-Specific Isotope Analysis Measured by NMR Spectrometry. *Anal Chem,* 87**,** 7550-4.

Becher, J. B., S. A. Beal, S. Taylor, K. Dontsova & D. E. Wilcox (2019) Photo-transformation of aqueous nitroguanidine and 3-nitro-1,2,4-triazol-5-one: Emerging munitions compounds. *Chemosphere,* 228**,** 418-426.

Berens, M. J., T. B. Hofstetter, J. Bolotin & W. A. Arnold (2020) Assessment of 2,4-Dinitroanisole Transformation Using Compound-Specific Isotope Analysis after In Situ Chemical Reduction of Iron Oxides. *Environ Sci Technol,* 54**,** 5520-5531.

Berens, M. J., Y. Tong, B. A. Ulrich, J. H. Strehlau, T. B. Hofstetter & W. A. Arnold. 2021. Compound Specific Isotope Analysis of Mineral-Mediated Abiotic Reduction of Nitro Compounds. University of Minnesota Minneapolis United States.

Berens, M. J., B. A. Ulrich, J. H. Strehlau, T. B. Hofstetter & W. A. Arnold (2019) Mineral identity, natural organic matter, and repeated contaminant exposures do not affect the carbon and nitrogen isotope fractionation of 2,4-dinitroanisole during abiotic reduction. *Environmental Science: Processes & Impacts,* 21**,** 51-62.

Bernstein, A., Z. Ronen, E. Adar, R. Nativ, H. Lowag, W. Stichler & R. U. Meckenstock (2008) Compound-specific isotope analysis of RDX and stable isotope fractionation during aerobic and anaerobic biodegradation. *Environ Sci Technol,* 42**,** 7772-7.

Bernstein, A., Z. Ronen & F. Gelman (2013) Insight on RDX Degradation Mechanism by Rhodococcus Strains Using C-13 and N-15 Kinetic Isotope Effects. *Environmental Science & Technology,* 47**,** 479-484.

Besler, B. H., K. M. Merz & P. A. Kollman (1990) Atomic Charges Derived from Semiempirical Methods. *Journal of Computational Chemistry,* 11**,** 431-439.

Bhatkhande, D. (2004) Photocatalytic and photochemical degradation of nitrobenzene using artificial ultraviolet light. *Chemical Engineering Journal,* 102**,** 283-290.

Blehert DS, Fox BG, Chambliss GH (1999) Cloning and Sequence Analysis of Two P*seudomonas* Flavoprotein Xenobiotic Reductases. *J. Bacteriology* 181:6254-6263.

Boddu, V. M., K. Abburi, A. J. Fredricksen, S. W. Maloney & R. Damavarapu (2009) Equilibrium and column adsorption studies of 2,4-dinitroanisole (DNAN) on surface modified granular activated carbons. *Environ Technol,* 30**,** 173-81.

Boddu, V. M., K. Abburi, S. W. Maloney & R. Damavarapu (2008) Thermophysical properties of an insensitive munitions compound, 2,4-dinitroanisole. *Journal of Chemical and Engineering Data,* 53**,** 1120-1125.

Brand, W. A., T. B. Coplen, A. T. Aerts-Bijma, J. K. Bohlke, M. Gehre, H. Geilmann, M. Groning, H. G. Jansen, H. A. Meijer, S. J. Mroczkowski, H. Qi, K. Soergel, H. Stuart-Williams, S. M. Weise & R. A. Werner (2009) Comprehensive inter-laboratory calibration of reference materials for delta18O versus VSMOW using various on-line high-temperature conversion techniques. *Rapid Commun Mass Spectrom,* 23**,** 999-1019.

Brazeau, B. J. & J. D. Lipscomb (2000) Kinetics and activation thermodynamics of methane monooxygenase compound Q formation and reaction with substrates. *Biochemistry,* 39**,** 13503-13515.

Buchachenko, A. L. (2001) Magnetic isotope effect: Nuclear spin control of chemical reactions. *The Journal of Physical Chemistry A,* 105**,** 9995-10011.

Caporaso, J. G., J. Kuczynski, J. Stombaugh, K. Bittinger, F. D. Bushman, E. K. Costello, N. Fierer, A. G. Peña, J. K. Goodrich, J. I. Gordon, G. A. Huttley, S. T. Kelley, D. Knights,

J. E. Koenig, R. E. Ley, C. A. Lozupone, D. McDonald, B. D. Muegge, M. Pirrung, J. Reeder, J. R. Sevinsky, P. J. Turnbaugh, W. A. Walters, J. Widmann, T. Yatsunenko, J. Zaneveld & R. Knight (2010) QIIME allows analysis of high-throughput community sequencing data. *Nature Methods,* 7**,** 335-336.

Cardenas-Hernandez, P. A., K. A. Anderson, J. Murillo-Gelvez, D. M. Di Toro, H. E. Allen, R. F. Carbonaro & P. C. Chiu (2020) Reduction of 3-Nitro-1,2,4-Triazol-5-One (NTO) by the Hematite-Aqueous Fe(II) Redox Couple. *Environ Sci Technol,* 54**,** 12191-12201.

Caytan, E., E. P. Botosoa, V. Silvestre, R. J. Robins, S. Akoka & G. S. Remaud (2007) Accurate quantitative 13C NMR spectroscopy: repeatability over time of site-specific 13C isotope ratio determination. *Anal Chem,* 79**,** 8266-9.

Chaintreau, A., W. Fieber, H. Sommer, A. Gilbert, K. Yamada, N. Yoshida, A. Pagelot, D. Moskau, A. Moreno, J. Schleucher, F. Reniero, M. Holland, C. Guillou, V. Silvestre, S. Akoka & G. S. Remaud (2013) Site-specific 13C content by quantitative isotopic 13C nuclear magnetic resonance spectrometry: a pilot inter-laboratory study. *Anal Chim Acta,* 788**,** 108-13.

Chudgar, R. & J. Oakes. 2014. Kirk-Othmer Encyclopedia of Chemical Technology-Section on Azo Dyes. John Wiley, Chichester.

Coplen, T. B. (1988) Normalization of Oxygen and Hydrogen Isotope Data. *Chemical Geology,* 72**,** 293-297.

Cornish, A., K. M. Nicholls, D. Scott, B. K. Hunter, W. J. Aston, I. J. Higgins & J. K. M. Sanders (1984) In vivo 13C NMR Investigations of Methanol Oxidation by the Obligate Methanotroph Methylosinus trichosporium OB3b. *Microbiology,* 130**,** 2565-2575.

Cretnik, S., K. A. Thoreson, A. Bernstein, K. Ebert, D. Buchner, C. Laskov, S. Haderlein, O. Shouakar-Stash, S. Kliegman, K. McNeill & M. Elsner (2013) Reductive dechlorination of TCE by chemical model systems in comparison to dehalogenating bacteria: insights from dual element isotope analysis (13C/12C, 37Cl/35Cl). *Environ Sci Technol,* 47**,** 6855-63.

Cwiertny, D. M., S. A. Snyder, D. Schlenk & E. P. Kolodziej (2014) Environmental designer drugs: when transformation may not eliminate risk. *Environ Sci Technol,* 48**,** 11737-45.

Dhar, N. R., S. P. Tandon, N. Biswas & A. K. Bhateacharya (1934) Photo-Oxidation of Nitrite to Nitrate. *Nature,* 133**,** 213-214.

Ding, K., C. Byrnes, J. Bridge, A. Grannas & W. Xu (2018) Surface-promoted hydrolysis of 2,4,6-trinitrotoluene and 2,4-dinitroanisole on pyrogenic carbonaceous matter. *Chemosphere,* 197**,** 603-610.

Dodard, S. G., M. Sarrazin, J. Hawari, L. Paquet, G. Ampleman, S. Thiboutot & G. I. Sunahara (2013) Ecotoxicological assessment of a high energetic and insensitive munitions compound: 2,4-dinitroanisole (DNAN). *J Hazard Mater,* 262**,** 143-50.

Dontsova, K., S. Taylor & R. Pesce-Rodriguez. 2018. Dissolution of NTO, DNAN and insensitive munitions formulations and their fates in soils. University of Arizona Tuscon United States.

Döpp, D. (1975) Reactions of aromatic nitro compounds via excited triplet states. *Triplet States II*,** 49-85.

Eiler, J., J. Cesar, L. Chimiak, B. Dallas, K. Grice, J. Griep-Raming, D. Juchelka, N. Kitchen, M. Lloyd, A. Makarov, R. Robins & J. Schwieters (2017) Analysis of molecular isotopic structures at high precision and accuracy by Orbitrap mass spectrometry. *International Journal of Mass Spectrometry,* 422**,** 126-142.

Elsner, M. (2010) Stable isotope fractionation to investigate natural transformation mechanisms of organic contaminants: principles, prospects and limitations. *J Environ Monit,* 12**,** 2005-31.

Elsner, M. & G. Imfeld (2016) Compound-specific isotope analysis (CSIA) of micropollutants in the environment - current developments and future challenges. *Curr Opin Biotechnol,* 41**,** 60-72.

Elsner, M., M. A. Jochmann, T. B. Hofstetter, D. Hunkeler, A. Bernstein, T. C. Schmidt & A. Schimmelmann (2012) Current challenges in compound-specific stable isotope analysis of environmental organic contaminants. *Anal Bioanal Chem,* 403**,** 2471-91.

Elsner, M., L. Zwank, D. Hunkeler & R. P. Schwarzenbach (2005) A new concept linking observable stable isotope fractionation to transformation pathways of organic pollutants. *Environ Sci Technol,* 39**,** 6896-916.

Evans, C. H., G. Arnadottir & J. C. Scaiano (1997) Reactivity of the 3-nitroanisole triplet: Methanol inhibition of photohydroxylation. *Journal of Organic Chemistry,* 62**,** 8777-8783.

Feilberg, A. & T. Nielsen (2000) Effect of aerosol chemical composition on the photodegradation of nitro-polycyclic aromatic hydrocarbons. *Environmental science & technology,* 34**,** 789-797.

Feilberg, A. & T. Nielsen (2001) Photodegradation of nitro-PAHs in viscous organic media used as models of organic aerosols. *Environmental science & technology,* 35**,** 108-113.

Fida, T. T., S. Palamuru, G. Pandey & J. C. Spain (2014a) Aerobic biodegradation of 2,4-Dinitroanisole by Nocardioides sp. strain JS1661. *Appl Environ Microbiol,* 80**,** 7725-31.

Fida, T. T., S. Palamuru, G. Pandey, J. C. Spain & R. E. Parales (2014b) Aerobic Biodegradation of 2,4-Dinitroanisole by Nocardioides sp. Strain JS1661. *Applied and Environmental Microbiology,* 80**,** 7725-7731.

Fishbein, L. (1979) Potential halogenated industrial carcinogenic and mutagenic chemicals II. Halogenated saturated hydrocarbons. *Science of The Total Environment,* 11**,** 163-195.

Foote, C. S. (1968) Mechanisms of photosensitized oxidation. *Science,* 162**,** 963-970.

Fournier D, Hawari J, Halasz A, Streger SH, McClay KR, Masuda H, Hatzinger PB (2009) Transformation of RDX and other energetic compounds by xenobiotic reductases XenA and XenB. *Applied Microbiology and Biotechnology* 84:535-544.

Fuller ME, McClay K, Hawari J, Paquet L, Malone TE, Fox BG, Steffan RJ (2009) Aerobic Biodegradation of N-Nitrosodimethylamine by the Propanotroph *Rhodococcus ruber* ENV425. *Applied and Environmental Microbiology* 75: 5088-5093

Fuller, M. E., L. Heraty, C. W. Condee, S. Vainberg, N. C. Sturchio, J. K. Bohlke & P. B. Hatzinger (2016) Relating Carbon and Nitrogen Isotope Effects to Reaction Mechanisms during Aerobic or Anaerobic Degradation of RDX (Hexahydro-1,3,5-Trinitro-1,3,5-Triazine) by Pure Bacterial Cultures. *Appl Environ Microbiol,* 82**,** 3297-309.

Fuller, M. E., R. T. Rezes, P. C. Hedman, J. C. Jones, N. C. Sturchio & P. B. Hatzinger (2020a) Biotransformation of the insensitive munition constituents 3-nitro-1,2,4-triazol-5-one (NTO) and 2,4-dinitroanisole (DNAN) by aerobic methane-oxidizing consortia and pure cultures. *Journal of Hazardous Materials*.

Fuller, M. E., P. G. K. van Groos, M. Jarrett, K. H. Kucharzyk, A. Minard-Smith, L. J. Heraty & N. C. Sturchio (2020b) Application of a multiple lines of evidence approach to document natural attenuation of hexahydro-1, 3, 5-trinitro-1, 3, 5-triazine (RDX) in groundwater. *Chemosphere,* 250**,** 126210.

García-Berríos, Z. I. & R. Arce (2012) Photodegradation mechanisms of 1-nitropyrene, an environmental pollutant: the effect of organic solvents, water, oxygen, phenols, and polycyclic aromatics on the destruction and product yields. *The Journal of Physical Chemistry A,* 116**,** 3652-3664.

George, C., M. Ammann, B. D'Anna, D. J. Donaldson & S. A. Nizkorodov (2015) Heterogeneous photochemistry in the atmosphere. *Chem Rev,* 115**,** 4218-58.

Gligorovski, S., R. Strekowski, S. Barbati & D. Vione (2015) Environmental Implications of Hydroxyl Radicals ((*)OH). *Chem Rev,* 115**,** 13051-92.

Goldstein, S. & J. Rabani (2007) Mechanism of nitrite formation by nitrate photolysis in aqueous solutions: the role of peroxynitrite, nitrogen dioxide, and hydroxyl radical. *J Am Chem Soc,* 129**,** 10597-601.

Gonfiantini, R. (1978) Standards for Stable Isotope Measurements in Natural Compounds. *Nature,* 271**,** 534-536.

Hadisaputra, S. & N. Prasetyo (2016) The Explosive Sensitivity on the Complex Formation of 3-Nitro-1,2,4-Triazol-5-One and Metal Ions Based on Density Functional Study. *Makara Journal of Science,* 20.

Halasz, A., J. Hawari & N. N. Perreault (2018) New Insights into the Photochemical Degradation of the Insensitive Munition Formulation IMX-101 in Water. *Environ Sci Technol,* 52**,** 589-596.

Hamad, B. M. 2009. *Studies on the biotransformation of chromium (VI) by methane oxidising bacteria.* Sheffield Hallam University (United Kingdom).

Harris, N. J. & K. Lammertsma (1996) Tautomerism, Ionization, and Bond Dissociations of 5-Nitro-2,4-dihydro-3H-1,2,4-triazolone. *Journal of the American Chemical Society,* 118**,** 8048-8055.

Hartenbach, A. E., T. B. Hofstetter, M. Aeschbacher, M. Sander, D. Kim, T. J. Strathmann, W. A. Arnold, C. J. Cramer & R. P. Schwarzenbach (2008a) Variability of nitrogen isotope fractionation during the reduction of nitroaromatic compounds with dissolved reductants. *Environ Sci Technol,* 42**,** 8352-9.

Hartenbach, A. E., T. B. Hofstetter, P. R. Tentscher, S. Canonica, M. Berg & R. P. Schwarzenbach (2008b) Carbon, hydrogen, and nitrogen isotope fractionation during light-induced transformations of atrazine. *Environ Sci Technol,* 42**,** 7751-6.

Hashimoto, S. & K. Kano (1972) The photochemical reduction of nitrobenzene and its reduction intermediates. X. The photochemical reduction of the monosubstituted nitrobenzenes in 2-propanol. *Bulletin of the Chemical Society of Japan,* 45**,** 549-553.

Hatzinger, P. B., J. K. Bohlke & N. C. Sturchio (2013) Application of stable isotope ratio analysis for biodegradation monitoring in groundwater. *Curr Opin Biotechnol,* 24**,** 542-9.

Hatzinger, P. B., J. K. Bohlke, N. C. Sturchio, B. Gu, L. J. Heraty & R. C. Borden (2009) Fractionation of stable isotopes in perchlorate and nitrate during in situ biodegradation in a sandy aquifer. *Environmental Chemistry,* 6**,** 44-52.

Hatzinger, P.B., Chu, K.-H., 2017. Role of acidophilic methanotrophs in long term natural Attenuation of cVOCs in low pH aquifers (Project ER-2531). Strategic Environmental Research and Development Program (SERDP) Final Report. SERDP, Washington, DC, USA. https://www.serdp-estcp.org/content/download/45520/424783/file/ ER-2531.

Hawari, J., F. Monteil-Rivera, N. N. Perreault, A. Halasz, L. Paquet, Z. Radovic-Hrapovic, S. Deschamps, S. Thiboutot & G. Ampleman (2015) Environmental fate of 2,4-dinitroanisole (DNAN) and its reduced products. *Chemosphere,* 119**,** 16-23.

Hesselsoe, M., S. Boysen, N. Iversen, L. Jørgensen, J. C. Murrell, I. McDonald, S. Radajewski, H. Thestrup & P. Roslev (2005) Degradation of organic pollutants by methane grown microbial consortia. *Biodegradation,* 16**,** 435-448.

Hoffmann, E.H., A. Tilgner, R. Wolke, H. Herrmann (2019) Enhanced Chlorine and Bromine Atom Activation by Hydrolysis of Halogen Nitrates from Marine Aerosols at Polluted Coastal Areas. *Environmental Science & Technology*, 53, 771-778.

Hofstetter, T. B. & M. Berg (2011) Assessing transformation processes of organic contaminants by compound-specific stable isotope analysis. *TrAC Trends in Analytical Chemistry,* 30**,** 618-627.

Hofstetter, T. B., J. Bolotin, S. G. Pati, M. Skarpeli-Liati, S. Spahr & R. S. Wijker (2014) Isotope Effects as New Proxies for Organic Pollutant Transformation. *CHIMIA International Journal for Chemistry,* 68**,** 788-792.

Hofstetter, T. B., A. Neumann, W. A. Arnold, A. E. Hartenbach, J. Bolotin, C. J. Cramer & R. P. Schwarzenbach (2008a) Substituent effects on nitrogen isotope fractionation during abiotic reduction of nitroaromatic compounds. *Environmental Science & Technology,* 42**,** 1997-2003.

Hofstetter, T. B., C. M. Reddy, L. J. Heraty, M. Berg & N. C. Sturchio (2007) Carbon and chlorine isotope effects during abiotic reductive dechlorination of polychlorinated ethanes. *Environ Sci Technol,* 41**,** 4662-8.

Hofstetter, T. B., J. C. Spain, S. F. Nishino, J. Bolotin & R. P. Schwarzenbach (2008b) Identifying competing aerobic nitrobenzene biodegradation pathways by compound-specific isotope analysis. *Environ Sci Technol,* 42**,** 4764-70.

Hohener, P., V. Silvestre, A. Lefrancois, D. Loquet, E. P. Botosoa, R. J. Robins & G. S. Remaud (2012) Analytical model for site-specific isotope fractionation in 13C during sorption: determination by isotopic 13C NMR spectrometry with vanillin as model compound. *Chemosphere,* 87**,** 445-52.

Hunkeler, D., R. U. Meckenstock, B. Lollar, T. C. Schmidt, J. T. Wilson, 2009. A Guide for Assessing Biodegradation and Source Identification of Organic Groundwater Contaminants Using Compound Specific Isotope Analysis (CSIA). U.S. Environmental Protection Agency, Washington, D.C., EPA/600/R-08/148, 2009.

Indest, K. J., D. E. Hancock, F. H. Crocker, J. O. Eberly, C. M. Jung, G. A. Blakeney, J. Brame & M. A. Chappell (2017) Biodegradation of insensitive munition formulations IMX101 and IMX104 in surface soils. *Journal of Industrial Microbiology and Biotechnology,* 44**,** 987-995.

Jain, M. R., S. S. Zinjarde, D. D. Deobagkar & D. N. Deobagkar (2004) 2,4,6-Trinitrotoluene transformation by a tropical marine yeast, Yarrowia lipolytica NCIM 3589. *Marine Pollution Bulletin,* 49**,** 783-788.

Jechorek, M., K. D. Wendlandt & M. Beck (2003) Cometabolic degradation of chlorinated aromatic compounds. *Journal of Biotechnology,* 102**,** 93-98.

Jin, B. & M. Rolle (2014) Mechanistic approach to multi-element isotope modeling of organic contaminant degradation. *Chemosphere,* 95**,** 131-9.

Jin, B. & M. Rolle (2016) Position-specific isotope modeling of organic micropollutants transformation through different reaction pathways. *Environ Pollut,* 210**,** 94-103.

Jochmann, M. A., M. Blessing, S. B. Haderlein & T. C. Schmidt (2006) A new approach to determine method detection limits for compound-specific isotope analysis of volatile organic compounds. *Rapid Commun Mass Spectrom,* 20**,** 3639-48.

Johnson, M. S., W. S. Eck & E. M. Lent (2017) Toxicity of Insensitive Munition (IMX) Formulations and Components. *Propellants, Explosives, Pyrotechnics,* 42**,** 9-16.

Julien, M., D. Gori, P. Hohener, R. J. Robins & G. S. Remaud (2020) Intramolecular isotope effects during permanganate oxidation and acid hydrolysis of methyl tert-butyl ether. *Chemosphere,* 248**,** 125975.

Julien, M., J. Parinet, P. Nun, K. Bayle, P. Hohener, R. J. Robins & G. S. Remaud (2015) Fractionation in position-specific isotope composition during vaporization of environmental pollutants measured with isotope ratio monitoring by (1)(3)C nuclear magnetic resonance spectrometry. *Environ Pollut,* 205**,** 299-306.

Karthikeyan, S., Z. Kurt, G. Pandey & J. C. Spain (2016) Immobilized Biocatalyst for Detection and Destruction of the Insensitive Explosive, 2,4-Dinitroanisole (DNAN). *Environ Sci Technol,* 50**,** 11193-11199.

Karthikeyan, S. & J. C. Spain (2016a) Biodegradation of 2,4-dinitroanisole (DNAN) by Nocardioides sp. JS1661 in water, soil and bioreactors. *Journal of Hazardous Materials,* 312**,** 37-44.

Karthikeyan, S. & J. C. Spain (2016b) Biodegradation of 2,4-dinitroanisole (DNAN) by Nocardioides sp. JS1661 in water, soil and bioreactors. *J Hazard Mater,* 312**,** 37-44.

Kennedy, A. J., A. R. Poda, N. L. Melby, L. C. Moores, S. M. Jordan, K. A. Gust & A. J. Bednar (2017) Aquatic toxicity of photo-degraded insensitive munition 101 (IMX-101) constituents. *Environ Toxicol Chem,* 36**,** 2050-2057.

Khatiwada, R., C. Olivares, L. Abrell, R. A. Root, R. Sierra-Alvarez, J. A. Field & J. Chorover (2018a) Oxidation of reduced daughter products from 2,4-dinitroanisole (DNAN) by Mn(IV) and Fe(III) oxides. *Chemosphere,* 201**,** 790-798.

Khatiwada, R., R. A. Root, L. Abrell, R. Sierra-Alvarez, J. A. Field & J. Chorover (2018b) Abiotic reduction of insensitive munition compounds by sulfate green rust. *Environmental Chemistry,* 15**,** 259-266.

Kim, J., Y. J. Choe, S. H. Kim, I. S. Choi & K. Jeong (2021) Deciphering Evolution Pathway of Supported NO3 (*) Enabled via Radical Transfer from (*)OH to Surface NO3 (-) Functionality for Oxidative Degradation of Aqueous Contaminants. *JACS Au,* 1**,** 1158-1177.

Kitts, C. L., C. E. Green, R. A. Otley, M. A. Alvarez & P. J. Unkefer (2000) Type I nitroreductases in soil enterobacteria reduce TNT (2,4,6-trinitrotoluene) and RDX (hexahydro-1,3,5-trinitro-1,3,5-triazine). *Canadian Journal of Microbiology,* 46**,** 278-282.

Klapötke, T. M., A. Penger, C. Pflüger & J. Stierstorfer (2016) Melt-cast materials: combining the advantages of highly nitrated azoles and open-chain nitramines. *New Journal of Chemistry,* 40**,** 6059-6069.

Kofman, T., M. S. Pevzner, L. Zhukova, T. A. Kravchenko & G. Frolova (1980) METHYLATION OF 3-NITRO-1,2,4-TRIAZOL-5-ONE. *ChemInform,* 11.

Koutsospyros, A., J. Pavlov, J. Fawcett, D. Strickland, B. Smolinski & W. Braida (2012) Degradation of high energetic and insensitive munitions compounds by Fe/Cu bimetal reduction. *Journal of Hazardous Materials,* 219-220**,** 75-81.

Krummen, M., A. W. Hilkert, D. Juchelka, A. Duhr, H.-J. Schlüter & R. Pesch (2004) A new concept for isotope ratio monitoring liquid chromatography/mass spectrometry. *Rapid Communications in Mass Spectrometry,* 18**,** 2260-2266.

Krzmarzick, M. J., R. Khatiwada, C. I. Olivares, L. Abrell, R. Sierra-Alvarez, J. Chorover & J. A. Field (2015a) Biotransformation and Degradation of the Insensitive Munitions Compound, 3-Nitro-1,2,4-triazol-5-one, by Soil Bacterial Communities. *Environ Sci Technol,* 49**,** 5681-8.

Krzmarzick, M. J., R. Khatiwada, C. I. Olivares, L. Abrell, R. Sierra-Alvarez, J. Chorover & J. A. Field (2015b) Biotransformation and Degradation of the Insensitive Munitions Compound, 3-Nitro-1,2,4-triazol-5-one, by Soil Bacterial Communities. *Environmental Science & Technology,* 49**,** 5681-5688.

Kutty, R. & G. N. Bennett (2005) Biochemical characterization of trinitrotoluene transforming oxygen-insensitive nitroreductases from Clostridium acetobutylicum ATCC 824. *Archives of Microbiology,* 184**,** 158-167.

Lai, C.-Y., L. Zhong, Y. Zhang, J.-X. Chen, L.-L. Wen, L.-D. Shi, Y.-P. Sun, F. Ma, B. E. Rittmann, C. Zhou, Y. Tang, P. Zheng & H.-P. Zhao (2016) Bioreduction of Chromate in a Methane-Based Membrane Biofilm Reactor. *Environmental Science & Technology,* 50**,** 5832-5839.

Larina, L. & V. Lopyrev. 2009. Application of Nitroazoles. In *Nitroazoles: Synthesis, Structure and Applications*, 407-432. New York, NY: Springer New York.

Le Campion, L., M. Delaforge, J. P. Noel & J. Ouazzani (1998) Metabolism of 14C-labelled 5-nitro-1,2,4-triazol-3-one (NTO): comparison between rat liver microsomes and bacterial metabolic pathways. *Journal of Molecular Catalysis B: Enzymatic,* 5**,** 395-402.

Le Campion, L., C. Giannotti & J. Ouazzani (1999) Photocatalytic degradation of 5-nitro-1,2,4-triazol-3-one NTO in aqueous suspention of TiO2. Comparison with Fenton oxidation. *Chemosphere,* 38**,** 1561-1570.

Le Campion, L., A. Vandais & J. Ouazzani (1999) Microbial remediation of NTO in aqueous industrial wastes. *FEMS Microbiology Letters,* 176**,** 197-203.

Lee, K.-Y. & M. D. Coburn. 1987. 3-nitro-1,2,4-triazol-5-one, a less sensitive explosive. United States: The United States of America as represented by the United States Department of Energy, Washington, D.C.

Lee, K. C. K., M. Ye & W.-C. Lee. 2010. Reverse ranking query over imprecise spatial data. In *Proceedings of the 1st International Conference and Exhibition on Computing for Geospatial Research & Application*, Article 17. Washington, D.C., USA: Association for Computing Machinery.

Lee, S.-W., D. R. Keeney, D.-H. Lim, A. A. Dispirito & J. D. Semrau (2006) Mixed Pollutant Degradation by <i>Methylosinus trichosporium</i> OB3b Expressing either Soluble or Particulate Methane Monooxygenase: Can the Tortoise Beat the Hare? *Applied and Environmental Microbiology,* 72**,** 7503-7509.

Liang, X., Y. Dong, T. Kuder, L. R. Krumholz, R. P. Philp & E. C. Butler (2007) Distinguishing abiotic and biotic transformation of tetrachloroethylene and trichloroethylene by stable carbon isotope fractionation. *Environ Sci Technol,* 41**,** 7094-100.

Lihl, C., B. Heckel, A. Grzybkowska, A. Dybala-Defratyka, V. Ponsin, C. Torrento, D. Hunkeler & M. Elsner (2020) Compound-specific chlorine isotope fractionation in biodegradation of atrazine. *Environ Sci Process Impacts,* 22**,** 792-801.

Lindner, A. S., C. Whitfield, N. Chen, J. D. Semrau & P. Adriaens (2003) Quantitative structure–biodegradation relationships for Ortho-substituted biphenyl compounds oxidized by Methylosinus trichosporium OB3b. *Environmental Toxicology and Chemistry,* 22**,** 2251-2257.

Linker, B. R., R. Khatiwada, N. Perdrial, L. Abrell, R. Sierra-Alvarez, J. A. Field & J. Chorover (2015) Adsorption of novel insensitive munitions compounds at clay mineral and metal oxide surfaces. *Environmental Chemistry,* 12**,** 74-84.

LinWu, S.-W., C.-J. Syu, Y.-L. Chen, A. H. J. Wang & F.-C. Peng (2009) Characterization of Escherichia coli nitroreductase NfsB in the metabolism of nitrobenzodiazepines. *Biochemical Pharmacology,* 78**,** 96-103.

Liu, A., Y. Jin, J. Zhang, B. J. Brazeau & J. D. Lipscomb (2005) Substrate radical intermediates in soluble methane monooxygenase. *Biochemical and Biophysical Research Communications,* 338**,** 254-261.

Liu, C., G. P. McGovern, P. Liu, H. Zhao & J. Horita (2018) Position-specific carbon and hydrogen isotopic compositions of propane from natural gases with quantitative NMR. *Chemical Geology,* 491**,** 14-26.

Liu, Y., M. Mekic, L. Carena, D. Vione, S. Gligorovski, G. Zhang & B. Jin (2020) Tracking photodegradation products and bond-cleavage reaction pathways of triclosan using ultra-high resolution mass spectrometry and stable carbon isotope analysis. *Environ Pollut,* 264**,** 114673.

Mack, J. & J. R. Bolton (1999) Photochemistry of nitrite and nitrate in aqueous solution: a review. *Journal of Photochemistry and Photobiology a-Chemistry,* 128**,** 1-13.

Madeira, C. L., O. Menezes, D. Park, K. V. Jog, J. K. Hatt, S. Gavazza, M. J. Krzmarzick, R. Sierra-Alvarez, J. C. Spain, K. T. Konstantinidis & J. A. Field (2021) Bacteria Make a Living Breathing the Nitroheterocyclic Insensitive Munitions Compound 3-Nitro-1,2,4-triazol-5-one (NTO). *Environ Sci Technol.*

Madeira, C. L., S. A. Speet, C. A. Nieto, L. Abrell, J. Chorover, R. Sierra-Alvarez & J. A. Field (2017) Sequential anaerobic-aerobic biodegradation of emerging insensitive munitions compound 3-nitro-1,2,4-triazol-5-one (NTO). *Chemosphere,* 167**,** 478-484.

Maier, M. P., S. De Corte, S. Nitsche, T. Spaett, N. Boon & M. Elsner (2014) C & N isotope analysis of diclofenac to distinguish oxidative and reductive transformation and to track commercial products. *Environ Sci Technol,* 48**,** 2312-20.

Marenich, A. V., C. J. Cramer & D. G. Truhlar (2009) Universal solvation model based on solute electron density and on a continuum model of the solvent defined by the bulk dielectric constant and atomic surface tensions. *J Phys Chem B,* 113**,** 6378-96.

Mark, N., J. Arthur, K. Dontsova, M. Brusseau & S. Taylor (2016) Adsorption and attenuation behavior of 3-nitro-1,2,4-triazol-5-one (NTO) in eleven soils. *Chemosphere,* 144**,** 1249-55.

Mark, N., J. Arthur, K. Dontsova, M. Brusseau, S. Taylor & J. Simunek (2017) Column transport studies of 3-nitro-1,2,4-triazol-5-one (NTO) in soils. *Chemosphere,* 171**,** 427-434.

Matsui, T., L. G. Hepler & D. V. Fenby (1973) Thermodynamic Investigation of Complex-Formation by Hydrogen-Bonding in Binary Liquid Systems - Chloroform with Triethylamine, Dimethyl Sulfoxide, and Acetone. *Journal of Physical Chemistry,* 77**,** 2397-2400.

McLafferty, F. W., F. Tureček & F. Turecek. 1993. *Interpretation of mass spectra.* University science books.

Meier-Augenstein, W. & A. Schimmelmann (2019) A guide for proper utilisation of stable isotope reference materials(). *Isotopes Environ Health Stud,* 55**,** 113-128.

Melsbach, A., V. Ponsin, C. Torrento, C. Lihl, T. B. Hofstetter, D. Hunkeler & M. Elsner (2019) (13)C- and (15)N-Isotope Analysis of Desphenylchloridazon by Liquid Chromatography-

Isotope-Ratio Mass Spectrometry and Derivatization Gas Chromatography-Isotope-Ratio Mass Spectrometry. *Anal Chem,* 91**,** 3412-3420.

Menezes, O., Y. Yu, R. A. Root, S. Gavazza, J. Chorover, R. Sierra-Alvarez & J. A. Field (2021) Iron(II) monosulfide (FeS) minerals reductively transform the insensitive munitions compounds 2,4-dinitroanisole (DNAN) and 3-nitro-1,2,4-triazol-5-one (NTO). *Chemosphere,* 285**,** 131409.

Meyer, A. H. & M. Elsner (2013) 13C/12C and 15N/14N isotope analysis to characterize degradation of atrazine: evidence from parent and daughter compound values. *Environ Sci Technol,* 47**,** 6884-91.

Meyer, A. H., H. Penning & M. Elsner (2009) C and N isotope fractionation suggests similar mechanisms of microbial atrazine transformation despite involvement of different enzymes (AtzA and TrzN). *Environ Sci Technol,* 43**,** 8079-85.

Moores, L. C., S. J. Jones, G. W. George, D. L. Henderson & T. C. Schutt (2020a) Photo degradation kinetics of insensitive munitions constituents nitroguanidine, nitrotriazolone, and dinitroanisole in natural waters. *Journal of Photochemistry and Photobiology A: Chemistry,* 386.

Moores, L. C., A. J. Kennedy, L. May, S. M. Jordan, A. J. Bednar, S. J. Jones, D. L. Henderson, L. Gurtowski & K. A. Gust (2020b) Identifying degradation products responsible for increased toxicity of UV-Degraded insensitive munitions. *Chemosphere,* 240**,** 124958.

Murillo-Gelvez, J., D. M. Di Toro, H. E. Allen, R. F. Carbonaro & P. C. Chiu (2021) Reductive Transformation of 3-Nitro-1,2,4-triazol-5-one (NTO) by Leonardite Humic Acid and Anthraquinone-2,6-disulfonate (AQDS). *Environ Sci Technol.*

Murillo-Gelvez, J., K. P. Hickey, D. M. Di Toro, H. E. Allen, R. F. Carbonaro & P. C. Chiu (2019) Experimental Validation of Hydrogen Atom Transfer Gibbs Free Energy as a Predictor of Nitroaromatic Reduction Rate Constants. *Environ Sci Technol,* 53**,** 5816-5827.

Najafi, M. & A. K. Samangani (2011) Non-Isothermal Kinetic Study of the Thermal Decomposition of Melamine 3-Nitro-1,2,4-triazol-5-one Salt. *Propellants Explosives Pyrotechnics,* 36**,** 487-492.

Nanayakkara, C. E., P. M. Jayaweera, G. Rubasinghege, J. Baltrusaitis & V. H. Grassian (2014) Surface photochemistry of adsorbed nitrate: the role of adsorbed water in the formation of reduced nitrogen species on alpha-Fe2O3 particle surfaces. *J Phys Chem A,* 118**,** 158-66.

Nash, K. M., A. Rockenbauer & F. A. Villamena (2012) Reactive nitrogen species reactivities with nitrones: theoretical and experimental studies. *Chem Res Toxicol,* 25**,** 1581-97.

Nelson, A. (1948) Toxicological investigations of compounds proposed for use as insect repellents. C. Pathological examination. *J. Pharmac. Expl Therapeutics,* 93**,** 26-39.

Niedzwiecka, J. B., S. R. Drew, M. A. Schlautman, K. A. Millerick, E. Grubbs, N. Tharayil & K. T. Finneran (2017) Iron and Electron Shuttle Mediated (Bio)degradation of 2,4-Dinitroanisole (DNAN). *Environ Sci Technol,* 51**,** 10729-10735.

NIST. 2021. 3H-1,2,4-Triazol-3-one, 1,2-dihydro-5-nitro-. In *NIST Chemistry WebBook, RD69.* http://webbook.nist.gov/.

Nudelman, N. S. & D. Palleros (1983) Reactions of Nitroanisoles .4. Reaction of 2,4-Dinitroanisole and 2,6-Dinitroanisole with Cyclohexylamine - Evidence of a Dimer Nucleophile. *Journal of Organic Chemistry,* 48**,** 1607-1612.

Nyanhongo, G. S., A. Erlacher, M. Schroeder & G. M. Gübitz (2006) Enzymatic immobilization of 2,4,6-trinitrotoluene (TNT) biodegradation products onto model humic substances. *Enzyme and Microbial Technology,* 39**,** 1197-1204.

Oh, B. T., G. Sarath & P. J. Shea (2001) TNT nitroreductase from a Pseudomonas aeruginosa strain isolated from TNT-contaminated soil. *Soil Biology and Biochemistry,* 33**,** 875-881.

Ojeda, A. S., E. Phillips, S. A. Mancini & B. S. Lollar (2019) Sources of Uncertainty in Biotransformation Mechanistic Interpretations and Remediation Studies using CSIA. *Anal Chem,* 91**,** 9147-9153.

Oldenhuis, R., R. L. Vink, D. B. Janssen & B. Witholt (1989) Degradation of chlorinated aliphatic hydrocarbons by Methylosinus trichosporium OB3b expressing soluble methane monooxygenase. *Applied and Environmental Microbiology,* 55**,** 2819-2826.

Olivares, C., J. Liang, L. Abrell, R. Sierra-Alvarez & J. A. Field (2013) Pathways of reductive 2,4-dinitroanisole (DNAN) biotransformation in sludge. *Biotechnology and Bioengineering,* 110**,** 1595-1604.

Olivares, C. I., L. Abrell, R. Khatiwada, J. Chorover, R. Sierra-Alvarez & J. A. Field (2016a) (Bio)transformation of 2,4-dinitroanisole (DNAN) in soils. *J Hazard Mater,* 304**,** 214-21.

Olivares, C. I., R. Sierra-Alvarez, C. Alvarez-Nieto, L. Abrell, J. Chorover & J. A. Field (2016b) Microbial toxicity and characterization of DNAN (bio)transformation product mixtures. *Chemosphere,* 154**,** 499-506.

Östmark, H., H. Bergman & G. Åqvist (1993) The chemistry of 3-mtro-1,2,4-triazol-5-one (NTO): thermal decomposition. *Thermochimica Acta,* 213**,** 165-175.

Ou, C. J., J. Y. Shen, S. Zhang, Y. Mu, W. Q. Han, X. Y. Sun, J. S. Li & L. J. Wang (2016) Coupling of iron shavings into the anaerobic system for enhanced 2,4-dinitroanisole reduction in wastewater. *Water Research,* 101**,** 457-466.

Ou, C. J., S. Zhang, J. G. Liu, J. Y. Shen, Y. Liu, X. Y. Sun, J. S. Li & L. J. Wang (2015) Removal of multi-substituted nitroaromatic pollutants by zero valent iron: a comparison of performance, kinetics, toxicity and mechanisms. *Physical Chemistry Chemical Physics,* 17**,** 22072-22078.

Oum, K.W., M.J. Lakin, D.O. DeHaan, T. Brauers, B.J. Finlayson-Pitts (1998) Formation of Molecular Chlorine from the Photolysis of Ozone and Aqueous Sea-Salt Particles. Science, 279, 74-76.

Pak JW, Knoke KL, Noguera DR, Fox BG, Chambliss GH (2020) Transformation of 2,4,6-trinitrotoluene by purified Xenobiotic reductase B from *Pseudomonas fluorescens* I-C. *Applied and Environmental Microbiology* 66:4742-4750.

Pang, H., Q. Zhang, X. Lu, K. Li, H. Chen, J. Chen, X. Yang, Y. Ma, J. Ma & C. Huang (2019) Nitrite-Mediated Photooxidation of Vanillin in the Atmospheric Aqueous Phase. *Environ Sci Technol,* 53**,** 14253-14263.

Pati, S. G., H. E. Kohler & T. B. Hofstetter (2017) Characterization of Substrate, Cosubstrate, and Product Isotope Effects Associated With Enzymatic Oxygenations of Organic Compounds Based on Compound-Specific Isotope Analysis. *Methods Enzymol,* 596**,** 291-329.

Pati, S. G., H. P. Kohler, A. Pabis, P. Paneth, R. E. Parales & T. B. Hofstetter (2016) Substrate and Enzyme Specificity of the Kinetic Isotope Effects Associated with the Dioxygenation of Nitroaromatic Contaminants. *Environ Sci Technol,* 50**,** 6708-16.

Peng, C. Y., P. Y. Ayala, H. B. Schlegel & M. J. Frisch (1996) Using redundant internal coordinates to optimize equilibrium geometries and transition states. *Journal of Computational Chemistry,* 17**,** 49-56.

Peng, C. Y. & H. B. Schlegel (1993) Combining Synchronous Transit and Quasi-Newton Methods to Find Transition-States. *Israel Journal of Chemistry,* 33**,** 449-454.

Peng, X., T. Wang, W. Wang, A.R. Ravishankara, C. George, M. Xia, M. Cai, Q. Li, C.M. Salvador, C. Lau, X. Lyu, C.N. Poon, A. Mellouki, Y. Mu, M. Hallquist, A. Saiz-Lopez, H. Guo, H. Herrmann, C. Yu, J. Dai, Y. Wang, X. Wang, A. Yu, K. Leung, S. Lee, J. Chen (2022) Photodissociation of particulate nitrate as a source of daytime tropospheric Cl_2. *Nature Communications*, 13, 939.

Penning, H., C. J. Cramer & M. Elsner (2008) Rate-dependent carbon and nitrogen kinetic isotope fractionation in hydrolysis of isoproturon. *Environ Sci Technol,* 42**,** 7764-71.

Penning, H., S. R. Sorensen, A. H. Meyer, J. Aamand & M. Elsner (2010) C, N, and H isotope fractionation of the herbicide isoproturon reflects different microbial transformation pathways. *Environ Sci Technol,* 44**,** 2372-8.

Platten, W. E., D. Bailey, M. T. Suidan & S. W. Maloney (2010) Biological transformation pathways of 2,4-dinitro anisole and N-methyl paranitro aniline in anaerobic fluidized-bed bioreactors. *Chemosphere,* 81**,** 1131-1136.

Prior, S. D. & H. Dalton (1985) Acetylene as a suicide substrate and active site probe for methane monooxygenase from Methylococcus capsulatus (Bath). *FEMS Microbiology Letters,* 29**,** 105-109.

Qi, H., T. B. Coplen, H. Geilmann, W. A. Brand & J. K. Bohlke (2003) Two new organic reference materials for delta13C and delta15N measurements and a new value for the delta13C of NBS 22 oil. *Rapid Commun Mass Spectrom,* 17**,** 2483-7.

Qi, H., T. B. Coplen, S. J. Mroczkowski, W. A. Brand, L. Brandes, H. Geilmann & A. Schimmelmann (2016) A new organic reference material, l-glutamic acid, USGS41a, for delta(13) C and delta(15) N measurements - a replacement for USGS41. *Rapid Commun Mass Spectrom,* 30**,** 859-66.

Qi, H., M. Groning, T. B. Coplen, B. Buck, S. J. Mroczkowski, W. A. Brand, H. Geilmann & M. Gehre (2010) Novel silver-tubing method for quantitative introduction of water into high-temperature conversion systems for stable hydrogen and oxygen isotopic measurements. *Rapid Commun Mass Spectrom,* 24**,** 1821-7.

Qu, S., E. P. Kolodziej, S. A. Long, J. B. Gloer, E. V. Patterson, J. Baltrusaitis, G. D. Jones, P. V. Benchetler, E. A. Cole, K. C. Kimbrough, M. D. Tarnoff & D. M. Cwiertny (2013) Product-to-Parent Reversion of Trenbolone: Unrecognized Risks for Endocrine Disruption. *Science,* 342**,** 347-351.

Rao, B., W. Wang, Q. Cai, T. Anderson & B. Gu (2013) Photochemical transformation of the insensitive munitions compound 2,4-dinitroanisole. *Sci Total Environ,* 443**,** 692-9.

Ratti, M., S. Canonica, K. McNeill, J. Bolotin & T. B. Hofstetter (2015a) Isotope Fractionation Associated with the Indirect Photolysis of Substituted Anilines in Aqueous Solution. *Environ Sci Technol,* 49**,** 12766-73.

Ratti, M., S. Canonica, K. McNeill, J. Bolotin & T. B. Hofstetter (2015b) Isotope Fractionation Associated with the Photochemical Dechlorination of Chloroanilines. *Environ Sci Technol,* 49**,** 9797-806.

Ratti, M., S. Canonica, K. McNeill, P. R. Erickson, J. Bolotin & T. B. Hofstetter (2015c) Isotope fractionation associated with the direct photolysis of 4-chloroaniline. *Environ Sci Technol,* 49**,** 4263-73.

Reinnicke, S., A. Bernstein & M. Elsner (2010) Small and reproducible isotope effects during methylation with trimethylsulfonium hydroxide (TMSH): a convenient derivatization method for isotope analysis of negatively charged molecules. *Anal Chem,* 82**,** 2013-9.

Reinnicke, S., A. Simonsen, S. R. Sorensen, J. Aamand & M. Elsner (2012) C and N isotope fractionation during biodegradation of the pesticide metabolite 2,6-dichlorobenzamide (BAM): potential for environmental assessments. *Environ Sci Technol,* 46**,** 1447-54.

Richard, T. & J. Weidhaas (2014a) Biodegradation of IMX-101 explosive formulation constituents: 2,4-Dinitroanisole (DNAN), 3-nitro-1,2,4-triazol-5-one (NTO), and nitroguanidine. *Journal of Hazardous Materials,* 280**,** 372-379.

Richard, T. & J. Weidhaas (2014b) Biodegradation of IMX-101 explosive formulation constituents: 2,4-dinitroanisole (DNAN), 3-nitro-1,2,4-triazol-5-one (NTO), and nitroguanidine. *J Hazard Mater,* 280**,** 372-9.

Richard, T. & J. Weidhaas (2014c) Dissolution, sorption, and phytoremediation of IMX-101 explosive formulation constituents: 2,4-dinitroanisole (DNAN), 3-nitro-1,2,4-triazol-5-one (NTO), and nitroguanidine. *J Hazard Mater,* 280**,** 561-9.

Rockne, K. J., H. D. Stensel, R. P. Herwig & S. E. Strand (1998) PAH Degradation and Bioaugmentation by a Marine Methanotrophic Enrichment. *Bioremediation Journal,* 1**,** 209-222.

Rubasinghege, G., S. N. Spak, C. O. Stanier, G. R. Carmichael & V. H. Grassian (2011) Abiotic mechanism for the formation of atmospheric nitrous oxide from ammonium nitrate. *Environ Sci Technol,* 45**,** 2691-7.

Rutkowski, J., R. Cirincione & C. Patel. 2010. Common low-cost insensitive munitions explosive to replace TNT and Comp B. In *2010 Insensitive Munitions and Energetic Materials Technology Symposium, 11–14 October, Munich, Germany.*

Salter-Blanc, A. J., E. J. Bylaska, J. J. Ritchie & P. G. Tratnyek (2013) Mechanisms and Kinetics of Alkaline Hydrolysis of the Energetic Nitroaromatic Compounds 2,4,6-Trinitrotoluene (TNT) and 2,4-Dinitroanisole (DNAN). *Environmental Science & Technology,* 47**,** 6790-6798.

Schmidt, T. C., L. Zwank, M. Elsner, M. Berg, R. U. Meckenstock & S. B. Haderlein (2004) Compound-specific stable isotope analysis of organic contaminants in natural environments: a critical review of the state of the art, prospects, and future challenges. *Anal Bioanal Chem,* 378**,** 283-300.

Schreglmann, K., M. Hoeche, S. Steinbeiss, S. Reinnicke & M. Elsner (2013) Carbon and nitrogen isotope analysis of atrazine and desethylatrazine at sub-microgram per liter concentrations in groundwater. *Anal Bioanal Chem,* 405**,** 2857-67.

Schutt, T. C. & M. K. Shukla (2019) Predicting the Impact of Aqueous Ions on Fate and Transport of Munition Compounds in the Environment. *J Phys Chem A,* 123**,** 4973-4979.

Schuttlefield, J., G. Rubasinghege, M. El-Maazawi, J. Bone & V. H. Grassian (2008) Photochemistry of adsorbed nitrate. *J Am Chem Soc,* 130**,** 12210-1.

Shankar, M. V., S. Nelieu, L. Kerhoas & J. Einhorn (2008) Natural sunlight NO(3)(-)/NO(2)(-)-induced photo-degradation of phenylurea herbicides in water. *Chemosphere,* 71**,** 1461-8.

Shelton DR, Tiedje JM (1984) Isolation and partial characterization of bacteria in an anaerobic consortium that mineralizes 3-chlorobenzoic acid. *Applied and Environmental Microbiology* 48:840-848.

Shukla, A. K., P. Vishwakarma, S. N. Upadhyay, A. K. Tripathi, H. C. Prasana & S. K. Dubey (2009) Biodegradation of trichloroethylene (TCE) by methanotrophic community. *Bioresource Technology,* 100**,** 2469-2474.

Skarpeli-Liati, M., M. Jiskra, A. Turgeon, A. N. Garr, W. A. Arnold, C. J. Cramer, R. P. Schwarzenbach & T. B. Hofstetter (2011) Using nitrogen isotope fractionation to assess the oxidation of substituted anilines by manganese oxide. *Environ Sci Technol,* 45**,** 5596-604.

Smith, M. W. & M. D. Cliff (1999) NTO-based explosive formulations: a technology review. DSTO-TR-0796, Defence Science and Technology Organization, Australia. Available at: http://apps.dtic.mil.

Somerville, C. C., S. F. Nishino & J. C. Spain (1995) Purification and characterization of nitrobenzene nitroreductase from Pseudomonas pseudoalcaligenes JS45. *Journal of Bacteriology,* 177**,** 3837-3842.

Spear, R. J., C. N. Louey & M. G. Wolfson. 1989. A preliminary assessment of 3-nitro-1, 2, 4-triazol-5-one (NTO) as an insensitive high explosive. Materials Research Labs, Ascot Vale, Australia.

Steffan RJ, McClay K, Vainberg S, Condee CW, Zhang D (1997) Biodegradation of the Gasoline Oxygenates Methyl *tert*-Butyl Ether, Methyl *tert*-Butyl Ether, and *tert*-Amyl Methyl Ether by Propane-Oxidizing Bacteria. *Applied and Environmental Microbiology* 63: 4216-4222.

Su, H., C. Christodoulatos, B. Smolinski, P. Arienti, G. O'Connor & X. Meng (2019) Advanced Oxidation Process for DNAN Using UV/H2O2. *Engineering,* 5**,** 849-854.

Sviatenko, L., C. Kinney, L. Gorb, F. C. Hill, A. J. Bednar, S. Okovytyy & J. Leszczynski (2014) Comprehensive investigations of kinetics of alkaline hydrolysis of TNT (2,4,6-trinitrotoluene), DNT (2,4-dinitrotoluene), and DNAN (2,4-dinitroanisole). *Environ Sci Technol,* 48**,** 10465-74.

Sviatenko, L. K., S. I. Okovytyy, L. Gorb & J. Leszczynski (2015) Theoretical Study on Alkaline Hydrolysis of Trinitrotoluene: Later Steps. *Bulletin of Dnipropetrovsk University-Series Chemistry,* 23**,** 1-7.

Tatsumi, K., T. Doi, N. Koga, H. Yoshimura, H. Koga & T. Horiuchi (1981) Studies on Oxygen-Insensitive Nitrofuran Reductase in Escherichia coli B/r 1. *The Journal of Biochemistry,* 89**,** 855-859.

Taylor, S., D. B. Ringelberg, K. Dontsova, C. P. Daghlian, M. E. Walsh & M. R. Walsh (2013) Insights into the dissolution and the three-dimensional structure of insensitive munitions formulations. *Chemosphere,* 93**,** 1782-1788.

Taylor, S., M. E. Walsh, J. B. Becher, D. B. Ringelberg, P. Z. Mannes & G. W. Gribble (2017) Photo-degradation of 2,4-dinitroanisole (DNAN): An emerging munitions compound. *Chemosphere,* 167**,** 193-203.

Temple, T., M. Ladyman, N. Mai, E. Galante, M. Ricamora, R. Shirazi & F. Coulon (2018) Investigation into the environmental fate of the combined Insensitive High Explosive constituents 2,4-dinitroanisole (DNAN), 1-nitroguanidine (NQ) and nitrotriazolone (NTO) in soil. *Science of The Total Environment,* 625**,** 1264-1271.

Tenailleau, E. & S. Akoka (2007) Adiabatic 1H decoupling scheme for very accurate intensity measurements in 13C NMR. *J Magn Reson,* 185**,** 50-8.

Tenailleau, E., P. Lancelin, R. J. Robins & S. Akoka (2004) NMR approach to the quantification of nonstatistical 13C distribution in natural products: vanillin. *Anal Chem,* 76**,** 3818-25.

Terracciano, A., C. Christodoulatos, A. Koutsospyros, Z. Zheng, T.-L. Su, B. Smolinski, P. Arienti & X. Meng (2018) Degradation of 3-nitro-1,2,4-trizole-5-one (NTO) in wastewater with UV/H2O2 oxidation. *Chemical Engineering Journal,* 354**,** 481-491.

Tobler, N. B., T. B. Hofstetter & R. P. Schwarzenbach (2007) Assessing iron-mediated oxidation of toluene and reduction of nitroaromatic contaminants in anoxic environments using compound-specific isotope analysis. *Environmental Science & Technology,* 41**,** 7773-7780.

Tupa PR, Matsuda H (2018) Comparative Proteomic Analysis of Propane Metabolism in *Mycobacterium* sp. Strain ENV421 and *Rhodococcus* sp. Strain ENV425. *J. Molecular Microbiology and Biotechnology* 28:107-115.

Ulrich, B. A., M. Palatucci, J. Bolotin, J. C. Spain & T. B. Hofstetter (2018) Different Mechanisms of Alkaline and Enzymatic Hydrolysis of the Insensitive Munition Component 2,4-Dinitroanisole Lead to Identical Products. *Environmental Science & Technology Letters,* 5**,** 456-461.

Valiauga, B., L. Misevičienė, M. H. Rich, D. F. Ackerley, J. Šarlauskas & N. Čėnas (2018) Mechanism of Two-/Four-Electron Reduction of Nitroaromatics by Oxygen-Insensitive Nitroreductases: The Role of a Non-Enzymatic Reduction Step. *Molecules,* 23**,** 1672.

Vione, D., V. Maurino, C. Minero & E. Pelizzetti (2005) Aqueous atmospheric chemistry: Formation of 2,4-dinitrophenol upon nitration of 2-nitrophenol and 4-nitrophenol in solution. *Environmental Science & Technology,* 39**,** 7921-7931.

Vione, D., V. Maurino, C. Minero, E. Pelizzetti, M. A. Harrison, R. I. Olariu & C. Arsene (2006) Photochemical reactions in the tropospheric aqueous phase and on particulate matter. *Chem Soc Rev,* 35**,** 441-53.

Vione, D., C. Minero, F. Housari & S. Chiron (2007) Photoinduced transformation processes of 2,4-dichlorophenol and 2,6-dichlorophenol on nitrate irradiation. *Chemosphere,* 69**,** 1548-54.

Vogt, C., C. Dorer, F. Musat & H. H. Richnow (2016) Multi-element isotope fractionation concepts to characterize the biodegradation of hydrocarbons - from enzymes to the environment. *Curr Opin Biotechnol,* 41**,** 90-98.

Walsh, M. R., M. E. Walsh, C. A. Ramsey, S. Thiboutot, G. Ampleman, E. Diaz & J. E. Zufelt (2014) Energetic Residues from the Detonation of IMX-104 Insensitive Munitions. *Propellants, Explosives, Pyrotechnics,* 39**,** 243-250.

Wang, C., M. E. Fuller, L. J. Heraty, P. B. Hatzinger & N. C. Sturchio (2021a) Photocatalytic mechanisms of 2,4-dinitroanisole degradation in water deciphered by C and N dual-element isotope fractionation. *Journal of Hazardous Materials* 411, 125109.

Wang, C., L. J. Heraty, A. F. Wallace, C. Liu, X. Li, G. P. McGovern, J. Horita, M. E. Fuller, P. B. Hatzinger & N. C. Sturchio (2021b) Position-specific isotope effects during alkaline hydrolysis of 2,4-dinitroanisole resolved by compound-specific isotope analysis, 13C NMR, and density-functional theory. *Chemosphere***,** 130625.

Wang, C., L. J. Heraty, H. Li, , M. E. Fuller, P. B. Hatzinger & N. C. Sturchio (2021c) Method for derivatization and isotopic analysis of the insensitive munition compound 3-nitro-1,2,4-triazol-5-one (NTO)*. Journal of Hazardous Materials Letters* 2, 100044.

Wang, C., A. F. Wallace, L. Heraty, H. Qi & N. C. Sturchio (2020a) Alkaline hydrolysis pathway of 2,4-dinitroanisole verified by ^{18}O tracer experiment. *J Hazard Mater,* 396**,** 122627.

Wang, H., H. Zhou, J. Ma, J. Nie, S. Yan & W. Song (2020b) Triplet Photochemistry of Dissolved Black Carbon and Its Effects on the Photochemical Formation of Reactive Oxygen Species. *Environ Sci Technol,* 54**,** 4903-4911.

Wang, Q., G. M. Garrity, J. M. Tiedje & J. R. Cole (2007) Bayesian Classifier for Rapid Assignment of rRNA Sequences into the New Bacterial Taxonomy. *Applied and Environmental Microbiology,* 73**,** 5261-5267.

Wang, S.-Q., Y.-F. Wang & Z. Xu (2019) Tetrazole hybrids and their antifungal activities. *European Journal of Medicinal Chemistry,* 170**,** 225-234.

Wang, X. S., L. Li, D. Q. Yuan, Y. B. Huang & R. Cao (2018) Fast, highly selective and sensitive anionic metal-organic framework with nitrogen-rich sites fluorescent chemosensor for nitro explosives detection. *J Hazard Mater,* 344**,** 283-290.

Ward, A. S., D. M. Cwiertny, E. P. Kolodziej & C. C. Brehm (2015) Coupled reversion and stream-hyporheic exchange processes increase environmental persistence of trenbolone metabolites. *Nat Commun,* 6**,** 7067.

Weidhaas, J., A. Panaccione, A. S. Bhattacharjee, R. Goel, A. Anderson & S. P. Acharya (2018) Whole community transcriptome of a sequencing batch reactor transforming 2, 4-dinitroanisole (DNAN) and 3-nitro-1, 2, 4-triazol--5-one (NTO). *Biodegradation,* 29**,** 71-88.

Xu, L., Y. Sun, L. Gan, J. Han, P. Wang, L. Yu, X. Mei, W. Li, B. Lyu, C. Pei & W. Chu (2019) Utilization of photochemical circulation between NO3− and NO2− in water to degrade photoinert dimethyl phthalate: Influence of organic media and mechanism study. *Applied Catalysis B: Environmental,* 259.

Yang, C., M. Dong, Y. Yuan, Y. Huang, X. Guo & C. Qiao (2007) Reductive transformation of parathion and methyl parathion by Bacillus sp. *Biotechnology Letters,* 29**,** 487-493.

Yuan, C., M. Chakraborty, S. Canonica, L. K. Weavers, C. M. Hadad & Y. P. Chin (2016) Isoproturon Reappearance after Photosensitized Degradation in the Presence of Triplet Ketones or Fulvic Acids. *Environ Sci Technol,* 50**,** 12250-12257.

Zewail, A. H. (1988) Laser femtochemistry. *Science,* 242**,** 1645-53.

Zewail, A. H. (2000) Femtochemistry: Atomic-Scale Dynamics of the Chemical Bond Using Ultrafast Lasers (Nobel Lecture) Copyright((c)) The Nobel Foundation 2000. We thank the Nobel Foundation, Stockholm, for permission to print this lecture. *Angew Chem Int Ed Engl,* 39**,** 2586-2631.

Zhao, Y. & D. G. Truhlar (2007) The M06 suite of density functionals for main group thermochemistry, thermochemical kinetics, noncovalent interactions, excited states, and transition elements: two new functionals and systematic testing of four M06-class functionals and 12 other functionals. *Theoretical Chemistry Accounts,* 120**,** 215-241.

Zhou, X., C. Lai, D. Huang, G. Zeng, L. Chen, L. Qin, P. Xu, M. Cheng, C. Huang, C. Zhang & C. Zhou (2018) Preparation of water-compatible molecularly imprinted thiol-functionalized activated titanium dioxide: Selective adsorption and efficient photodegradation of 2, 4-dinitrophenol in aqueous solution. *J Hazard Mater,* 346**,** 113-123.

Zuo, Y., Y. Deng (1998) The near-UV absorption constants for nitrite ion in aqueous solution. *Chemosphere*, 36, 181-188.

Appendix A. Supplemental information

Supplemental Tables

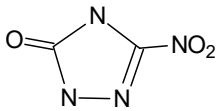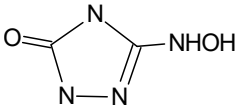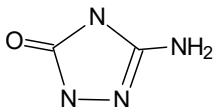Table S1. Chemical structures of NTO, DNAN, and their respective breakdown products.

Name	Alt Name	Abbrev	Alt Abrrev	Structure
5-nitro-1,2,4-triazol-3-one	nitrotriazolone	NTO		
3-hydroxylamino-1,2,4-triazol-5-one		HTO		
3-amino-1,2,4-triazol-5-one		ATO		

Table S1 (cont.)
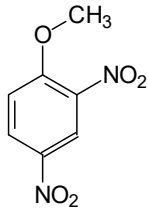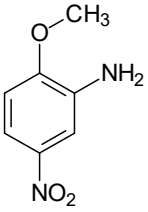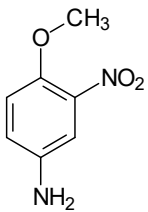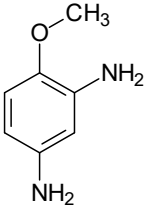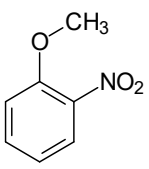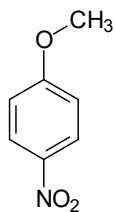
Name	Alt Name	Abbrev	Alt Abrrev	Structure
2,4-dinitroanisole		DNAN		
2-amino-4-nitroanisole	2-methoxy-5-nitroaniline	2ANAN	MENA	
4-amino-2-nitroanisole	4-methoxy-3-nitroaniline	4ANAN		
2,4-diaminoanisole (analytical standard and sulfate)		DAAN		
2-nitroanisole	o-nitroanisole	2-NA		
4-nitroanisole	m-nitroanisole	4-NA		

Table S1 (cont.)
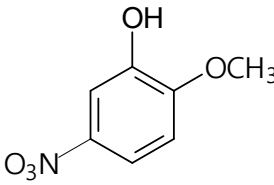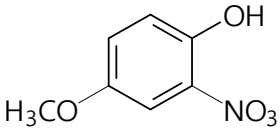
Name	Alt. Name	Abbrev	Alt. Abbrev.	Structure
2-methoxy-5-nitrophenol	5-Nitroguaiacol	2-M-5-NP		
4-methoxy-2-nitrophenol	methoxybenzene	4-M-2-NP		

Table S2. Side reaction steady-state kinetics in the presence of DNAN.

Reactants	Oxygen Consumption Rate (nmoles/min/mg)
MMOR + NADH	49
MMOR + NADH + DNAN (96 µM)	300
MMOR + NADH + DNAN (480 µM)	1042
NADH + DNAN (96 µM)	0

Table S3. sMMO single turnover transient kinetics.

Substrate	Concentration (mM)	$Q_{formation}$ (s^{-1})	Q_{decay} (s^{-1})
No substrate	--	2.4	0.03
Methane[1]	0.1	2.8	1.50
	0.7	3.0	6.60
Furan[1]	0.1	3.2	0.40
	1.0	2.3	4.90
DNAN	0.2	2.2	0.04
NTO	1.1	2.2	0.04

[1]Methane and furan are known sMMO substrates.

Supplemental Figures

Figure S1. Representative methane addition (spikes in line trace) and methane consumption by the IH57 and Dahlgren consortia and pure culture OB3b. Note difference in x-axis values. Initial culture OD was 0.4.
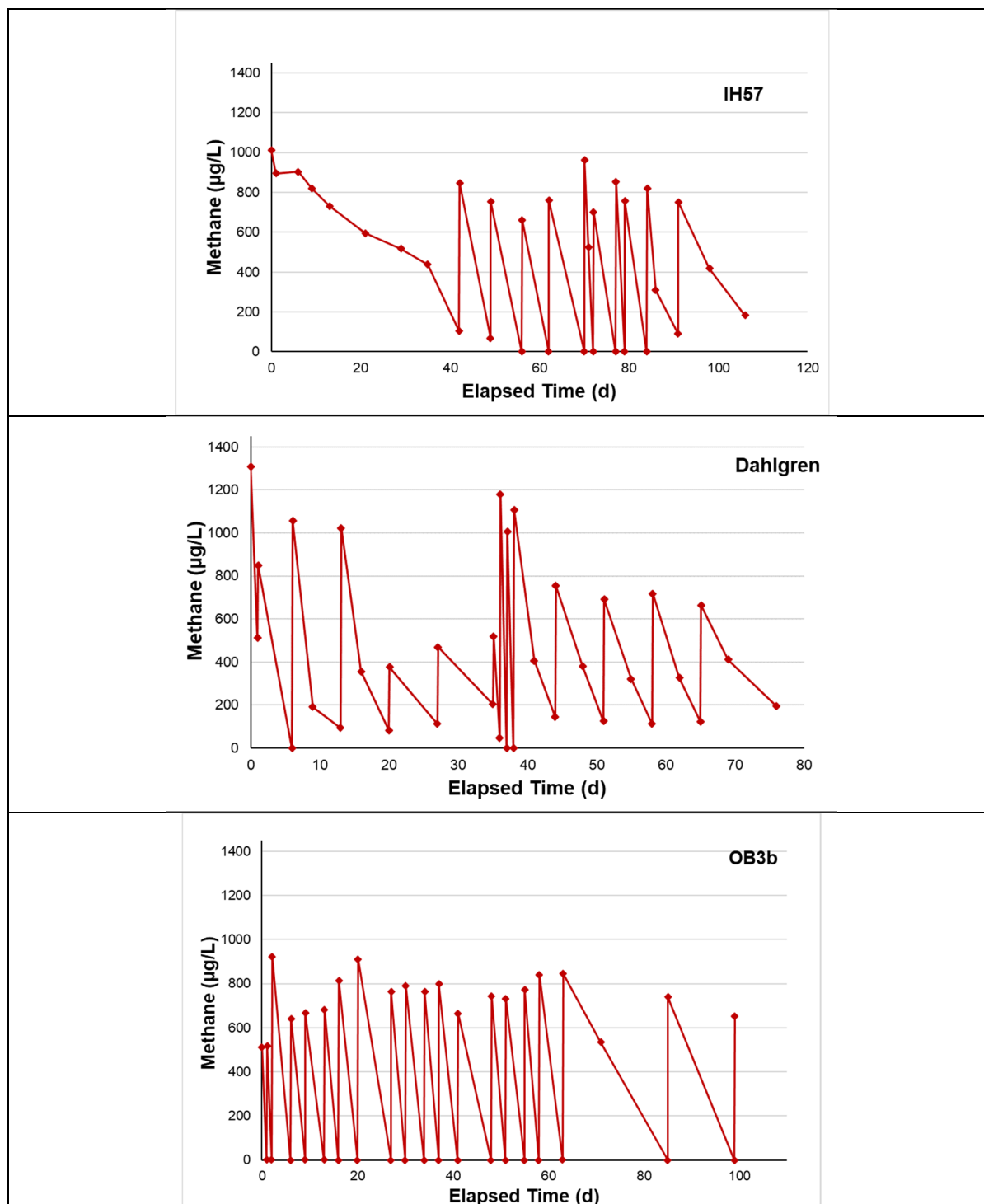
Figure S2. Results of next generation sequencing of the IH57 and Dahlgren methanotrophic consortia.

Dominant genera as relative percent of population detected in the IH57 consortium.

Dominant genera as relative percent of population detected in the Dahlgren consortium.
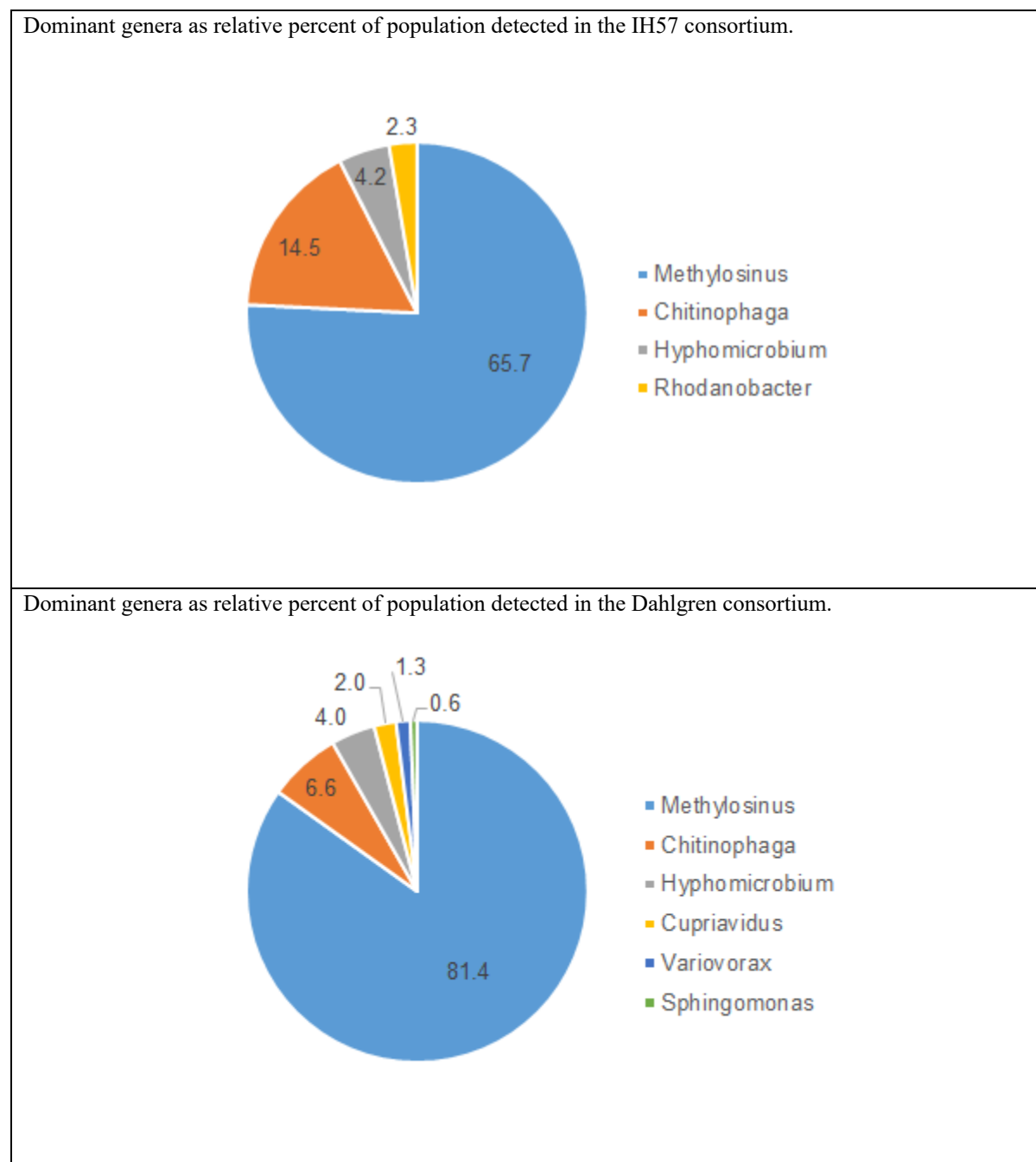
Figure S3. Degradation of NTO and DNAN by IH57 and Dahlgren and calculated equilibrium dissolved oxygen concentrations over time in nitrogen-free medium. Methane spikes were 3-5% (v:v) during this experiment. Initial culture OD was 1.0.
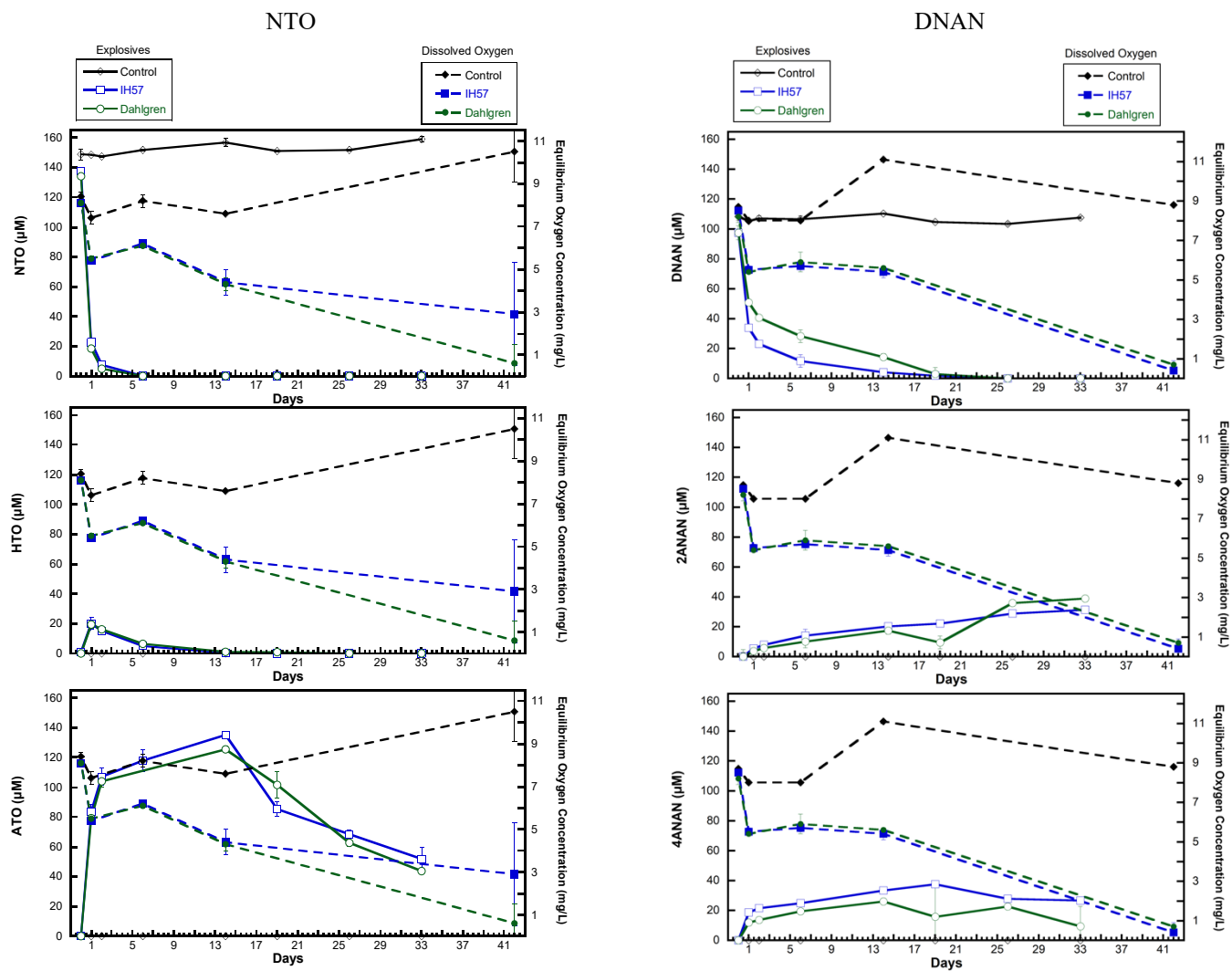
Figure S4. Degradation of NTO and DNAN by IH57 and Dahlgren methanotrophic consortia in the presence and absence of acetylene. Methane spikes were 3-5% (v:v) during this experiment. Initial culture OD was 0.4.
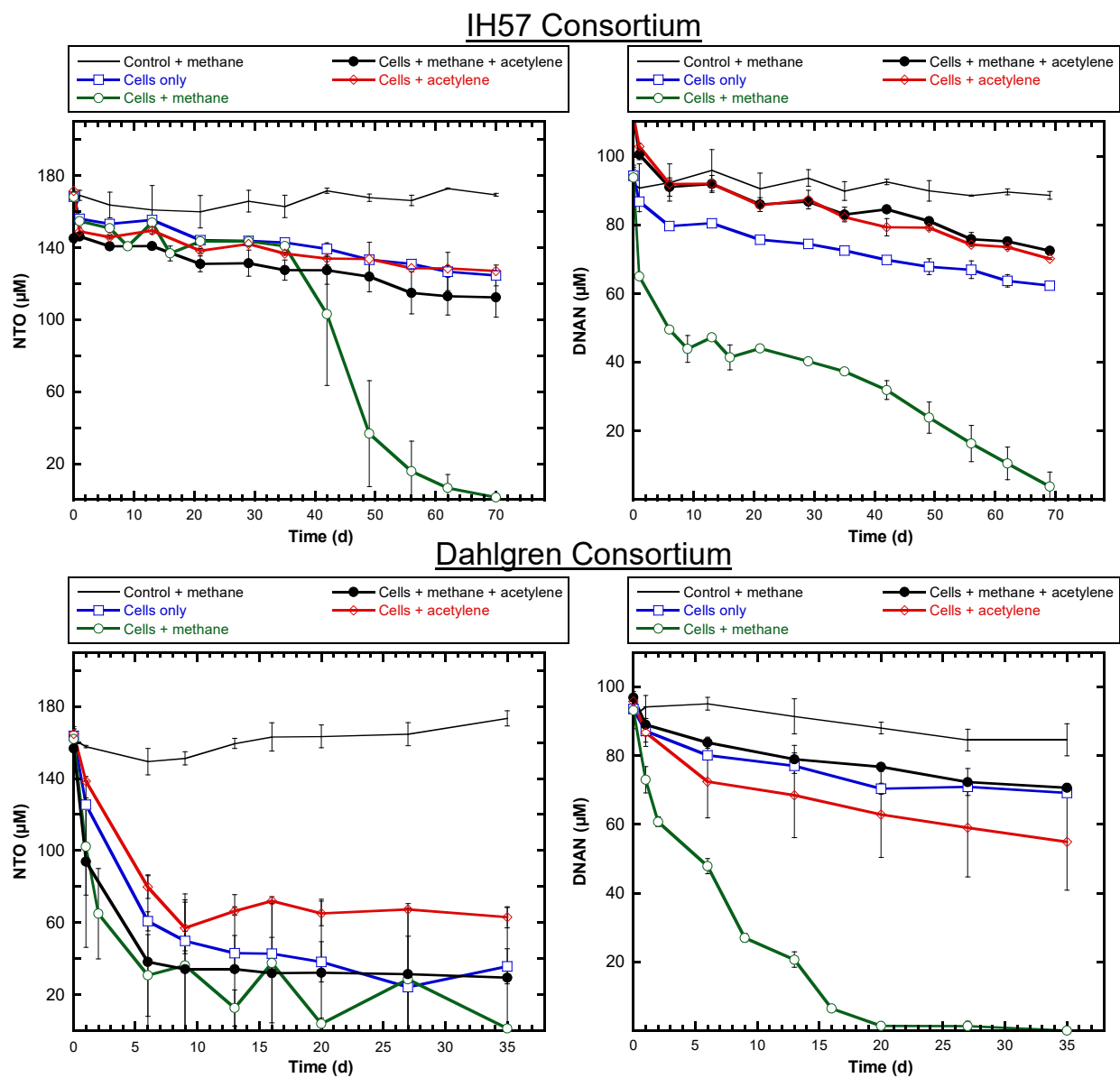
Figure S5. Degradation of NTO by IH57 and Dahlgren methanotrophic consortia grown on either methane or formate, then supplied with no carbon source, methane, or formate (900 mg/L). No cell controls were are also presented. Methane spikes were 3-5% (v:v) during this experiment. Initial culture OD was 0.3.

GROWTH ON >   Methane   Formate
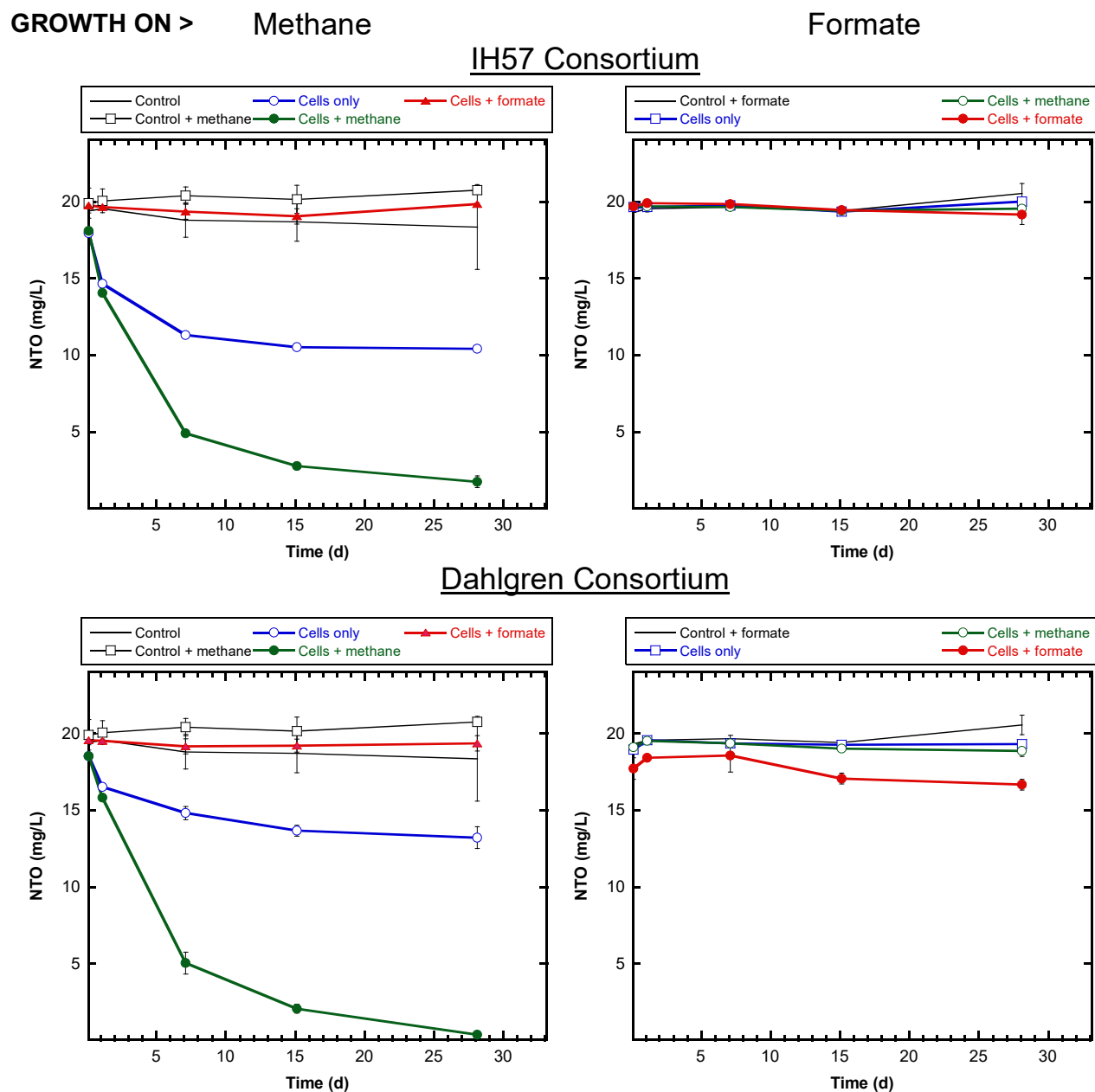
IH57 Consortium

Dahlgren Consortium

Figure S6. Degradation of DNAN by IH57 and Dahlgren methanotrophic consortia grown on either methane or formate, then supplied with no carbon source, methane, or formate (900 mg/L). One replicate of the control (no cells) was lost, and the no cells + methane controls became contaminated during the study, so those results are not presented. Methane spikes were 3-5% (v:v) during this experiment. Initial culture OD was 0.4.
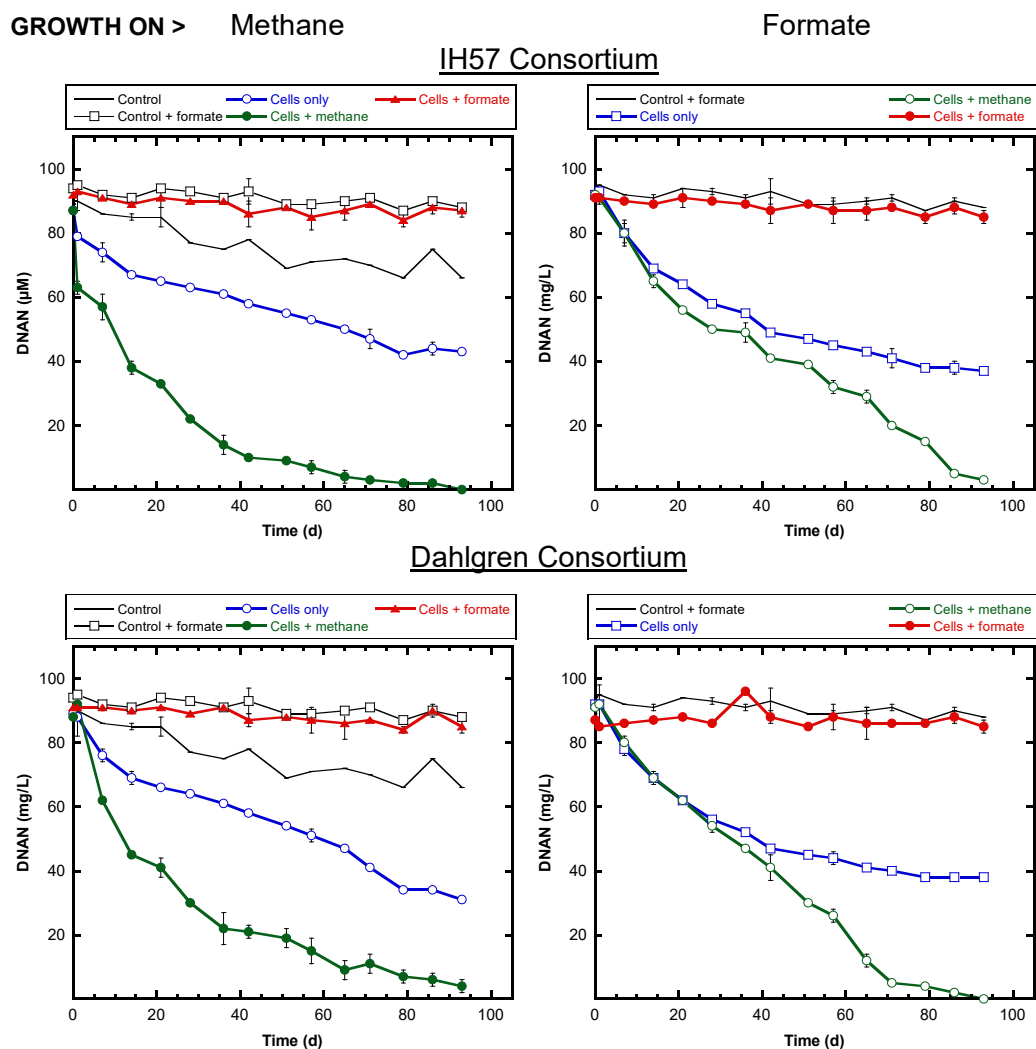
Figure S7. Degradation of NTO and DNAN by OB3b in the presence and absence of the nitroreductase inhibitors dicoumarol and 2-IBA. Data represent average ± standard deviation of duplicate bottles. Methane spikes were 3-5% (v:v) during this experiment. Initial culture OD was 0.4.
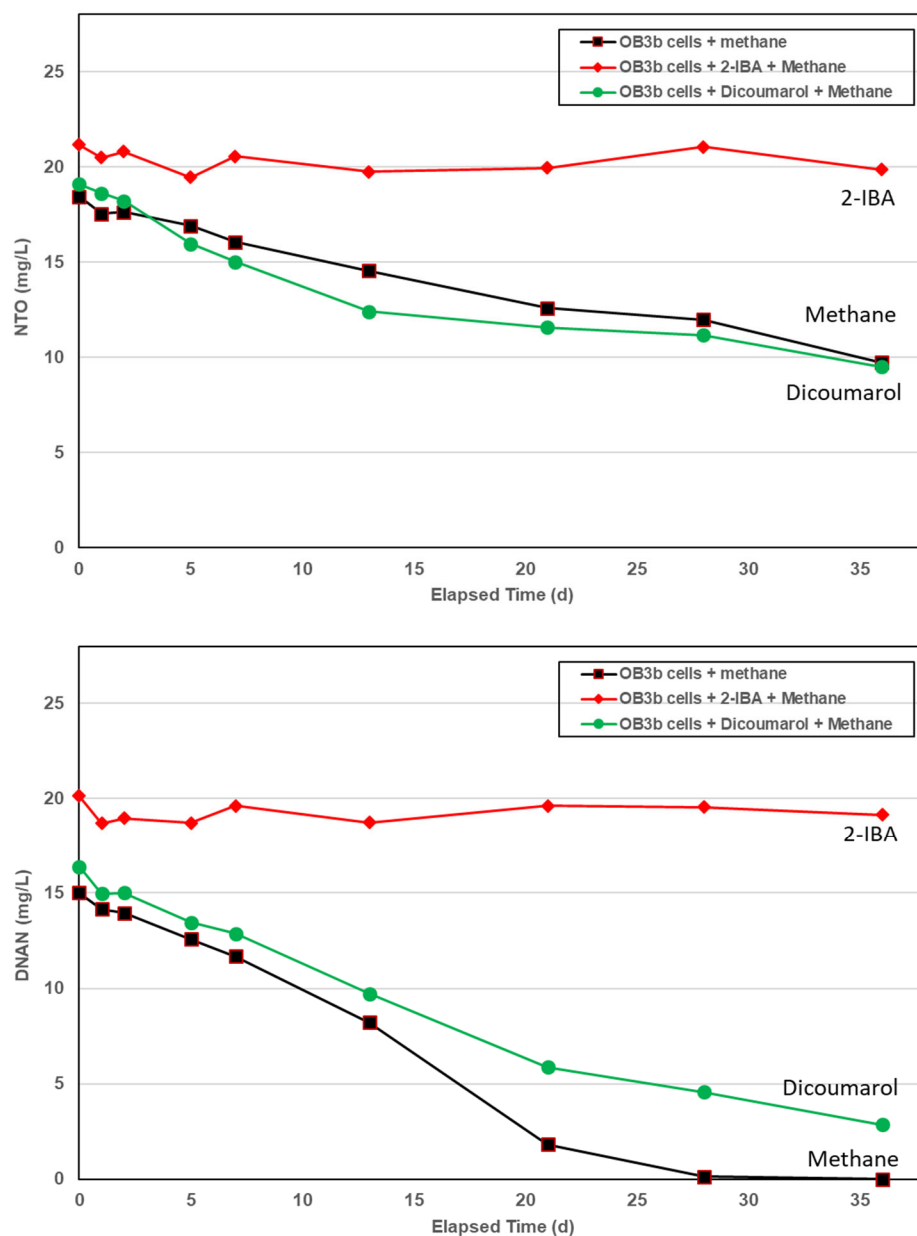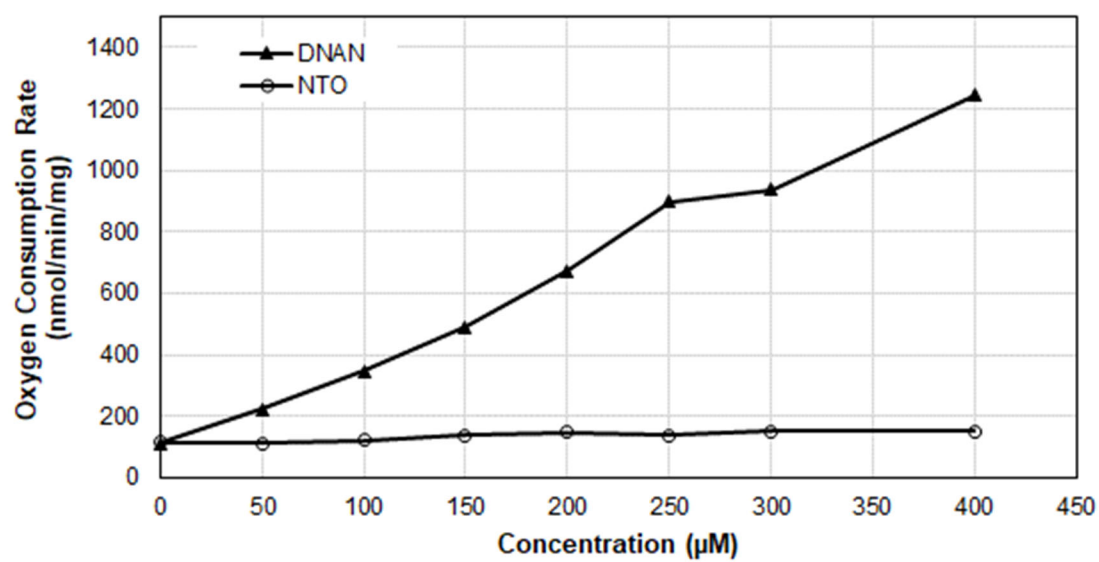
Figure S8. Oxygen consumption by purified *Mt* sMMO during steady-state kinetic assays in the presence of NTO and DNAN.

Appendix B: List of scientific/technical publications

1. Articles in peer-reviewed journals

Fuller M, Rezes R, Hedman P, Jones J, Sturchio NC, Hatzinger P, 2021. Biotransformation of the insensitive munition constituents 3-nitro-1,2,4-triazol-5-one (NTO) and 2,4-dinitroanisole (DNAN) by aerobic methane-oxidizing consortia and pure cultures. *Journal of Hazardous Materials* 407:24341. doi.org/10.1016/j.hazmat.2020.124341.

Wang CL, Wallace AF, Heraty LJ, Qi H, Sturchio NC, 2020. Alkaline Hydrolysis Pathway of 2,4-Dinitroanisole Verified by ^{18}O Tracer Experiment. *Journal of Hazardous Materials* 396:122627.

Wang C, Fuller ME, Heraty LJ, Hatzinger PB, Sturchio NC, 2021a. Photocatalytic mechanisms of 2,4-dinitroanisole degradation in water deciphered by C and N dual-element isotope fractionation. *Journal of Hazardous Materials* 411:125109, doi.org/10.1016/j.jhazmat.2021.125109.

Wang CL, Heraty LJ, Wallace AF, Liu C, Li X, McGovern GP, Horita J, Fuller ME, Hatzinger PB, Sturchio NC, 2021b. Position-specific isotope effects during alkaline hydrolysis of 2,4-dinitroanisole resolved by compound-specific isotope analysis, ^{13}C NMR, and density-functional theory. *Chemosphere* 280:130625.

Wang CL, Heraty LJ, Li H, Fuller ME, Hatzinger PB, Sturchio NC, 2021c. Method for derivatization and isotopic analysis of the insensitive munition compound 3-nitro-1,2,4-triazol-5-one (NTO). *Journal of Hazardous Materials Letters* 2:100044.

Note: Two additional manuscripts are in preparation to be submitted for publication.

2. Technical reports

Arnold WA, Hofstetter TB, Sturchio NC, 2021. Guidance for using Compound Specific Isotope Analysis (CSIA) for the Assessment of Transformation of Nitroaromatic Explosives and RDX. *ESTCP Guidance Document*, Project ER-2618. Available at: https://www.serdp-estcp.org/Program-Areas/Environmental-Restoration/Contaminated-Groundwater/Persistent-Contamination/ER-2618.

3. Conference/symposium presentations/abstracts

Wang C, NC Sturchio, ME Fuller, LJ Heraty, PB Hatzinger, 2022. Deciphering Abiotic and Biotic Transformations of Insensitive Munitions Compounds via Stable Isotope Analysis. *Gordon Research Conference, Environmental Sciences: Water*, Holderness School, Holderness, New Hampshire, USA, Jun. 19 - 24, 2022.

Wang C, LJ Heraty, AF Wallace, ME Fuller, PB Hatzinger, NC Sturchio, 2022. Understanding the photochemical transformation mechanisms of insensitive munitions DNAN and NTO via ^{13}C- and ^{15}N- compound-specific isotope analysis. *American Chemical Society 2022 Spring Meeting*, San Diego, CA, USA, Mar. 20 - 24, 2022.

Hatzinger PB, Sturchio NC, Heraty LJ, Wang C, Fuller ME, 2021. Application of Stable Isotope Analysis for Assessing the Environmental Fate of Insensitive Munitions. *REMTEC Europe*, September 2021 [virtual presentation].

Wang CL, Heraty LJ, Fuller ME, Hatzinger PB, Sturchio NC, 2021. C and N isotope effects during UV-induced photocatalytic degradation of 2,4-dinitroanisole (DNAN) and 3-nitro-1,2,4-triazol-5-one (NTO). *Goldschmidt 2021 Conference,* Lyon, France [virtual presentation].

Fuller ME, Hatzinger PB, Rezes RT, Hedman PC, Sturchio NC, Jones JC, 2020. Aerobic degradation of NTO and DNAN by Methanotrophic Bacteria. *SERDP-ESTCP Symposium 2020,* Washington D.C. [virtual presentation].

Sturchio NC, Wang CL, Heraty LJ, Fuller ME, Hatzinger PB, 2020. Application of C and N Stable Isotope Analysis to Evaluate Biotic and Abiotic Degradation of DNAN and NTO (ER-2726). *SERDP-ESTCP Symposium 2020,* Washington, D.C. [virtual presentation].

Wang CL, Heraty LJ, Fuller ME, Hatzinger PB, Sturchio NC, 2020. Abiotic and biotic transformation mechanisms of DNAN and NTO resolved by compound-specific isotopic analysis of C and N. *SERDP-ESTCP Symposium 2020,* Washington, D.C. [virtual presentation].

Wang CL, Heraty LJ, Fuller ME, Hatzinger PB, Sturchio NC, 2019. Development and application of C and N isotope analysis to investigate abiotic and biotic transformation mechanisms of DNAN and NTO. *SERDP-ESTCP Symposium 2019,* Washington, D.C. [poster presentation].

Sturchio NC, 2019. Application of C and N stable isotope analysis to evaluate biotic and abiotic degradation of DNAN and NTO. *Abiotic Workshop*, Minneapolis, MN, October 2019 [Invited talk].

Sturchio NC, 2019. Application of C and N stable isotope analysis to evaluate biotic and abiotic degradation of DNAN and NTO. IPR Presentation, Washington, D.C.

Wang CL, Heraty LJ, Wallace AF, Fuller ME, Hatzinger PB, Sturchio NC, 2020. Application of compound-specific isotope analysis combined with molecular modeling to evaluate abiotic and biotic degradation of DNAN and NTO. *American Chemical Society 2020 Spring Meeting,* Philadelphia, PA [virtual presentation].

Sturchio, NC, 2018. Application of C and N Stable Isotope Analysis to Evaluate Biotic and Abiotic Degradation of DNAN and NTO. *SERDP-ESTCP Symposium,* Washington D.C. [Invited talk].

Wang C, Heraty L, Sturchio NC, Fuller M, Hatzinger P, 2018. Development and Application of C and N Isotope Analysis in Investigating Alkaline Hydrolysis Mechanism of 2, 4-Dinitroanisole. *Abstracts of the 2018 Goldschmidt Conference,* Boston, MA [poster presentation].

Wang CL, Heraty LJ, Sturchio NC, Fuller ME, Hatzinger PB, 2018. Development and application of C and N isotope analysis to investigate abiotic and biotic transformation mechanisms of DNAN and NTO. *SERDP-ESTCP Symposium 2018,* Washington, D.C. [poster presentation].